INAUGURAL – DISSERTATION

zur
Erlangung der Doktorwürde
der
Naturwissenschaftlich-Mathematischen Gesamtfakultät
der
Ruprecht-Karls-Universität Heidelberg

vorgelegt von
Asha E. Roberts LLB BSc
aus Warwick, Queensland, Australien

Tag der mündlichen Prüfung: 20. Juli 2018

Experimental and computational investigations into the ligand field effects on the anisotropy of mononuclear 4f complexes

Gutachter:
Prof. Dr. Peter Comba
Prof. Dr. Rüdiger Klingeler

This thesis has been accomplished at the Institute of Inorganic Chemistry at Heidelberg University in the time period of July 2015 to July 2018 under the supervision of Prof. Dr. Peter Comba and Prof. Dr. Rüdiger Klingeler. Experimental work has also been carried out under the supervision of Prof. Dr. Mark Riley at the University of Queensland, Brisbane, Australia in March and April of 2016 and April 2018. The high frequency electron paramagnetic resonance (HF-EPR) experiments were performed by Johannes Werner and Dr. Changhyun Koo under the supervision of Prof. Dr. Rüdiger Klingeler. Pulse magnetisation measurements were carried out by Denis I. Gorbunov in the Hochfeld-Magnetlabor Dresden (HLD-EMFL) at the Helmholtz-Zentrum Dresden-Rossendorf, Dresden.

Part of this thesis has been published in:

- Comba, P.; Daumann, L. J.; Klingeler, R.; Koo, C.; Riley, M. J.; Roberts, A. E.; Wadepohl, H.; Werner, J., Correlation of Structural and Magnetic Properties in a Set of Mononuclear Lanthanide Complexes, *Chem. Eur. J.* **2018**, *24*, 5319-5330.

Ligands discussed in this thesis

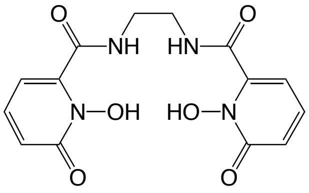

L^{1}
(2LI)

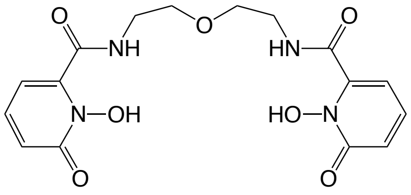

L^{2}
(5LIO)

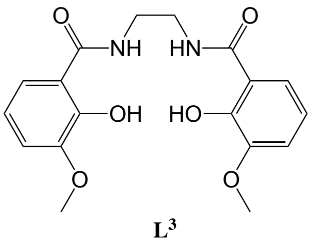

L^{3}

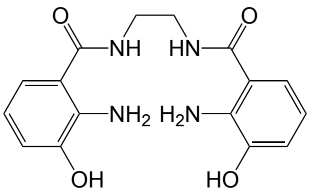

L^{4}

Abbreviations

A	absorbance
ac	alternating current
ANO-RCC	atomic natural orbitals relativistically core-correlated
AO	atomic orbital
AOM	atomic overlap model
B	external magnetic field
BTPR	bisaugmented trigonal prism
CASSCF	complete active space SCF
CF	crystal field
CI	configuration interaction
Cp	1,2,4-tri(tert-butyl)cyclopentadienide
CU	cube
D	axial ZFS parameter
d	day
dc	direct current
DCM	dichloromethane
DKH	Douglas-Kroll-Hess
DMF	N,N-dimethylformamide
E	energy / rhombic ZFS parameter
EPR	electron paramagnetic resonance
eq	mole equivalent
eq.	equivalents
Eq.	equation
ESO	extended Stevens operators
et al.	et alii
Et_2O	diethyl ether
g_J	Landé g factor
h	hour(s)
HF	Hartree-Fock
HF-EPR	high frequency EPR
J	total angular momentum quantum number
JBTPR	Johnson polyhedron bisaugmented trigonal prism (regular faces)
JSD	Johnson polyhedron snub disphenoid (regular faces)
KD	Kramers doublet
L	orbital angular momentum quantum number
LF	ligand field
μ_B	Bohr magneton
m/z	mass-to-charge ratio

MC-SCF	multi-configurational SCF
MCD	magnetic circular dichroism
MeOH	methanol
MO	molecular orbital
MS	mass spectrometry
NMR	nuclear magnetic resonance
o	ortho
p	para
Pc	phthalocyanine
PTFE	polytetrafluoroethylene
Py	pyridine
RASSI	restricted active space state interaction
rt	room temperature
S	spin quantum number
SAPR	square antiprism
SCF	self-consistent field
SMM	single molecule magnet
SOC	spin-orbit coupling
SQUID	superconducting quantum interference device
T	Tesla
TDD	triangular dodecahedron
ZFS	zero-field splitting
RASSCF	restricted active space SCF

Abstract

The aim of this thesis is to combine experimental and computational methods in order to gain a deeper understanding of the ligand field effects of lanthanide(III) ions. Because the magnetic properties of mononuclear lanthanide complexes are determined primarily by the electronic structure of the isolated ion, a thorough understanding of the ligand field effects is essential in order to rationally design new complexes to function as single molecule magnets (SMMs). In this work a variety of experimental techniques are utilised in combination with a detailed theoretical analysis by way of a highly powerful *ab initio* approach. The approach involves the determination of CASSCF wave functions, from which spin-orbit coupled states are calculated by construction of a state interaction matrix. The magnetic properties are determined by the effective Hamiltonian theory, which yields parameters such as the electron-Zeeman interaction g and also ligand field parameters. Importantly, the validation of the *ab initio* approach is illustrated not only by comparison with magnetometric results but also by using the highly sensitive optical spectroscopic technique, magnetic circular dichroism. Thorough ligand field analysis of the experimental data was possible utilising the *ab initio* calculated ligand field parameters, illustrating the accuracy of the computational method.

The first part of this thesis investigates the sensitivity of the electronic structure of terbium(III) and dysprosium(III) to very slight changes of the ligand field. Two different ligands, L^1 and L^2, were employed that provide coordination spheres comprised of eight homoleptic oxygen donors, meaning the differences in the ligand field of these complexes is purely of geometrical origin. Differences in the magnetic susceptibility of all four complexes revealed different splitting of the ground state J multiplet induced by the two ligand fields. Loose powder magnetisation measurements indicated differences in the ground state g values, which were in qualitative agreement with the calculated values. High frequency electron paramagnetic resonance (HF-EPR) studies of the terbium(III) complexes provided insight into the composition of the ground state M_J levels. *Ab initio* calculations are utilised to rationalise the experimental results and further illustrate the effect of the structural features on the electronic and magnetic properties of the different complexes. Magnetic circular dichroism (MCD) spectra of the dysprosium(III) complexes illustrate fine details highlighting the differences in the splitting of the J multiplets and allowed for a thorough ligand field analysis. The analysis utilised the ab initio calculated ligand field parameters in order to produce a reasonable fit of the experimental data, illustrating the accuracy of the computational methods. The calculated properties indicated no significant SMM behaviour of the

different complexes, leading to the design of a new set of ligands based on L^1, which are explored in the second part of this thesis.

The second part of this thesis focuses on the difference in f-electron density of dysprosium(III) and erbium(III), and how more pronounced differences in the ligand field affect the electronic structures of the oblate and prolate ions, respectively. Two ligands were designed that, upon coordination to a lanthanide(III) ion, provide strong electron density in the axial L^3 and equatorial regions L^4, respectively. The calculated properties indicate that the more strongly axial ligand field promotes strong anisotropy and a large magnetic blocking of dysprosium(III), whereas the strongly equatorial ligand field induces extensive mixing of the M_J states and a large transversal moment. Conversely, the properties of the complexes of erbium(III), having a prolate f electron density, produce the opposite effect. MCD spectra of dysprosium(III) and erbium(III) complexes of ligands L^3 and L^1 are compared. As in the first part of the thesis, a thorough ligand field analysis was possible utilising the *ab initio* methods.

Kurzfassung

Das Ziel der in vorliegenden Arbeit ist ein tiefreichendes Verständnis von Ligandenfeldeffekten Lanthanid(III)-Komplexen durch die Kombination von experimentellen Methoden mit computerchemischen Simulationen zu gewinnen. Die magnetischen Eigenschaften von mononuklearen Lanthanid-Komplexen werden vorrangig von der Elektronenstruktur des isolierten Ions bestimmt. Die detaillierte Kenntnis des Ligandenfeldeffektes erlaubt die gezielte Entwicklung neuer Komplexe für den Einsatz als Einzelmolekülmagnete (SMMs). Eine Vielzahl von experimentellen Techniken wird in dieser Arbeit mit einem leistungsstarken *ab initio* Konzept kombiniert. Hierbei werden CASSCF Wellenfunktionen bestimmt, aus denen Spin-Bahn gekoppelte Zustände durch Konstruktion einer *state-interaction* Matrix berechnet werden. Die magnetischen Eigenschaften ergeben sich aus der effektiven Hamiltonian Theorie, wodurch die Elektron-Zeeman Wechselwirkung und die Ligandenfeldparameter erhalten werden. Die Validierung des *ab initio* Konzeptes erfolgt sowohl durch den Vergleich mit magnetometrischen Ergebnissen, als auch mit Hilfe des magnetischen Zirkulardichroismus. Bei letzterem handelt es sich um eine sehr sensible optisch-spektroskopische Methode. Eine vollständige Ligandenfelduntersuchung der experimentellen Daten kann mit Hilfe der *ab initio*-berechneten Ligandenfeldparameter durch-geführt werden, um die Präzision der angewandten computerchemischen Methode zu bestimmen.

In der Arbeit wird zunächst die Empfindlichkeit der Elektronenstruktur von Terbium(III)- und Dysprosium(III)-Ionen auf sehr kleine Ligandenfeldveränderungen untersucht. Es wurden zwei Liganden, L^1 und L^2, hergestellt, deren Koordinationssphären acht homoleptische Sauerstoffdonoren bereitstellen, woraus folgt, dass die Unterschiede im Ligandenfeld der resultierenden Komplexe sich alleine auf geometrische Unterschiede zurückführen lassen. Aufgrund des Vorliegens unterschiedlicher Ligandenfelder werden unterschiedliche Aufspaltung des J-Multipletts niedrigster Energie beobachtet, die zu unterschieden in der magnetischen Suszeptibilität von allen vier Komplexen führen. Magnetisierungsmessungen mit losem Pulver zeigen Unterschiede in den g-Werten des Grundzustandes. Dieses Resultat wird von berechneten Werten bestätigt. Darüber hinaus geben hochfrequente Elektronenspinresonanz-Studien an Terbium(III)-Komplexen Aufschluss über die verschiedenen Beiträge der M_J Projektionen zum Grundzustand. *Ab initio* Rechnungen bestätigen die experimentellen Ergebnisse und verdeutlichen den Effekt der strukturellen Gegebenheiten auf die elektronischen und magnetischen Eigenschaften der Komplexe. Hochaufgelöste magnetische Zirkulardichroismus-Spektren der Dysprosium(III)-Komplexe bestärken zusätzlich die Annahme der Aufspaltung des J-Multipletts und ermöglichen die vollständige Untersuchung des Liganden-

feldes. Hierbei werden die mit Hilfe des *ab initio* Ansatzes berechneten Ligandenfeldparameter verwendet, um eine sinnvolle Annäherung an die experimentellen Daten zu erhalten, wodurch die Präzision der angewandeten computer-chemischen Methode widergespiegelt wird. Die berechneten Eigenschaften deuten auf keine signifikanten Einzelmolekülmagneteigenschaften der verschiedenen Komplexe hin, was zur Entwicklung einer weiteren Gruppe von Liganden, basierend auf L^1, führte, welche im darauffolgenden Teil der vorliegenden Arbeit behandelt wird.

Der zweite Teil der Arbeit beschäftigt sich mit den Unterschieden der f-Elektronendichte des freien Dysprosium(III)- und Erbium(III)-Ions und wie diese durch verschiedenen Merkmale im Ligandenfeld beeinflusst werden kann. Zwei weitere Liganden wurden konzipiert, welche nach Koordination an Lanthanid(III)-Ionen ein hohes Maß an Elektronendichte in der axialen, L^3, oder äquatorialen Umgebung, L^4, liefern. Berechnungen deuten darauf hin, dass das stärker axiale Ligandenfeld ausgeprägte Anisotropie und die charakteristische magnetische Abschirmung des Dysprosium(III)-Zentrums zeigt, während das stärker äquatoriale Ligandenfeld durch Mischen der M_J Zustände ein großes transversales Moment hervorruft. Die Erbium(III)-Komplexe, welche eine gestreckte f-Elektronendichte aufweisen, zeigen den gegenläufigen Effekt. MCD Spektren der Dysprosium(III)- und Erbium(III)-Komplexe der Liganden L^3 und L^1 zeigen vergleichbare Resultate. Analog zum ersten Teil der Arbeit wurde eine vollständige Ligandenfelduntersuchung mit Hilfe des *ab initio* Konzeptes durchgeführt.

Contents

1 Introduction 1

1.1 The development of the single molecule magnet 1

1.2 Lanthanide based SMMs 5

1.2.1 Magnetic anisotropy 5

1.2.2 Design of the ligand field 6

1.3 Quantum chemical calculations 11

2 Aims 13

3 Theory 15

3.1 Magnetism 15

3.1.1 Angular momentum and the magnetic moment 15

3.1.2 Spin Hamiltonians 16

3.2 Magnetic circular dichroism 19

3.3 Ligand field theory 21

3.3.1 Stevens' formalism 21

3.3.2 Wybourne's formalism 22

3.3.3 Standardisation 23

3.3.4 The angular overlap model 23

3.4 Quantum chemical methods 25

3.4.1 Hartree-Fock 25

3.4.2 Post-HF and the complete active space self-consistent field . . 26

3.4.3 Relativistic effects 27

3.4.4 General method 29

4 Magnetostructural correlations of homoleptic mononuclear Ln^{III} complexes 31

4.1 Introduction 31

4.2 Synthesis and structural properties 35

4.2.1 X-ray crystal structures 35

4.2.2 DFT optimised structures 39
4.3 Magnetism 41
4.4 High-frequency electron paramagnetic resonance (HF-EPR) 47
4.5 Magnetic circular dichroism 51
4.5.1 Fitting of the MCD data with OriginPro 54
4.5.2 Qualitative interpretation 54
4.6 Ligand field theory calculations 55
4.7 *Ab initio* calculations 61
4.7.1 Fitting of experimental data 62
4.7.2 SMM potential 64
4.8 Conclusion 69

5 Enhancing the ligand field of mononuclear Ln^{III} complexes 71
5.1 Introduction 71
5.2 Synthesis and structural data 73
5.2.1 Synthesis of L^3 73
5.2.2 Synthesis of Ln^{III}-L^3 complexes 73
5.2.3 Mass spectrometry 73
5.2.4 NMR titration 74
5.2.5 DFT optimised structures 76
5.2.6 SHAPE analysis 79
5.3 Magnetic circular dichroism 81
5.3.1 Qualitative interpretation 86
5.4 Ligand field theory calculations 91
5.5 *Ab initio* calculations 95
5.5.1 Fitting of MCD 95
5.5.2 Magnetic properties 98
5.6 Conclusion 103

6 Conclusion and outlook 105

7 Experimental section 107
7.1 Experimental methods 107
7.1.1 DC SQUID 107
7.1.2 Pulse-field magnetisation 107
7.1.3 High-frequency electron paramagnetic resonance (HF-EPR) . 107
7.1.4 Magnetic circular dichroism (MCD) 108
7.1.5 X-ray crystal structure determinations 108

7.1.6 Elemental analysis 108
7.1.7 NMR 108
7.2 Synthesis of Ligands 109
7.2.1 General 109
7.2.2 Synthesis of 2-bromo-6-carboxypyridine-1-oxide 109
7.2.3 Synthesis of 1-hydroxy-6-oxo-1,6-dihydropyridine-2-carboxylic acid (1,2-HOPO) 110
7.2.4 Synthesis of 1-(benzyloxy)-6-oxo-1,6-dihydropyridine-2-carboxylic acid (1,2-HOPOBn) 110
7.2.5 Synthesis of 1-(benzyloxy)-6-oxo-1,6-dihydropyridine-2-carbonyl chloride 111
7.2.6 General synthesis of nLIm-1,2-HOPOBn 111
7.2.7 General synthesis of nLIm-1,2-HOPO 112
7.2.8 Synthesis of *N*,*N'*-(ethane-1,2-diyl)bis(2-hydroxy-3-methoxybenzamide): 2LI-2,3-HOMOPH (L^3) 113
7.3 Synthesis of Complexes 114
7.3.1 Synthesis of $[(2LI\text{-}1,2\text{-}HOPO)_2Ln]^-$ (Ln^{III}-2LI) complexes . . 114
7.3.2 Synthesis of mononuclear $[Ln(5LIO\text{-}1,2\text{-}HOPO)_2]^-$ complexes 115
7.3.3 *In situ* preparation of the $[Ln(2LI\text{-}2,3\text{-}HOMOPH)_2]^-$ complexes for MCD 116
7.3.4 ^{1}H NMR titration of Lu^{III}-L^3 116

A **119**

A.1 Appendices to Chapter 4 119
A.2 Appendices to Chapter 5 140

Bibliography **157**

Acknowledgments **169**

1. Introduction

1.1 The development of the single molecule magnet

Single molecule magnets (SMMs) are a class of complexes that exhibit superparamagnetism of purely molecular origin at low temperatures. The first observed case of this phenomenon was published in 1993 by Sessoli *et al.*, in a mixed valence $\mathrm{Mn^{III}}_8\mathrm{Mn^{IV}}_4$ complex, now commonly referred to as Mn_{12}.[1–4] The complex $[\mathrm{Mn}_{12}\mathrm{O}_{12}$ $(\mathrm{O}_2\mathrm{CMe})_{16}((\mathrm{H}_2\mathrm{O})_4]$ is comprised of eight $\mathrm{Mn^{III}}$ and four $\mathrm{Mn^{III}}$, which are antiferromagnetically coupled to give a total spin of $S = 10$. The authors reported pronounced magnetic hysteresis of this complex below 4 K, which indicated the presence of a bistable ground state ($+M_S$ and $-M_S$) and an energy barrier U_{eff} between the two states of 61 K. The discovery sparked considerable interest, not only because of its fundamental significance in both chemistry and physics, but also due to the possibility of creating the next generation of storage devices or quantum computing. More recently, the field has started to progress into multifunctional compounds, combining magnetic properties with other properties such as luminescence.[5]

Before discussing the development in of SMMs, it is important to note that experimentally there are two ways to quantify SMM behaviour, the blocking temperature T_B and the spin reversal barrier U_{eff}. The use of the former is somewhat problematic, as there are several ways in which to define T_B.* The second method for detection of SMM behaviour is to measure how the material responds to an alternating current (ac) magnetic field. If a barrier to spin reversal exists, the magnetisation of the complex will lag behind the alternating field and an out-of-phase (χ'') component will appear. The frequency dependence of χ'' for each temperature is plotted; the frequency ν at which

---

*T_B has been reported as the temperature at which hysteresis of the magnetisation curve is observed, this however, is dependent on the sweep rate and no standard scan rate has been defined in this field. A second definition is the temperature at which magnetisation is retained for 100 s. However, this length of time is arbitrary and this definition is also not universally used. It is therefore advisable to use the textbook definition of T_B, which is the temperature at which a maximum in the zero field cooling susceptibility occurs (not to be confused with the temperature at with the field cooling and zero field cooling diverge (T_{IRREV})).

χ'' reaches a maximum is used to calculate the relaxation time τ, where $\tau = 1/(2\pi\nu)$. A plot of τ *vs.* T can then be fitted using an exponential law (Eq. (1.1)), analogous to the Arrhenius-Néel law used for superparamagnets to give the reversal barrier U_{eff},[6,7] rendering U_{eff} a much more useful value for easy comparison of different complexes.[†]

$$\tau = \tau_0 \exp^{U_{eff}/k_BT} \tag{1.1}$$

Note also that resistance of a compound to an alternating field and the resulting χ'' component may also be induced by the application of a dc field. This then gives rise to the classification of two kinds of SMMs; those that exhibit an out-of-phase component with a dc field (field induced), and those with an out-of-phase component in zero dc field (zero field).

The basic principle behind SMM behaviour is illustrated in Figure 1.1. Essential for this kind of behaviour is the presence of a bistable magnetic ground state ($\pm M_S$ or $\pm M_J$ for d- and f- block metals, respectively). In the absence of an external magnetic field (B) the bistable ground states are equally populated. Upon application of B the $+M_S$ microstates (or $+M_J$) are lifted due to the Zeeman effect and the disordered electron spins align in the $-M_S$ (or $-M_J$) state, *i.e.* the complex is magnetised. Removal of B restores degeneracy and the energy barrier U prevents relaxation of magnetisation. For transition metal systems the reversal barrier has been defined as:

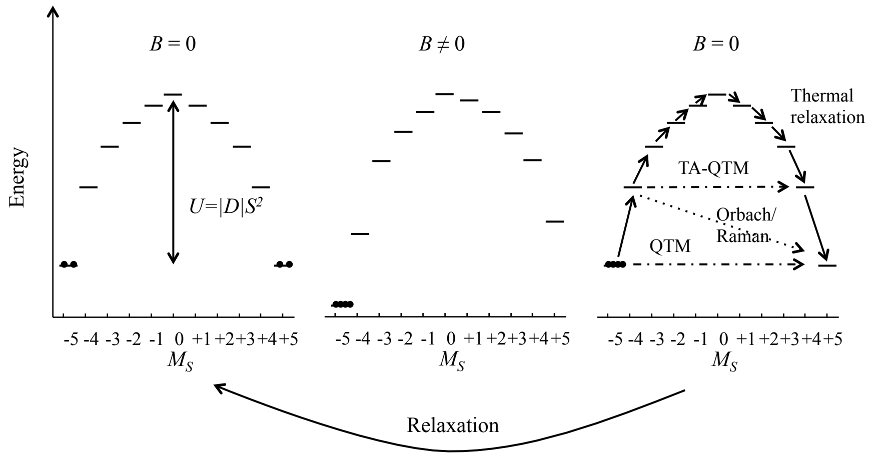

Figure 1.1: Schematic representation of the magnetisation and relaxation of an SMM, where the x-axis represents the orientation of the spin projection for an S = 5 system, and the y-axis is energy.

[†] This technique, however, does not provide definitive proof of SMM behaviour, as intermolecular interactions are also capable of creating such signals, and should be reported in combination with direct current (dc) magnetic field data.[8]

$$U = |D|S^2 \tag{1.2}$$

$$U = |D|(S^2 - 1/4) \tag{1.3}$$

for systems with odd and even electron counts, respectively. Three principle processes exist by which magnetisation may be relaxed. Relaxation may occur *via* the excited states over U, simply referred to as thermal relaxation. Quantum tunnelling of magnetism may also occur directly between two $\pm M_S$ ($\pm M_J$) states, either in the ground state (QTM) or thermally activated *via* an excited state (TA-QTM). Orbach/Raman relaxations are spin/lattice processes that allow relaxation between different M_S (M_J) states. Due to QTM and Orbach/Raman processes the experimental value of U is often smaller than theoretically predicted and is referred to as U_{eff}.

Initially research in this area was focussed on enhancing the barrier by increasing the value of S. This led to the synthesis and characterisation of an extensive range of oligonuclear transition metal complexes, with complexes containing up to 19 metal ions. The ineffectiveness of this approach, however, was illustrated in 2006 with the publication of an $S = 83/2$ system which exhibited no magnetic blocking due to negligible anisotropy ($D \approx 0$).[9] Later theoretical studies revealed that, while the barrier is proportional to S^2, the zero field splitting parameter $|D|$ is inversely proportional to S^2, rendering the strategy to increase U counterproductive, and it was proposed that the barrier for transition metal complexes is better defined as $U = |D|S^0$.[10] A shift in focus then followed, from increasing the total spin of the system, to increasing the anisotropy. Due the large spin-orbit coupling of most rare earth metals, the $4f$-block became the new focus and since, record values of the reversal barrier have been achieved using simple mononuclear lanthanide complexes in which the single ion anisotropy has been enhanced.[11]

1.2 Lanthanide based SMMs

1.2.1 Magnetic anisotropy

Due to shielding of the $4f$ orbitals by the fully occupied $5s$ and $5p$ orbitals, the orbital angular momentum (L) remains unquenched and the magnetic field generated by this motion interacts strongly with that generated by S. This spin-orbit coupling results in a total angular momentum J, the values of which are $L + S$, $L + S - 1$,..., $L - S$, and this gives rise to the term ${}^{2S+1}L_J$ to describe the free ion. The splitting of these J states is in the order of about 10^4 cm^{-1}, meaning that only the lowest energy J state needs to be considered at room temperature. Lanthanides with a less than half-filled shell will have a ground J state of $L - S$, for shells more than half-filled the ground state will be $L + S$. For every J state there exist $(2J + 1)$ M_J microstates, which are degenerate in the free ion but are split in the presence of a ligand field. This interaction, as depicted in Figure 1.2, is much weaker than the spin-orbit coupling ($\sim 10^2$ cm^{-1}), however, it is this splitting that gives rise to the anisotropy barrier essential for SMM behaviour.

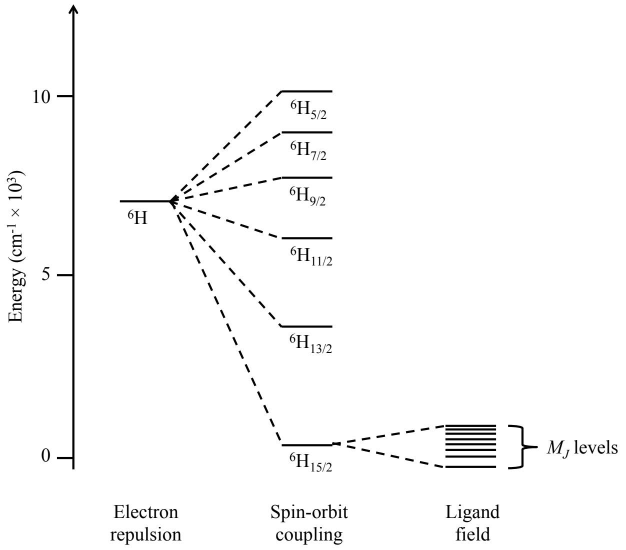

Figure 1.2: Electron-electron repulsion, spin-orbit coupling and ligand field splitting of the $(2J + 1)$ M_J states of the ${}^6H_J$ ground state multiplet of dysprosium(III).

For the purpose of increasing the SMM behaviour of lanthanide based complexes, three general criteria should be considered. The fulfilment of these criteria necessitates two considerations, namely, (i) the choice of lanthanide and, (ii) the design of the ligand field. The first requirement, as mentioned above, is bistability of the magnetic ground state. This is a precondition to the existence of an anisotropy barrier and can be easily fulfilled through the use of a Kramers ion (odd electron count), the M_J states of which will always be degenerate in zero field due to time-reversal considerations.[12]

For a non-Kramers ion (even electron count), this can be achieved through an appropriate ligand field. Secondly, the ground state should have a large M_J value in order to increase the magnetic moment at low temperatures; having $J = L+S$ ground states, $4f$-ions with their valence shell more than half filled are favoured. However, in order to split the M_J such that the largest M_J level is stabilised and the states are not mixed, the ligand field plays an essential role. Lastly, for strong anisotropy and an increased barrier, the first excitation energy should be large; assuming a thermally initiated relaxation mechanism, this energy will often correspond to the energy required for spin reversal. As already emphasised, this splitting is a product of the ligand field. For these reasons Tb$^{\text{III}}$, Dy$^{\text{III}}$, Ho$^{\text{III}}$ and Er$^{\text{III}}$ are desirable candidates, with Tb$^{\text{III}}$ and Dy$^{\text{III}}$ most commonly used in this field. The ligand field must then be designed in order to complement the chosen lanthanide.

1.2.2 Design of the ligand field

In 2011 Rinehart and Long published a theoretical study which revealed that the strong angular dependence of the f orbitals causes the electron cloud of each ion to differ.[13] As illustrated in Figure 1.3 depending on how many orbitals are occupied, the electron density distribution will be oblate (Ce$^{\text{III}}$, Pr$^{\text{III}}$, Nd$^{\text{III}}$, Tb$^{\text{III}}$, Dy$^{\text{III}}$ and Ho$^{\text{III}}$), prolate (Pm$^{\text{III}}$, Sm$^{\text{III}}$, Er$^{\text{III}}$, Tm$^{\text{III}}$ and Yb$^{\text{III}}$), or spherical (Gd$^{\text{III}}$ and Lu$^{\text{III}}$). In order to increase the anisotropy of a system, the ligand field must be designed so as to reduce electrostatic repulsion between the ligands and $4f$-electrons. For example, dysprosium(III) ($4f^9$) has an oblate shaped electron density which occupies the xy-plane. Repulsive interactions can be minimised using a ligand field concentrated above and below the xy-plane (axial ligand field). This will cause stabilisation of the larger $\pm M_J$ states, while

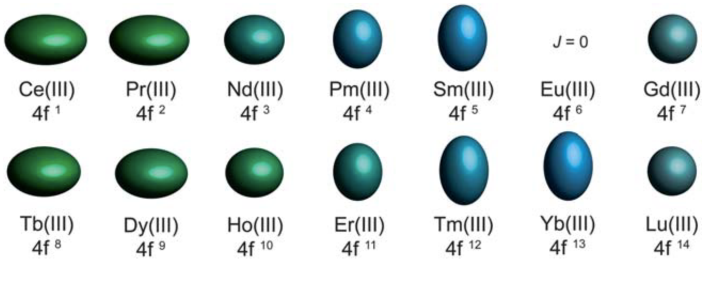

Figure 1.3: Depiction of the quadrupole approximations of the $4f$-shell electron distributions for the Ln$^{\text{III}}$ free ions. The image has been reproduced with permission from Ref[13].

the smaller $\pm M_J$ states will be destabilised (Figure 1.4). Conversely, the anisotropy of ions with a prolate electron density, such as erbium(III), can be enhanced with a strongly equatorial ligand field. Since its publication in 2011, this elegantly simple guide has been broadly used as the primary rule of thumb in the design of new lanthanide based SMMs. The robustness of this *oblate-prolate* guide has been experimentally illustrated in the extensively studied phthalocyanine (Pc) based complexes and their derivatives (Figure 1.5).[14] These sandwich-type complexes provide electron density ideal for oblate-type ions and have achieved record reversal barriers using the oblate ions $\mathrm{Tb^{III}}$ and $\mathrm{Dy^{III}}$, whereas the prolate $\mathrm{Er^{III}}$ equivalent displays no SMM behaviour.

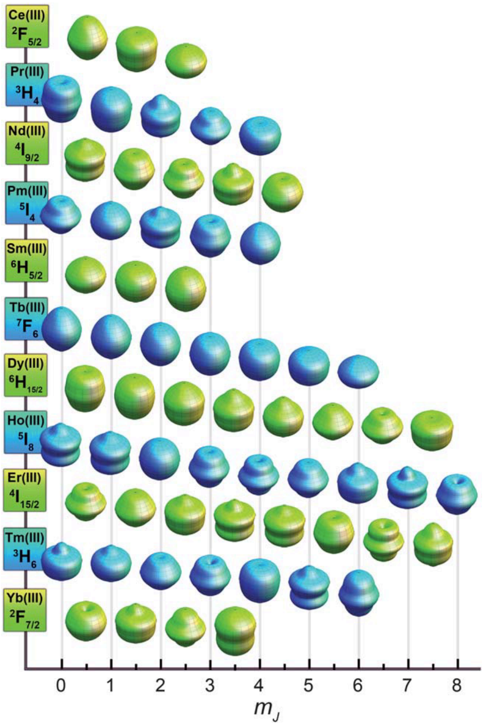

Figure 1.4: Illustrations of the approximated angular dependence of the total $4f$ charge densities of the M_J states of the ground J multiplet of each $\mathrm{Ln^{III}}$. The image has been reproduced with permission from Ref[13].

A theoretical study published in 2015 explored the magnetic properties of simple model $\mathrm{Dy^{III}}$ complexes and illustrated that, with $\mathrm{Dy^{III}}$ coordinated to only two ligands in a linear arrangement (Figure 1.6), a reversal barrier of up to 3000 $\mathrm{cm^{-1}}$ could be achieved.[15] Even with an O-Dy-O bend angle of 135° a significant barrier could still be expected. This has subsequently been illustrated experimentally through the synthesis of both $[\mathrm{Dy(O^tBu)_2(py)_5}]^+$ and $[\mathrm{Cp^{ttt}{}_2Dy}]^+$.[11,16] The values of U_{eff} and T_B of these complexes are presented in Table 1.1. Note that the authors of $[\mathrm{DyCp^{ttt}{}_2}]^+$ reported a *record* magnetic blocking temperature of 60 K. This value, however, was determined by the opening of the hysteresis loop. In Table 1.1, the T_B value given was determined as the maximum in the ZFC susceptibility (see the SI of the Ref[11]) for ease of comparison with $[\mathrm{Dy(O^tBu)_2(py)_5}]^+$.[‡] The difference of the blocking temperatures is therefore 31 K, not 46 K. This is still a significant improvement on the $[\mathrm{Dy(O^tBu)_2(py)_5}]^+$ complex, but it does illustrate the need to carefully evaluate how T_B is determined before making any comparisons.

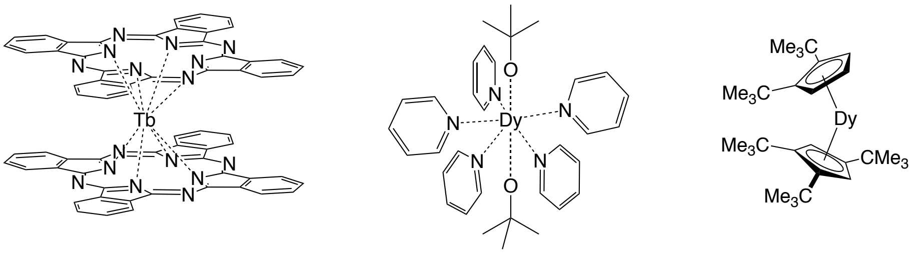

Figure 1.5: Illustrations of $[\mathrm{Pc_2Tb}]^-$, $[\mathrm{Dy(O^tBu)_2(py)_5}]^+$ and $[\mathrm{Cp^{ttt}{}_2Dy}]^+$.

Table 1.1: Effective barrier and blocking temperature of a selection of reported complexes. Note the different techniques used for the determination of T_B.

	U_{eff} [cm^{-1}]	T_B [K]	Ref
$[\mathrm{Pc_2Dy}]^-$	28	11.5[a]	[14]
$[\mathrm{Pc_2Tb}]^-$	230	40[a]	[14]
$[\mathrm{Pc_2Tb}]^*$	410	50[a]	[17]
$[\mathrm{Dy(O^tBu)_2(py)_5}]^+$	1261	14[b]	[16]
$[\mathrm{Cp^{ttt}{}_2Dy}]^+$	1277	45[b]	[11]

[a] Temperature at which the hysteresis curve opens, scan rate of 1000 Hz. [b] Maximum temperature in ZFC susceptibility.

Other methods have been used to improve the SMM behaviour of a single lanthanide ion, including the introduction of a radical ligand,[17,18] strategic placement of diamagnetic ions,[19,20] and the design of homo- or hetero-oligonuclear complexes that increase spin and introduce favourable exchange interactions.[21–23] Challenges can arise in this last approach, as the misalignment of the individual magnetic axes can result in the loss of overall anisotropy of the system.[24] Therefore, enhancing the

---

[‡] Note also that the authors incorrectly report the ZFC T_{IRREV} value as T_B, which has a value of 60 K, thereby falsely corroborating the values determined by the opening of the magnetic hysteresis loop.

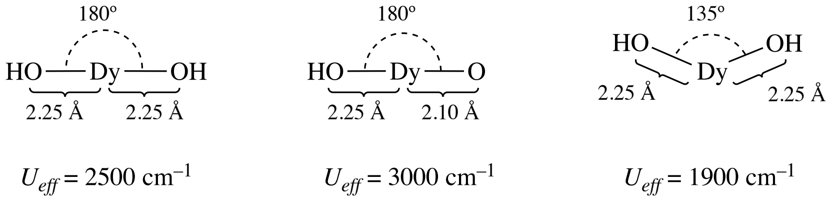
180°
HO—Dy—OH
2.25 Å 2.25 Å
U_{eff} = 2500 cm^{-1}
180°
HO—Dy—O
2.25 Å 2.10 Å
U_{eff} = 3000 cm^{-1}
135°
HO Dy OH
2.25 Å 2.25 Å
U_{eff} = 1900 cm^{-1}

Figure 1.6: Model Dy^{III} complexes, [Dy(OH)$_2$]$^-$, [Dy(OH)O] and [Dy(OH)$_2$]$^-$ and their predicted reversal barriers.[15] The O–H distance was set to 0.96 Å with a Dy–O–H angle of 109.47°.

ligand field of mononuclear complexes appears to be an elegant and effective approach to achieve large anisotropy barriers. Additionally, although the basic relationship between the ligand field and M_J splitting has been established, much is still to be learnt about the finer splitting of the microstates in different ligand fields. The use of simple mononuclear lanthanide complexes is an attractive approach to explore these effects.

1.3 Quantum chemical calculations

Progress in the area of SMMS has been facilitated by the development of highly sophisticated *ab initio* quantum chemical calculations. Because the magnetic properties of these complexes are related to the electronic structure of the metal site and, therefore, to the molecular structure, the magnetic properties are theoretically predictable. The method commonly used is based on the complete active space self-consistent field (CASSCF) approach (see Chapter 3) and is widely used in the field of SMMs.[25–27]

The spin-free states of the magnetic centre are described using a CASSCF wave function. Spin-orbit coupling is then introduced by the construction of a state interaction matrix. Effective spin Hamiltonians (S = 1/2) are then used to determine different properties of the magnetic centre. The calculations provide information about the g-tensors (anisotropy of each doublet), the orientation of the main magnetic axis, the zero-field splitting, the composition of the sub-levels (whether mixing of the M_J levels is expected), likely relaxation pathways and therefore the predicted U_{eff}, as well as the ligand field parameters. If oligonuclear complexes are under investigation, a fragmentalised approach is used, in which each magnetic centre is described individually and the interaction between the fragments is accounted for using the Lines model.[28–31]

If the crystal structure is known, the magnetic properties can be predicted and experimental magnetic data interpreted. A large reversal barrier will be expected when the relaxation processes illustrated in Figure 1.1 are prevented, and a large barrier is usually predicted when the computed values fulfil the following:

- A large first excitation energy from the ground M_J to the lowest lying M_J state in order to prevent thermal relaxation, *i.e.* $>$ 100 cm^{-1};
- Strong anisotropy, i.e. Ising type ions, will quench quantum tunnelling of magnetisation (QTM). Therefore the x and y components of the g-value should be effectively zero and the z-component should approach its maximum theoretical value. For dysprosium(III), having a maximum g-value of 20, this would require $g_x = g_y < 0.2$ and $g_z > 18$;
- Alignment of local magnetic axes of the ground and excited states should prevent the Orbach/Raman processes.

Although this method has become a standard procedure, it is not without criticism.[32] Apart from magnetic studies, which only provide for qualitative/semi-quantitative correlations, rigorous validation of these computational methods is rarely reported.[33–36] Commonly, only the experimental reversal barrier U_{eff} is used to compare with the calculated values, as well as fitting of the magnetic susceptibility data. This provides little insight into the fine splitting of the microstates, and rarely are the calculations compared with optical spectroscopic data. Such data provide quantitative information regarding the ligand field induced splitting of the microstates, and knowledge of these energies would allow for a more rigorous validation of this *ab initio* method.[37]

2. Aims

Due to the almost sole reliance on magnetometric data to validate the *ab initio* method, the most recent work within the Comba group in this area has focussed on combining the computational results with a range of magnetometric and spectroscopic techniques. A variety of oligonuclear complexes have been investigated, combining computed values with alternating and direct current (ac and dc) SQUID, high frequency EPR (HF-EPR) and magnetic circular dichroism (MCD) data, including extensive ligand field analysis based on angular overlap model (AOM) calculations.[24,34,38]

Due to the simplicity of mononuclear systems, as well as the multiple illustrations of the effectiveness of single ion lanthanide based SMMs, the focus of this thesis is on mononuclear lanthanide complexes. Since the ligand field splitting of the M_J states is determinative of the magnetic properties, it is of interest to investigate how the splitting of different lanthanide ions differ with slightly varying ligand fields. Therefore, the aims of this thesis were to use a combination of computational and experimental techniques to:

- Investigate the sensitivity of the lanthanide ligand field;
- Explore the oblate-prolate model; and
- Validate the computational results using experimental techniques.

A highly sensitive and accurate technique to determine the energies of the M_J levels is MCD. With the use of ligand field theory, significant information can be acquired from experimental data and used to compare with the computed values. Therefore, in combination with HF-EPR and magnetic measurements, the primary technique for validating the *ab initio* calculated data will be MCD.

3. Theory

3.1 Magnetism

3.1.1 Angular momentum and the magnetic moment

The ratio of the magnetic moment and angular momentum of a particle or system is given by the gyromagnetic ratio γ. For a single electron, this is defined as $\gamma_e = -g_e e/2m_e = -g_e\mu_B/\hbar$, with the electron spin g-factor g_e (2.002319), the Bohr magneton ($\mu_B = e\hbar/2m_e = 9.273 \times 10^{-24}\ A\ m^2$), and the atomic unit of angular momentum $\hbar = h/2\pi$. The magnetic moment of an electron is, therefore, dependent on the angular momentum of the electron spin and γ_e, as given in Eq. (3.1). The total spin moment of an open-shell system is then equal to the sum of the individual electronic dipole moments, and results in a magnetic moment given by Eq. (3.2). Analogously, orbital angular momentum ($\mathbf{L}$), resulting from the circular motion of electrons about the nucleus, gives rise to an orbital magnetic moment, Eq. (3.3), where the gyromagnetic ration is defined as $\gamma_l = -\mu_B/\hbar$.

$$\vec{\mu}_s = -g_e(\frac{\mu_B}{\hbar})\vec{\mathbf{s}} \tag{3.1}$$

$$\vec{\mu}_S = -g_e(\frac{\mu_B}{\hbar})\vec{\mathbf{S}} \tag{3.2}$$

$$\vec{\mu}_L = -(\frac{\mu_B}{\hbar})\vec{\mathbf{L}} \tag{3.3}$$

Spin-orbit coupling occurs when the magnetic field of the intrinsic electron spin interacts with the magnetic field of its orbit, and results in a total angular momentum, the magnetic moment being defined as:

$$\vec{\mu}_J = -g_J(\frac{\mu_B}{\hbar})\vec{\mathbf{J}} \tag{3.4}$$

where the Landé factor g_J is defined as:

$$g_J = 1 + \frac{S(S+1) - L(L+1) + J(J+1)}{2J(J+1)} \tag{3.5}$$

A significant orbital angular momentum only occurs in the case where an electron can change from one orbital to another by a simple rotation about an axis. This entails three requirements, degeneracy of the two orbitals, equivalency of the two orbitals (*e.g.* d_{xz} and d_{yz}) and, if both orbitals are occupied, the conservation of the Pauli principle. Due to strong ligand field induced splitting of the $3d$ orbitals, this effect is often largely quenched. On the other hand, shielding of the $4f$ orbitals results in very weak ligand field splitting, and an unquenched orbital angular momentum. The Russel-Saunders coupling scheme describes this coupling between the total spin and total orbital angular momenta, such that:

$$\mathbf{J} = \mathbf{L} + \mathbf{S} \tag{3.6}$$

where J has the magnitude of

$$|\mathbf{J}| = [J(J+1)]^{\frac{1}{2}}\hbar \tag{3.7}$$

S is no longer a good quantum number and the term ${}^{2S+1}L_J$ is more informative when describing systems with strong spin orbit coupling, such as lanthanides. Analogous to the different orientations of spin projections (M_S) of a spin only system, for each J state there exist $2J$+1 M_J microstates. These are degenerate in the absence of a ligand field, and ligand field induced splitting is what gives rise to the magnetic anisotropy of the rare earth metals.

3.1.2 Spin Hamiltonians

The electronic and magnetic properties of a spin system can be described theoretically using a spin Hamiltonian. First described by Abgragam and Pryce, the Hamiltonian can be written as:[39]

$$\hat{H}_S = \hat{H}_{EE} + \hat{H}_{LF} + \hat{H}_{SOC} + \hat{H}_{SS} + \hat{H}_{EZ} + \hat{H}_N + \hat{H}_{NZ} \tag{3.8}$$

where the individual Hamiltonians describe the electron-electron repulsion, the ligand field, the spin-orbit coupling, the spin-spin coupling, the electron Zeeman interaction, the hyperfine interactions and the nucleus Zeeman interaction, respectively. It should be noted that this is not a universal form for the spin Hamiltonian. Depending on the properties of interest, different terms may be included or omitted.

Spin-orbit coupling

As mentioned above, spin-orbit coupling describes the interaction between the magnetic moment of an electron spin with the magnetic moment of its orbit. Additionally, a spin magnetic moment may interact with the orbit of another electron, known as spin-other-orbit coupling. Both interactions are accurately taken into consideration in the Breit-Pauli spin-orbit coupling Hamiltonian, which takes the form:

$$\begin{aligned}\hat{H}_{BP}^{SO} = \frac{e^2\hbar}{2m^2c^2}\left[\sum_i\sum_\alpha Z_a\mathbf{s}_i\Big(\frac{\mathbf{r}_{i\alpha}}{r_{i\alpha}^3}\times\mathbf{p}_i\Big) - \sum_{i\neq}\Big((\frac{\mathbf{r}_{ij\alpha}}{r_{ij\alpha}^3}\times\mathbf{p}_i\Big)\cdot(\mathbf{s}_i + 2\mathbf{s}_j\right] \\ \equiv \sum_i \hat{H}^{SO}(i) + \sum_{ij}\hat{H}^{SO}(i,j) \quad (3.9)\end{aligned}$$

Z_α is the effective charge of the αth nucleus, $\mathbf{r}_{ij}$ and $\mathbf{r}_{i\alpha}$ denote the distance of the ith electron from the jth electron and αth nucleus, respectively, $\mathbf{p}_i$ is the momentum operator for the ith electron, and $\mathbf{s}_i$ and $\mathbf{s}_j$ are spin operators. The inclusion of the two-electron interactions makes this Hamiltonian rather complex, however, the matter may be simplified by its removal or replacement. An attractive approach to this is to approximate the two electron Hamiltonian using a one-electron Hamiltonian. Hess and coworkers proposed a atomic mean field approximation in which the two-electron contributions to the spin-orbit matrix element are averaged over the valence shell.[40,41] That is to say that the movement of a valence electron is considered in the average field of the occupied orbitals. The advantage in using atomic mean field integrals (AMFI) is that multi-centre one- and two-electron spin orbit integrals need not be calculated. This significantly reduces the computational cost with little compromise on accuracy, and this approach is implemented in the MOLCAS package used in this work.[25]

The Zeeman term

The Zeeman term of the spin Hamiltonian describes the interaction of the angular momentum with an external field and can be expressed as in Eq. (3.10).

$$\hat{H} = \mu_B\hat{B}g\hat{S} = \mu_B\begin{bmatrix}B_x & B_y & B_z\end{bmatrix}\begin{bmatrix}g_{xx} & g_{xy} & g_{xz}\\ g_{yx} & g_{yy} & g_{yx}\\ g_{zx} & g_{zy} & g_{zz}\end{bmatrix}\begin{bmatrix}\hat{S}_x\\ \hat{S}_y\\ \hat{S}_z\end{bmatrix} \tag{3.10}$$

Symmetry commonly allows only the diagonal terms of the 3 $\times$ 3 g-tensors matrix to be considered, resulting in three g-tensors to describe magnitude and anisotropy of the magnetic moment. Depending on the magnitude of these tensors, the magnetic moment of a system may be (i) isotropic, $g_{xx} = g_{yy} = g_{zz}$ (ii) axial, $g_{xx} = g_{yy} \neq g_{zz}$; or rhombic: $g_{xx} \neq g_{yy} \neq g_{zz}$. For efficient magnetic blocking an extreme axial case is desired where $g_{xx} = g_{yy} << g_{zz}$, known as Ising type anisotropy. If the tensors are such that $g_{xx} = g_{yy} >> g_{zz}$, the anisotropy is described as transversal.[42] The energy of the dipole moment of an electron in an applied magnetic field will differ depending on its orientation to the external field. For a single electron s = 1/2 this yields two orientations, i.e. parallel and antiparallel ($m_s = \pm$ 1/2). The energy difference between these two orientations is given by:

$$\Delta E = \mu_B \mathbf{g}_e B \tag{3.11}$$

and it is this basic relationship between B and g$_e$ that allows for the EPR determination of g$_e$. For lanthanides, this relationship is given by:

$$\Delta E = \mu_B g_J \Delta M_J B \tag{3.12}$$

with the Landé factor g_J described in Eq. (3.5).

3.2 Magnetic circular dichroism

Magnetic circular dichroism (MCD) is an optical spectroscopic technique that measures the difference in absorbance of left (l) and right (r) circularly polarised light in the presence of a uniform longitudinal magnetic field (H_z), *i.e.* parallel to the propagation direction of light. The light is modulated between left and right circular polarisations at a fixed frequency which allows the signal to be detected by a lock-in amplifier at that frequency. The signal is proportional to $\Delta\varepsilon = \varepsilon_l - \varepsilon_r$.[43] By convention, the absorption of left circularly polarised light gives rise to a positive signal and the absorption of right circularly polarised light gives rise to a negative signal. MCD has advantages over other spectroscopic techniques in that it can detect extremely weak transitions that would otherwise by buried under signals due to the absorption of the coordinating ligand or organic impurities. Traditionally, the MCD signal can be considered as a superposition of three different terms, namely $\mathscr{A}$, $\mathscr{B}$ and $\mathscr{C}$. This is according to Stephens' formalism and is explained in Figure 3.1 using a simple example $^1\mathrm{P} \leftarrow {}^1\mathrm{S}$. The $\mathscr{A}$ term arises due to the Zeeman splitting of degenerate levels of excited states. Transitions due to the absorption of l and r occur to the upper (+) and lower (–) Zeeman components, respectively, and results in a total signal as illustrated in Figure 3.1(a).

The $\mathscr{B}$ term arises with magnetic field induced mixing of other states into the ground and/or excited states. Unlike the $\mathscr{A}$ and $\mathscr{C}$ terms, it does not rely on any degeneracy of the levels. It is temperature independent, and its appearance is as an $\mathscr{A}$ term if the two transitions lie close enough together. The mixing is a second order perturbation, meaning this term is expected to be small. Mixing of the $^1\mathrm{P_y}$ and $^1\mathrm{P_x}$ levels in Figure 3.1(b) results in states with unequal amounts of $^1\mathrm{P_{+1}}$ and $^1\mathrm{P_{-1}}$ character. The levels are defined as $^1\mathrm{P_y} = \mathrm{i}/\sqrt{2}(^1\mathrm{P_{-1}} + {}^1\mathrm{P_{+1}})$ and $^1\mathrm{P_x} = \mathrm{i}/\sqrt{2}(^1\mathrm{P_{-1}} + {}^1\mathrm{P_{+1}})$. If the positive component dominates in one, the negative component will dominate in the other to the same magnitude. In this example $^1\mathrm{P_y}$ contains more $^1\mathrm{P_{+1}}$, resulting in stronger l absorption, conversely, $^1\mathrm{P_x}$ contains more $^1\mathrm{P_{-1}}$, resulting in stronger r absorption (as indicated in Figure 3.1(b) by $\underline{\mathrm{l}}$,r and $\underline{\mathrm{r}}$,l).

The $\mathscr{C}$ term only exists when the ground state is degenerate. Under an applied field l and r will induce transitions from the different split states. When the absorption of the l is larger than r, the $\mathscr{C}$ term will be positive and appears as an absorption-like band. At low temperatures l transitions predominate but, as temperature increases and the upper Zeeman levels occurs, the magnitude of the two transitions changes. This results in the decrease of the $\mathscr{C}$ term with increasing temperature and, if the splitting of the levels is large enough, the appearance of negative signals at lower energy, commonly referred to

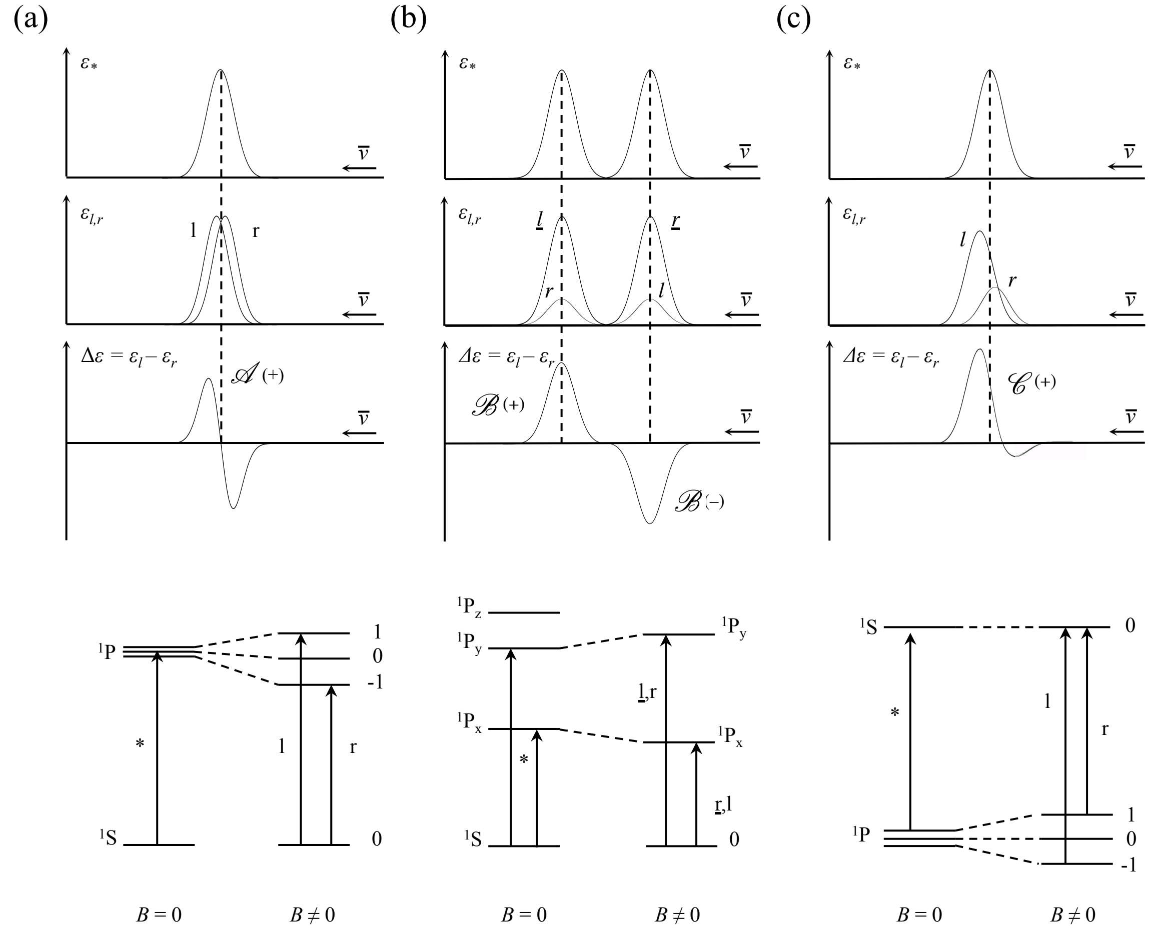
(a)
(b)
(c)
ε_*
$\bar{\nu}$
$\varepsilon_{l,r}$
l
r
$\Delta\varepsilon = \varepsilon_l - \varepsilon_r$
$\mathscr{A}$ (+)
$\mathscr{B}$ (+)
$\mathscr{B}$ (−)
$\mathscr{C}$ (+)
^{1}P
^{1}S
1
0
-1
*
^1P_z
^1P_y
^1P_x
l,r
r,l
B = 0
B ≠ 0

Figure 3.1: Definition of the $\mathscr{A}$, $\mathscr{B}$ and $\mathscr{C}$ terms. Splitting of the degenerate states under an external magnetic field (B). Arrows illustrate transitions due to non-polarised light (*), and left (*l*) and right (*r*) circularly polarised light.

as hot bands. Therefore, this splitting also gives rise to an $\mathscr{A}$ term type signal. Because Kramers' ions, such as dysprosium(III) or erbium(III), have double degeneracy of their ground states, the $\mathscr{C}$ term is typical of compounds containing such ions. Because the signals produced by MCD can be a the result of a combined effect all of these terms, such spectra require detailed and thorough analysis. Through the use of ligand field theory, MCD data can be used to gain important details about the electronic structure of the system under investigation.

3.3 Ligand field theory

The Hamiltonian for the electronic structure of a coordinated lanthanide is described by the free ion Hamiltonian and the crystal field Hamiltonian:[44]

$$\hat{H} = \hat{H}_{free\ ion} + \hat{H}_{CF} \tag{3.13}$$

The free ion Hamiltonian is given by

$$\begin{aligned}\hat{H}_{free\ ion} = E_{AVE} + \sum_{k=2,4,6} F^k f_k + \zeta_{4f} A_{SO} + \alpha L(L+1) + \beta G(G_2) + \\ \gamma G(R_7) + \sum_{i=2,3,4,6,7,8} t_i T_k + \sum_{k=0,2,4} m_k M^k + \sum_{k=2,4,6} p_k P^k\end{aligned} \tag{3.14}$$

In this Hamiltonian, parameter E_{AVE} shifts the energy of the whole $4f^n$ configuration, F^k are the Slater parameters that account for electron repulsion, and ζ_{4f} is the spin-orbit coupling constant. The parameters α, β and γ are for the two body configuration interaction, L is the total orbital angular momentum, M^k the Mavin integrals, and P^k electrostatic correlated spin-orbit interaction parameter. T_k are the three-body parameters of Coulomb interactions and A_{SO} is the angular part of the spin-orbit interaction. $G(G_2)$ and $G(R_7)$ are Casimir's operators for operator groups G_2 and R_7, respectively, and $f_k,\ m_k,\ p_k,\ t_i$ are the operators associated with the above mentioned parameters. Averaged values for all the free ion parameters for all the lanthanides are reported in the literature.[44] If necessary, the adjustment of E_{AVE}, F^k, or ζ_{4f} can produce an improvement of a fit. The different formalisms for the crystal field Hamiltonian are discussed below.

3.3.1 Stevens' formalism

The Stevens formalism[45] describes the ligand field potential using the Hamiltonian:

$$\mathbf{U}_{CF} = \hat{\mathbf{H}}^{Stev}_{CF} = \sum_{k=2,4,6} \rho^k \sum_{q=-k}^{k} A^q_k \langle r^k \rangle \hat{\mathbf{O}}^q_k \tag{3.15}$$

where $A^q_k \langle r^k \rangle$ is a parameter, $\hat{\mathbf{O}}^q_k$ is the operator equivalent of the crystal potential, and ρ^k is a number which differs depending on the f^n configuration and value of k. This last term accounts for the proportionality between the electrostatic potential and $\hat{\mathbf{O}}^q_k$ corresponding to that configuration. The Stevens' formalism neglects mixing between the different ${}^{2S+1}L_J$ multiplets and, therefore, is limited to uses where only the ground multiplet is considered, such as for EPR.[12,46–48] The method becomes too involved when excited states are included, such as in optical spectroscopy, where the use of Wybourne's formalism is preferred.

3.3.2 Wybourne's formalism

In the Wybourne formalism[49] the Hamiltonian used is

$$\mathbf{U}_{CF} = \hat{\mathbf{H}}_{CF}^{Wyb} = \sum_{k=0}^{\infty} \Bigg[B_0^0 C_0^0(i) + \\ \sum_{q=1}^{k} B_q^k (C_{-q}^k(i) + (-1)^q C_q^k(i)) + i B_q^{\prime k} (C_{-q}^k(i) - (-1)^q C_q^k(i)) \Bigg] \tag{3.16}$$

where B_q^k and $B_q^{\prime k}$ are the crystal field coefficients (real) and $C_q^k(i)$ are tensor operators. These tensor operators are related to the spherical harmonics $Y_q^k(i)$ by

$$C_q^k(i) = \sqrt{\frac{4\pi}{2k+1}} Y_q^k(i) \tag{3.17}$$

An advantage of these parameters over the Stevens notation is that the relative magnitudes of B_q^k correspond more closely to the relative contributions to the crystal field splitting, and therefore, provide a better indication of the ligand field. Note, that confusion regarding the notation of these parameters has been caused by a publication in 1968 where the authors used the notation B_k^q. This notation is also often used in spin Hamiltonians.[50,51] In this thesis, the original notation of B_q^k will be used throughout.[49] The values of k are limited by k $\leq$ 6 for f-electrons and values of q are limited by the point symmetry of the site, and range from $-k$ to k. Even values of k (k = 0, 2, 4, 6) describe the CF splitting, with axial CF parameters having q = 0. The odd part (k = 1, 3, 5, 7) is important for the intensity of induced electric dipole transitions. Because the latter is only relevant in optical spectroscopy, it is often ignored for calculations of the magnetic properties.[52,53] As optical spectroscopic techniques provide extremely accurate data regarding the electronic structure of lanthanides, the use of the Wybourne approach to interpret such data is highly advantageous in the area of molecular magnetism. The composition of the wave function as affected by the coupling of excited states, will affect both static and dynamic magnetic properties. Therefore, this approach is complementary to magnetic and EPR studies to provide comprehensive information about the electronic structure, how the LF affects it, and how these effects influence the magnetic properties.

3.3.3 Standardisation

In both formalisms, the values of the CF parameters differ depending on the coordinate system. This necessitates conventions for the assignment of the reference framework, which requires that

(i) The z-direction be defined by the principle symmetry axis;

(ii) Provided there is an additional two-fold symmetry axis, the y-axis should coincide with it;

(iii) The x-axis is then perpendicular to both the z- and y- axes in order to form a right-handed coordinate system.

Different conventions apply in cases of lower symmetry, and if the coordinate system is not defined in such a way, comparison of the CF parameters is not possible unless standardisation of the parameters, by rotation of the reference system, is carried out.[54]

3.3.4 The angular overlap model

Several different methods exist to determine the CF parameters, ranging from the simplest, the point-charge electrostatic model, which considers only point-charges and neglects covalent ligand-metal interactions, to the lone-pair covalent effective charge (LPEC).[54] The latter successfully describes the CF of a system involving ligands with directional lone-pairs, and its effectiveness has been clearly illustrated in its application to the phthalocyanine sandwich complexes.[55] One of the most relevant approaches is the angular orbital overlap model (AOM).[56–58] The AOM is a Hamiltonian approach based on the sum of the local potentials of each ligand. The model is based on the molecular orbital formalism where the ligand-metal interaction is taken to be a product of a radial parameter and an angular factor. Four parameters are used to define the energies, e_σ, e_π, e_δ and e_φ. Each parameter considers a different symmetry of the interaction between the ligand and f orbitals, however, the last two terms are often assumed to be negligible in comparison to e_σ and e_π, and commonly only these two terms are considered. The parameter e_π describes isotropic π interactions or, with the introduction of a second e_π parameter, the anisotropic effects of this interaction can be included. Three assumptions characterise this approach:[54]

(i) The ligand effect is considered as a correction or perturbation to the energies of the f-orbital (E_f), which is proportional to the metal-ligand overlap integrals squared;

(ii) In a coordinate system where the f-orbitals are defined relative to the xyz-axes, the perturbation matrix of a ligand on the z-axis will be diagonal;

(iii) The ligand contributions are additive.

3.4 Quantum chemical methods

3.4.1 Hartree-Fock

Developed in 1928, the Hartree-Fock (HF) theory is a wave function method that forms the basis upon which all other electronic structure methods have been developed.[59] The Hartree wave function can be written as a product of individual one-electron wave functions, or molecular orbitals ψ_i, which are made up of linear combinations of atomic orbitals or basis functions as shown in Eq. (3.18).

$$\psi_i(r_i) = \sum_{\mu} C_{\mu i}\chi_{\mu}(r_i) \tag{3.18}$$

Considering the H_2 molecule, with two nuclei and two electrons, the wave function involves just four coordinates and the wave function is given by

$$\Psi(r_1, r_2) = \psi_1(r_1)\psi_2(r_2) \tag{3.19}$$

As a postulate of quantum mechanics, the wave function must be antisymmetric with respect to the exchange of electron coordinates. As this is not satisfied by the Hartree wave function

$$\Psi(r_2, r_1) = \psi_1(r_2)\psi_2(r_1) = \Psi(r_1, r_2) \tag{3.20}$$

the introduction of signed permutations, creates an antisymmetric wave function, known as the Hartree-Fock wave function

$$\Psi(r_1, r_2) = \frac{1}{\sqrt{2}}[\psi_1(r_1)\psi_2(r_2) - \psi(r_2)\psi_2(r_2)] \tag{3.21}$$

This new wave function can be written as a single Slater determinant and ensures that the exchange of any two electrons results in a change of sign to the wave function. For a system with N electrons the wave function is represented as in Eq. (3.4.1)

$$\Psi = \frac{1}{\sqrt{N!}} \begin{vmatrix} \psi_1(r_1) & \psi_2(r_1) & \cdots & \psi_N(r_1) \\ \psi_1(r_2) & \psi_2(r_2) & \cdots & \psi_N(r_2) \\ \vdots & \vdots & \ddots & \vdots \\ \psi_1(r_N) & \psi_2(r_N) & \cdots & \psi_N(r_N) \end{vmatrix}$$

An important approximation of this method is that each electron does not interact individually with the surrounding electrons, but rather, an individual electron interacts with the average field of all other electrons.The energies of the one-electron wave functions are minimised in reference to the mean field of all other electrons. Therefore, the HF equation depends on its own solution and the energy of the system must be minimised iteratively based on this field. The iterative solving procedure that is used here is the self-consistent field method (SCF). In simple terms, the steps of this approach are

- An inital guess is made for the spin orbitals and the average field experienced by each other electron is calculated;
- The eigenvalue equation is solved to get a new set of spin orbitals;
- A new average field is calculated based on the new set of spin orbitals;
- The above steps are repeated until the field no longer changes.

The result of this is that the correlation energy (E_C) is not considered, but HF theory accounts for about 99 % of the total energy of a system. This difference is small but leads to large errors, as this last 1 % is extremely important for accurately describing the chemical properties of a system. The computation of this energy is considered one of the most important problems in quantum chemistry.

$$E_C = E_{exact} - E_{HF} \tag{3.22}$$

3.4.2 Post-HF and the complete active space self-consistent field

Several post-HF methods have been and are still being developed to quantify the E_C, the discussion of which would fall outside the scope of this thesis. The preferred method in the field of SMMs is a multi-configuration self-consistent field (MC-SCF) approach that considers all electronic configurations in a given active space, namely the complete active space self-consistent field (CASSCF).

In the classical configuration interaction method (CI) E_C is described by the linear combination of Slater determinants describing different electronic configurations. The determinants are configuration state functions built from spin orbitals; for a single excitation a spin orbital is swapped with a single virtual orbital of the HF determinant, for a double excitation two spin orbitals are exchanged, and so on and so forth.

$$\Psi_{CI} = a_0\Phi_{HF} + \sum_S a_S\Phi_S + \sum_D a_D\Phi_D + \sum_T a_T\Phi_T + \cdots = \sum_{i=0} a_i\Phi_i \tag{3.23}$$

The aim for CI is now to minimise the energy by determining the expansion coefficients a_i to the orbitals Φ_i. If this is done for all possible excitations, this would be the full and exact solution of the Schrödinger equation within a basis set, called a full-CI. However, as possible combinations of the position of electrons within the orbitals grow exponentially with the system size, the full-CI approach is not applicable to most systems. In order to reduce the computational cost, it is common to limit the number of excitations to single and/or double excitations (CIS, CISD and CID, respectively). This, however, leads to a new problem, namely that those variants are no longer size-consistent nor size-extensive. A further issue can arise from the fact the the HF-type wave function is used as the reference within the CI. If the reference wave function chosen is not good, the CI calculated energy will reflect this.

One solution is the MC-SCF method, which not only optimises the coefficients but also molecular orbitals in the determinants. Unfortunately, this also increases the computational cost, meaning the size of treatable systems and number of configurations are even more restricted than for the CI method. Careful selection of the configurations is necessary to calculate a certain property, and this is far from trivial. This problem can be solved by partitioning the MOs into *active* and *inactive* spaces, and considering all possible configurations of the electrons in the orbitals of the *active* space. This is the basis of the CASSCF method. Commonly the active space will contain a number of the HOMOs and LUMOs, while the inactive space comprises orbitals that are either doubly occupied, or unoccupied from the initial HF calculation. Selection of an appropriate active space can be rather challenging for organic molecules and even transition metal complexes. However, due to the relatively good isolation of the $4f$ orbitals from the surrounding ligands, the use of this method in lanthanide based complexes can provide highly accurate results by inclusion of only the $4f$ orbitals in the active space.

3.4.3 Relativistic effects

Spin-orbit coupling is purely relativistic in origin, therefore, in order to accurately describe the electronic properties of lanthanide ions, relativistic effects cannot be ignored. Several methods have been developed to account for these effects, although there is no universally agreed upon approach to do this. A relativistic correction is possible by simply including pertubative operators to the non-relativistic wave function. However, as higher order corrections are required, this approach becomes rather cumbersome and a better approach is arguably to solve the Dirac equation directly. While the application of Dirac's theory of the electron increases the accuracy of calculated energies, it is far from straightforward. As a consequence of the theory, there exists a continuum state additional to those in the non-relativistic solution. The continuum states with energies above $+2m_ec^2$ (m_ec^2 being the rest energy of an electron) are known as the electronic states, while the additional continuum states have energies below $-2m_ec^2$ are known as the positronic states. The inclusion of the positronic states is unnecessary for describing electron-only systems and results in unwanted complications, and a large part of the effort has been focused on the decoupling of these state terms from the electronic terms.[60] The positronic states arise from the fact that the Dirac Hamiltonian is a matrix operator that has a 2 × 2 superstructure:

$$\begin{aligned}\hat{\mathbf{H}}_D &= \begin{pmatrix} \mathcal{E}^{UU} + m_ec^2 & \mathcal{O}^{UL} \\ \mathcal{O}^{LU} & \mathcal{E}^{LL} - m_ec^2 \end{pmatrix} \\ &= \underbrace{\begin{pmatrix} \mathcal{E}^{UU} & 0 \\ 0 & \mathcal{E}^{LL} \end{pmatrix}}_{\mathcal{E}'} + \underbrace{\begin{pmatrix} 0 & \mathcal{O}^{UL} \\ \mathcal{O}^{LU} & 0 \end{pmatrix}}_{\mathcal{O}} + \underbrace{\begin{pmatrix} +m_ec^2 & \\ & -m_ec^2 \end{pmatrix}}_{\text{Dirac rest energy operator}} \end{aligned} \tag{3.24}$$

where the label U is for upper and L for lower (also sometimes referred to as *large* and *small*, respectively). The block-diagonal terms $\mathcal{E}$ are denoted as *even*, while the off-diagonal terms $\mathcal{O}$ as *odd*. $\mathcal{E}'$ contains the electrostatic interaction between the electron charge q_e and a scalar potential ϕ, such that $\mathcal{E}' = q_e\phi = V$. Possible contributions to this interaction include interactions with atomic nuclei, external electric or magnetic fields, or even between the electron and other electrons. Recovering the positive-energy without the negative-energy continuum states (positronic states) is hindered by the presence of the off-diagonal terms, or coupling-terms, $\mathcal{O}^{LU}$ and $\mathcal{O}^{UL}$. A unitary transformation that would eliminate these terms whilst preserving all physics, would produce an electrons-only Hamiltonian to describe all relativistic effects and the block-diagonal term describing the negative states could be neglected

$$\tilde{\mathbf{H}}_D = \mathbf{U}\hat{\mathbf{H}}_D\mathbf{U}^\dagger = \begin{pmatrix} \tilde{\mathcal{E}}^{UU} & 0 \\ 0 & \tilde{\mathcal{E}}^{LL} \end{pmatrix} \tag{3.25}$$

The direct calculation of $\tilde{\mathcal{E}}^{UU}$ is desirable, and methods that achieve this are called *two-component methods*, whereas a *four-component method* manipulates H_D to produce $\tilde{H}_D$. The challenge in the former approach lies in finding a unitary operator to achieve complete block diagonalisation of the Dirac Hamiltonian. Douglas and Kroll developed a sequential unitary decoupling scheme ($U = \cdots U_2U_1U_0$) in which the external potential V, is used as a formal-order parameter in order to classify the contributions to $\tilde{\mathcal{E}}^{UU}$.[61] This method was applied in quantum chemistry by Hess in 1986, leading to the now widely used Douglas-Kroll-Hess (DKH) theory.[62] The method makes no reference to $\tilde{\mathcal{E}}^{LL}$ and is, therefore, truly two-componental. In DKH theory, it is possible to express the block-diagonal Hamiltonian of Eq. (3.25) as a series of even terms of the order k in the external scalar potential V^k

$$\hat{\mathbf{H}}\mathbf{s}_{DKH} = \sum_{k-0}^{\infty} \begin{pmatrix} \tilde{\mathcal{E}}_k^{UU} & 0 \\ 0 & \tilde{\mathcal{E}}_k^{LL} \end{pmatrix} = \tilde{\mathbf{H}}_D \tag{3.26}$$

In each unitary transformation the even terms of different order k in V^k are produced. By a proper choice of the individual unitary matrices, the odd terms can be eliminated. The DKH methods are then defined by the order k of the external scalar potential, termed as DKHk. DKH∞ would result in solution of the full four-component Dirac equation, however, lower order methods suffice in producing results of acceptable accuracy. The DKH2 method is utilised in the MOLCAS 8.0 program and provides a sufficient amount of the relativistic effects, while requiring only very little additional computational effort.

3.4.4 General method

In this thesis the *ab initio* calculations have been carried out using the MOLCAS program package[63–65] which utilises methods largely developed by Chibotaru and Ungur.[66,67] For mononuclear lanthanide complexes, the method involves six different modules of the program and the inclusion of relativistic effects is essential. The modules used are:

(1) SEWARD

(2) GUESSORB

(3) GRIDIT

(4) RASSCF

(5) RASSI-SO

(6) SINGLE_ANISO

Scalar relativistic effects are included through the use of a Douglas-Kroll (DK2) Hamiltonian, and adding the corresponding terms to the one-electron integrals in (1) SEWARD. This then necessitates the use of relativistic basis sets with relativistic contracted core, namely, all electron atomic natural orbitals with relativistic contracted core (ANO-RCC). Spin-orbit coupling is introduced after the CASSCF calculations as an *a posteriori* procedure. This is carried out through the use of the RASSI module, which includes the spin-orbit part of the DK Hamiltonian.

Following SEWARD, the program makes an initial "guess" of the molecular orbitals using (2) GUESSORB. This is achieved by the use of a wave function method, however, the user may opt to use DFT in this step (not recommended). Once the initial guess has been calculated, the orbitals are printed using (3) GRIDIT, allowing visualisation of the molecular orbitals for partitioning into inactive (fully occupied and unoccupied) and active spaces.

Spin-free wave functions are generated using the (4) RASSCF module, however by restricting the electrons to the Ras2 space, a CASSCF calculation can be carried out. The wave functions and coefficients are optimised in the desired multiplicities, with the number of stationary points (roots) determining the number of configurations considered within a given multiplicity. Calculation of all configuration of the spin states is computationally too expensive and does not significantly increase the accuracy of the results, therefore, these are often limited to no more than 50 or 100 roots per multiplicity.

The interaction between the different multiplicities, as well as the spin-orbit coupling part of the DK Hamiltonian are then included with the (5) RASSI-SO module. Using the spin-free eigenstates as a basis, a state interaction matrix is built, the diagonalisation of which produces the eigenvalues and eigenvectors of the SOC Hamiltonian. Finally, the magnetic properties are calculated non-pertubatively within the (6) SINGLE_ANISO module, which utilises various pseudospin Hamiltonians, for example the Zeeman interaction Hamlitonian.

4. Magnetostructural correlations of homoleptic mononuclear Ln^{III} complexes[†]

4.1 Introduction

Despite being fairly weak for lanthanides, the ligand field effects are determinative of the M_J splitting and, therefore, the SMM behaviour of Ln^{III} based complexes. With this in mind, this Chapter utilises both *ab initio* quantum chemical and experimental methods to explore the sensitivity of lanthanide ions to subtle changes to the ligand field through the use of a series of octacoordinate mononuclear Ln^{III} complexes (Ln^{III} = Tb^{III} and Dy^{III}). Two homoleptic ligands from a published series known as the LI-series (see Figure 4.1) are employed for this purpose.[68,69] The ligands are comprised of two bidentate donors (1-hydroxy-pyridin-2-one, 1,2-HOPO) with a linking backbone. The nomenclature *n*LI*m* is such that *n* indicates the number of atoms in the linking chain, and *m* indicates additional features on the chain.

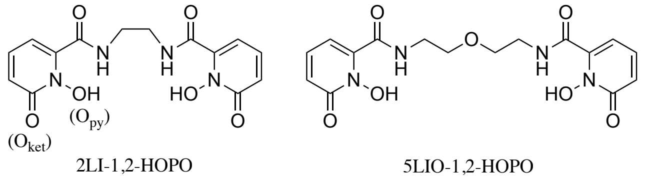

Figure 4.1: Ligands L^1 and L^2 used in this Chapter to form Ln^{III}L$_2$ complexes (Ln^{III} = Tb^{III} and Dy^{III}). For consistency with published works, the ligands will be referred as 2LI and 5LIO, respectively. In the text the two oxygen donor atoms will be referred to as O$_{py}$ and O$_{ket}$, as illustrated on 2LI.

Two ligands per metal ion results in octacoordinate complexes of only oxygen donors and depending on the identity of the linker, different geometries at the Ln^{III}

[†] Main parts of this Chapter have been published in Comba, P.; Daumann, L. J.; Klingeler, R.; Koo, C.; Riley, M. J.; Roberts, A. E.; Wadepohl, H.; Werner, J., Correlation of Structural and Magnetic Properties in a Set of Mononuclear Lanthanide Complexes, *Chem. Eur. J.* **2018**, *24*, 5319-5330. The text of this Chapter has in part been taken *verbatim* from this publication.

centre are observed. Two primary binding modes exist for these ligands, the classification of which is based on the location of the linker in reference to a perfect triangular dodecahedron (Figure 4.2).[68–70] While the 1,2-HOPO chelators will be positioned along the *m*-edges of the triangular dodecahedron, the bridges may occupy the *a*-edges (bridge is stretched) or the *g*-edges (bridge is folded). Within these modes there are different symmetries, the aliphatic bridges of the stretched backbone may align perpendicular or parallel to each other, resulting in S_4 and D_2 symmetries for the *a*-edged structures. The longer folded backbones of the *g*-edged structures may be arranged

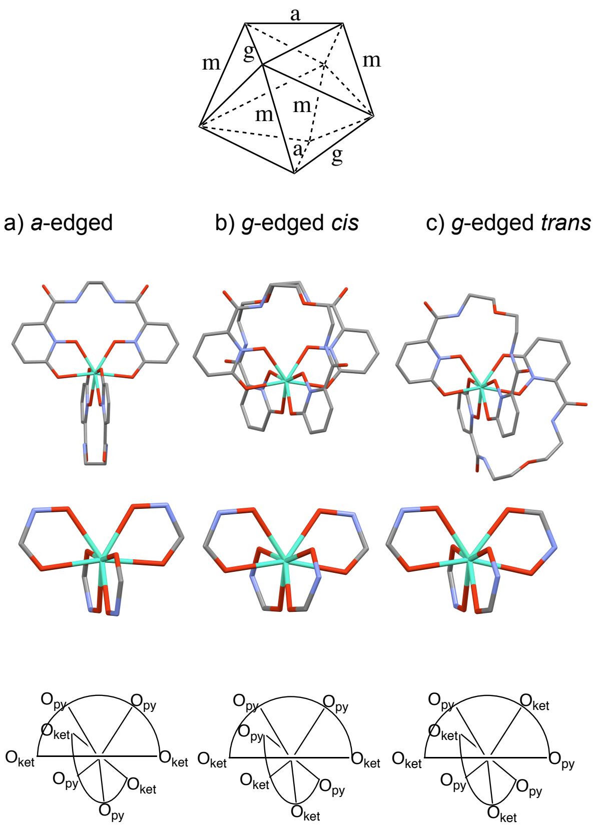

a) *a*-edged b) *g*-edged *cis* c) *g*-edged *trans*

Figure 4.2: The dodecahedron has been reproduced from Ref[70] and illustrates the *a*- and *g*-edges occupied by the ligand backbones, *m*-edges are always occupied by the bidentate 1,2-HOPO moieties. Optimsed structures and illustration of donor distribution for (a) *a*-edged (Ln^{III}-2LI), (b) *g*-edged *cis* and (c) *g*-edged *trans* (Ln^{III}-5LIO) coordination modes.

"*cis*" or "*trans*" to each other. DFT optimisations and solid state structures have shown that shorter bridges (two to four atoms) tend to favour the *a*-edged mode. Longer bridges (five to eight atoms) favour the *g*-edged mode, with *trans* symmetry preferred over *cis* due to steric interactions.[68] Previously, the ligands have been investigated for their luminescent properties with Eu^{III} and Sm^{III}.[68,69] The imposed geometry of the ligands in these complexes was shown to have a significant impact on quantum yields. In this Chapter, the LI-series are investigated for their ligand field effects. In the interest of simplicity, only two ligands were selected for this purpose with chain lengths of two and five atoms (Figure 4.1). These represent L^1 and L^2 of this work but will be referred to as 2LI and 5LIO for consistency with the published works.

4.2 Synthesis and structural properties

Syntheses of the two ligands and four respective mononuclear Ln^{III} complexes (Ln^{III} = Dy^{III} and Tb^{III}) were carried out as reported elsewhere.[68,69] Details of the syntheses are also provided in Chapter 7. The respective ligand (2.5 eq.), the lanthanide trichloride hexahydrate salt (1 eq.) and pyridine as a base were heated to reflux in methanol (MeOH) for 24 hours. Characterisation by mass spectrometry and elemental analysis was carried out for all complexes.

4.2.1 X-ray crystal structures

X-ray quality crystals were obtained for [Tb^{III}(2LI-1,2-HOPO)2]PyH (**Tb^{III}-2LI**) and [Dy^{III}(2LI-1,2-HOPO)2]PyH (**Dy^{III}-2LI**) by vapour diffusion of diethyl ether into a dimethylformamide (DMF) solution of the complex (type A), and by recrystallisation from hot DMF (type B) (Figure 4.3). The crystals were found to have either one or two crystallographically independent complex molecules, depending on the crystallisation technique. The crystallographic data are given in the Appendix and selected bond lengths are given in Table 4.1. In the absence of Tb^{III} and Dy^{III} structures of the Ln^{III}-5LIO complex, and in order to illustrate the expected structure of these complexes, an ORTEP diagram of a Eu^{III}-5LIO[71] structure is also presented in Figure 4.3. The coordinates of the Eu^{III}-5LIO structure and a Gd^{III}-5LIO structure[72] are used in the *ab initio* calculations discussed below. The coordination sphere of the complexes is comprised of four negatively charged pyridinolate and four keto oxygen donors. In the crystal structures presented here two different arrangements of these donors around the metal centre are observed as illustrated in Figure 4.2: 4.2a represents that of the

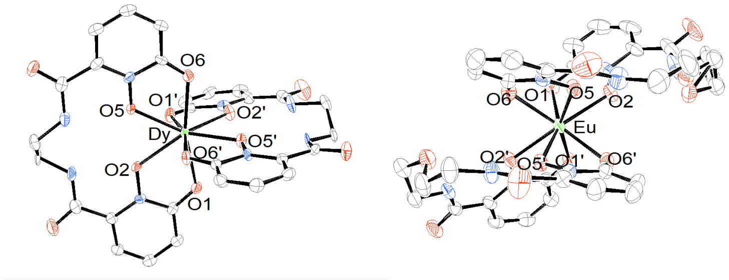

Figure 4.3: ORTEP diagrams of [Dy^{III}(2LI-1,2-HOPO)$_2$]PyH (this work) and [Eu^{III}(5LIO-1,2-HOPO)$_2$]PyH.[71] Counterions, solvent molecules and hydrogen atoms have been omitted for clarity; displacement ellipsoids drawn at 50 % probability.

a-edged Ln$^{\mathrm{III}}$-2LI structure, in which the O$_{\mathrm{pyO}}$ donors occupy the axial positions (with a bite angle of about 60 °), while the O$_{\mathrm{ket}}$ are arranged in the equatorial position. Figure 4.2c illustrates the *g*-edged *trans* structure of Eu$^{\mathrm{III}}$-5LIO and Gd$^{\mathrm{III}}$-5LIO, where the different donors are distributed alternately, and this is expected to be the case for the Dy$^{\mathrm{III}}$-5LIO and Tb$^{\mathrm{III}}$-5LIO structures. The *g*-edged *cis* mode in which the donors are also distributed alternately (Figure 4.2b) has been observed in a Sm$^{\mathrm{III}}$-5LIO crystal structure.[68,69,71,72]

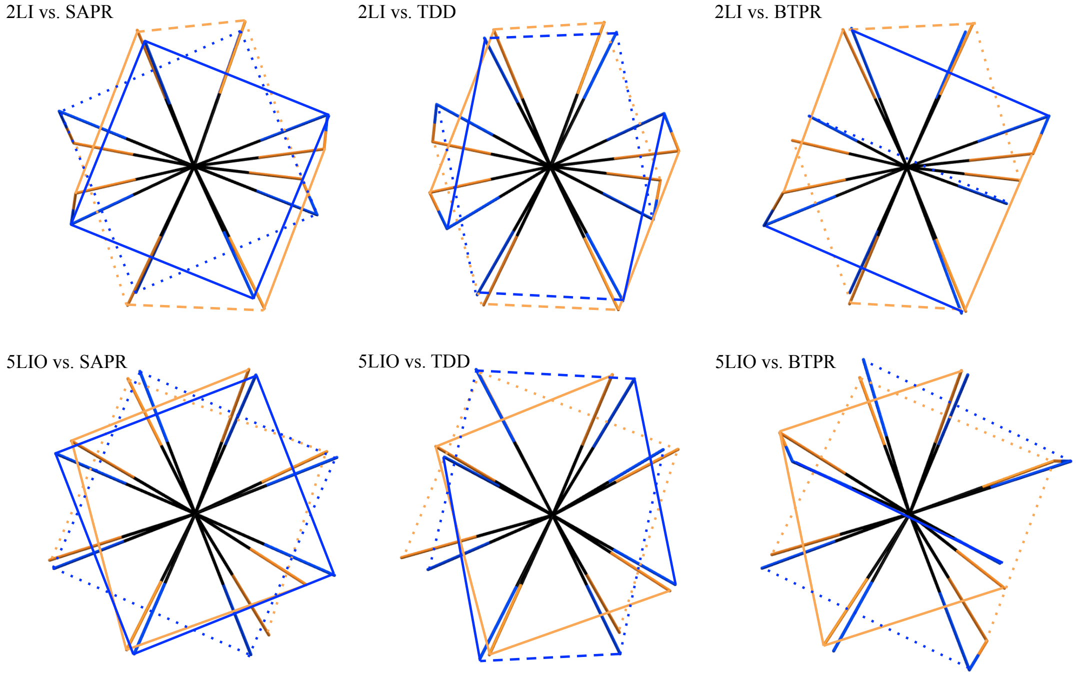

Figure 4.4: Overlay of the ideal geometries square anti-prism (SAPR), triangular dodecahedron (TDD) and bisaugmented trigonal prism (BTPR) with the first coordination sphere of the crystal structures of Tb$^{\mathrm{III}}$-2LI (type B) and Gd$^{\mathrm{III}}$-5LIO. The crystal structures are represented in orange, and the ideal geometries in blue. The orange connecting lines represent the edges occupied by a single ligand. The connecting blue lines have been added to better illustrate the perfect geometries.

Comparison of the bond lengths indicates no significant difference between the two types of donors. In the case of the *a*-edged structures the Ln-O$_{\mathrm{pyO}}$ and Ln-O$_{\mathrm{ket}}$ bond lengths differ by only 0.019-0.043 Å, while the bond lengths of the Gd$^{\mathrm{III}}$ *g*-edged structure exhibit the opposite trend. The Eu$^{\mathrm{III}}$ structure does not exhibit any strong trend between donor type and bond length. It may be concluded that the coordination bond lengths are more strongly influenced by steric effects of the ligand rather than electronic properties of the donor atoms. Continuous shape analysis of each structure was carried out using the program SHAPE 2.1,[73] and the continuous shape measures

(CShM) are also presented in Table 4.1. The CShM is a dimensionless value which ranges from 0 to 100, 0 indicating the perfect polyhedron.[74–77] According to these values, the coordination spheres of the Ln^{III}-2LI structures are closest to a triangular dodecahedron (TDD, D_{2d}) and bisaugmented trigonal prism (BTPR, C_{2v}), while the Ln^{III}-5LIO structures exhibit geometries closest to a regular square anti-prism (SAPR, D_{4d}). From these results the Ln^{III}-2LI geometry would be expected to promote a larger magnetic anisotropy for both Tb^{III} and Dy^{III} than the Ln^{III}-5LIO geometry.[78] This conclusion is however misleading, and when comparing the CShM values between the different complexes for these three ideal geometries, the values of the Ln^{III}-5LIO complexes are consistently smaller than the Ln^{III}-2LI structures. For SAPR, TDD and BTPR, the average CShM values of Ln^{III}-5LIO are 1.4, 2.1 and 2.5, respectively. For the Ln^{III}-2LI structures, these values range 6.5-5.1, 4.2-3.3 and 4.3-3.3, respectively. It is also important to reiterate that these values can range from 0-100. An overlay of the ideal geometries with the first coordination sphere of the Gd^{III}-5LIO and Tb^{III}-2LI (type B) is given in Figure 4.4 and illustrates more clearly the differences indicated by the CShM values. Close inspection of the Ln^{III}-5LIO structure reveals axial elongation of the SAPR, which is expected to increase the anisotropy of both Tb^{III} and Dy^{III}.[78] Additionally, the distribution of different bond lengths will have an effect on the overall anisotropy of each complex, making a simple comparison with ideal geometries slightly challenging. As stated above, in the Ln^{III}-2LI complexes, the axial Ln-O_{py} bond lengths are slightly shorter than those in the equatorial region, which may assist in promoting a larger anisotropy of both complexes.[13]

Table 4.1: Selected bond lengths of the crystal structures utilised in the *ab initio* calculations (see below) and CShM values from the SHAPE analysis of these structures. Note that numbering of the oxygen atoms is only valid for the structures published here. The SHAPE analysis was restricted to square anti-prism (SAPR), triangular dodecahedron (TDD), J-bisaugmented trigonal prism (JBTPR), bisaugmented trigonal prism (BTPR) and J-snub disphenoid (JSD).

	a-edged						g-edged	
	Tb^{III}-2LI (Type A)	Tb^{III}-2LI[a] (Type A)	Tb^{III}-2LI (Type B)	Dy^{III}-2LI (Type A)	Dy^{III}-2LI[a] (Type A)	Dy^{III}-2LI (Type B)	Eu^{III}-5LIO[b]	Gd^{III}-5LIO[c]
Dy-$O2_{pyO}$	2.339(3)	2.335(3)	2.358(2)	2.350(3)	2.337(3)	2.334(7)	2.372(3)	2.331(10)
Dy-$O5_{pyO}$	2.357(2)	2.364(2)	2.402(2)	2.326(3)	2.328(3)	2.356(5)	2.434(3)	2.325(10)
Dy-$O2'_{pyO}$	2.366(2)	2.335(2)	2.346(2)	2.319(4)	2.356(3)	2.359(7)	2.371(3)	2.328(10)
Dy-$O5'_{pyO}$	2.332(3)	2.347(2)	2.334(2)	2.358(3)	2.328(3)	2.336(6)	2.457(3)	2.344(9)
Dy-$O1_{ket}$	2.388(3)	2.402(3)	2.388(2)	2.357(3)	2.375(3)	2.374(6)	2.383(3)	2.295(8)
Dy-$O6_{ket}$	2.365(2)	2.370(3)	2.376(2)	2.382(3)	2.391(3)	2.368(7)	2.380(3)	2.323(12)
Dy-$O1'_{ket}$	2.375(2)	2.400(3)	2.407(2)	2.389(3)	2.362(3)	2.393(5)	2.394(3)	2.331(10)
Dy-$O6'_{ket}$	2.399(2)	2.383(3)	2.381(2)	2.365(3)	2.388(3)	2.328(6)	2.385(3)	2.265(10)
Dy-O_{avpyO}	2.349	2.345	2.360	2.338	2.337	2.347	2.409	2.332
Dy-O_{avket}	2.382	2.367	2.388	2.373	2.379	2.362	2.386	2.304
ΔDy-O_{av}	0.033	0.022	0.028	0.035	0.042	0.015	-0.023	-0.028
SAPR, D_{4d}	5.231	5.661	6.482	5.068	5.448	5.311	1.397	1.422
TDD, D_{2d}	3.884	4.223	4.205	3.679	4.073	3.332	2.233	2.044
JBTPR,[d] C_{2v}	4.158	4.221	4.967	4.043	4.081	4.461	3.358	2.930
BTPR,[d] C_{2v}	3.482	3.432	4.298	3.367	3.277	3.686	2.628	2.419
JSD,[d] D_{2d}	4.69	5.059	4.840	4.559	4.939	4.173	5.504	5.342

[a] Two independent complex molecules are present in the asymmetric unit of the Type A crystal structures. In the CIF file the labels of this molecule appear with an "a" in the notation to distinguish it from the other molecule, *e.g.* O1' appears as O1a'. [b] Previously published structure.[71] [c] Previously published structure.[72] [d] J indicates a Johnson polyhedron, *i.e.* having regular faces and all edges the same length, the BTPR on the other hand is spherical with nonequivalent edges.

4.2.2 DFT optimised structures

In order to represent the solution state structures present in the MCD, DFT geometry optimisations of the Dy^{III} complexes were performed using Gaussian 09 (B3LYP/6-31G(d,p) for C, H, N and O; MWB55[79,80] for Dy^{III}). Previously published Eu^{III} optimised structures were used as input structures.[68] Plots of the final structures are presented in Figure 4.5 and a standard input example as well as the output coordinates can be found in the Appendix. Only the lowest energy conformations were considered, as these are expected to be the predominant species in solution, *i.e.* *a*-edged for Dy^{III}-2LI, and *g*-edged for Dy^{III}-5LIO (see Table A.3).[68] As expected, the optimised structures show higher symmetry than the crystal structures, with two sets of equivalent bond lengths for the *a*-edged complexes and four sets of equivalent bond lengths for the *g*-edged complexes (Table 4.2). As observed in the crystal structures of the *a*-edged species the Dy-O_{pyO} bonds are slightly shorter than the Dy-O_{ket} distances. For the *g*-edged species, however, the opposite is observed for the *cis* configuration, while no significant difference is observed for the *trans* structure. Continuous shape analysis was also performed on the optimised structures, the resulting CShM values can be found in Table 4.2.

Table 4.2: Coordination bond lengths (Å), relative energies (kcal mol^{-1}), and CShM values of the DFT optimised complexes.

	Dy^{III}-2LI-*a*		Dy^{III}-5LIO-*g*	
	D_2	S_4	*cis*	*trans*
Dy-$O2_{pyO}$	2.383	2.386	2.412	2.376
Dy-$O5_{pyO}$	-	-	2.449	2.424
Dy-$O1_{ket}$	2.429	2.429	2.402	2.404
Dy-$O6_{ket}$	-	-	2.366	2.404
Dy-O_{avpyO}	2.383	2.386	2.4305	2.400
Dy-O_{avket}	2.429	2.429	2.384	2.404
Dy-O_{av}	0.046	0.043	-0.0465	0.004
Energy	0.00	0.43	0.93	0.00
SAPR (D_{4d})	3.973	5.923	1.701	2.861
TDD (D_{2d})	3.728	3.576	2.576	1.727
JBTPR (C_{2v})	4.464	5.442	3.350	3.534
BTPR (C_{2v})	3.828	4.804	2.700	2.893
JSD (D_{2d})	4.757	4.495	4.698	3.671

Dy$^{\text{III}}$-2LI-*a*-D$_2$

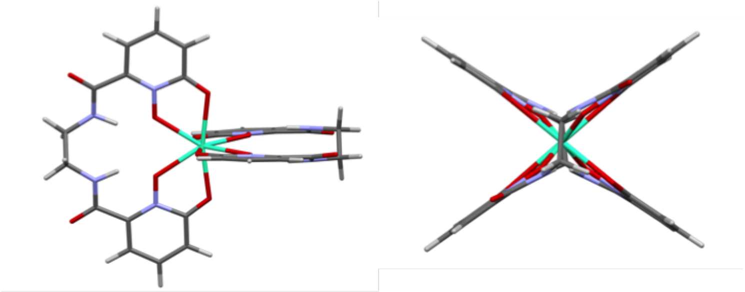

Dy$^{\text{III}}$-2LI-*a*-S$_4$

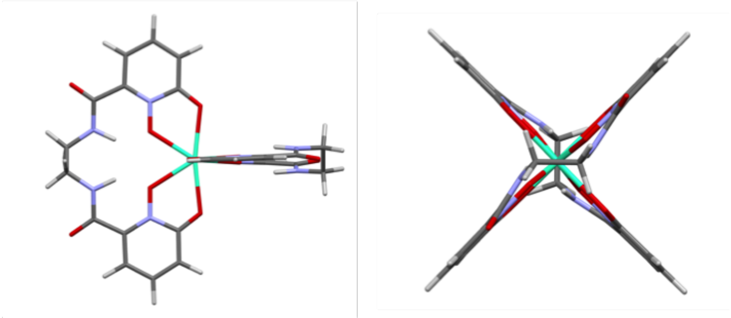

Dy$^{\text{III}}$-5LIO-*g*-*trans*

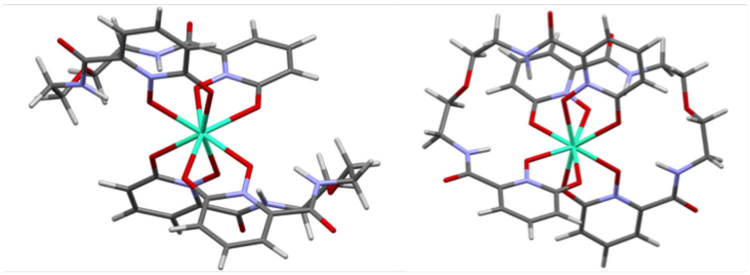

Dy$^{\text{III}}$-5LIO-*g*-*cis*

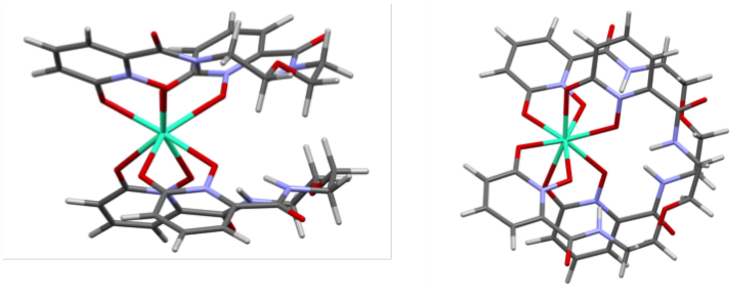

Figure 4.5: DFT optimised Dy$^{\text{III}}$ structures of the lowest energy ligand arrangements of 2LI and 5LIO.

4.3 Magnetism

Magnetic susceptibilities of the Ln^{III}-2LI and Ln^{III}-5LIO complexes were measured on powder samples at 0.05 and 0.1 Tesla over the temperature range 2-300 K. The χ_{M}T versus T plots are presented in Figure 4.6. The room temperature χ_{M}T values amount to 12.27(11), 10.52(9), 14.81(13) and 13.92(13) cm^3 K mol^{-1}, for compounds Tb^{III}-2LI, Tb^{III}-5LIO, Dy^{III}-2LI and Dy^{III}-5LIO, respectively. The χ_{M}T values of the Ln^{III}-5LIO complexes are below the respective free ion values, whereas the Ln^{III}-2LI complexes are slightly above these values (Tb^{III} = 11.82 cm^3 K mol^{-1}, Dy^{III} = 14.17 cm^3 K mol^{-1}). The values are, however, within the range previously found for mononuclear Dy^{III} and Tb^{III} complexes.[81–86] The magnetic susceptibilities experience a slight decrease with decreasing temperature, attributed to depopulation of the ground state M_J levels (^{7}F$_6$ and ^{6}H$_{15/2}$ for Tb^{III} and Dy^{III}, respectively). The more pronounced drop of χ_{M}T at low temperature is likely due to magnetic anisotropy. Low temperature field dependent magnetisation was measured for all complexes. Experimental values were found to be significantly lower than the theoretical values for the $M_J = \pm 6$ and $M_J = \pm 15/2$ ground states (9 μ_B and 10 μ_B, respectively), and non-saturation of magnetisation at high field suggests the presence of appreciable magnetic anisotropy and/or of low-lying excited states (Figure 4.7).[87] This conclusion is supported by non-superposition of the M $vs.$ B/T plots at higher field (see Appendix).[88–91]

In order to obtain further information about the ground state M_J levels, loose powder samples were also measured. Field alignment of the samples was evidenced by significantly higher values of M as compared to the fixed powder measurements for all complexes except Dy^{III}-2LI (Figure 4.7). For the Tb^{III} complexes the maximum magnetisation values of the loose powder measurements are 6.24(10) μ_{B} and 6.96(5) μ_{B} (theoretical M = 9 μ_{B}), as compared to the fixed powder values of 4.69(4) μ_{B} and 4.48(4) μ_{B} for Tb^{III}-2LI and Tb^{III}-5LIO, respectively. The maximum values of the loose powder Dy^{III} samples are 5.73(13) μ_{B} and 7.10(15) μ_{B} (theoretical M = 10 μ_{B}) as compared to the fixed powder values of 5.30(5) μ_{B} and 5.30(5) μ_{B} for Dy^{III}-2LI and Dy^{III}-5LIO, respectively.

The maximum magnetisation values of the loose powder measurements are, however, still lower than the theoretical values for $M_J = \pm 6$ and $M_J = \pm 15/2$ ground states of Tb^{III} and Dy^{III}, respectively, and incomplete plateaus exist for all four samples even up to 5 T. Magnetisation measurements of loose powders have recently been successfully carried out on a set of trinuclear Cu^{II}-Dy^{III}-Cu^{II} complexes, with full saturation of magnetisation observed for two of the three reported complexes and elevated values much closer to the theoretical values than observed here.[21] The magnetisation values

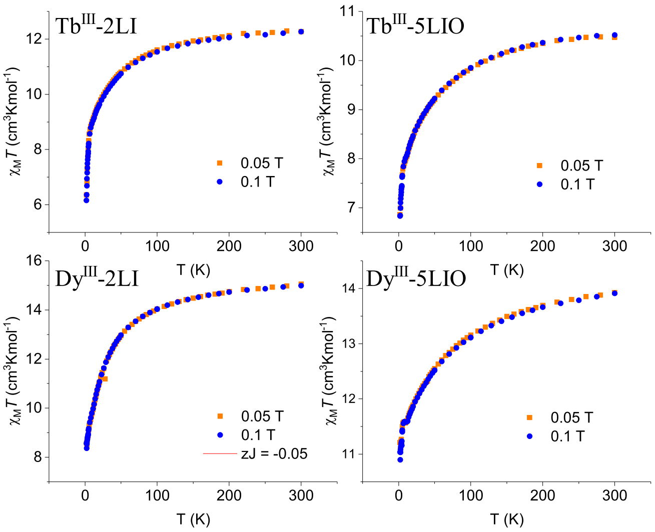

Figure 4.6: Magnetic susceptibility times T of Tb^{III}-2LI, Tb^{III}-5LIO, Dy^{III}-2LI, and Dy^{III}-5LIO (the full lines in the magnetic susceptibility curves are simulations based on the *ab initio* calculations, see below).

increased from the fixed powder value of 7.3 μ_B to 11 μ_B (theoretical M = 12 μ_B). In the single case of non-saturation of magnetisation, the fixed and loose powder values did not differ significantly, ascribed to the composition of the unit cell of the crystal structure. To be specific, for that complex four independent molecules exist per unit cell, resulting in four different orientations of the easy axes. This yields a reduced value of the magnetisation because the magnetic moments are canted from the applied field due to the strong anisotropy of Dy^{III}.

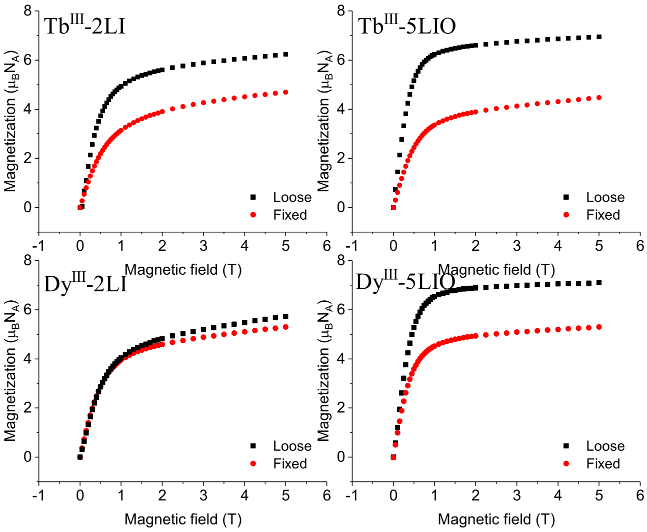

Figure 4.7: Low temperature (2 K) magnetisation data of fixed (black squares) and loose (red circles) powder samples of Tb^{III}-2LI, Tb^{III}-5LIO, Dy^{III}-2LI and Dy^{III}-5LIO.

In the present study, the Ln^{III}-2LI samples were found to contain either one or two independent molecules per unit cell, depending on the crystallisation technique. The Ln^{III}-2LI samples used for the loose powder measurements were prepared from hot DMF and are expected to contain only one molecule per unit cell (type B, see Section 4.2.1). Considering the results, however, the possibility of two molecules per unit cell cannot be excluded. In order to account for the possibility of this occurring in the Ln^{III}-2LI complexes, the z-component of the ground state g-values from the *ab initio* results (see below) of the type A structures (two molecules per unit cell) were used in order to calculate the average g-value. The easy axis orientations of the two molecules are almost perpendicular to each other, with an angle of about 84 ° between the two in both the Tb^{III} and Dy^{III} structures. A schematic of this is presented in Figure 4.8, and the average g_z values are 11.33 and 13.45 for Tb^{III}-2LI and Dy^{III}-2LI, respectively.

The effective g-value of a given doublet is related to the magnetisation of that doublet through equations (4.1) and (4.2).

$$g_{eff} = g_J \Delta M_J \tag{4.1}$$

$$M = g_J M_J \tag{4.2}$$

If, as in this case, the g-value is of an M_J doublet, ΔM_J can be written as $2M_J$ and

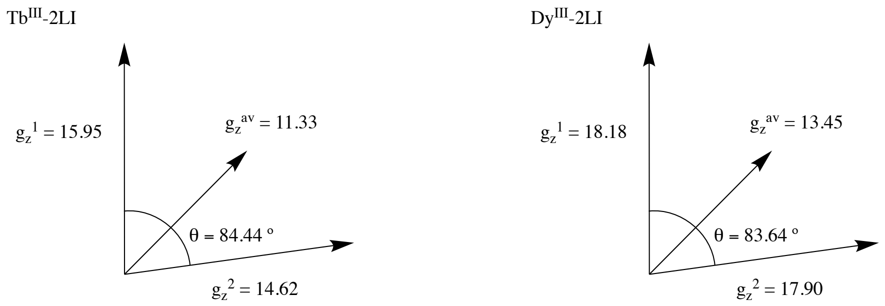

Figure 4.8: Schematic representation of the vector average of the z-components of the ground state g-values for the two molecules in the unit cell of the type A Tb^{III}-2LI and Dy^{III}-2LI crystals. The magnetisation values are calculated using equation (4.3) to yield 5.7 and 6.7 μ_B, respectively (see main text for details).

the magnetisation can be calculated using equation (4.3)

$$M = g_{eff}/2 \tag{4.3}$$

which then yields the maximum theoretical magnetisation values of 5.7 and 6.7 μ_B for Tb^{III}-2LI and Dy^{III}-2LI, respectively. As these values represent the *maximum* magnetisation values expected for the case of two perpendicular g_z axes, it is expected that the experimental value must be lower than this upper limit. Therefore, a value larger than the calculated value would indicate no averaging of two magnetic axes, and hence only one molecule per unit cell. Comparing the calculated values with the experimental results of 6.24(10) and 5.73(13) μ_B, of the Tb^{III} and Dy^{III} complexes, respectively, it may be concluded that Dy^{III}-2LI experiences an average magnetisation, whereas, the larger experimental value of Tb^{III}-2LI would suggest that this value represents the true, although not maximum, magnetisation of a single molecule. In the case of the Ln^{III}-5LIO complexes no crystal structures could be produced, however, crystal structures of the Sm^{III}, Eu^{III} and Gd^{III} analogues were found to contain only a single molecule per unit cell, and it is considered reasonable to conclude that this is also case for the two complexes reported here. It is then suggested that the reduced values could be due to weak anisotropy, but could also originate from incomplete alignment due to differences in the domain and particle sizes of the sample and/or the composition of the powder particles preventing reorientation in the magnetic field. The loose powder saturation magnetisation therefore provides a lower limit for the ground state anisotropy. The results indicate that the ground state anisotropy of Tb^{III}-5LIO is larger than that of Tb^{III}-2LI, however, it is difficult to draw the same conclusion for the Dy^{III} complexes. It should also be noted that the 5 T magnetisation values of the two Tb^{III} complexes are consistent with the HF-EPR determined g-values (see below), suggesting that the M values for these two complexes may be reasonable. In order to obtain further information on the magnetic ground state of Tb^{III}-2LI and Tb^{III}-5LIO, loose powder samples were measured in pulsed magnetic fields up to 58 T (Figure 4.9). The data were collected by Denis I. Gorbunov in the Hochfeld-Magnetlabor Dresden (HLD-EMFL) at the Helmholtz-Zentrum Dresden-Rossendorf, Dresden. The obtained pulsed field data are consistent with the static field magnetisation data at B = 5 T. For both samples, the magnetisation shows a sharp increase up to about 6.2(6) μ_B for Tb^{III}-2LI and 6.8(4) μ_B for Tb^{III}-5LIO in the static field range, followed by a smooth increase to the maximum field of 58 T. No saturation of the magnetisation is observed even at the maximum field. The measured maximum values of the magnetisation are 8.1(2) μ_B and 8.45(8) μ_B for Tb^{III}-2LI and Tb^{III}-5LIO, respectively. Although no significant step or kink feature appears in the data, it is concluded that the smooth increase of the magnetisation represents the field induced mixing of higher states to the B = 0 ground state. From the low field data, a ground state of $M_J = \pm 4$ and $M_J = \pm 5$ for Tb^{III}-2LI and Tb^{III}-5LIO are estimated, respectively (with the Tb^{III} Landé g-factor of 1.5), which is in qualitative agreement with the HF-EPR data presented below. The magnetisation values at 58 T approach the value expected for a ground state of $M_J = \pm 6$, $M = 9$ μ_B, indicating a large contribution of $M_J = \pm 6$ to the ground state/low-lying states of both complexes.

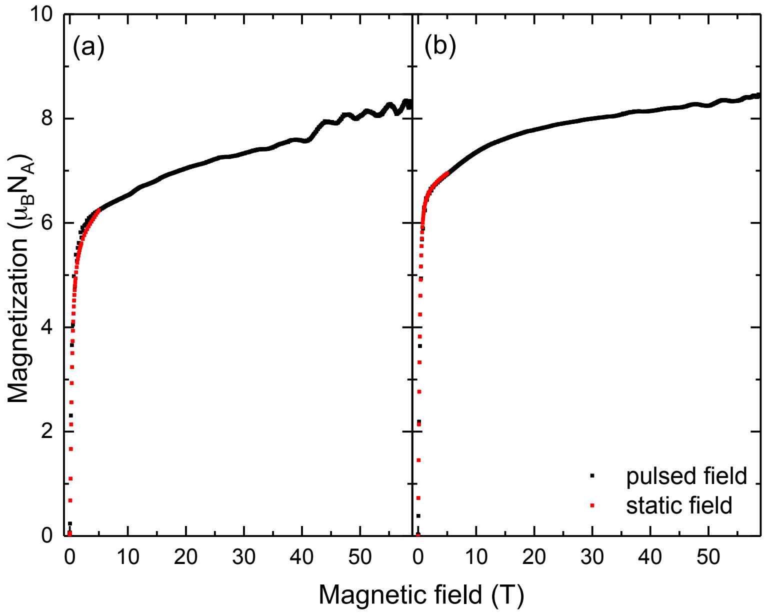

Figure 4.9: Magnetisation of (a) Tb^{III}-2LI and (b) Tb^{III}-5LIO measured in pulsed magnetic field up to 58 T at 1.5 K. For comparison, the static field magnetisation data up to 5 T are also shown as red data points.

4.4 High-frequency electron paramagnetic resonance (HF-EPR)

The HF-EPR experiments and data analysis were carried out within the group of Prof. Rüdiger Klingeler at the Kirchhoff Institute for Physics by Johannes Werner and Dr. Changhyun Koo. Fixed powder HF-EPR spectra were collected for both Ln^{III}-2LI and Ln^{III}-5LIO complexes of Tb^{III} and Dy^{III}, however, the Dy^{III} spectra show a broad resonance feature with a wide line width of 3 T, which is not clear enough to be evaluated. A single resonance feature is observed for both the Tb^{III} complexes (B = 0-16 T). Figure 4.10 presents a selection of the low temperature spectra with resonance fields measured at various frequencies. The single resonance feature appears at low magnetic fields ($B < 2$ T) with no additional resonance features identifiable at higher temperatures (Figure 4.11). The linear dependence on frequency of the resonance fields (Figure 4.10) has a slope much steeper than the g-factor g = 1.5 of the allowed transition, therefore, this resonance is attributed to forbidden transitions. A linear fit of the data produced an estimated g-value and the zero field splitting (ZFS) of g = 11(2) and ΔZFS = 52(4) GHz, respectively for Tb^{III}-2LI, and g = 15(8) for Tb^{III}-5LIO. ΔZFS of Tb^{III}-5LIO is negligible. For the Tb^{III}-2LI complex, no EPR signal is observed below 44 GHz down to the lowest frequency of the experimental set-up used. The single

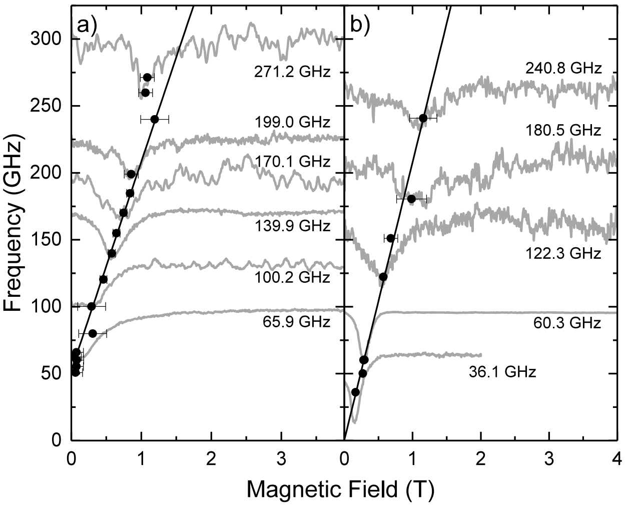

Figure 4.10: Resonance field position of (a) Tb^{III}-2LI and (b) Tb^{III}-5LIO complexes at various frequencies, at 2 K. Representative EPR spectra are shown with corresponding frequency values. The solid lines represent the linear fitting lines. See the text for the fitting parameters.

resonance feature observed in a wide magnetic field and temperature range indicates that the resonance originates from the ground state excitation, with a reasonably large energy difference between the ground state and the first excited state, *i.e.*, $\Delta \geq 20$ K (14 cm^{-1}). In the general case of a system with no single ion anisotropy resulting in no ZFS, all of the resonances overlay in the same magnetic field and it appears as only a single resonance feature in the EPR spectrum with $g_{\mathrm{Landé}}$. However, the anisotropy of Tb$^{\mathrm{III}}$ is not negligible and is supposed to cause state mixing. Correspondingly, the observed resonance shows a large g-value implying that the resonance is due to a forbidden transition that does not follow the conventional magnetic dipole selection rule. Due to the large energy difference between the ground state and the excited state, conventional, *i.e.*, so-called allowed, resonances following the selection rule do not show up in the studied frequency range but only the forbidden resonance appears, which is observed in the specific magnetic field orientation where state mixing is induced by transverse anisotropy. This is corroborated by the experimental data since the observed resonance does not exhibit the typical shape for a powder EPR spectrum.

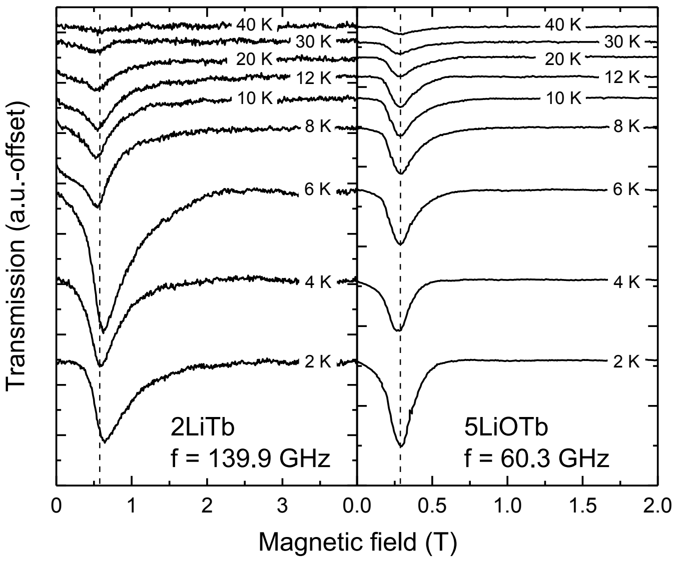

Figure 4.11: HF-EPR spectra of (a) Tb$^{\mathrm{III}}$-2LI and (b) Tb$^{\mathrm{III}}$-5LIO complexes at various temperatures, with f = 139.9 GHz and 60.3 GHz, respectively. Corresponding temperatures are labelled in the spectra. The vertical dashed lines are guides to the eye.

Applying the Landé g-factor of the Tb$^{\mathrm{III}}$ ion, $g_{\mathrm{Landé}} = 1.5$, the slopes of the resonance branches suggest differences of the angular momentum corresponding to the energy states related to the resonance of about 7.4 and 10 for Tb$^{\mathrm{III}}$-2LI and Tb$^{\mathrm{III}}$-5LIO, respectively. In the case of an integer angular momentum like Tb^{III} (J = 6), the possible transitions with the above g-factors are $M_J = -4 \rightarrow +4$ and $M_J = -5 \rightarrow +5$ for Tb^{III}-2LI and Tb^{III}-5LIO, respectively. Hence, the HF-EPR data suggest for both complexes that the $M_J = 6$ state is not the ground state, leading to the conclusion that the studied complexes lack axial symmetry. It is interesting that a ZFS is observed for the Tb^{III}-2LI complex, while not for the Tb^{III}-5LIO complex. The observed ZFS in the Tb^{III}-2LI complex may be ascribed to the energy splitting between the ground doublet states, which is induced by the transverse anisotropy. The absence of a ZFS in Tb^{III}-5LIO can hence be understood in terms of a relatively weak transverse anisotropy that might be so small, that the ZFS is not resolved, and this conclusion is consistent with the *ab initio* results (see Table 4.7 below). However, due to the non-negligible transverse anisotropy and misalignment of spins in the fixed powder sample, the forbidden resonance still appears.

4.5 Magnetic circular dichroism

In order to illustrate the subtle ligand field effects of the two main binding modes on the M_J splitting, MCD spectra of the Dy$^{\mathrm{III}}$ complexes were measured. The transitions of Tb$^{\mathrm{III}}$ occur largely outside the measurable range of the experimental set-up used and these complexes were not measured. Spectra of the Dy$^{\mathrm{III}}$ complexes were obtained from glass samples in 1:2 MeOH/DMF solutions at 5 T over the temperature range 2-75 K. An overview of the full spectra of both complexes can be found in Figures 4.13 and 4.14, with assignments of the bands to the appropriate multiplets. Detailed spectra of selected transitions are shown in Figure 4.12. The absorption electronic spectra were also measured but were of low quality due to small extinction coefficients and large background noise. The very weak ΔA signals are easily detected with the phase-sensitive detection used in MCD and the $f-f$-transitions are distinctly observed. Dy$^{\mathrm{III}}$ has 1001 Kramers doublets, of which 46 are expected to occur within the range of 7 000-24 000 cm^{-1}. These correspond to the multiplets ^{6}H$_{9/2}$, ^{6}H$_{7/2}$, ^{6}H$_{5/2}$, ^{6}F$_{11/2}$, ^{6}F$_{9/2}$, ^{6}F$_{7/2}$, ^{6}F$_{5/2}$, ^{6}F$_{3/2}$, ^{6}F$_{1/2}$, ^{4}F$_{9/2}$ and ^{4}I$_{15/2}$. The transition ^{6}H$_{15/2}$ $\rightarrow$ ^{6}F$_{1/2}$ is forbidden due to $\Delta J > 6$ and is not observed experimentally.[92] The energies of these transitions are predominantly determined by the free ion terms and the spectra of the two complexes therefore appear to be very similar. However, small features, such as hot bands, differences in relative intensities and slight shifts in energy reveal differences in the ligand field splitting of the multiplet levels.

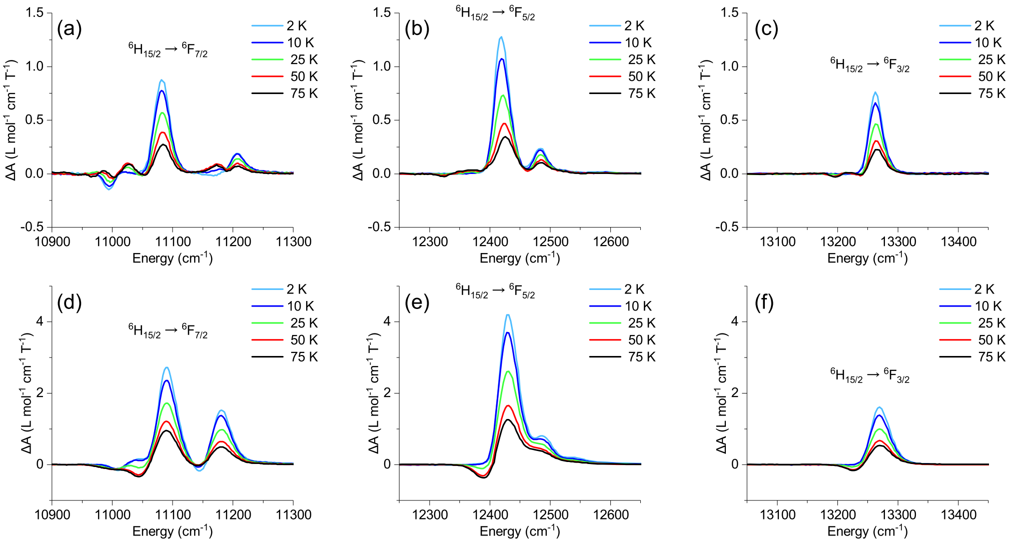

Figure 4.12: Temperature dependence of selected MCD transitions of Dy$^{\mathrm{III}}$-2LI (a)-(c) and Dy$^{\mathrm{III}}$-5LIO (d)-(f).

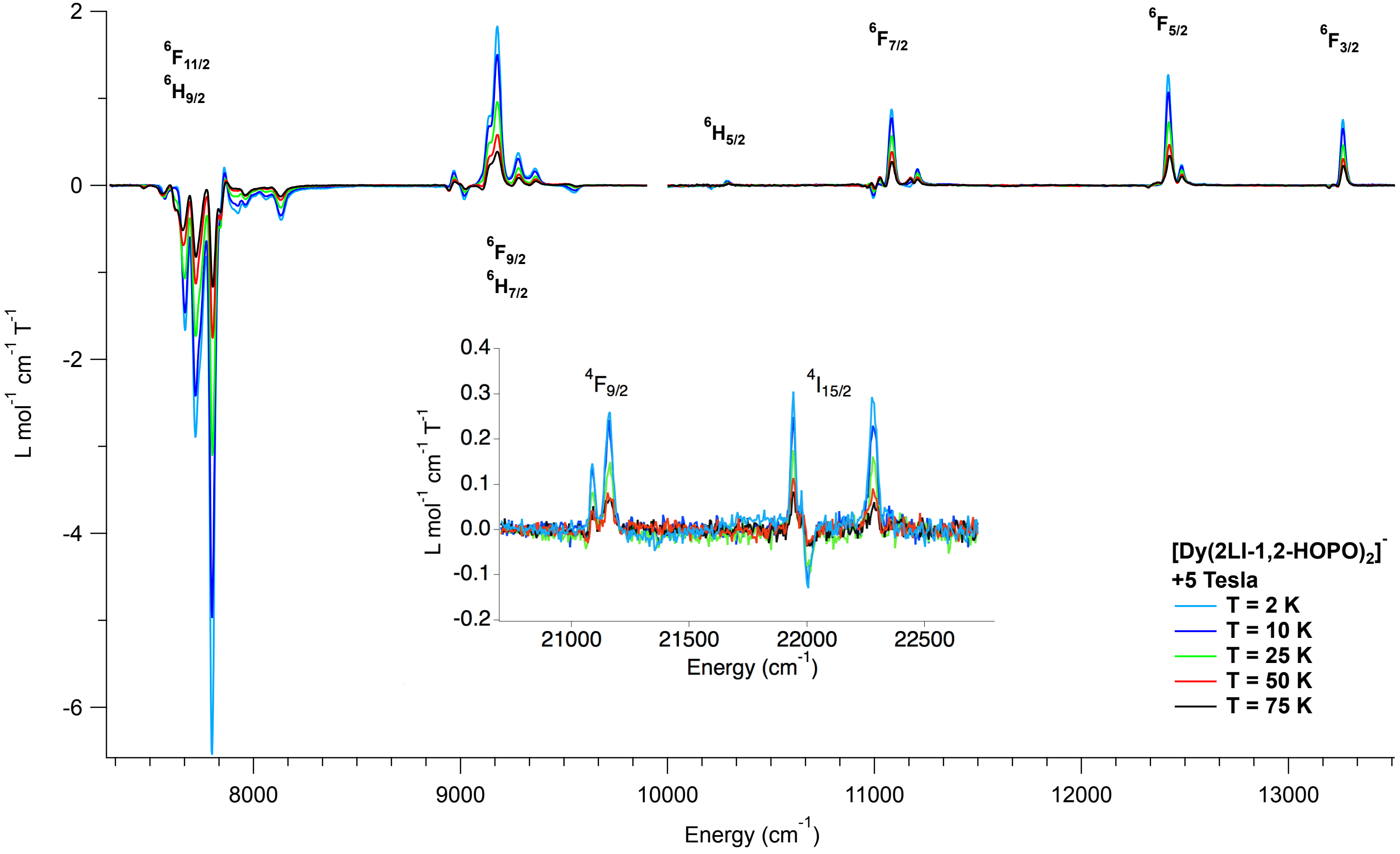

Figure 4.13: Temperature dependent MCD spectra of [Dy(2LI-1,2-HOPO)$_2$]$^-$.

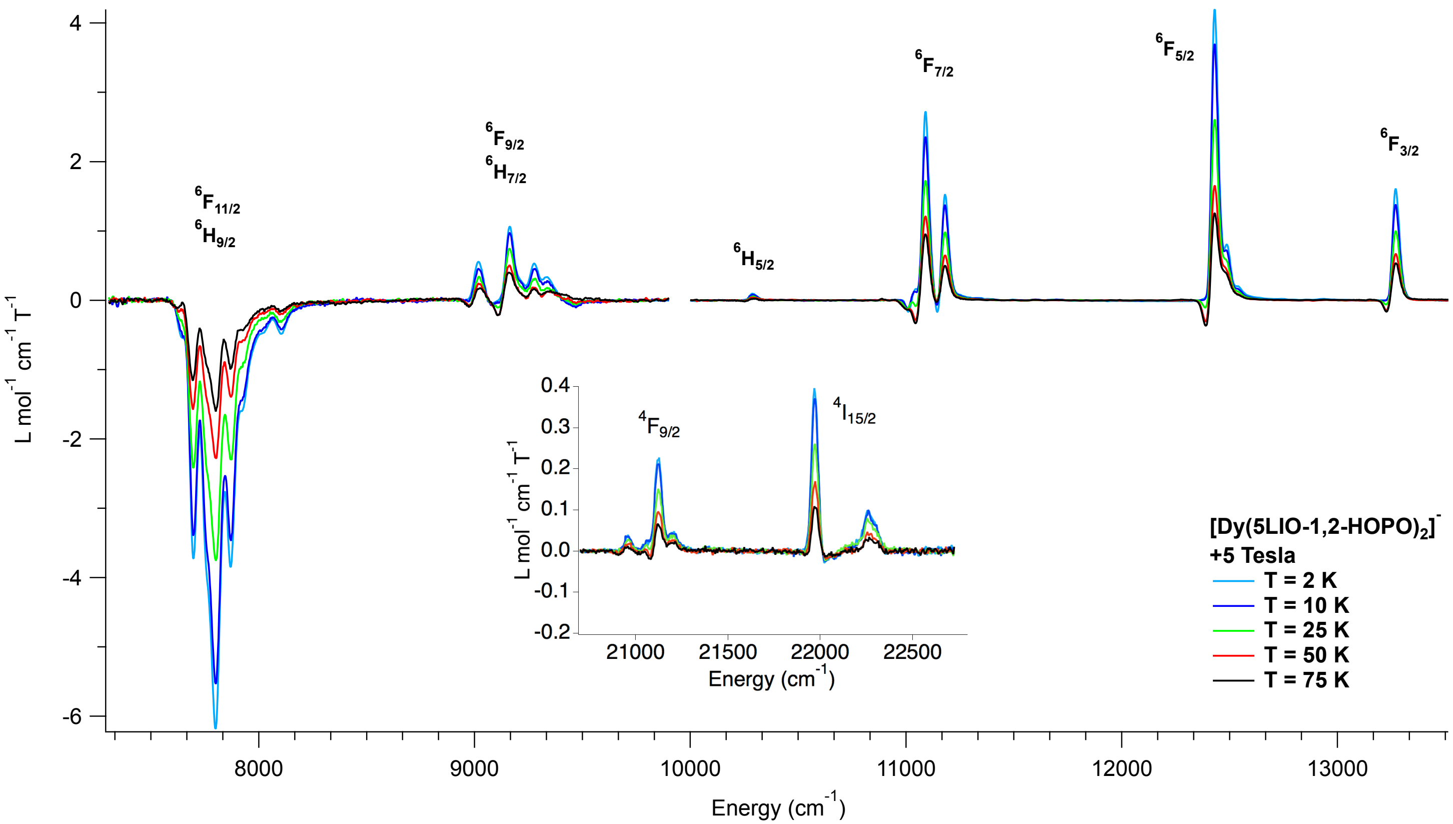

Figure 4.14: Temperature dependent MCD spectra of $[Dy(5LIO\text{-}1,2\text{-}HOPO)_2]^-$.

4.5.1 Fitting of the MCD data with OriginPro

The individual transitions were carefully extracted using the fitting function in OriginPro 2017.[93] Spectra at all measured temperatures were analysed in order to obtain a consistent set of energies and relative intensities of both the main transitions and hot bands. Details of all the fitted transitions, along with illustrations of the fits of the 2 K and 75 K spectra are provided in the Appendix. In some cases the number of fitted transitions does not correspond to the number of transitions theoretically expected. As the spectra were measured in frozen solution and the complexes lack perfect symmetry, the usual selection rules do not apply and it was considered more accurate to fit the spectra without adhering to strict theoretical constraints. Coincidence of the energies of the $^6H_{9/2}$, $^6H_{7/2}$ multiplets with the $^6F_{11/2}$, $^6F_{9/2}$ multiplets, respectively, results in a large number of transitions in both these regions; nonetheless, a best attempt to extract these transitions was made and can be found in the Appendix. The transition $^6H_{15/2} \rightarrow {}^6H_{5/2}$ is observed around 10 250 cm^{-1} but was considered too weak to fit. Figure 4.12 presents the temperature dependence of the transitions $^6H_{15/2} \rightarrow {}^6F_{7/2}$, $^6F_{5/2}$ and $^6F_{3/2}$, for both Dy^{III}-2LI and Dy^{III}-5LIO.

4.5.2 Qualitative interpretation

These transitions show clear $\mathscr{C}$ term behaviour, as is expected for a system possessing a degenerate ground state. Decreasing signal intensities with increasing temperature indicate that the population of the upper level of the split Kramers doublet is of the opposite sign, leading to cancellation of the low temperature transitions, and means the energies of the transitions originating from the two components of the split doublet are not resolved. Hot bands can be observed with increasing temperature and are due to transitions from thermally occupied low-lying excited states. The respective energy shifts of the hot bands for the transitions to multiplets $^6F_{5/2}$ and $^6F_{3/2}$ were found to be about 100 and 70 cm^{-1} for Dy^{III}-2LI, and 40 cm^{-1} for both transitions of Dy^{III}-5LIO. These negative signals appearing at lower energy to the main peaks indicate that the effective g-value in this thermally populated state is of the opposite sign to the ground state. The larger intensities of these signals of Dy^{III}-5LIO in comparison to Dy^{III}-2LI are indicative of a greater effective g-value of the ground state of Dy^{III}-5LIO. In low-temperature glass where the molecules are randomly oriented, it would appear that MCD for light parallel to g_z is more effective at including MCD intensity in the Dy^{III}-5LIO complex as compared to the Dy^{III}-2LI complex.

4.6 Ligand field theory calculations

The results of a full f^9 ligand field calculation is shown in Figure 4.16 as a stick spectrum indicating the upper state multiplet of the various transitions, and these calculated energies as well as the experimental energies are presented in Table 4.5. The Hamiltonian is described in Section 3.3 and includes electron repulsion (F^k), spin-orbit coupling (ζ), two body CI terms (α, β, γ), the three body parameters (T^k), the magnetic parameters (M^k) describing spin-spin and spin-other orbit interaction and the electrostatically correlated spin-orbit interaction (P^k). The ligand environment is accounted for by using the Angular Overlap Model (AOM), which uses structural information about the complex and parameters that describe the weak σ and π bonding interactions. The calculation has been made in the full 2002×2002 basis of all f^9 free ion states, with symmetry used where possible to block the matrices

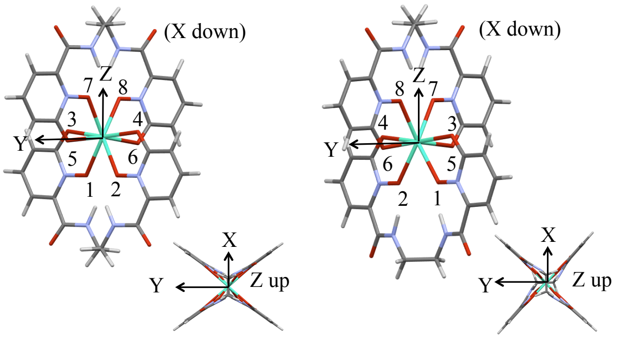

Figure 4.15: Orientation of xyz-axes for definition of AOM angles of Dy^{III}-2LI-*a*-D$_2$ (left) and Dy^{III}-2LI-*a*-S$_4$ (right).

The 2LI ligand in either D$_2$ or S$_4$ symmetry (see Figure 4.15) is attractive as it can be determined with a small number of parameters. The 8 coordinating oxygen atoms have two unique positions which are related to the others by the C$_2$ or S$_4$ axes. This means that there are only two sets of AOM angles θ, ϕ and two sets of e_σ, e_π bonding parameters. However, it is expected that the π-bonding will be anisotropic due to the five membered chelate ring with aromatic character. The χ angle in Table 4.3 is defined such that the local ligand y-axis is directed within the plane containing the Dy^{III} and the two oxygens of the ring (see Figure 4.15). There are two e_π parameters with respect to these local axes and one would expect $e_{\pi x} > e_{\pi y}$. The definition of the AOM angles has been described in detail.[94] The description of the ligand field in terms of the AOM parameters is entirely equivalent to the use of the crystal field parameters as given in Ref[44]. The 27 possible B_q^k, $B_q^{k\prime}$ parameters are related to the 27 matrix elements of 7×7 AOM matrix in the basis of real f orbitals (upper triangle – trace) as given in the

Table 4.3: Defined AOM angles for Dy$^{\text{III}}$-2LI-a-D$_2$ and Dy$^{\text{III}}$-2LI-a-S$_4$. Bond lengths are defined as r_1 = 2.382 Å (Dy-O1, O2, O7, O8), and r_2 = 2.428 Å (Dy-O3, O4, O5, O6).

	L	e_σ	$e_{\pi x}$	$e_{\pi y}$	ϑ	ϕ	χ	
D$_2$	O1	$e_{\sigma 1}$	$e_{\pi x 1}$	$e_{\pi y 1}$	$180-\vartheta_1$	ϕ_1	$90-\chi_1$	$\vartheta_1 = 33.05$
	O2	$e_{\sigma 1}$	$e_{\pi x 1}$	$e_{\pi y 1}$	$180-\vartheta_1$	$180+\phi_1$	$90-\chi_1$	$\vartheta_2 = 83.69$
	O3	$e_{\sigma 2}$	$e_{\pi x 2}$	$e_{\pi y 2}$	ϑ_2	ϕ_2	$90-\chi_2$	$\phi_1 = 38.12$
	O4	$e_{\sigma 2}$	$e_{\pi x 2}$	$e_{\pi y 2}$	ϑ_2	$180+\phi_2$	$90-\chi_2$	$\phi_2 = 48.80$
	O5	$e_{\sigma 2}$	$e_{\pi x 2}$	$e_{\pi y 2}$	$180-\vartheta_2$	$180-\phi_2$	$90-\chi_2$	$\chi_1 = 11.83$
	O6	$e_{\sigma 2}$	$e_{\pi x 2}$	$e_{\pi y 2}$	$180-\vartheta_2$	$-\phi_2$	$90-\chi_2$	$\chi_2 = 6.46$
	O7	$e_{\sigma 1}$	$e_{\pi x 1}$	$e_{\pi y 1}$	ϑ_1	$180-\phi_1$	$90-\chi_1$	
	O8	$e_{\sigma 1}$	$e_{\pi x 1}$	$e_{\pi y 1}$	ϑ_1	$-\phi_1$	$90-\chi_1$	
S$_4$	O1	$e_{\sigma 1}$	$e_{\pi x 1}$	$e_{\pi y 1}$	$180-\vartheta_1$	$270-\phi_1$	$90-\chi_1$	$\vartheta_1 = 32.41$
	O2	$e_{\sigma 1}$	$e_{\pi x 1}$	$e_{\pi y 1}$	$180-\vartheta_1$	$90-\phi_1$	$90-\chi_1$	$\vartheta_2 = 83.93$
	O3	$e_{\sigma 2}$	$e_{\pi x 2}$	$e_{\pi y 2}$	ϑ_2	$180+\phi_2$	$90-\chi_2$	$\phi_1 = 39.53$
	O4	$e_{\sigma 2}$	$e_{\pi x 2}$	$e_{\pi y 2}$	ϑ_2	ϕ_2	$90-\chi_2$	$\phi_2 = 45.09$
	O5	$e_{\sigma 2}$	$e_{\pi x 2}$	$e_{\pi y 2}$	$180-\vartheta_2$	$270+\phi_2$	$90-\chi_2$	$\chi_1 = 5.96$
	O6	$e_{\sigma 2}$	$e_{\pi x 2}$	$e_{\pi y 2}$	$180-\vartheta_2$	$90+\phi_2$	$90-\chi_2$	$\chi_2 = 3.21$
	O7	$e_{\sigma 1}$	$e_{\pi x 1}$	$e_{\pi y 1}$	ϑ_1	$-\phi_1$	$90-\chi_1$	
	O8	$e_{\sigma 1}$	$e_{\pi x 1}$	$e_{\pi y 1}$	ϑ_1	$180-\phi_1$	$90-\chi_1$	

literature.[57] For anisotropic π-bonding, one requires the AOM factors using all three angles and this may be achieved by substituting the Eulerian transformation matrix for the directional cosines in Eq. (5) and Table 1 of Urland,[57] resulting in the F(f) matrix. While the AOM is equivalent to the CF parameterisation, it remains to be seen how chemically meaningful the parameters are. They are not well-defined, but the trend from previous studies is that $e_\sigma < 400$ cm^{-1} is smaller and the e_π/e_σ ratio is larger than in transition metal complexes. The e_π anisotropy has previously been shown to be significant in a single crystal polarised spectral study.[58] A drawback of using crystal field parameters is that the same ligand field can be described by a completely different set of parameter values depending on the definition of the coordinate system. This is a particular problem with low symmetry complexes and is important because the choice of coordinate system defines the basis functions and the description of the electronic state. For example, if one is seeking a ground state with a high $|\pm M_J>$ value, this will depend on the definition of the coordinate system.

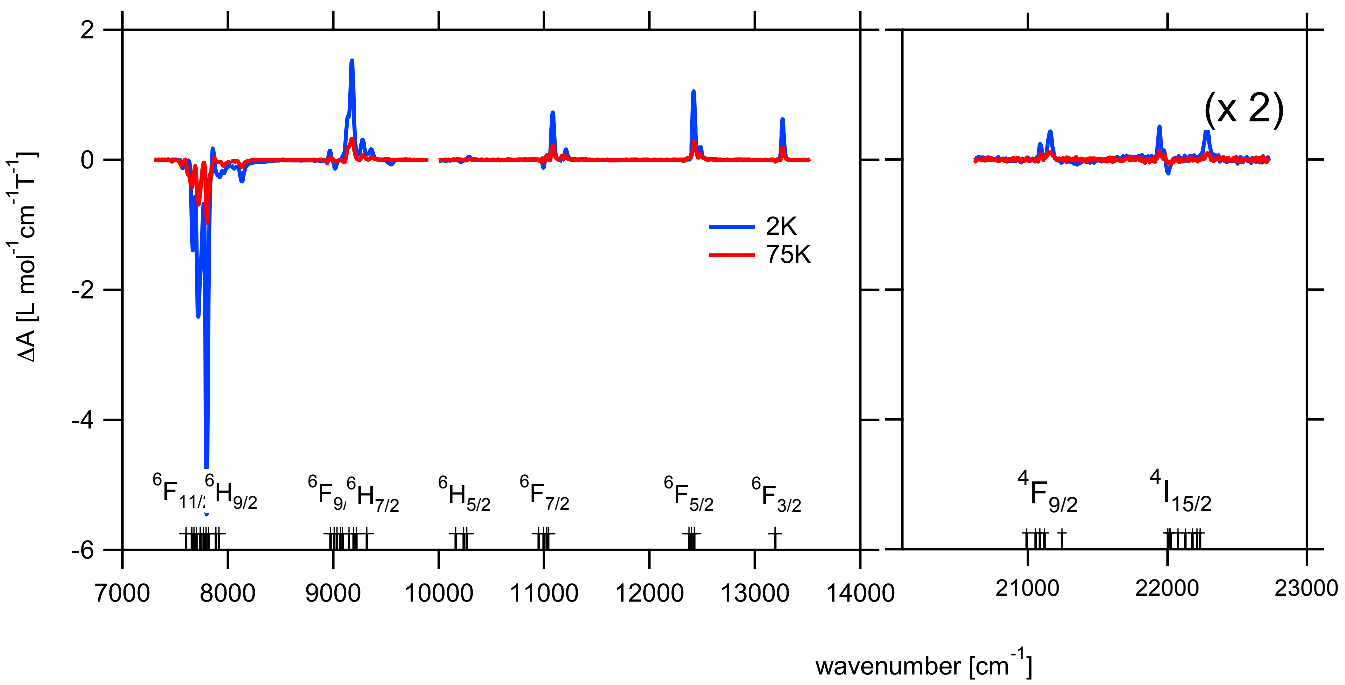

Figure 4.16: The MCD spectra of Dy^{III}-2LI at 5 Tesla and 2 (blue) and 75 K (red). The calculated energies are shown as stick plots below with the excited state multiplet involved in the transition. The calculated energies are using the geometry and parameters of Tables 4.3 and 4.4, together with reported free ion values.[95]

Table 4.4: *Ab initio* calculated and ligand field parameters and the corresponding fitted AOM parameters for Dy$^{\mathrm{III}}$-2LI-a-D$_2$.

k	q	B_q^k (CASSCF) [cm^{-1}]	B_q^k (AOM fit) [cm^{-1}]	AOM parameters
2	0	138.889	137.203	$e_{\sigma 1}$ = 236.2
2	2	–53.727	–12.241	$e_{\pi x1}$ = 112.8
4	0	96.663	98.589	$e_{\pi y1}$ = 49.0
4	2	201.820	194.920	$e_{\sigma 2}$ = 223.9
4	4	–639.759	–643.757	$e_{\pi x2}$ = 49.1
6	0	–756.937	–756.740	$e_{\pi y2}$ = 66.6
6	2	12.153	11.145	
6	4	251.911	249.755	
6	6	196.626	196.723	

The ligand field parameters of the Dy$^{\mathrm{III}}$ complexes have also been calculated *ab initio* as coefficients to extended Stevens operators as zero field parameters in a pseudo spin Hamiltonian with an effective S = 15/2 ground state (see Section 4.7) and are presented in Table 4.6.[66] Much similar information can be gained about the magnetic properties of the ground state as in a full ligand field calculation but it remains to be seen whether the two approaches are consistent. It therefore is of interest to compare the *ab initio* calculated values with ligand field parameters obtained in a full f^9 diagonalisation. Ryabov has given relationships between the standard Wybourne B_q^k parameters and the B_q^k(ESO) parameters by considering the B_q^k operating within a particular LSJ multiplet.[96] However, the multiplet that the ligand field operates in is only 93% pure ^{6}H$_{15/2}$ multiplet, spin-orbit coupling and other atomic terms mix other J = 15/2 free ion states such as: ^{4}I(3)$_{15/2}$ and ^{4}I(1)$_{15/2}$. Ideally, one should diagonalise the atomic terms and take the eigenvectors of the lowest multiplet as a basis for further calculation with the ligand field. Then a direct comparison could be made with the ligand field matrix elements within the lowest multiplet and those of the ESO basis. However, this proved difficult as the degenerate set of 16 eigenvectors found with such an approach has to be ordered appropriately according to M_J values and, importantly, the phases need be fixed to allow a comparison of matrix elements.

A much easier approach is to calculate B_q^k from B_q^k(ESO) and then fit the AOM parameters to these B_q^k values by varying the e_σ, e_π parameters. For the Dy$^{\mathrm{III}}$-2LI complex, the B_q^k(ESO) have been calculated for both D$_2$ and S$_4$ symmetry (Table A.8) These symmetries will have 9 and 7 B_q^k parameters when the coordinate system is aligned with the symmetry axes. In D$_2$ all imaginary terms are zero, with the non-zero

Table 4.5: Full f^9 ligand field calculated and experimental (2 K) energies (cm^{-1}) of the [Dy(2LI-1,2-HOPO)$_2$]$^-$ MCD spectrum.

Term	Calc	Exp	Term	Calc	Exp	Term	Calc	Exp
^{6}H$_{15/2}$	0.000	-	^{6}H$_{9/2}$ + ^{6}F$_{11/2}$	7678.3	7716.4	^{6}F7/2	10950	10994
	36.146	-		7701.8	7740.8		10996	11083
	48.920	-		7738.4	7798.4		11026	11209
	88.574	-		7741.9	7810.6		11040	
	120.74	-		7769.9	7863.0	^{6}F$_{5/2}$	12374	12420
	194.81	-		7794.1	7888.4		12399	12483
	212.91	-		7815.7	7920.2		12424	
	271.05	-		7885.7	7963.2	^{6}F$_{3/2}$	13192	13261
^{6}H$_{13/2}$	3519.6	-		7916.0	8010.3		13193	13271
	3547.3	-			8061.7	^{6}F$_{1/2}$	13741	-
	3556.8	-			8133.4	^{4}F$_{9/2}$	20990	21090
	3563.5	-	^{6}H$_{7/2}$ + ^{6}F$_{9/2}$	8974.4	8968.5		21056	21159
	3584.7	-		9010.5	9019.4		21086	-
	3633.7	-		9036.3	9106.9		21118	-
	3645.0	-		9067.9	9135.6		21245	-
^{6}H$_{11/2}$	5845.1	-		9088.5	9177.7	^{4}I$_{15/2}$	22004	21942
	5874.8	-		9149.2	9277.3		22016	21980
	5892.8	-		9193.6	9358.4		22023	22002
	5905.0	-		9220.8	9545.2		22077	22282
	5923.4	-		9319.3	-		22129	-
	5942.5	-	^{6}H$_{5/2}$	10163	-		22178	-
	7602.8	7574.4		10238	-		22212	-
	7658.6	7669.2		10267	-		22234	-

terms listed in Table 4.4.

The B^k_q(ESO) parameters with the extended Stevens operators in the S = 15/2 basis give exactly the same eigenvalues if the equivalent B^k_q parameters are used in a ^{6}H$_{15/2}$ multiplet in isolation (as mentioned above, this is not strictly true). The pseudo spin approach can also include higher order zero-field terms for k = 8,10,12, .. but these terms are small and their neglect changes the eigenvalues by $<$ 1 cm^{-1}. A similar approach was made for the S$_4$ geometry but in this case there were some non-negligible B^k_q(ESO) components inconsistent with S$_4$ symmetry (B^2_2, B^4_2, B^6_2, B^6_6). If these were ignored, the AOM fit could not be consistently made.

The AOM values listed in Table 4.4 are not unreasonable. For each independent ligand set $e_\sigma > e_\pi$. The AOM parameters $e_{\sigma 1} > e_{\sigma 2}$ are consistent with $r_1 < r_2$, i.e. the axial ligands having slightly shorter bond lengths. The out-of-plane π-bonding is larger than the in-plane for the axial ligands ($e_{\pi x1} > e_{\pi y1}$), as expected; but not for the equatorial ligands. Therefore, the pseudo spin Hamiltonian used appears to give chemically reasonable parameters, making it a promising approach to determine a large number of parameters in low symmetry lanthanide complexes.

4.7 *Ab initio* calculations

Wave functions were computed *ab initio* with MOLCAS 8.0, details of this method can be found in the Section 4.7. Calculations were carried out on the crystal structure coordinates of Dy$^{\text{III}}$-2LI, Tb$^{\text{III}}$-2LI (this work), Eu$^{\text{III}}$-5LIO and Gd$^{\text{III}}$-5LIO.[71,72] All counter ions, solvent molecules and (if present) disorder in the crystal structures have been omitted from the input structural data. For the purpose of analysis of the MCD results, calculations were also carried out on DFT optimised Dy$^{\text{III}}$ structures (see Section 4.2.2). ANO-RCC basis sets were used to describe all atoms; triple zeta on all atoms but hydrogen (double zeta), with polarisation included for only the lanthanide and oxygen atoms. Active spaces of eight and nine electrons (for Tb$^{\text{III}}$ and Dy$^{\text{III}}$, respectively) in seven $4f$ orbitals were selected for the complete active space self-consistent field method (CASSCF).[97] The inclusion of dynamic correlation (second-order perturbation theory) was not considered necessary, as it is known to have only small effects for lanthanides.[98] For Tb$^{\text{III}}$ ($4f^8$), there exist 7 septet, 140 quintet, 200 triplet, and 200 singlet states. In a balance of cost and accuracy 7, 100, 100 and 100 states, were considered, respectively. For Dy$^{\text{III}}$ ($4f^9$) of the 21 sextet, 224 quartet, and 490 doublet states, all sextet, 100 quartet, and 100 doublet states were considered.[38] Spin-orbit coupling was introduced to the spin-free wave functions in each case through the restricted active space state interaction method (RASSI).[25] Due to the large number of states and associated calculation cost, only a limited number of states can be mixed by spin-orbit coupling. Therefore, for Tb$^{\text{III}}$ all septet, 50 quintet, triplet and singlet states were included. Similarly, all sextet, 50 quartet and doublet states were included for Dy$^{\text{III}}$. Finally, the MOLCAS SINGLE-ANISO module was utilised to calculate the local electronic and magnetic properties of each complex.

The resulting energies, g-tensors, relative orientations of local magnetic axes and decomposition of the RASSI wave functions for the first two doublet levels of the four different complexes are presented in Table 4.7. *Ab initio* calculations were carried out on all the available crystal structures, however, the results of a representative few are presented here. The remaining results are listed in the Appendix. Plots of the most likely relaxation pathways for complexes (c-3) and (d-1) are presented in the Appendix along with a summary of the relevant processes for all Dy$^{\text{III}}$ complexes.

4.7.1 Fitting of experimental data

Magnetic data

Simulations of the magnetic susceptibility of all measured complexes show acceptable agreement with the experimental data of the Ln^{III}-2LI and Ln^{III}-5LIO complexes (Figure 4.17). Note that the simulation of Ln^{III}-5LIO was carried out using the Gd^{III}-5LIO crystal structure. The simulations using the Eu^{III}-5LIO structure coordinates are less satisfactory. A comparison of the calculations based on the two different structures for both Tb^{III} and Dy^{III} is presented in Figure 4.18. This is likely due to the lanthanide contraction, the coordination bond lengths are expected to be such that Eu^{III} $>$ Gd^{III} $>$ Tb^{III} $>$ Dy^{III}.[99] Therefore, it is reasonable to expect that the Gd^{III}-5LIO structure would more closely represent the structure of the Tb^{III} and Dy^{III} complexes. Additionally, the simulation of the Tb^{III}-5LIO magnetic susceptibility using the Eu^{III}-5LIO structure is notably better than that of the Dy^{III} analogue, which may also be explained considering the relative ionic radii. This illustrates the high sensitivity of this computational method and the importance of using experimentally determined crystal structures.

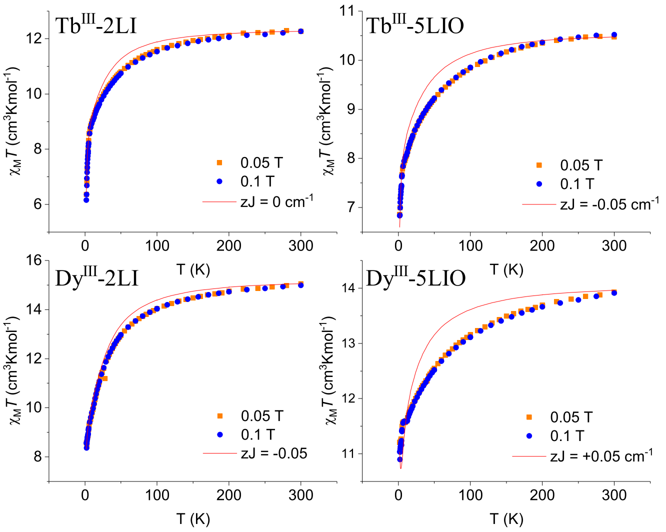

Figure 4.17: *Ab initio* simulations (red lines) of the magnetic susceptibility times T results of Tb^{III}-2LI, Tb^{III}-5LIO, Dy^{III}-2LI and Dy^{III}-5LIO.

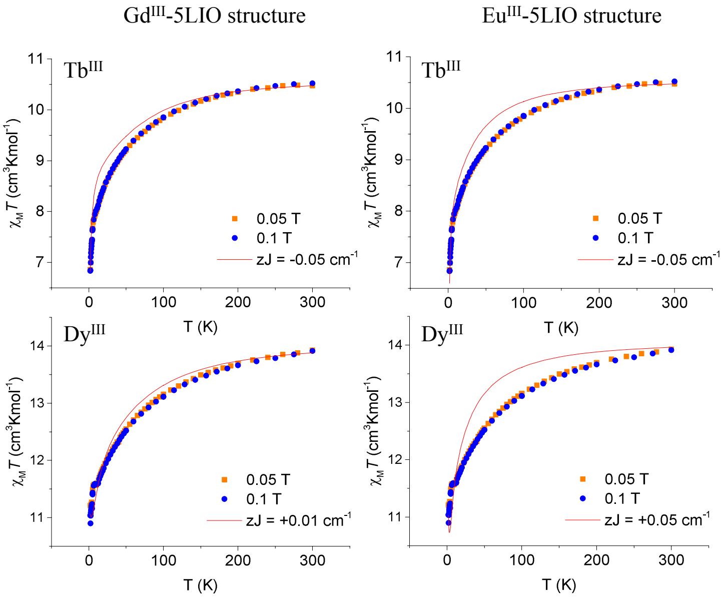

Figure 4.18: *Ab initio* simulations (red lines) of the magnetic susceptibility times T results of Tb^{III}-5LIO and Dy^{III}-5LIO using the crystal structure coordinates of Gd^{III}-5LIO and Eu^{III}-5LIO.

HF-EPR

The calculated g-tensors and composition of the ground state of the Tb^{III} complexes show acceptable qualitative agreement with the loose powder magnetisation and HF-EPR results, and indicate that the g-edged binding mode induces a more axial ligand field/larger M_J ground state than the a-edged arrangement. From the calculations, the ground states of the two Dy^{III} complexes appear not to differ significantly. However, due to inconclusive experimental data for Dy^{III}-2LI, no real comparison can be made with the loose powder magnetisation measurements.

MCD

With respect to the MCD results, the *ab initio* ligand field parameters as coefficients to the ESO of the optimised structures are presented in Tables 4.6, these have been converted to the standard Wybourne B_q^k values given in Table 4.4 (see discussion above). The Extended Stevens operators (ESO) of the ground multiplet are calculated by SINGLE_ANISO within MOLCAS 8.0. The decoupling of the wave function is in terms of the ESO Crystal-Field Hamiltonian:

$$H_{CF} = \sum_{k-2,4,6} \sum_{q=-k,k} [B_q^k O_q^k] \tag{4.4}$$

The AOM parameters required to reproduce this ligand field can be found by varying e_σ, $e_{\pi x}$, $e_{\pi y}$ while keeping coordinates fixed (Table 4.3). The B_q^k parameters found in this way together with the fitted AOM parameters also given in Table 4.4 demonstrate that *ab initio* ligand field parameters are reasonable.

4.7.2 SMM potential

Considering now the potential SMM behaviour of the four complexes, all first excitation energies are relatively small (Table 4.7), which increases the likelihood of thermally activated relaxation pathways. According to these results, quantum tunnelling of magnetisation is only relevant in the first excited state of Dy$^{\mathrm{III}}$-2LI and Dy$^{\mathrm{III}}$-5LIO (thermally activated quantum tunnelling of magnetisation, TA-QTM), despite mixing of the M_J states in both the ground and first excited states of all complexes, excluding the ground state of Tb$^{\mathrm{III}}$-5LIO. This mixing induces significant transversal moments, and leads to reduced magnetic anisotropy. Note that the g_x and g_y values of Tb$^{\mathrm{III}}$ (non-Kramers ion) are zero according to Griffith's theorem.[12]

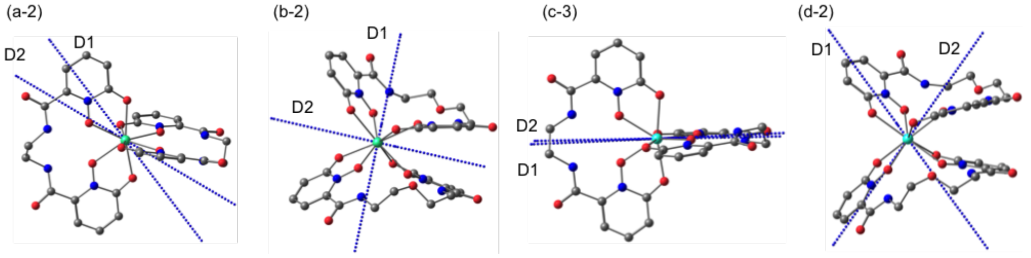

Figure 4.19: Orientations of the *ab initio* calculated main magnetic axes of the ground state doublets and first excited state doublets of (a-2) Tb$^{\mathrm{III}}$-2LI, (b-2) Tb$^{\mathrm{III}}$-5LIO, (c-3) Dy$^{\mathrm{III}}$-2LI and (d-2) Dy$^{\mathrm{III}}$-5LIO (see Table 4.7).

The orientations of the calculated magnetic axes of the two lowest states of structures (a-2), (b-2), (c-3) and (d-2) are illustrated in Figure 4.19, and the coordinates of the magnetic orientations of the remaining structures can be found in the supporting information of Ref[100]. Non-alignment of the local magnetic axes is likely to promote Orbach and Raman relaxation processes.[101] In the case of the *a*-edged complexes, the axis of Tb$^{\mathrm{III}}$-2LI is rotated approximately 34 degrees in comparison to Dy$^{\mathrm{III}}$-2LI, which is directed between the two sets of shorter Ln-O bonds of the pyridinolate oxygen donors. Due to relatively high symmetry of the type B Dy$^{\mathrm{III}}$-2LI complex, the magnetic axis of the first excited state is well aligned with the ground state, however this is not the case for the type A structures (c-1) and (c-2), the first excited states of which are rotated by about 50 degrees. The orientations of the two type A Tb$^{\mathrm{III}}$-2LI structures are similar to each other, and the first excited state of both is rotated by about 20 degrees from the ground state. The type B Tb^{III}-2LI shows different alignment of the ground state and rotation of about 80 degrees of the third excited state (the second being a singlet state). The main magnetic axis of the ground state of the Tb^{III}-5LIO calculated using the Gd^{III} structure (b-2) is oriented along C$_4$ axis of the twisted SAPR and rotates by 90 degrees from the ground state to the first excited state. This is also the case when using the Eu^{III} structure (b-1), however, with the orientations of first and second doublets (D1 and D2) are exchanged. For Dy^{III}-5LIO, however, the orientations of the main magnetic axes do not clearly coincide with the structural features, *e.g.* shortest bonds or symmetry axes, and non-alignment with the ground state is also observed. As is the case for Tb^{III}, the orientations of D1 and D2 of the Dy^{III} complexes are exchanged when comparing the Eu^{III}-5LIO and Gd^{III}-5LIO structures. According to Table A.9, Orbach and Raman processes are likely in to occur via the first excited state for all Dy^{III} complexes. Based on these results, it was concluded that none of the complexes would show promise as single molecule magnets, and hence, their dynamic magnetic properties were not determined experimentally.

Table 4.6: Crystal field parameters to describe the J = 15/2 ground-state multiplet splitting of Dy$^{\mathrm{III}}$-2LI optimised structures. The parameters are calculated for the optimised structures by decoupling of the wave function in terms of Extended Stevens operators and are given in cm^{-1}. These parameters result in a recovery factor of the crystal field matrix of 97.05 % and 97.18 %, respectively.

		Dy$^{\mathrm{III}}$-2LI-a-D$_2$			Dy$^{\mathrm{III}}$-2LI-a-S$_4$
k	q	B_k^q	k	q	B_k^q
2	-2	-0.00004	2	-2	-0.00033
2	-1	0.00018	2	-1	-0.00029
2	0	-0.51880	2	0	-0.58877
2	1	0.00003	2	1	-0.00001
2	2	0.28870	2	2	0.00150
4	-4	-0.00001	4	-4	0.01130
4	-3	0.00000	4	-3	0.00005
4	-2	0.00000	4	-2	0.00001
4	-1	0.00000	4	-1	0.00001
4	0	-0.00098	4	0	-0.00092
4	1	0.00000	4	1	0.00000
4	2	-0.00917	4	2	-0.00004
4	3	0.00001	4	3	-0.00003
4	4	0.04209	4	4	-0.04173
6	-6	0.00000	6	-6	0.00000
6	-5	0.00000	6	-5	0.00000
6	-4	0.00000	6	-4	0.00008
6	-3	0.00000	6	-3	0.00000
6	-2	0.00000	6	-2	0.00000
6	-1	0.00000	6	-1	0.00000
6	0	-0.00005	6	0	-0.00005
6	1	0.00000	6	1	0.00000
6	2	-0.00003	6	2	0.00000
6	3	0.00000	6	3	0.00000
6	4	0.00013	6	4	-0.00013
6	5	0.00000	6	5	0.00000
6	6	0.00014	6	6	0.00000

Table 4.7: Representative *ab initio* calculated excitation energies, g-tensors, magnetic axis orientations, and total coefficients of the M_J projections of the RASSI coupled wave function of the doublets of the first two doublets of a selected crystal structures. Details of all the $^6H_{15/2}$ doublet levels for all the calculated crystal structures are given in the Appendix.

	Doublets	Energy [cm^{-1}]	g-tensors g_x	g_y	g_z	∠D1-Dy-DX °	Total coefficients of the M_J projections of function the RASSI coupled wave
(a-2)	Tb^{III}-2LI[a] (Type A)						
	1	0.000/ 2.898	0.000	0.000	15.9450	-	0.73|±6>; 0.19|±4>/ 0.79|±6>; 0.16|±4>
	2	44.175/ 61.818	0.000	0.000	11.0712	24.1	0.49|±5>; 0.28|±3>; 0.14|±1>/ 0.73|±5>; 0.18|±2>
(b-2)	Tb^{III}-5LIO[c]						
	1	0.000/ 0.344	0.0000	0.0000	17.8574	-	0.99|±6>/ 1.00|±6>
	2	57.496/ 57.558	0.000	0.0000	17.5679	84.7	0.78|±1>; 0.12|±3>/ 0.48|0>; 0.39|±2>
(c-3)	Dy^{III}-2LI (Type B)						
	1	0.000	1.0006	1.6009	16.4739	-	0.74|±15/2>; 0.21|±7/2>
	2	59.543	11.0495	7.5633	2.3655	3.14	0.51|±5/2>; 0.29|±3/2>
(d-2)	Dy^{III}-5LIO[c]						
	1	0.000	0.1101	0.4429	18.3100	-	0.81|±15/2>
	2	36.549	0.0663	0.6558	17.3249	65.5	0.21|±5/2>; 0.20|±3/2>; 0.19|±7/2>; 0.16|±1/2>

[a] Two independent complex molecules are present in the asymmetric unit of the type A crystal structures. In the CIF file the labels of this molecule appear with an "a" in the notation to distinguish it from the other molecule, e.g. O1' appears as O1a'. [c] Calculations were carried out using the coordinates from the previously published Gd^{III}-5LIO crystal structure.[72]

4.8 Conclusion

Through the use of ligands 2LI-1,2-HOPO and 5LIO-1,2-HOPO, the ligand field effects of two very similar coordination geometries have been investigated. The difference in the M_J splitting is evident for both Tb$^{\mathrm{III}}$ and Dy$^{\mathrm{III}}$ from the dc magnetic susceptibility of the four complexes. For the Tb$^{\mathrm{III}}$ complexes, static field loose powder magnetisation indicates a larger ground state M_J value of the Tb$^{\mathrm{III}}$-5LIO than the Tb$^{\mathrm{III}}$-2LI complex. This is supported by pulsed field magnetisation measurements and HF-EPR, the data of which suggest that the ground state of the complexes is not $M_J = \pm 6$ at zero field but $M_J = \pm 4$ for Tb$^{\mathrm{III}}$-2LI and $M_J = \pm 5$ for Tb$^{\mathrm{III}}$-5LIO, and this is in qualitative agreement with the *ab initio* calculated composition of the respective M_J ground states. From the analysis of the EPR data it is concluded that in both complexes the Tb$^{\mathrm{III}}$ ion has a non-axial symmetry environment.

MCD spectra of the two Dy$^{\mathrm{III}}$ complexes has also illustrated differences in ligand field splitting of the M_J multiplets of the ground and excited states. Qualitative analysis of the ligand field strength is in agreement with *ab initio* calculations. The good agreement between ligand field theory and the pseudo spin Hamiltonian approach used in the *ab initio* calculations is a further important validation for the quantum chemical approach. The pseudo spin Hamiltonian used appears to give chemically reasonable parameters, making it a promising approach to determine a large number of parameters in low symmetry lanthanide complexes.

According to the *ab initio* calculations, none of the four complexes are expected to exhibit significant magnetic blocking, as no significant axial ligand field is provided by the ligands. This leads to small excitation energies, mixing of the M_J states, significant transversal moments and non-alignment of the local magnetic axes. The high symmetry and arrangement of the donor atoms in the Ln$^{\mathrm{III}}$-2LI complexes, however, provide a promising foundation for the design of complexes with strong ligand fields in either the axial or equatorial regions. Additionally, the fitting approach used for the MCD data was only possible in the case of the Dy$^{\mathrm{III}}$-2LI due to the high symmetry of this complex in solution requiring only very few ligand field parameters for accurate description. Therefore, this ligand architecture is attractive for further MCD studies and will form the focus of the next Chapter. Nonetheless, it is apparent from this study that small differences in geometry can have a notable effect on the magnetic and electronic properties, despite the ligand field effects in lanthanide complexes being relatively weak.

5. Enhancing the ligand field of mononuclear $\mathrm{Ln^{III}}$ complexes

5.1 Introduction

In contrast to the previous Chapter, in which the different arrangement of homoleptic donor atoms around the lanthanide ions was the source of the different ligand field splitting, this Chapter explores the effect of changing the donor atoms of a single basic geometry. By using the basic architecture of 2LI (Figure 5.1(b)) and changing the identity of the donor atoms at the *ortho* ($\mathrm{R^1}$) and *meta* positions ($\mathrm{R^2}$) of the carboxylic acid (Figure 5.1(a)), it is possible to adjust the ligand field without significantly altering the coordination geometry. Upon coordination to a trivalent lanthanide (Figure 5.1(c)), donor atoms in the *ortho* position will occupy the axial region, and those in the *meta* position will be positioned equatorially, allowing for easy achievement of strongly axial or equatorial ligand fields.

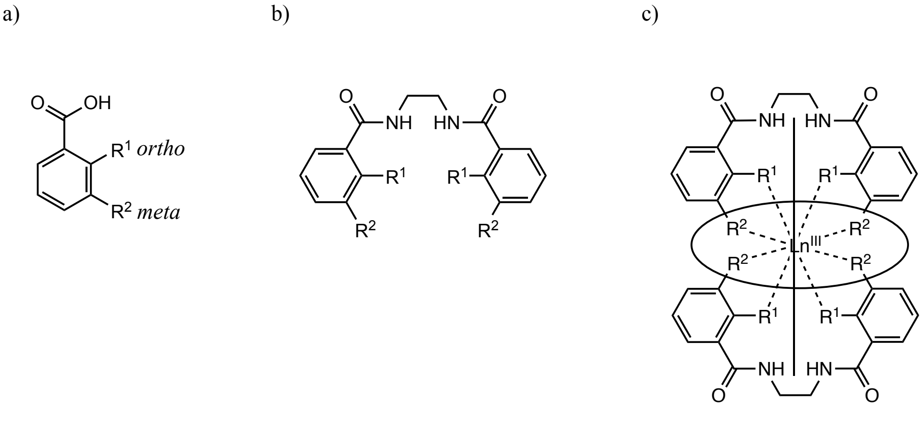

Figure 5.1: Illustration of the ligand design and resulting complex for controlling the strength of the ligand field.

Figure 5.2 presents the ligands discussed in this Chapter. The 2LI ligand was used in the investigation in Chapter 4 and was shown to provide a somewhat spherical ligand field. Based on this ligand, L^3 and L^4 were designed to provide a stronger ligand field in the axial and equatorial regions, respectively. The synthesis of L^3 is described here, while L^4 was synthesised by Thomas Josephy and is described in his Master thesis. Unfortunately, due to issues of solubility, the effects of this ligand could not be examined experimentally but are explored purely computationally (see Section 5.5).

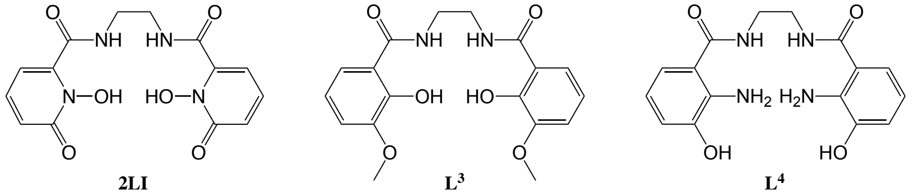

2LI
2LI-1,2-HOPO

L^3
2LI-2,3-HOMOPH

L^4
2LI-2,3-AHOPH

Figure 5.2: Ligands discussed in this Chapter.

By using this ligand design, the oblate-prolate model, as described by Rinehart and Long, can be explored and illustrated, whilst producing complexes of predictable and well defined coordination geometry that should promote SMM behaviour. In this Chapter, MCD spectroscopy, ligand field theory analysis and *ab inito* calculations are used to give greater insight into the ligand field effects of lanthanides.

5.2 Synthesis and structural data

5.2.1 Synthesis of L^3

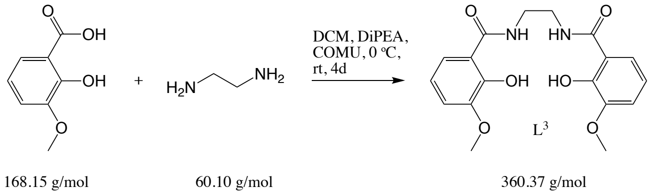

L^3 was synthesised by a simple peptide coupling reaction of 2-hydroxy-3-methoxybenzoic acid with ethylenediamine in DCM. The white powder which precipitated from the reaction mixture was isolated by filtration.

5.2.2 Synthesis of Ln^{III}-L^3 complexes

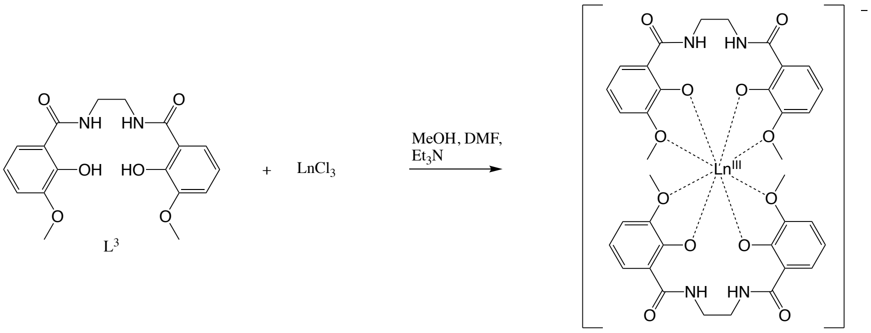

Complexes of L^3 were formed by adding 1 equivalent of the metal salt in methanol to 2 equivalents of the ligand in DMF, the mixture was heated, triethylamine was added as a base and the mixture was refluxed over night. The presence of the 2:1 complex in solution was confirmed by mass spectrometry, however, solids formed by diffusion of diethyl ether into the mixture appeared to consist of a ligand to metal ratio of 1:1 and no crystals suitable for X-ray crystallography were obtained. Therefore, the MCD measurements were carried out using frozen solutions of the complexes prepared *in situ*, and formation of the complexes were evidenced by mass spectrometry and by NMR titrations using the diamagnetic ion lutetium(III).

5.2.3 Mass spectrometry

Spectra of the complexes prepared *in situ* along with the simulated spectra are presented in Figure 5.3. The spectra exhibit the expected isotopic pattern for Dy^{III} and

Er$^{\mathrm{III}}$, respectively, and illustrate exclusive formation of the complexes. However, as this method is not quantitative and signal intensity is related to strength of ionisation, it was necessary to carry out an NMR titration.

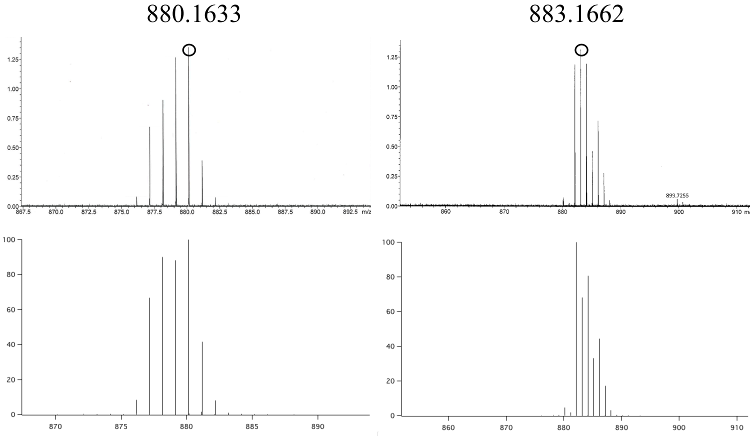

Figure 5.3: Mass spectrometry experimental (above) and calculated (below) of Dy$^{\mathrm{III}}$-L^3 (left) and Er$^{\mathrm{III}}$-L^3 (right).

5.2.4 NMR titration

The samples were prepared using the same method as for the MCD samples but with the use of deuterated solvents. The ligand was dissolved in DMF-d$_6$, the anhydrous lanthanide salt in methanol-d$_4$ was then added and the mixture was heated. Subsequently, an excess of triethylamine was added as a base and the mixture was heated again. Four different samples were prepared of ligand to metal ratios of 1:0, 3:1, 2:1 and 1:1; it was anticipated that the 2:1 species would be the predominant complex present. The change in the NMR spectra is presented in Figure 5.5. The spectra show clear shifts of the aromatic protons, the ethylene bridge and methoxy protons, indicating the formation of a complex. The aromatic protons H^2 and H^3, and the methoxy proton experience upfield shifts from 6.95, 6.59 and 3.79 ppm to 6.79, 6.50 and 3.75 ppm, respectively. As one might expect electron density in this region to decrease upon coordination of the oxygens to a Lewis acid, it is likely that this shielding is due to geometric effects. As illustrated in Figure 5.7, these protons come in close contact to those of the second ligand, thereby, shielding each other. Conversely, aromatic proton H^4 and the ethylene bridge experience and downfield shift (7.47 to 7.59 and 3.60 to 3.72, respectively) likely due to deshielding caused by the lack of free rotation of the ligand. As expected, in the ratio 3:1, two equivalents of the ligand appear to have formed a complex, while the third equivalent is in excess and remains uncoordinated. With a ratio of 2:1, full complexation is observed and no additional signals arise in the spectrum with excess metal (ratio of 1:1). Therefore, it can be concluded that, prepared in this way, the ligand forms exclusively a 2:1 complex with the lanthanide ion.

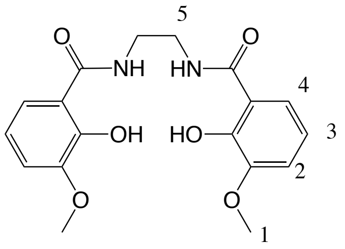

Figure 5.4: H atom numbering for NMR titration interpretation.

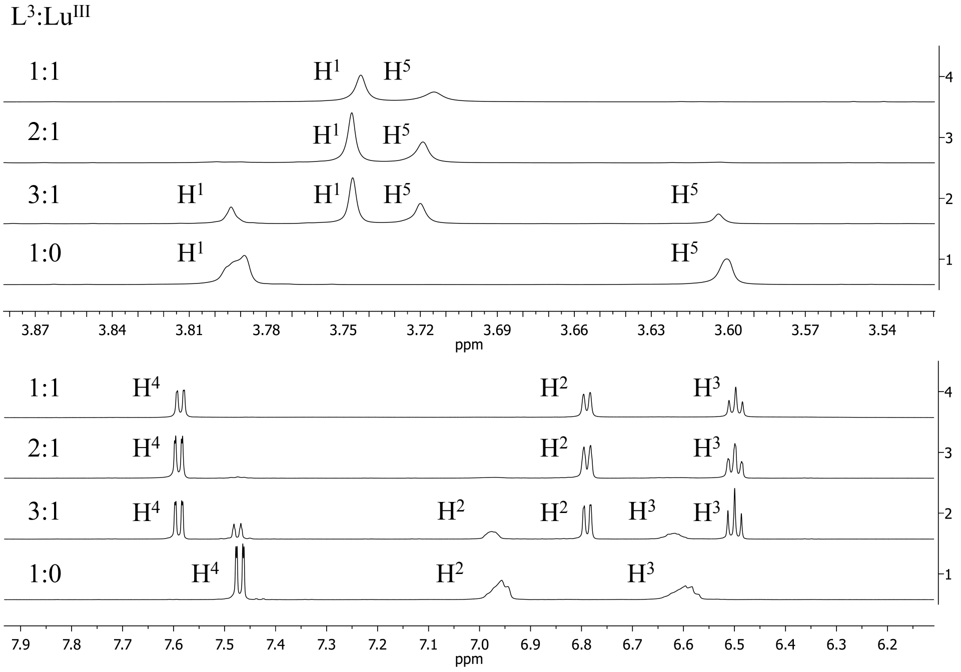

Figure 5.5: NMR spectra of L^3/Lu^{III} mixture illustrating exclusive formation of the mononuclear 2:1 complex in solution. Shifts are assigned based on the numbering represented in Figure 5.4.

5.2.5 DFT optimised structures

For the purpose of the ligand field theory and *ab initio* calculations, geometry optimised structures were obtained using DFT. The optimised structures are presented in Figure 5.7. The B3LYP functional was used in Gaussian 09,[102] with MWB[79,80] (large core) basis sets on the lanthanide ions and 6-31G(d,p) basis sets to describe all other atoms. Frequency calculations were carried out to check for false minima. An example input is given in the Appendices for Chapter 4 and the output xyz coordinates can be found in the Appendices for this Chapter. For the Ln^{III}-2LI and L^3 complexes, symmetries of both S_4 and D_2 were calculated. Due to structural requirements of the L^4 ligand, only a conformation halfway between the two symmetries is possible. The coordination bond lengths of these complexes are presented in Table 5.1. As expected, the bond lengths decrease with the lanthanide contraction.[99] The average bond lengths of the complexes follow the trend 2LI < L^3 < L^4. The coordination sphere of 2LI is neither strongly axial nor equatorial, having bond lengths within 0.043 Å of each other. The complexes of L^3 exhibit significantly shorter axial bond lengths, on average of 0.103 Å shorter, than the 2LI complexes, with equatorial bond lengths 0.165 Å longer than the 2LI complexes. Conversely, the complexes of L^4 exhibit much shorter bond lengths in the equatorial region (Δ = 0.076 Å) than for 2LI, with very elongated bonds of Ln–NRH$_2$ in the axial region (Δ = 0.209 Å). From this information alone, it is expected that L^3 and L^4 will promote high anisotropy in oblate and prolate lanthanide ions, respectively, while 2LI is unlikely to promote high anisotropy in either ion.

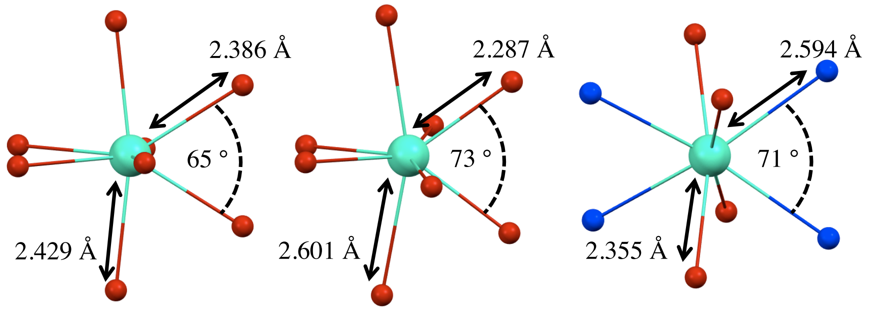

Figure 5.6: First coordination sphere of Dy^{III}-2LI-*a*-S_4 (left), Dy^{III}-L^3-*a*-S_4 (centre), and Dy^{III}-L^4 (right). Bond lengths for D_2 symmetries and the Er^{III} complexes are listed in Table 5.1.

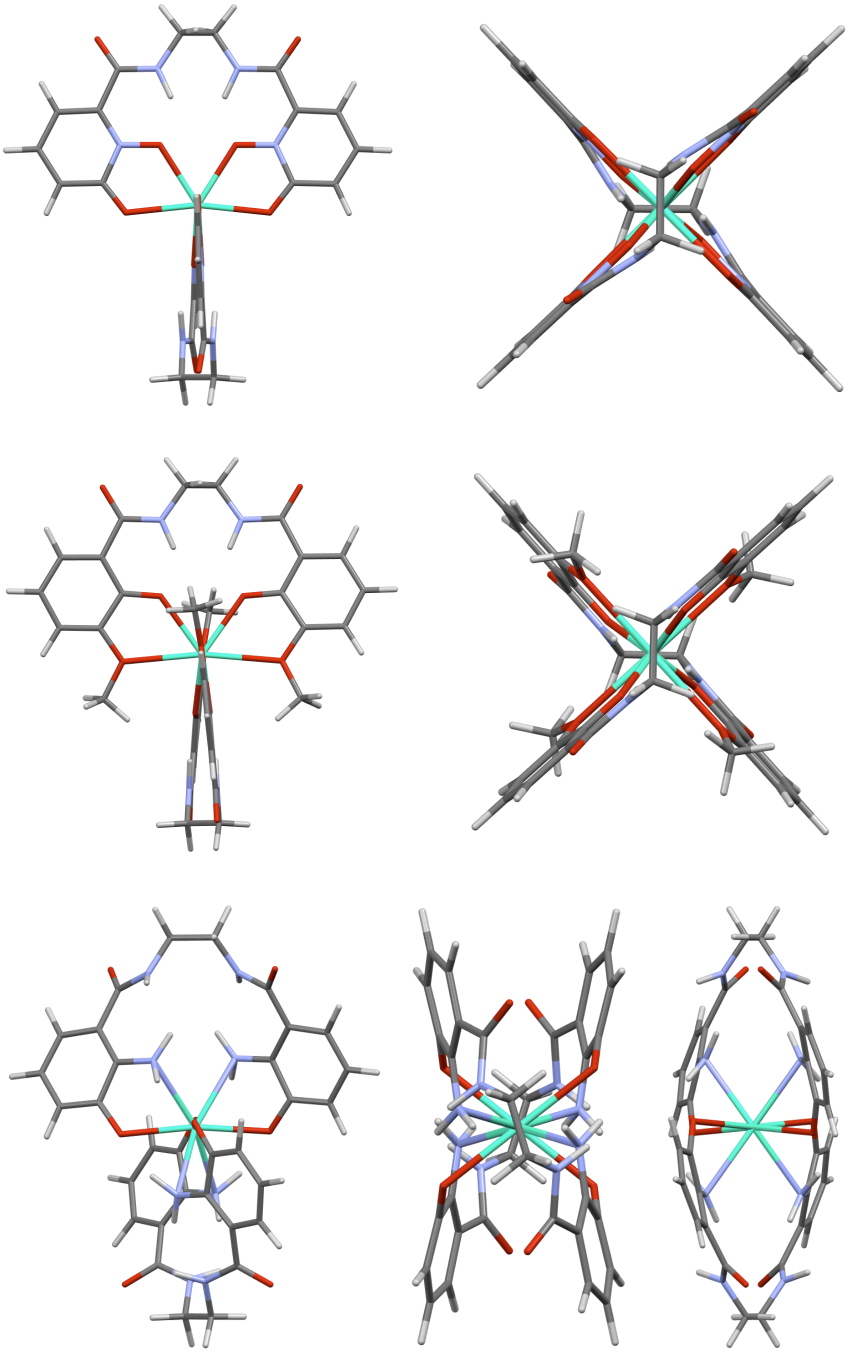

Figure 5.7: DFT optimised structures of Dy^{III}-2LI (top), Dy^{III}-L^{3} (centre) and Ln^{III}-L^{4} (bottom).

Table 5.1: Axial and equatorial coordination bond lengths (Å) of optimised structures utilised in the MCD analysis and *ab initio* calculations (see below), relative energies of the S_4 and D_2 symmetries, and SHAPE analysis of these structures. The SHAPE analysis was restricted to cube (CU), square anti-prism (SAPR), triangular dodecahedron (TDD), J-bisaugmented trigonal prism (JBTPR), bisaugmented trigonal prism (BTPR), J-snub disphenoid (JSD) and triakis tetrahedron (TT).

	2LI-S_4		2LI-D_2		L^3-S_4		L^3-D_2		L^4	
	Dy^{III}	Er^{III}	Dy^{III}	Er^{III}	Dy^{III}	Er^{III}	Dy^{III}	Er^{III}	Dy^{III}	Er^{III}
Axial	2.386	2.383	2.368	2.361	2.287	2.263	2.281	2.256	2.594	2.574
Equatorial	2.429	2.429	2.406	2.409	2.601	2.564	2.593	2.574	2.355	2.330
Average	2.408	2.406	2.387	2.385	2.444	2.413	2.437	2.415	2.475	2.452
Delta	-0.043	-0.046	0.038	0.047	-0.314	-0.302	-0.311	-0.318	0.239	0.244
Energy	0.43	0.83	0.00	0.00	0.95	1.31	0.00	0.00	-	-
CU (O_h)	10.890	10.962	7.730	7.442	12.510	12.677	9.462	9.550	4.661	4.679
SAPR (D_{4d})	5.923	5.791	3.973	3.402	5.030	4.616	2.556	2.355	6.354	6.014
TDD (D_{2d})	3.576	3.426	3.728	3.627	2.503	2.051	2.952	2.842	5.410	5.177
JBTPR[a] (C_{2v})	5.442	5.311	4.464	4.161	5.915	5.534	4.781	4.707	6.287	5.999
BTPR (C_{2v})	4.804	4.667	3.828	3.501	4.506	4.133	3.363	3.256	6.502	6.219
JSD[a] (D_{2d})	4.495	4.353	4.757	4.751	6.061	5.680	6.551	6.591	6.520	6.275
TT (T_d)	11.714	11.787	8.592	8.308	13.325	13.492	10.315	10.403	5.563	5.581

[a] J indicates a Johnson polyhedron, i.e. having regular faces and all edges the same length, the BTPR on the other hand is spherical with nonequivalent edges.

5.2.6 SHAPE analysis

The continuous shape measures (CShM) from the SHAPE analyses of the different complexes are presented in Table 5.1.[73] The values indicate that, like the 2LI complexes, the coordination sphere of the L^3 complexes is closest to a triangular dodecahedron (TDD) or square anti-prism (SAP) geometries with D_{2d} and D_{4d} symmetry. The complexes of L^4 exhibit a more cube like (CU, O_h symmetry) coordination geometry. As mentioned in the previous Chapter, the CShM is an adimensional value ranging from 0 to 100, 0 indicating the perfect polyhedron.[74–77] Therefore, consideration of the values alone can be misleading. An overlay of the first coordination sphere with these geometries provides a better comparison to the perfect geometries. In the interest of simplicity, only the TDD and CU geometries are presented in Figure 5.8.

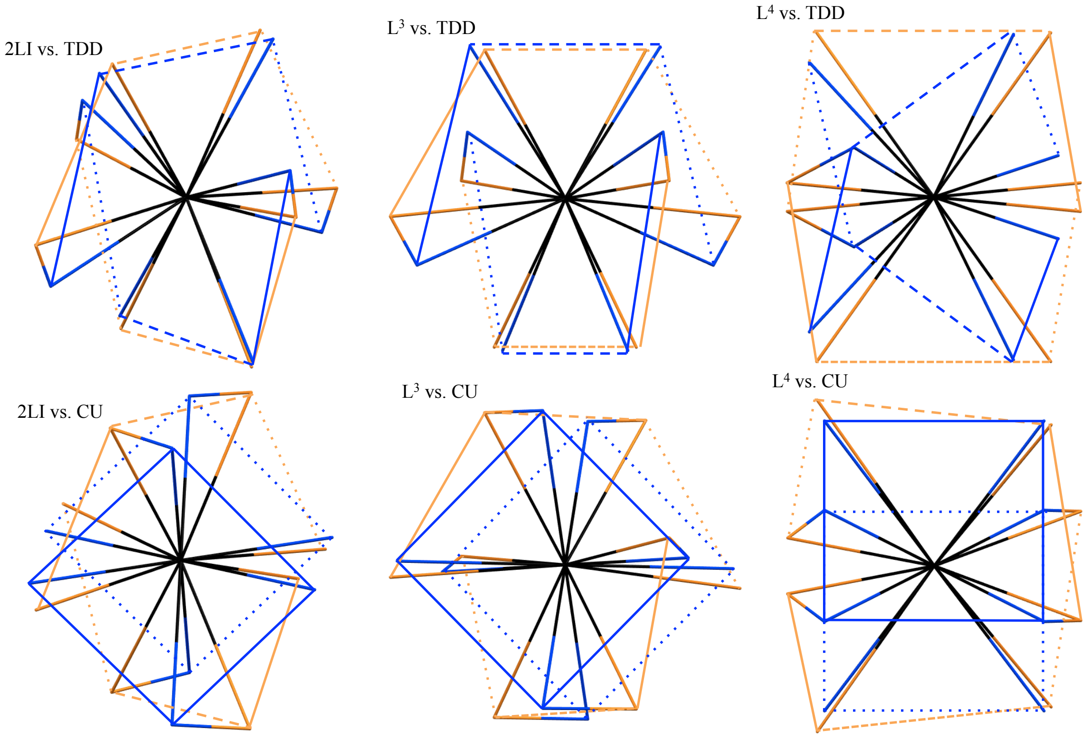

Figure 5.8: Comparison of the first coordination sphere of the three different complexes with perfect triangular dodecahedron (TDD) and cube (CU) geometries. The optimised structures are represented in orange, and the perfect structures in blue. The orange connecting lines represent the edges occupied by a single ligand. The connecting blue lines have been added to better illustrate the perfect geometries.

5.3 Magnetic circular dichroism

The MCD spectra of Dy^{III}-L^3, Er^{III}-L^3 and Er^{III}-2LI were measured at temperatures 10, 75 and 115 K, at a field of 5 T. Overviews of the spectra are presented in Figures 5.10-5.12 with the appropriate multiplets assigned to the different bands. An overview of the Dy^{III}-2LI spectrum from the previous Chapter is reproduced here for comparison in Figure 5.9. The measurements were carried out in frozen solutions of the complexes (7 mM) in a 2:1 ratio of DMF and methanol. The Er^{III}-2LI sample was prepared using the previously obtained solid. Complexes of L^3 were prepared *in situ* in the same manner as for the NMR titration, however, in order to ensure no presence of the free metal ions, a slight excess of the ligand (2.2:1) was used. A high quality glass was achieved by fast cooling of the samples.

Of the 1001 Dy^{III} Kramers' doublets, 46 are expected to occur within the range of 7 000 - 22 500 cm^{-1} (see Chapter 4 for details). In contrast to Dy^{III}-2LI, the transitions for Dy^{III}-L^3 to $^4F_{9/2}$ and $^4I_{15/2}$ were too weak to be detected, therefore, the Dy^{III} spectra in this Chapter include only 33 Kramers' doublets in the energy range 7 000 - 14 000 cm^{-1}. Er^{III} has 182 Kramers' doublets, 44 of which are expected in the range of 9 500 - 24 000 cm^{-1}. These correspond to $^4I_{11/2}$, $^4I_{9/2}$, $^4F_{9/2}$, $^4S_{3/2}$, $^2H_{11/2}$, $^4F_{7/2}$, $^4F_{5/2}$, $^4F_{3/2}$, $^2H_{9/2}$ and $^4G_{11/2}$.

As observed in the previous Chapter, the energies of these f-f transitions are predominantly determined by the free ion terms, however, small features, such as hot bands, differences in relative intensities and slight shifts in energy reveal differences in the ligand field effects. The individual transitions were carefully extracted using the fitting function in OriginPro 2017 and the experimental energies are plotted in Figures 5.15 and 5.16, these energies are also presented in a tabulated form in the Appendix.

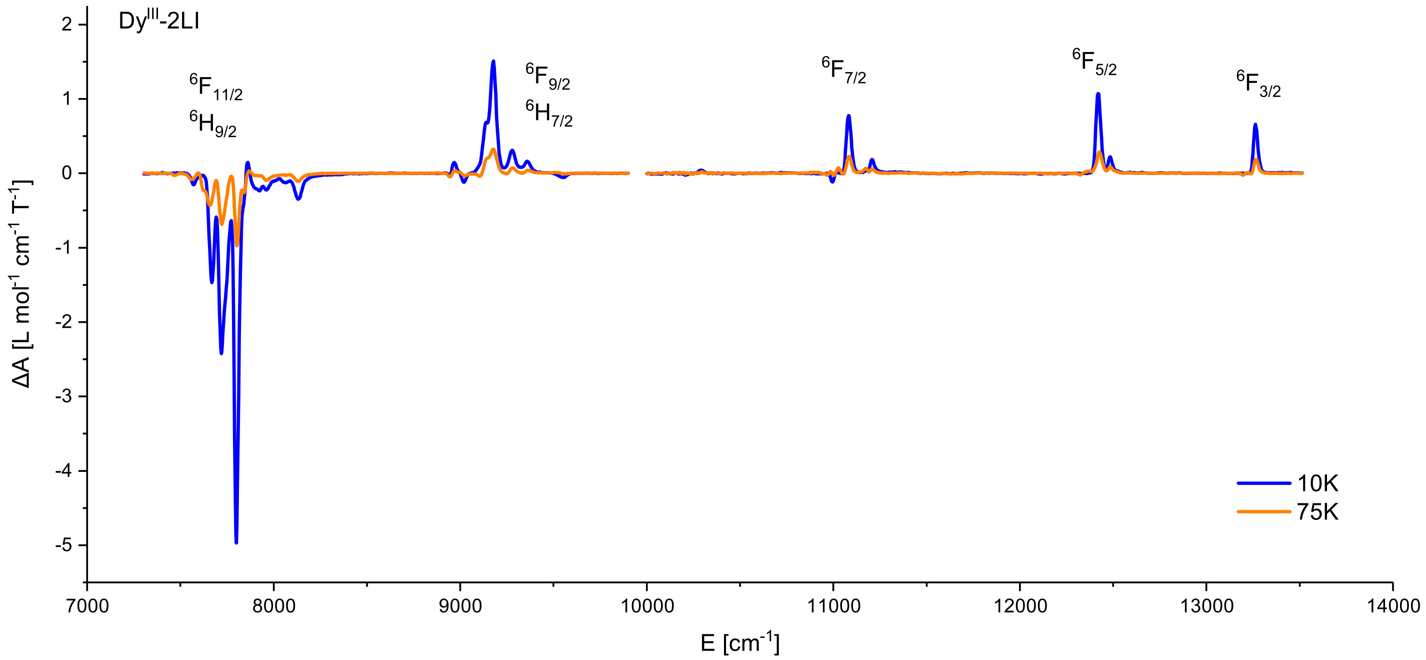

Figure 5.9: Temperature dependent MCD spectra of Dy^{III}-2LI.

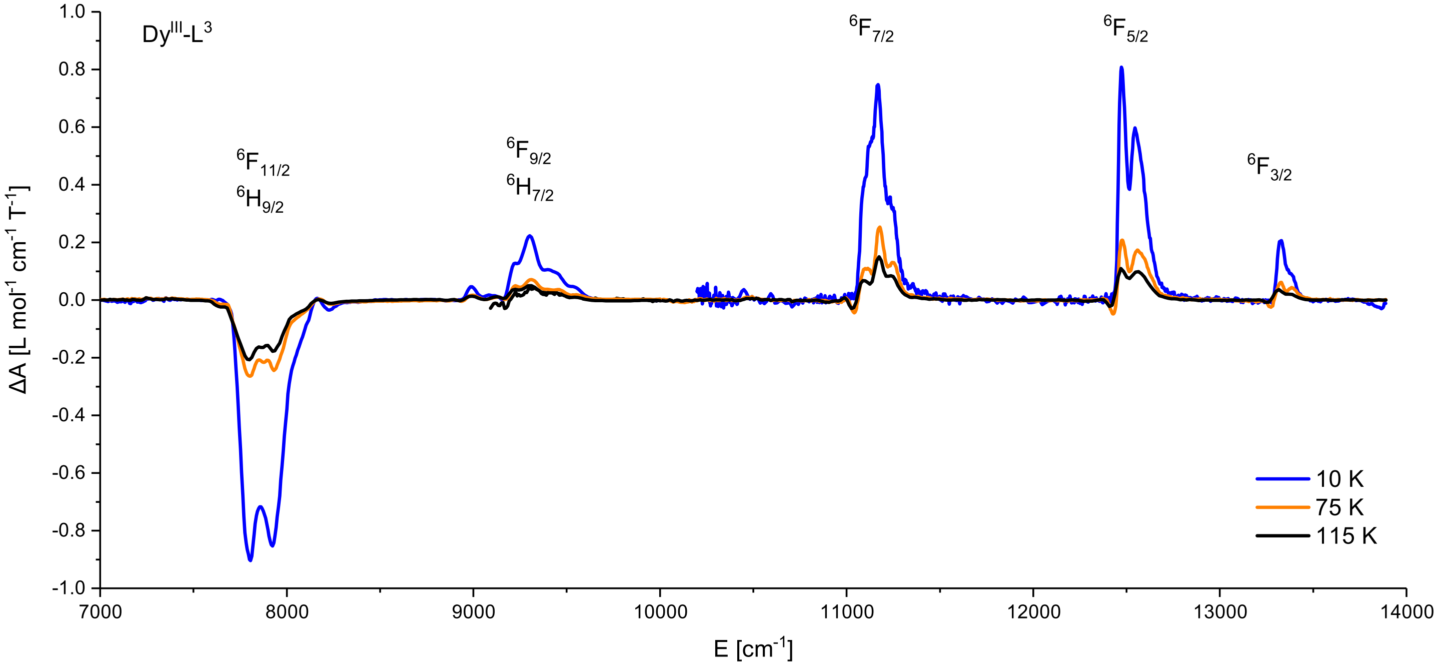

Figure 5.10: Temperature dependent MCD spectra of Dy^{III}-L^3.

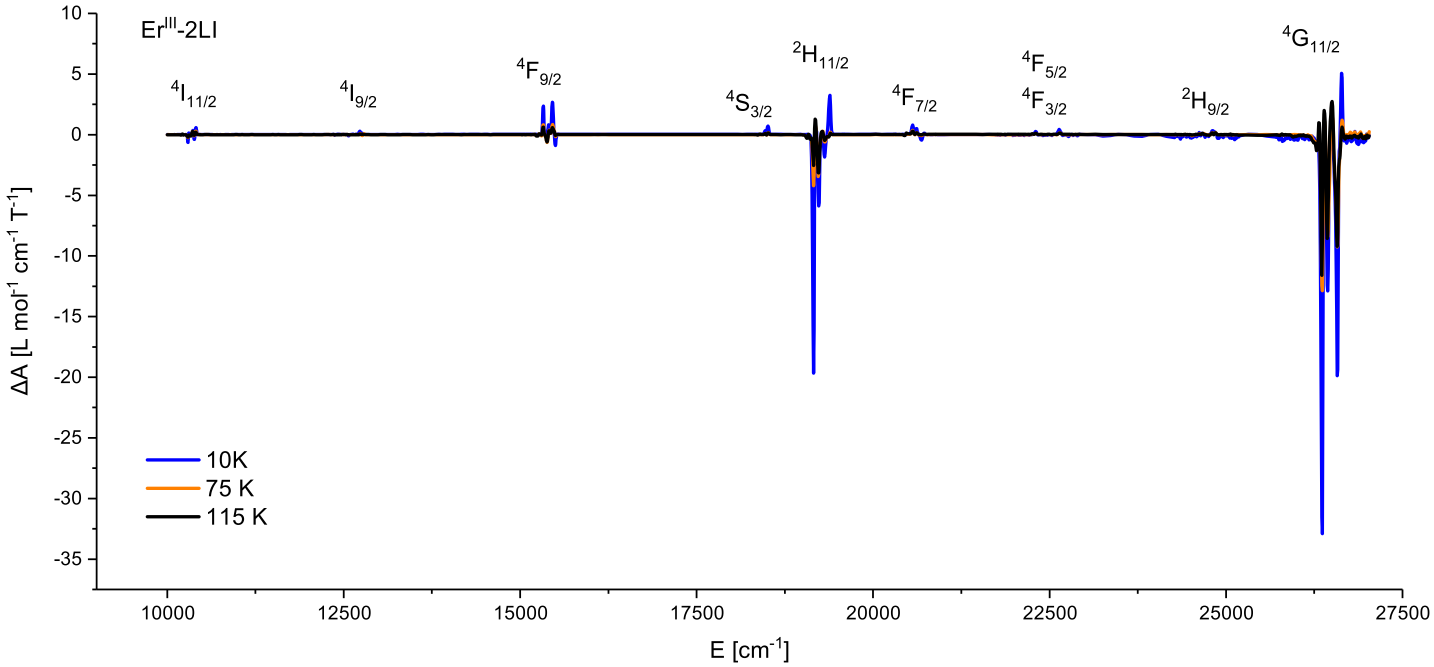

Figure 5.11: Temperature dependent MCD spectra of Er^{III}-2LI.

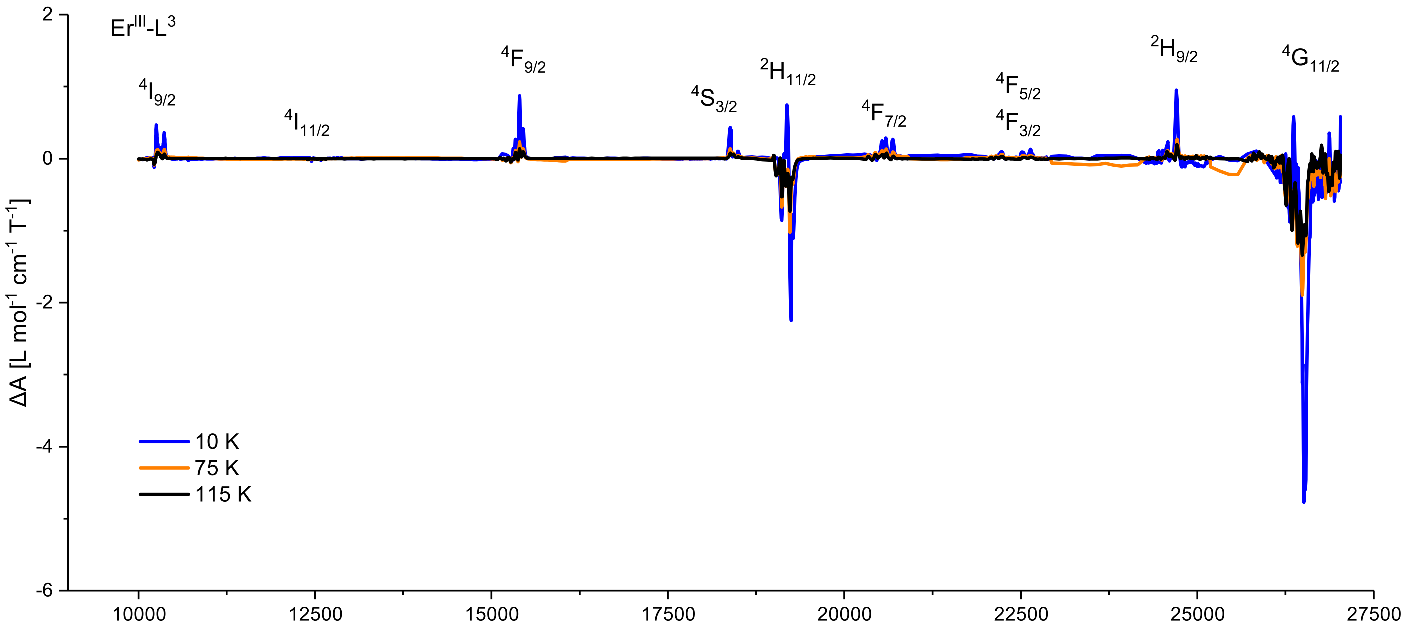

Figure 5.12: Temperature dependent MCD spectra of Er$^{\mathrm{III}}$-L^{3}.

5.3.1 Qualitative interpretation

A comparison of the 10 K spectra of the two sets of complexes are presented in Figures 5.13 and 5.14. In general, the transitions of the 2LI complexes are more intense than those of the L^3 complexes, therefore the spectra have been scaled for ease of comparison. The transitions of all complexes exhibit clear $\mathscr{C}$-term behaviour due to the presence of a degenerate ground state. The signal intensities decrease with increasing temperature as the population of the upper level (having the opposite sign) of the split Kramers doublet increases and transitions from this level occur.

Considering first the average energies of the transitions, for Dy^{III} the transitions with ligand L^3 have are shifted to higher energy relative to the 2LI complex. Such a strong trend is not observed in the Er^{III} case, however, on average the opposite trend is subtly present. A shift in the total energy of the levels is attributed to E_{AVE}, a free ion term which contains the spherically symmetric ligand field term B_0^0.[44] Assuming the excited state M_J multiplets also follow the oblate-prolate trend, one might expect greater splitting of the Dy^{III} multiplets when coordinated to L^3 compared to 2LI, and the opposite trend for Er. Distribution of the fitted transitions, however, does not unequivocally support this conclusion. Larger splitting of the Dy^{III}-L^3 levels is observed only for the transitions in Figures 5.13(b), (c) and (e). Conversely, larger splitting of the Er^{III}-2LI levels is evident in Figures 5.14(a), (b) and (i). However, more pronounced splitting of the Er^{III}-L^3 levels is also observed for the levels in Figures 5.14(d) and (g). Interestingly, an apparent inversion of the levels is observed in Figures 5.14(d) and (e), which may indicate opposite stabilisation of the M_J levels by the different ligand fields. As these individual transitions have not been unambiguously assigned, this conclusion is made only tentatively, as differences in mixing and transition intensities may also play a role.

For both Dy^{III} and Er^{III}, transitions of the L^3 based complexes are significantly broader than for the 2LI complexes. This broadening is likely due to an increased bandwidth of the excited states in the former case. In the case of luminescence spectroscopy, this could be related to differences in the strengths of electron-phonon coupling.[103,104] However, in the current method, broadening of the line widths is more likely due to different ligand fields experienced by the ions.[105] This would indicate that in solution, the metal ions do not all experience the same ligand field. While the NMR titrations reveal the presence of only one species, it may be possible that some shift of the ligand not detected in the NMR experiments alters the splitting of the multiplets enough to be observed in the MCD spectra.

The intensities of the transitions also differ between the complexes of 2LI and L^3

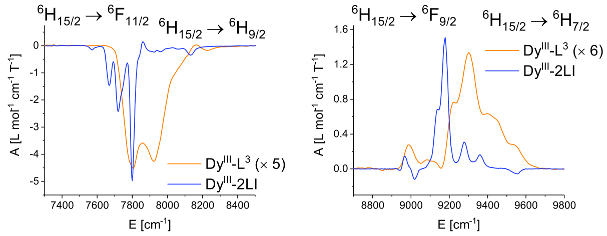

(a) $^6H_{9/2} + {}^6F_{11/2}$ (b) $^6H_{7/2} + {}^6F_{9/2}$

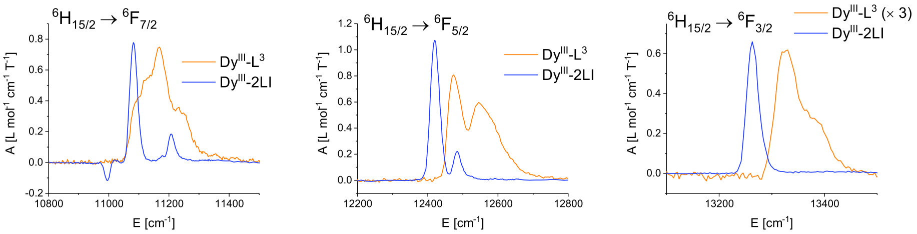

(c) $^6F_{7/2}$ (d) $^6F_{5/2}$ (e) $^6F_{3/2}$

Figure 5.13: Comparison of the splitting of the MCD transitions of Dy^{III}-2LI (blue) and Dy^{III}-L^3 (orange) at 10 K. The spectra have been scaled for ease of comparison. Scale factors are indicated in the legend of each figure.

for both ions. The differences in intensity between the two ligands for all transitions of the two ions are given in Table 5.2. The intensities of most electron dipole transitions commonly vary by a factor of 2-3.[92] Those that experience a greater difference between different coordination environments are known as *hypersensitive transitions*.[92,106] The intensities of such transitions can increase by a factor of 200, from free ions in an aqueous solution to coordinated complexes.[107,108] All known hypersensitive transitions follow the selection rules $|\Delta S| = 0$, $|\Delta L| \leq 2$, $|\Delta J| \leq 2$.[106][*] Known hypersensitive transitions for Dy^{III} and Er^{III} are[109]

$$\begin{array}{lll} Dy^{III} & ^6H_{15/2} \rightarrow & ^6F_{11/2} \\ Er^{III} & ^4I_{15/2} \rightarrow & ^2H_{11/2} \\ & ^4I_{15/2} \rightarrow & ^4G_{11/2} \end{array}$$

---

[*] These selection rules apply also to quadrupole transitions. However, such transitions are extremely weak in comparison and no quadrupole transitions have been observed for Ln^{III} ions. Therefore, the *hypersensitive* transitions are also known as *pseudo-quadrupole transitions*.

Table 5.2: Factors by which the intensities of the Ln^{III}-L^3 spectra differ from Ln^{III}-2LI (2LI/L^3) for each transition measured at 10 K.

Dy^{III}		Er^{III}	
$^6H_{15/2} \rightarrow$	Scale Factor	$^4I_{15/2} \rightarrow$	Scale Factor
$^6F_{11/2}$ + $^6H_{9/2}$	1.6	$^4I_{11/2}$	1.4
$^6F_{9/2}$ + $^6H_{7/2}$	2.4	$^4I_{9/2}$	6.9
$^6F_{7/2}$	0.3	$^4F_{9/2}$	3.0
$^6F_{5/2}$	0.4	$^4S_{3/2}$	1.1
$^6F_{3/2}$	1.2	$^2H_{11/2}$	5.2
		$^4F_{7/2}$	3.3
		$^4F_{5/2}$ + $^4F_{3/2}$	1.6
		$^2H_{9/2}$	0.7
		$^4G_{11/2}$	4.9

The Dy^{III} hypersensitive transition to $^6F_{11/2}$ does not differ significantly in intensity from L^3 to 2LI. Er^{III} exhibits hypersensitivity for the transitions to $^2H_{11/2}$ and $^4G_{11/2}$, with additional hypersensitivity apparent for the transition to $^4I_{9/2}$.

Factors that have been found to affect the intensity of hypersensitive transitions include ligand character, bond length and symmetry,† with the pK_a found to have a much larger affect than the site symmetry, especially for dibasic ligands compared to monobasic ligands.[110,111] Three factors were then proposed that strongly affect the transition intensity:[112]

- Absorption intensity increases with increasing basicity of the coordinating ligands
- Intensity increases with decreasing metal-ligand bond lengths
- Increasing the number of coordinated ligands (more basic) increase intensity

According to the DFT calculated structures, the coordination bond lengths of the Ln^{III}-2LI complexes are marginally longer in the axial region (hydroxypyridine *vs.* phenol) but significantly shorter in the equatorial region (ketone *vs.* methoxy), leading to an average bond length 0.03 Å shorter than for the Ln^{III}-L^3 complexes. While this difference is not large, it may explain the increase in intensity of the hypersensitive transitions. Remembering that a hypersensitive transition may vary in intensity by a factor of up to

---

† In general, the intensity of both hypersensitive and regular electric dipole transitions decrease with increasing symmetry.[92]

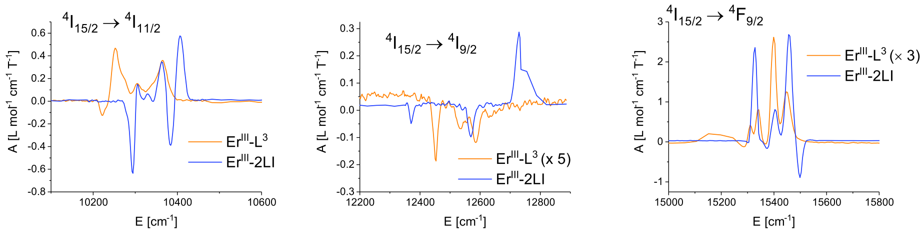

(a) $^4I_{11/2}$ (b) $^4I_{9/2}$ (c) $^4F_{9/2}$

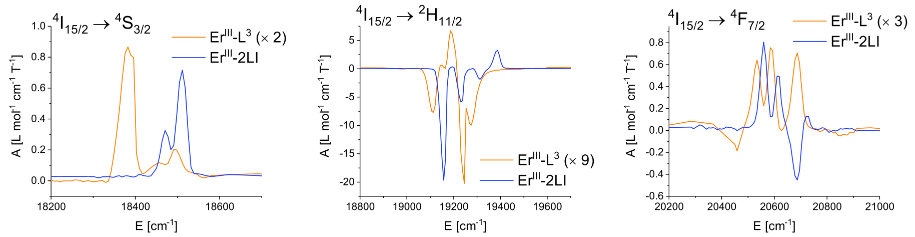

(d) $^4S_{3/2}$ (e) $^2H_{11/2}$ (f) $^4F_{7/2}$

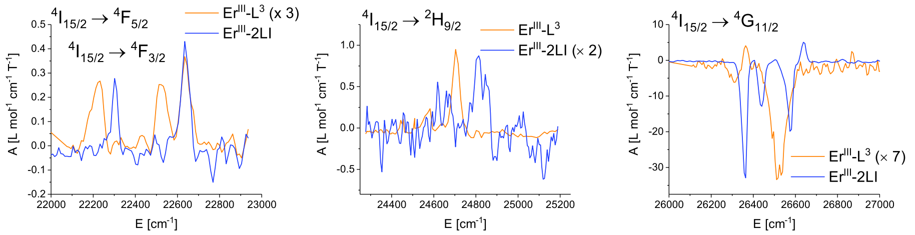

(g) $^4F_{5/2}$ + $^4F_{3/2}$ (h) $^2H_{9/2}$ (i) $^4G_{11/2}$

Figure 5.14: Comparison of the MCD transitions from the $^4I_{15/2}$ ground state of Er^{III}-2LI (blue) and Er^{III}-L^3 (orange) at 10 K. The spectra have been scaled for ease of comparison. Scale factors are indicated in the legend of each figure.

200,[107,108] it is not unreasonable to expect that such a small difference in bond lengths could produce an in increase in intensity of a factor 5-7. It should also be reiterated that broadening of the L^3 transitions might indicate that the DFT calculated structures for these complexes may not be the only present in solution. It is unusual, however, that hypersensitivity is observed for Er^{III} but not for Dy^{III}, since they should experience similar differences in the ligand field.

The additional hypersensitive transition to $^4I_{9/2}$ for Er^{III} does not follow the selection rules above, however it is possible that it experiences what is known as *ligand-mediated pseudo-hypersensitivity*, also referred to as *pseudo-hypersensitivity*.[113,114] Misra *et al.* have argued that in the presence of certain ligands, transitions that would normally not show hypersensitivity can be hypersensitive.[113,114] Factors that may affect the sensitivity of a non-hypersensitive transition to varying degrees include the coordination number, coordinating power, hapticity, bite angle, and the chelate ring size.

Pseudo-hypersensitive transitions have been observed for Pr$^{\text{III}}$, Nd$^{\text{III}}$ and Eu$^{\text{III}}$,[113–115] however, a literature search revealed no reports of such transitions for Er$^{\text{III}}$. Therefore, this transitions is only tentatively designated as pseudo-hypersensitive.

5.4 Ligand field theory calculations

For the fitting of the MCD data described in Chapter 4, the Wybourne B_q^k parameters of the complexes were converted from the B_q^k parameters from the *ab initio* calculations and a fit was achieved by varying the AOM parameters e_σ, $e_{\pi x}$ and $e_{\pi y}$. In the current Chapter a different approach is explored. The free ion terms are set according to Ref[44], and the *ab initio* calculated ligand field parameters (Table 5.3) are used directly to calculate the energies of the ground J = 15/2 multiplets. The calculations were carried out in both the ground J multiplet and the full basis (2002 for Dy$^{\text{III}}$, 364 for Er$^{\text{III}}$) and the results are compared with the *ab initio* results in Table 5.4. Limiting the LF calculation to just the ground multiplet results in energies almost identical to the *ab initio* energies. Due to mixing of the higher states, the energies calculated in the full basis decrease by about 30 cm^{-1}. After establishing the consistency of the two methods, the energies of the higher energy J multiplets were calculated and the upper state multiplets of each transition are presented as stick spectra in Figures 5.15 and 5.16 along with the 10 K experimental energies. The results are presented so that a comparison between the two different ligand fields of 2LI and L^3 can be compared. The overall energies and splitting of the resulting calculated multiplets show very good agreement with the experimental energies of the dysprosium(III) complexes, with only slight shifts in energy for some multiplets. While, the energies for the erbium(III) complexes experience slightly larger shifts, the splitting patterns are well reproduced by the LF theory calculations for the two different ligand fields.

Table 5.3: Wybourne B_q^k parameters converted from the B_q^k parameters to the ESO calculated *ab initio*.

k	q	Dy-L^3-*a*-S$_4$	Er-2LI-*a*-S$_4$	Er-L^3-*a*-S$_4$
2	0	1274.889	85.635	1388.923
4	-4	-350.779	492.887	377.250
4	0	-557.400	125.279	-518.961
4	4	-257.819	-435.863	-163.079
6	-4	-65.657	-114.930	125.508
6	0	-601.224	-778.868	-498.751
6	4	-179.588	179.827	-32.299

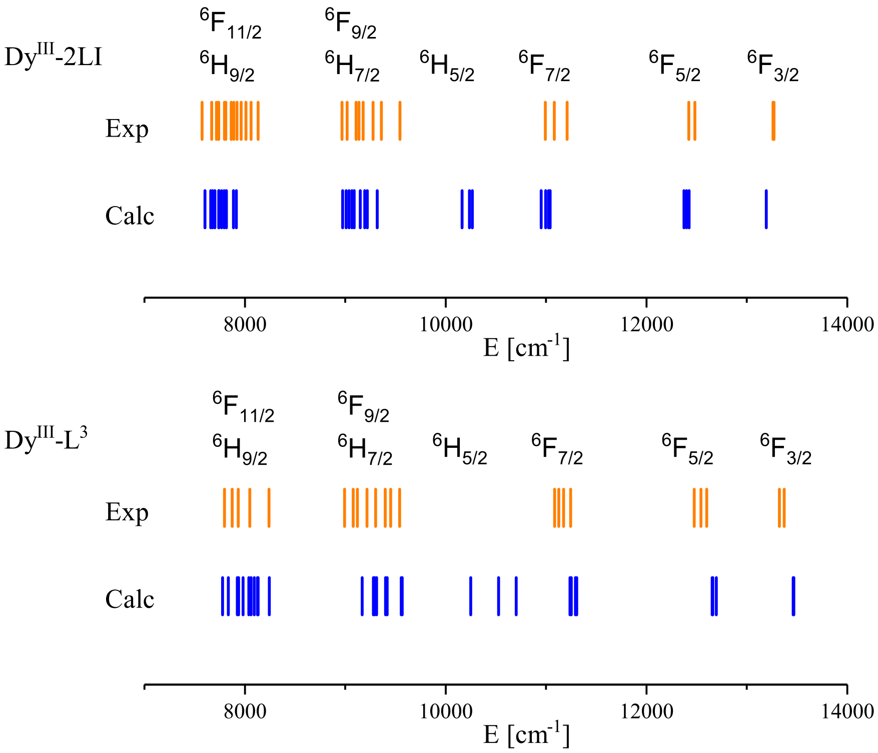

Figure 5.15: Experimental and LF calculated energies of the split J multiplets of Dy^{III}-2LI (see Chapter 4), and Dy^{III}-L^3. The calculated values of Dy^{III}-L^3 are based on the *ab initio* calculated ligand field parameters of the optimised structure Dy^{III}-L^3-*a*-S$_4$

Table 5.4: Comparison of the ground state J multiplet splitting (cm^{-1}) as calculated *ab initio*, with ligand field theory in the $^6H_{15/2}$ (Dy^{III}) or $^4I_{15/2}$ (Er^{III}) multiplet basis (LF$_{GJ}$), and in the full 2002 basis (LF$_{full}$). Presented are Dy-L^3-*a*-S$_4$, Er-2LI-*a*-S$_4$ and Er-L^3-*a*-S$_4$.

	KD	*Ab initio*	LF$_{GJ}$	LF$_{full}$	$\Delta E_{full-GJ}$
Dy^{III}-L^3-*a*-S$_4$					
	1	0.00	0.00	0.00	0.00
	2	175.67	177.78	164.18	-13.61
	3	248.79	248.33	230.83	-17.50
	4	320.67	319.00	300.55	-18.44
	5	419.94	420.69	397.97	-22.72
	6	522.63	526.83	497.90	-28.93
	7	699.45	699.94	668.49	-31.45
	8	750.03	748.66	716.07	-32.59
Er^{III}-2LI-*a*-S$_4$					
	1	0.00	0.00	0.00	0.00
	2	34.15	36.00	32.50	-3.50
	3	60.36	61.40	59.06	-2.34
	4	96.59	97.50	97.32	-0.19
	5	203.92	204.30	198.60	-5.71
	6	247.77	248.70	246.09	-2.61
	7	293.01	293.50	289.22	-4.28
	8	326.06	327.30	318.24	-9.06
Er^{III}-L^3-*a*-S$_4$					
	1	0.00	0.00	0.00	0.00
	2	12.21	11.40	14.61	3.21
	3	40.79	40.00	37.83	-2.17
	4	59.47	58.40	58.33	-0.07
	5	132.20	132.10	136.78	4.68
	6	224.14	223.40	242.97	19.57
	7	267.37	266.70	275.68	8.98
	8	375.34	374.90	385.73	10.83

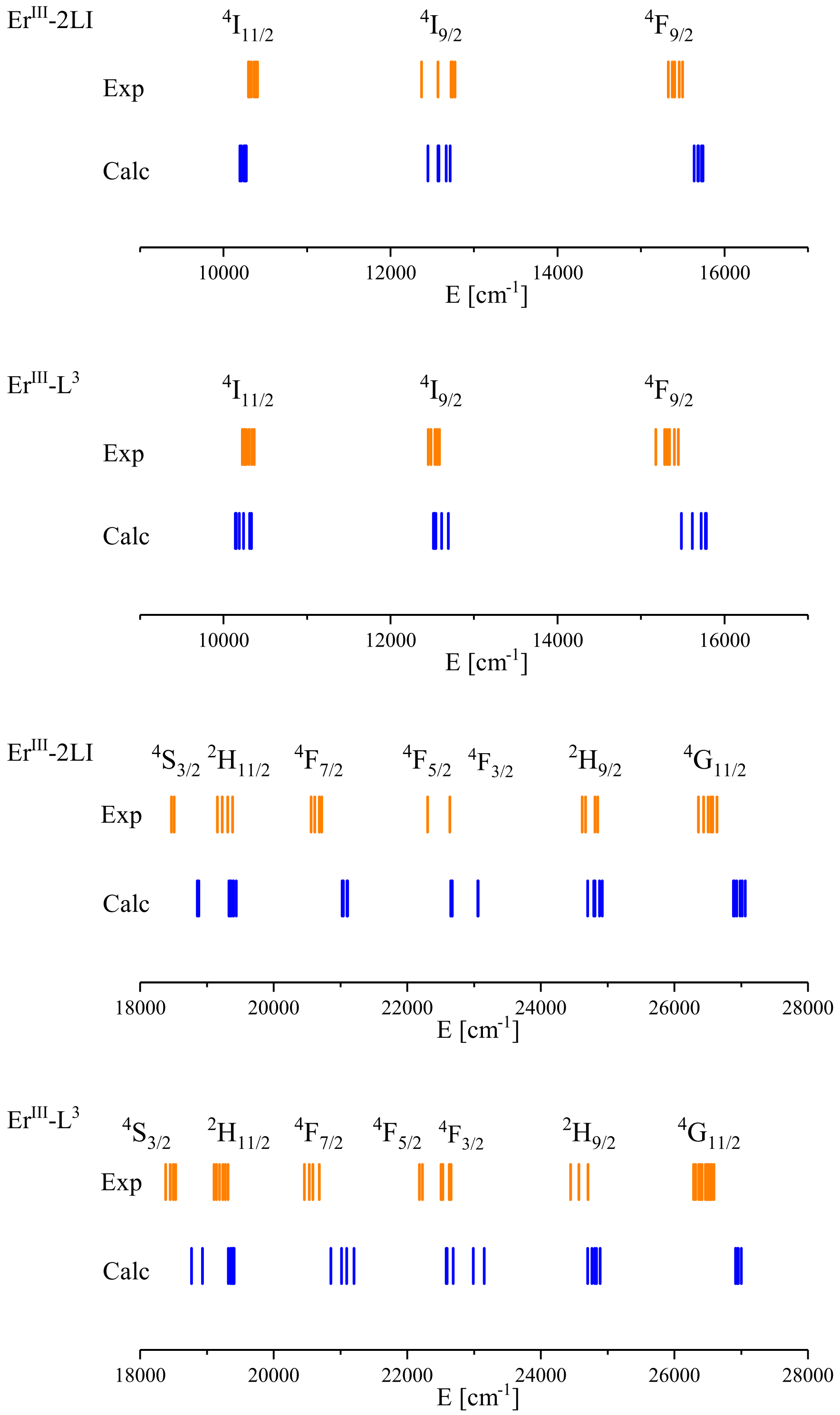

Figure 5.16: Experimental and LF calculated energies of the split J multiplets between energies 9 000 cm^{-1} and 28 000 cm^{-1} of Er^{III}-2LI and Er^{III}-L^3. The calculated values are based on the *ab initio* calculated ligand field parameters of the optimised structure of S$_4$ symmetry

5.5 *Ab initio* calculations

Details of the method can be found in Sections 3.4.4 and 4.7. ANO-RCC basis sets were used to describe all atoms; triple zeta with polarisation on the atom types of the first coordination sphere ($\mathrm{Ln}^{\mathrm{III}}$, O and for L^4 N), and double zeta on all other atoms. Active spaces of nine and 11 electrons (for $\mathrm{Dy}^{\mathrm{III}}$ and $\mathrm{Er}^{\mathrm{III}}$, respectively) in seven $4f$ orbitals were selected for the complete active space self-consistent field method (CASSCF).[97] For the $\mathrm{Dy}^{\mathrm{III}}$ complexes, all 21 sextet states were considered for both the CASSCF and state interaction calculations. All 35 quartet states and 100 doublet states were included in the CASSCF calculation of the $\mathrm{Er}^{\mathrm{III}}$ complexes, and all quartet and 50 of the doublet states were included in the RASSI calculation. The resulting calculated properties can be found in Tables 5.5 and 5.6

5.5.1 Fitting of MCD

The splitting of the M_J ground doublets are presented in Table 5.4 along with the ligand field determined energies. The LF energies were calculated based on the converted *ab initio* ligand field parameters as coefficients to the ESO of the optimised structures (Table 5.3). The LF calculations were carried out in both the ground J multiplet and full basis. Because the *ab initio* method does not include configurations of all spin states, the doublet energies are over estimated compared to full basis LF calculations. Use of these ligand field parameters to calculated the MCD transitions gives reasonable results, both in terms of energy shifts and M_J splitting. The results indicate that both the *ab initio* calculated M_J splitting and ligand field parameters are reasonable, providing an important validation of the *ab initio* method.

Table 5.5: *Ab initio* calculated excitation energies, g-tensors, magnetic axis orientations, and total coefficients of the M_J projections of the RASSI coupled wave function of the Kramers doublets (KD) of the first few relevant doublets of the optimised Dy$^{\mathrm{III}}$ structures. The results for the 2LI structures are reproduced from Chapter 4.

	KD	E [cm^{-1}]	g_x	g_y	g_z	∠KD1-Dy-KDX [°]	Total coefficients of the M_J projections of function to RASSI coupled wave
Dy$^{\mathrm{III}}$-2LI-a-D$_2$	1	0.00	0.789	2.642	16.488	-	0.75|±15/2>; 0.18|±7/2>
	2	48.55	10.670	6.571	0.212	0	0.26|±5/2>; 0.22|±3/2>; 0.14|±9/2>; 0.13|±7/2>; 0.11|±11/2>; 0.10|±1/2>
Dy$^{\mathrm{III}}$-2LI-a-S$_4$	1	0.00	1.106	1.126	16.902	-	0.77|±15/2>; 0.19|±7/2>
	2	56.30	9.705	8.999	2.394	0	0.52|±5/2>; 0.29|±3/2>; 0.10|±11/2>
Dy$^{\mathrm{III}}$-L^3-a-D$_2$	1	0.00	0.003	0.003	19.885	-	0.98|±15/2>
	2	159.79	0.067	0.076	17.013	0	0.96|±13/2>
	3	238.00	0.248	0.396	14.573	0	0.96|±11/2>
	4	311.57	0.364	0.995	11.938	0	0.94|±9/2>
	5	402.18	2.154	3.328	8.611	0	0.93|±7/2>
Dy$^{\mathrm{III}}$-L^3-a-S$_4$	1	0.00	0.000	0.000	19.985	-	1.00|±15/2>
	2	175.67	0.023	0.023	17.221	0	1.00|±13/2>
	3	248.79	0.012	0.027	14.563	0	1.00|±11/2>
	4	320.67	1.001	1.017	11.745	0	0.99|±9/2>
	5	419.94	0.871	0.936	8.789	0	0.97|±7/2>
Dy$^{\mathrm{III}}$-L^4	1	0.00	0.175	0.549	16.029	-	0.78|±13/2>; 0.22|±9/2>
	2	33.20	0.084	0.276	17.027	0	0.51|±15/2>; 0.43|±11/2>

Table 5.6: *Ab initio* calculated excitation energies, g-tensors, magnetic axis orientations, and total coefficients of the M_J projections of the RASSI coupled wave function of the Kramers doublets (KD) of the first few relevant doublets of the optimised Er^{III} structures.

	KD	E [cm^{-1}]	g_x	g_y	g_z	∠D1-Dy-DX [°]	Total coefficients of the M_J projections of function to RASSI coupled wave
Er^{III}-2LI-*a*-D$_2$	1	0.00	2.455	5.176	10.733	-	0.43|±15/2>; 0.26|±11/2>; 0.12|±7/2>; 0.11|±5/2>
	2	38.64	0.995	1.608	10.983	90	0.33|±5/2>; 0.17|±13/2>; 0.16|±3/2>; 0.15|±15/2>
	3	62.23	0.347	1.008	9.437	90	0.33|±3/2>; 0.20|±9/2>; 0.17|±7/2>; 0.10|±1/2>
Er^{III}-2LI-*a*-S$_4$	1	0.00	3.302	3.611	7.590	-	0.83|±7/2>
	2	34.15	8.258	7.949	3.488	0	0.74|±5/2>; 0.26|±3/2>
	3	60.36	2.805	2.828	9.248	0	0.92|±9/2>
Er^{III}-L^3-*a*-D$_2$	1	0.00	0.450	0.829	14.736	-	0.62|±15/2>; 0.21|±11/2>
	2	33.87	1.530	2.502	14.803	90	0.41|±1/2>; 0.25|±5/2>; 0.16|±3/2>; 0.10|±9/2>
Er^{III}-L^3-*a*-S$_4$	1	0.00	8.341	7.474	3.672	-	0.74|±5/2>; 0.24|±3/2>
	2	12.21	5.655	5.026	4.192	90	0.71|±7/2>; 0.25|±1/2>
Er^{III}-L^4	1	0.00	0.103	0.196	16.235	-	0.74|±15/2>; 0.19|±11/2>
	2	122.10	3.943	4.109	9.684	0	0.75|±9/2>; 0.12|±13/2>
	3	151.19	4.430	4.712	8.291	90	0.56|±7/2>; 0.14|±5/2>; 0.10|±3/2>; 0.10|±1/2>

5.5.2 Magnetic properties

Details of the first few relevant Kramers' doublets (KD) of all calculated complexes are presented in Tables 5.5 and 5.6. The orientations of the primary magnetic axes of each doublet are depicted in Figure 5.17. Plots representing the most likely relaxation pathways are presented in Figure 5.18. Complexes of 2LI and L^3 exhibit symmetries D$_2$ and S$_4$, and while the results for both are presented in Tables 5.5 and 5.6, for simplicity the following discussion will focus on the S$_4$ symmetry, unless explicitly stated otherwise. As discussed in the previous Chapter, the ligand field provided by the 2LI ligand is not strongly axial enough to produce a large and pure splitting of the Dy^{III} M_J states. Similarly, the ligand does not provide a sufficiently equatorial field, as the results of the Er^{III} analogue also indicate that no significant SMM behaviour would be expected of this complex, with mixing of the states even more pronounced than for Dy^{III}. The g-tensors of the ground states indicate large transversal moments, and the first excitation energies are only 56 and 39 cm^{-1} for Dy^{III} and Er^{III}, respectively. This is of little surprise considering the relatively similar O-Ln^{III} bond lengths and even distribution of the donors of these complexes. While the main magnetic axes are collinear for all levels of both Dy^{III} and Er^{III} in the S$_4$ symmetry, this is not observed in the case

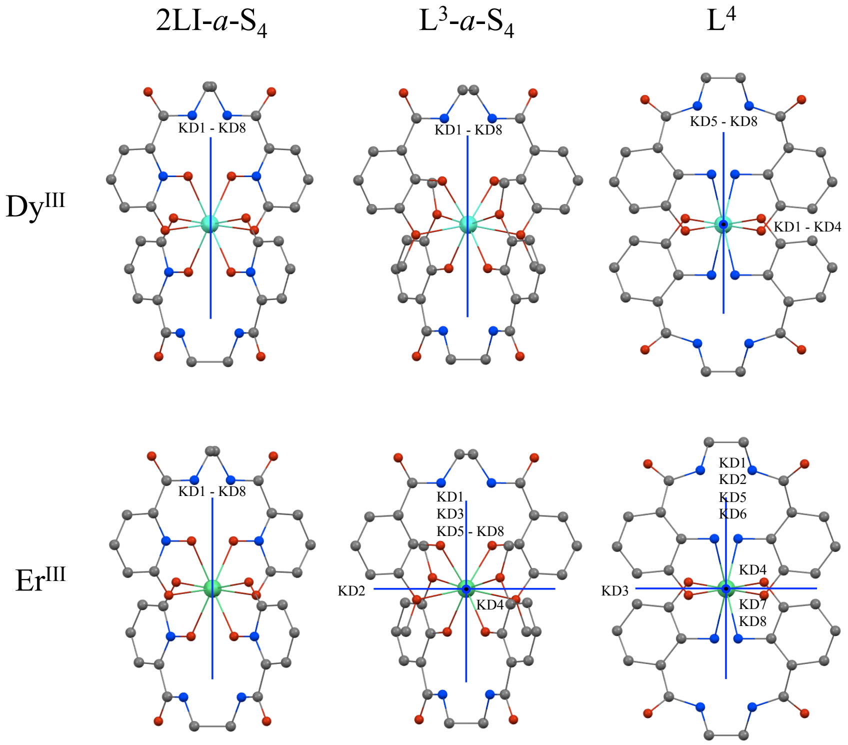

Figure 5.17: Orientations of the *ab initio* calculated main magnetic axes of all eight Kramers' doublets (KD) of the optimised Dy^{III} and Er^{III} complexes.

of the 2LI-a-D_2 complexes, for which KD3 and KD2 are perpendicular to KD1, for Dy^{III} and Er^{III} respectively. Interestingly, an $[Er^{III}(CO_3)_4]^{5-}$ complex has been reported exhibitting zero-field SMM behaviour despite having a similar coordination geometry to the Er^{III}-2LI complex.[116] In order to compare the two complexes, *ab initio* calculations using the crystal structure of the reported complex were also carried out.[117] The calculated first excitation energy is 38 cm^{-1}, with g_x = 0.075, g_y = 5.176, and g_z = 10.733, compared with the 2LI results of ΔE = 39 cm^{-1}, g_x = 2.455, g_y = 4.736, and g_z = 9.971. This would indicate no significant magnetic blocking of either the $[Er^{III}(CO_3)_4]^{5-}$ or Er^{III}-2LI complex, experimentally, however, blocking is observed in the former. This observation is difficult to explain, however, AC susceptibility measurements of the Er^{III}-2LI complex were not conducted.

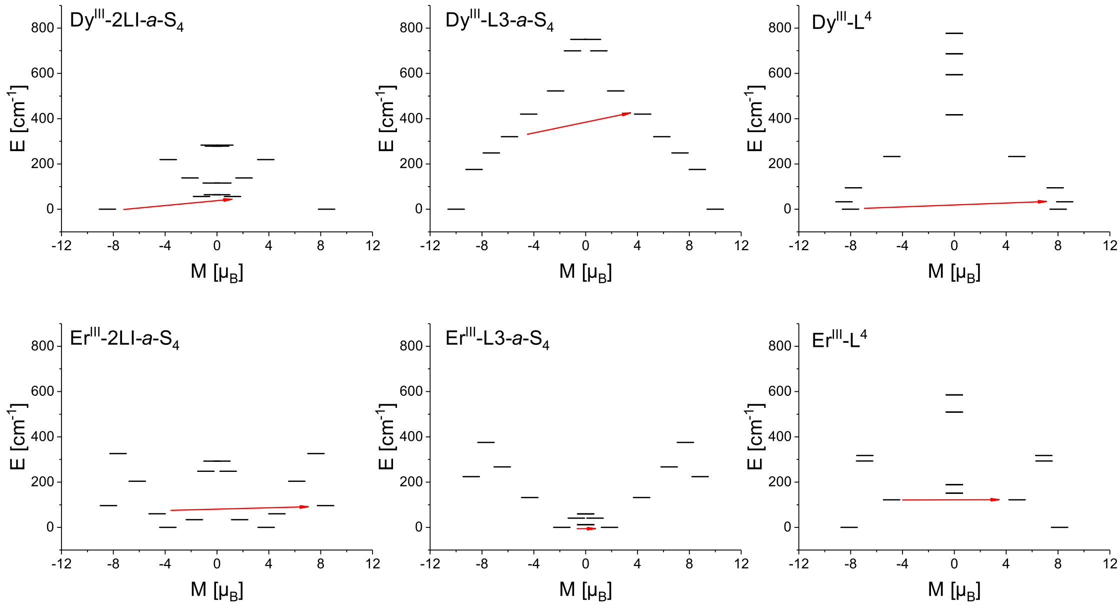

Figure 5.18: CASSCF+RASSI calculated reversal barrier for Dy^{III} and Er^{III} complexes with ligands 2LI, L^3 and L^4. The horizontal black lines represent the Kramers doublets. The red arrows represent the first matrix element indicating relaxation of magnetisation. Only the S_4 symmetry of Dy^{III}-2LI and Dy^{III}-L^3 are shown here for simplicity.

Shortening of the axial, and elongation of the equatorial Ln^{III}-O bonds by 0.103 and 0.165 Å, respectively, of the L^3 complexes appear to be effective in increasing the axial nature of the total ligand field. The first excitation energy (ΔE) of the Dy^{III} complex is 175 cm^{-1} and significant mixing of the states is first observed only for the sixth KD. High anisotropy is evident up to the third doublet, with alignment of the main magnetic axes seen up to the fifth and eighth KD, for symmetries D_2 and S_4, respectively. The predicted relaxation path of this complex occurs *via* Orbach/Raman processes between the third and fourth, fourth and fifth KDs for symmetries D_2 and S_4, indicating barriers of 238 and 321 cm^{-1}, respectively.

The coordination sphere of Dy^{III}-L^3 may be compared to that of a trinuclear Zn^{II}-Dy^{III}-Zn^{II} complex recently published by Sun *et al.*[20] Details of the two coordination spheres are presented in Figure 5.19. Structurally, the first coordination spheres are similar, however, the bonds of the trinuclear complex are slightly longer; on average by 0.04 Å in the axial region and 0.07 Å in the equatorial region. Additionally, the bite angle created by the axial donors in the trinuclear complex is smaller than the current complex by 8 °. Lastly, the trinuclear complex has a chloride ion coordinated in the equatorial plane (Dy–Cl = 2.695 Å). This complex is reported to have a predicted first excitation energy of 355 cm^{-1}, and a ground g_z-tensor of 19.962, experimentally, this complex is reported to have a U_{eff} of 299 cm^{-1}, which is in reasonable agreement with the predicted excitation energy. Compared to Dy^{III}-L^3, the ΔE of the trinuclear complex is almost double in energy. What majorly distinguishes the two complexes, and is the likely cause of the larger ΔE, is the presence of additional axial electron density introduced by the diamagnetic Zn^{II} ions. The careful positioning of diamagnetic ions has been shown experimentally and computationally to increase the splitting of the M_J levels due to increased electrostatic interactions,[19] and it would appear in this case that the additional electron density in the equatorial region of the chloride ion is not sufficient to counteract this effect.

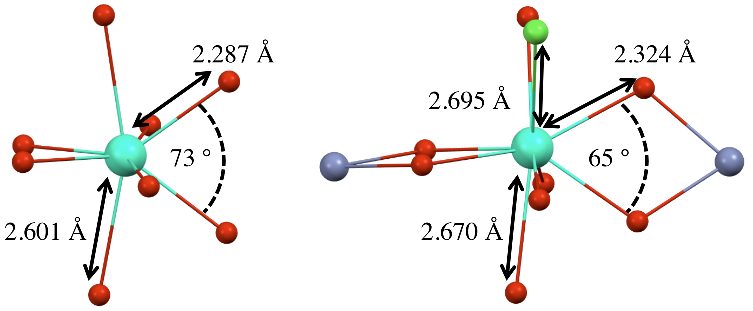

Figure 5.19: First coordination sphere of Dy^{III}-L^3-*a*-S_4 (left) compared with a trinuclear Zn^{II} -Dy^{III} -Zn^{II} complex (right) from Sun *et al.*[20] In the latter case, the bond lengths shown are averaged for the axial (2.302 and 2.345 Å) and equatorial (2.724 and 2.616 regions, respectively. The equatorial Dy-Cl bond length of 2.695 Å is indicated separately.

As the oblate-prolate model would predict, the ligand field provided by L^3 does not promote any pure splitting of the $^4I_{15/2}$ microstates. An averaged first excitation energy of 23 cm^{-1} is predicted, and large mixing of the Er^{III} M_J states results in ground and excited states with significant transversal moments, increasing the likelihood of QTM relaxation processes. Additionally, no alignment of the low lying magnetic axes is expected, which should result in significant Orbach/Raman processes. Conversely, the elongated axial Ln^{III}-N bonds of the L^4 complexes promote favourable M_J splitting of Er^{III} with a larger ΔE of 122 cm^{-1}. However mixing of the M_J states is observed for all KD levels. The predicted barrier for this complex is 122 cm^{-1} due to TA-QTM in KD2. The Dy^{III}-L^4 is predicted to have a barrier of only 33 cm^{-1} and extensive mixing of all KDs. Notably, the ±15/2 ground state is destabilised and has contributions to second and third KD, while the ground KD is composed of ±13/2 and ±9/2 states.

5.6 Conclusion

In this Chapter a new set of ligands was proposed in order to investigate the oblate-prolate electron density distribution of different lanthanide ions, namely Dy^{III} and Er^{III}. The two new ligands (L^3 and L^4) were designed based on the 2LI ligand from the previous Chapter, as this would lead to complexes exhibiting high symmetry and predictable structure needed to conduct a ligand field theory analysis. DFT optimisations indicate that Ln^{III}-L^3 complexes exhibit longer equatorial Ln-O bonds, reducing the electron density in this region and, hence complementing the electron density distribution of oblate ions, such as Dy^{III}. Conversely, Ln^{III}-L^4 complexes experience elongation in the axial region due to the weakly donating amine groups, and compression in the equatorial regions, ideal for prolate ions. Successful synthesis of L^3 led to the isolation of the respective complexes in solution only, and neither a pure solid nor crystals of X-ray quality could be produced. The formation of the complexes was evidenced by mass spectrometry and an NMR titration using the diamagnetic ion Lu^{III}, which showed sole formation of the Lu^{III}-L^3 species in solution. The synthesis of L^4 forms part of the Masters thesis of Thomas Josephy; so far, however, complexes have not be produced due to issues of solubility of this ligand.

Because of low solubility of the complexes, characterisation was limited to solutions state methods where a high concentration was not required. MCD spectra of frozen solution of L^3 complexes of both Dy^{III} and Er^{III} were collected and compared with the respective complexes of the 2LI ligand. Broadening of the signals for both L^3 complexes have been observed in comparison to the 2LI complexes, which indicates that the L^3 complex does not maintain one discrete ligand field in solution. Although the NMR titration results indicate the presence of only one species in solution, the broadening may be due to dis- and re-association of the loosely coordinated methoxy groups. The intensity of the Ln^{III}-L^3 transitions were found to vary from the 2LI complexes. Hypersensitive transitions of Er^{III} were identified, which decreased in intensity from Er^{III}-2LI to Er^{III}-L^3 by factors of 5. Additionally, the transition to $^4I_{9/2}$ has been tentatively designated as a pseudo-hypersensitive transition due to a decrease in intensity by a factor of 7. The differences in intensity may be attributed to longer coordination bond lengths of L^3 complexes and an overall decrease in basicity due to the methoxy donors in the L^3 ligand. However, no hypersensitivity was observed for Dy^{III}.

As in the previous Chapter, the *ab initio* ESO B_q^k parameters were used to fit the MCD data and produced chemically reasonable results for all four complexes. Additionally, good agreement was found between the *ab initio* and LF theory determined splitting of the ground state multiplet of both Dy^{III} and Er^{III} for the two ligands investigated, which is a further and important validation of the methods used.

Because attempts to produce crystal structures and pure solids of these complexes were unsuccessful so far, the CASSCF calculations were carried out on the DFT optimised structure of the whole series. As the oblate-prolate model would predict, the ligand field of L^3 promotes large and pure splitting of Dy^{III} ground state J multiplet, whilst extensive mixing of the M_J states is experienced by Er^{III}. The first excitation energies for Dy^{III} increase in the order L^4 < 2LI < L^3, while for Er^{III} this order is reversed. Strong anisotropy and collinear magnetisation axes of Dy^{III}-L^3 result in a predicted reversal barrier of 240 - 320 cm^{-1}, indicating that this complex could function as a single molecule magnet if successfully isolated. While L^4 is predicted to induce a first excitation energy of 122 cm^{-1} for Er^{III}, mixing of the states is still observed even in the ground state and large transversal moments are expected in the excited states. Magnetic blocking may be expected of this complex, however, QTM in the first excited state limits the energy barrier to the energy of the first excitation.

6. Conclusion and outlook

This thesis has combined experimental and computational methods in order to investigate the ligand field effects of trivalent lanthanide ions. In the first part of this work a set of ligands have been synthesised, the resulting lanthanide complexes of which possess homoleptic coordination spheres of eight oxygen donor. The two different ligands (2LI and 5LIO) induced small geometric changes in the arrangement of the donors, meaning the differences in the ligand field were only very small. Nonetheless, the sensitivity of dysprosium(III) and terbum(III) could be illustrated through magnetometric techniques, HF-EPR as well as MCD measurements. The *ab initio* calculated properties of these complexes also highlight the sensitivity of the M_J state splitting, and agreement with the experimental data provide an important validation of this computational method. Importantly, use of the *ab initio* calculated ESO B_q^k parameters of $\mathrm{Dy^{III}}$-2LI in the ligand field theory calculations to fit the dysprosium(III) MCD data resulted in a set of reasonable AOM parameters and good reproduction of the MCD spectrum. This type of fitting is complicated in cases of lower symmetry, where higher order B_q^k values cannot be ignored, therefore, the basic architecture of the 2LI ligand is ideal for this purpose. While none of the four complexes were predicted to exhibit significant magnetic blocking, the sensitivity of the lanthanides to very small changes in the ligand field was clearly illustrated.

In the second part of this thesis, the different free ion f-electron densities of dysprosium(III) (oblate) and erbium(III) (prolate) were investigated. Due to the high symmetry of 2LI complexes, two new ligands were designed in order to promote axial L^3 or equatorial L^4 coordination spheres. L^3 and its resulting complexes were synthesised, however, difficulties with the synthesis of L^4 meant the resulting complexes were investigated purely computationally. MCD spectra of the L^3 complexes were compared with those of the corresponding 2LI complexes, again illustrating the sensitivity of these lanthanides to ligand field effects. As in the first part of this thesis, the ligand field theory calculations were carried out in combination with the *ab initio* calculated ligand field parameters. Comparison of the *ab initio* and ligand field theory calculated ground state J multiplet splitting illustrated the consistency of the two approaches. The calculation of the experimental energies using ligand field theory provided important validation of both methods used. The results of the *ab initio* calculations indicate that the ligand fields complement the electron densities of the dysprosium(III) and erbium(III) in the orders $L^3 > 2LI > L^4$ and $L^4 > 2LI > L^3$, respectively. This is consistent with the oblate-prolate model proposed by Rinehart and Long. Based on DFT optimised structures, Dy^{III}-L^3 should promote large and pure splitting of the M_J states, high anisotropy of the states, and alignment of their individual easy axes. An effective barrier of 321 cm^{-1} is predicted, with relaxation occurring *via* an Orbach/Raman process between the 4th and 5th Kramers' doublets.

While the ligand field theory calculations reproduce the energies of the MCD transitions, calculation of the intensities of these transitions is still to be achieved. A possible approach for this is through the use of Yb^{III} (f^{13}). The accurate calculation of the intensities would provide important information for the assignment of the experimental data, and an approach that combines ligand field theory and *ab initio* calculations is highly attractive.

7. Experimental section

7.1 Experimental methods

7.1.1 DC SQUID

The magnetic data were collected using an MPMS-XL5 (Quantum Design) SQUID magnetometer. Fixed powder samples were prepared by pressing the powder into PTFE tape. Loose powder samples were prepared in polycarbonate capsules that were sealed with kapton tape. Data were corrected for diamagnetic contributions of the sample holders and, using Pascal's constants, of the samples themselves.

7.1.2 Pulse-field magnetisation

Pulse-field magnetisation measurements were carried out by Denis I. Gorbunov in the Hochfeld-Magnetlabor Dresden (HLD-EMFL) at the Helmholtz-Zentrum Dresden-Rossendorf, Dresden. The magnetisation of Tb^{III}-2LI and Tb^{III}-5LIO in high magnetic fields was measured in the pulsed magnetic field facility of the Helmholtz Zentrum Dresden Rossendorf. The measurements were performed on loose powder samples at 1.5 K with the magnetic field swept up to 58 T. The magnetic field rise time was 7 ms, and the total pulse duration was 25 ms. In order to induce the self-alignment of the powder samples, a pulsed negative field of -8 T was applied before the measurements. Absolute values of the magnetisation measured in pulsed fields were calibrated using static-field data.

7.1.3 High-frequency electron paramagnetic resonance (HF-EPR)

The HF-EPR experiments were performed by Johannes Werner and Dr. Changhyun Koo under the supervision of Prof. Dr. Rüdiger Klingeler at the Kirchhoff-Institute for Physics, Heidelberg University. Measurements of the Tb^{III} monomer complexes, i.e., Tb^{III}-2LI, and Tb^{III}-5LIO, have been carried out in the frequency range of 35 - 300 GHz and in the temperature range of 2 - 60 K. A millimetre vector network analyser (MVNA) by ABmm was used as a phase stable source and sensitive detector of microwaves for the measurements. A superconducting magnet by Oxford instruments provides magnetic field up to 16 T and the sample was placed in a variable temperature insert (VTI). The powder samples have been fixed by eicosane in the transmission type sample stage of the home-built EPR probe.[38]

7.1.4 Magnetic circular dichroism (MCD)

Measurements were carried out at the University of Queensland, Australia in the MCD laboratory of Assoc. Prof. Mark Riley at the School of Chemistry and Molecular Biosiences. Spectra over a range of 7 000 - 23 000 cm^{-1} were obtained using a Jobin Yvon 750s monochromator. A Hinds photoelastic modulator was used in order to generate the circularly polarised modulation with either a Si-avalanche photodiode (visible region) or an InGaAs detector (near-IR region). Signals were acquired using Stanford SR830 lock-in amplifiers at chopped and polarized modulations to allow simultaneous measurement of absorption and MCD spectra. An Oxford SM-4 Spectramag provided the magnetic field of 5 T, in which the spectra were collected over a temperature range of 2-75 K using an Oxford ITC504 controller. The samples were prepared as 7 mM solutions in 2:1 dimethylformamide/methanol. Quartz cells of 2 mm thickness were used and quality glasses were achieved by fast cooling to around 5 K.

7.1.5 X-ray crystal structure determinations

X-ray data were collected and structures solved by Prof. Hubert Wadephol at the Inorganic Chemistry Institute, Heidelberg University. Crystal data and details of the determination of the structures can be found in the Supporting Information of Ref[100]. CCDC 1578942-1578945 contains the supplementary crystallographic data for that paper. These data can be obtained free of charge from The Cambridge Crystallographic Data Centre via https://www.ccdc.cam.ac.uk/data_request/cif.

7.1.6 Elemental analysis

Elemental analysis were obtained from the microanalytical laboratory of the Chemical Institutes of the University of Heidelberg.

7.1.7 NMR

NMR spectra were recorded at room temperature with the following spectrometers: 200 MHz: Bruker Avance I, 400 MHz: Bruker Avance III, 600 MHz: Bruker Avance

III. Chemical shifts are reported in δ units relative to $CHCl_3$ (δH = 7.26), DMSO-d_6 (δH = 2.50), MeOD (δH = 3.31), DMF-d_7 (δH = 2.92). The following abbreviations were used throughout: s = singlet, bs = broad signal, d = doublet, t = triplet, dd = doublet of doublet *etc*., m = multiplet. Coupling constants (J) are given in Hz and refer to H,H-couplings.

7.2 Synthesis of Ligands

7.2.1 General

All chemicals and solvents were used from Sigma-Aldrich Laborchemikalien GmbH, abcr GmbH, Acros Organics and were used as received without further purification. Deuterated solvents were obtained from Deutero GmbH. Syntheses 7.2.2 to 7.2.7 were carried out according to literature reported procedures and the analyses of these compounds are in accordance with the literature reported values.[68,69]

7.2.2 Synthesis of 2-bromo-6-carboxypyridine-1-oxide

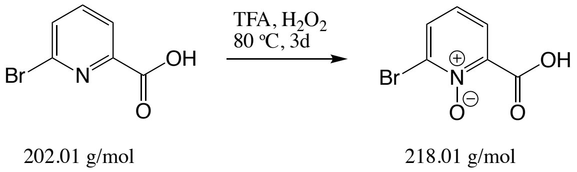

6-bromopicolinic acid (10 g, 49.5 mmol) was dissolved in trifluoroacetic acid (130 mL) in a 1 L round bottom flask. Hydrogen peroxide (30 %, 25 mL) was carefully added to the orange solution, which was then stirred at 80 °C for 24h. The solution was allowed to cool before another 20 mL of H_2O_2 (35 %) were added and the solution was stirred at 80 °C for a further 24h. A sample was checked using NMR to ensure completion of the reaction. The completed reaction was reduced to one quarter volume and poured into 500 mL of water. The pale pink product was collected on a fritted glass filter, washed with water (2 × 50 mL), and dried under high vacuum over night. Yield 8.89 g (82 %).

^{1}H NMR (400 MHz, DMSO-d_6, 300 K): δ (ppm) 7.71 (t, J = 8.1 Hz, 1H, H_{arom}), 8.26 (dd, J = 7.9, 1.9 Hz, 1H, H_{arom}), 8.31 (dd, J = 8.2, 1.9 Hz, 1H, H_{arom}).

7.2.3 Synthesis of 1-hydroxy-6-oxo-1,6-dihydropyridine-2-carboxylic acid (1,2-HOPO)

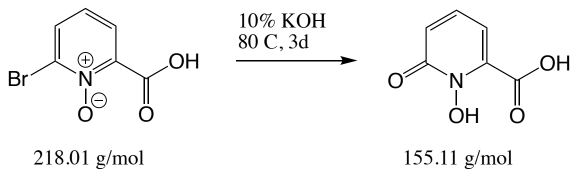

2-bromo-6-carboxypyridine-1-oxide (8.82 g, 40.5 mmol) was dissolved in 200 mL 10 % aqueous potassium hydroxide solution and stirred at 80 °C for 3d. The solution was allowed to cool and concentrated hydrochloric acid (100 mL) was added. The resulting white precipitate was collected on a fritted glass filter and dried under high vacuum. Yield 5.44 g (86 %).

^{1}**H NMR** (200 MHz, DMSO-d_6, 300 K): δ (ppm) = 6.64 (dd, J = 7.0, 1.7 Hz, 1H, H_{arom}), 6.72 (dd, J = 9.1, 1.7 Hz, 1H, H_{arom}), 7.45 (dd, J = 9.1, 7.0 Hz, 1H, H_{arom}).

7.2.4 Synthesis of 1-(benzyloxy)-6-oxo-1,6-dihydropyridine-2-carboxylic acid (1,2-HOPOBn)

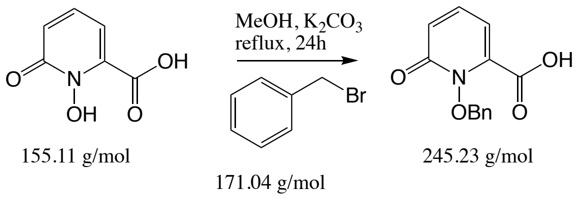

The following reaction was carried out under argon atmosphere. 1,2-HOPO (10.65 g, 69.3 mmol) was placed in a Schlenk flask to which anhydrous methanol (150 mL) was added. Following the addition of benzylbromide (14.29 g, 83.5 mmol, ρ 1.43 g cm^{-3}, 10 mL) and dry K_2CO_3 (19.15 g, 138.6 mmol), the solution was heated to reflux for 24h. Once cooled, the mixture was filtered over a fritted glass filter to remove K_2CO_3, and the solvent was removed *in vacuo*. The yellow oil was dissolved in water (60 mL) and acidified to pH 2 with a 6 M hydrochloric acid solution (30 mL). The white precipitate was collected on a fritted glass filter, dried on the filter and subsequently in high vacuum to yield 1,2-HOPOBn in quantitative amounts.

^{1}**H NMR** (400 MHz, DMSO-d_6, 300 K): δ (ppm) = 5.28 (s, 2H, CH_2), 6.56 (dd, J

= 6.8, 1.7 Hz, 1H, H_{arom}), 6.74 (d, J = 9.3, 1.7 Hz, 1H, H_{arom}), 7.35-7.51 (m, 6H, H_{arom}).

7.2.5 Synthesis of 1-(benzyloxy)-6-oxo-1,6-dihydropyridine-2-carbonyl chloride

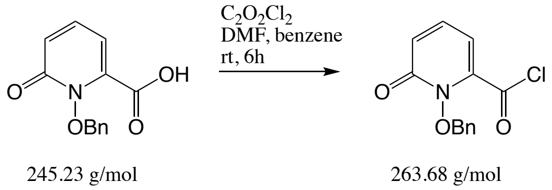
$C_2O_2Cl_2$
DMF, benzene
rt, 6h
O
N
OH
OBn
O
Cl
245.23 g/mol
263.68 g/mol

The following reaction was carried out under argon atmosphere, solvents were either dried over molecular sieve or purchased anhydrous. Benzene (30 mL) was added to 1,2-HOPOBn (2.00 g, 8.00 mmol) to form a suspension, to which oxalylchloride (2 g, 7.8 mmol) was added. Upon the addition of a few drops of DMF, gas evolved. The addition of DMF was repeated every couple of hours until no further gas evolution could be observed. The solvent and excess oxalylchloride were removed in high vacuum and the product allowed to dry overnight. The product was used in the following step without purification.

^{1}H NMR (200 MHz, $CDCl_3$, 300 K): δ (ppm) = 5.35 (s, 2H, CH_2), 6.91 (dd, J = 6.9, 1.6 Hz, 1H, H_{arom}), 7.00 (dd, J = 9.4, 1.6 Hz, 1H, H_{arom}), 7.36-7-63 (m, 6H, H_{arom}).

7.2.6 General synthesis of nLIm-1,2-HOPOBn

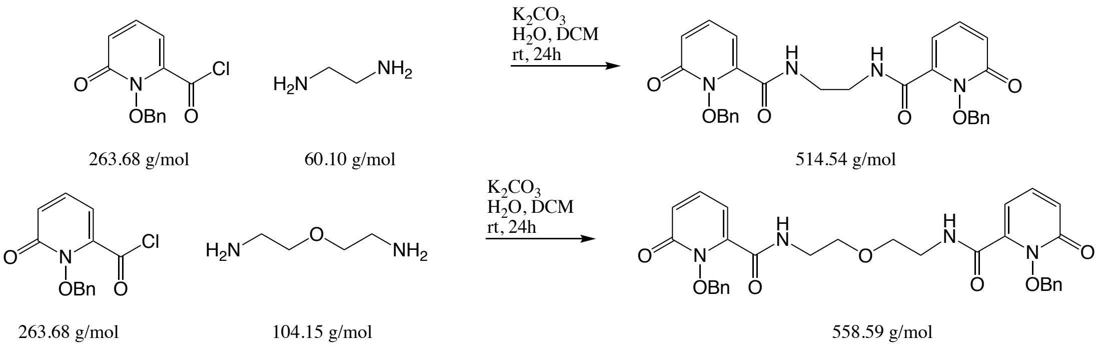
K_2CO_3
H_2O, DCM
rt, 24h
H_2N
NH_2
H
N
O
OBn
Cl
263.68 g/mol
60.10 g/mol
514.54 g/mol
K_2CO_3
H_2O, DCM
rt, 24h
263.68 g/mol
104.15 g/mol
558.59 g/mol

Potassium carbonate (2.21 g, 16 mmol, 5 eq.) was dissolved in distilled water (100 mL) in a large round-bottom flask. DCM (5 mL) and the amine (3.2 mmol, 1 eq; ethylenediamine ρ 0.899 g cm^{-3}, 218 μL; 2-(2-aminoethoxy)ethylamine ρ 0.984 g cm^{-3}, 339 μL) were added to the solution. Under vigorous stirring the acid chloride from Synthesis 7.2.5 (2.15 g, 8 mmol, 2.5 eq.) in anhydrous DCM (40 mL) was added over a period of 5 minutes. The reaction mixture was stirred at room temperature for 24h. The aqueous layer was extracted with DCM (5 × 50 mL). The combined organic phases were removed *in vacuo*. The colourless crude product was purified by flash column chromatography (SiO2, 5% MeOH in DCM, detection with UV-light (254 nm)) to afford the pure product as a colourless solid.

N,N'-(ethane-1,2-diyl)bis(1-benzyloxy)-6-oxo-1,6-dihydropyridine-2-carboxamide) (**2LI-1,2-HOPOBn**): Yield, 1.39 g (84 %). **^{1}H NMR** (200 MHz, $CDCl_3$, 300 K): δ (ppm) = 3.50 (s, 4H, N-CH_2), 5.23 (s, 4H, CH_2), 6.29 (dd, J = 6.8, 1.6 Hz, 2H, H_{arom}), 6.59 (dd, J = 9.2, 1.6 Hz, 2H, H_{arom}), 7.19 (dd, J = 9.2, 6.8 Hz, 2H, H_{arom}), 7.31-7.43 (m, 12H, H_{arom}), 7.52 (bs, 2H, NH).

N,N'-(oxybis(ethane-2,1-diyl)bis(1-benzyloxy)-6-oxo-1,6-dihydropyridine-2-carboxamide) (**5LIO-1,2-HOPOBn**): Yield, 1.59 g (89 %). **^{1}H NMR** (400 MHz, $CDCl_3$, 300 K): δ (ppm) = 3.23 (s, 8H, CH_2), 5.25 (s, 4H, CH_2), 6.27 (dd, J = 6.8, 1.6 Hz, 2H, H_{arom}), 6.37 (dd, J = 9.2, 1.3 Hz, 2H, H_{arom}), 7.25 (m, 2H, H_{arom}), 7.26-7.44 (m, 12H, H_{arom}), 7.58 (s, 2H, NH).

7.2.7 General synthesis of nLIm-1,2-HOPO

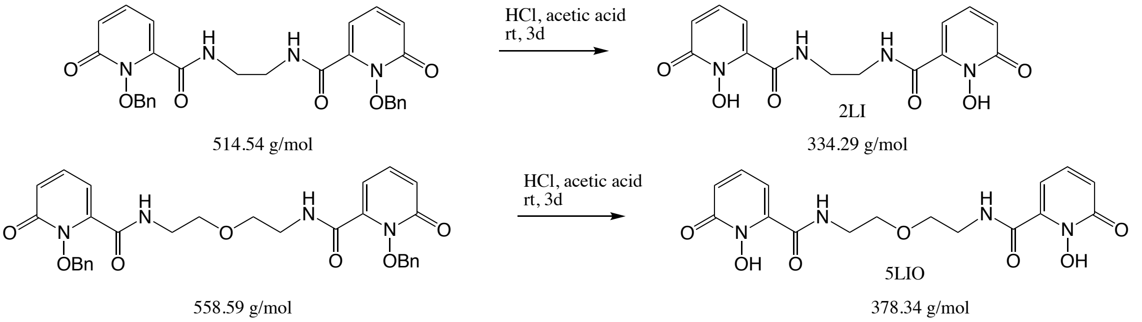

All glassware and stirrer bars were treated with a solution of EDTA to remove any residual iron. The respective nLIm-1,2-HOPOBn was dissolved in a mixture of hydrochloric acid (50 mL) and acetic acid (50 mL). The colourless solution was stirred for three days at room temperature after which the mixture was reduced to about 10 % *in vacuo*. Water (10 mL) was added and subsequently removed *in vacuo*, and this was repeated with methanol (30 mL). The deprotected ligand was then dried under high vacuum overnight to yield the final ligands in quantitative amounts.

N,N'-(ethane-1,2-diyl)bis(1-hydroxy-6-oxo-1,6-dihydropyridine-2-carboxamide) (**2LI-1,2-HOPO**): **^{1}H NMR** (400 MHz, DMSO-d$_6$, 300 K): δ (ppm) = 3.36 (s, 4H, N-CH$_2$), 6.35 (dd, J = 6.9, 1.7 Hz, 2H, $\mathrm{H_{arom}}$), 6.58 (dd, J = 9.1, 1.7 Hz, 2H, $\mathrm{H_{arom}}$), 7.40 (dd, J = 9.1, 6.9 Hz, 2H, $\mathrm{H_{arom}}$), 8.83 (s, 2H, NH).

(N,N'-(oxybis(ethane-2,1-diyl)bis(1-hydroxy-6-oxo-1,6-dihydropyridine-2-carboxamide) **5LIO-1,2-HOPO**): **^{1}H NMR** (200 MHz, MeOD, 300 K): δ (ppm) = 3.64 (dd, J = 4.8, 14.90 Hz, 4H, CH$_2$), 6.86 (m, 4H, $\mathrm{H_{arom}}$), 7.63 (dd, J = 7.1.6, 9.01, 2H, $\mathrm{H_{arom}}$).

7.2.8 Synthesis of *N,N'*-(ethane-1,2-diyl)bis(2-hydroxy-3-methoxybenzamide): 2LI-2,3-HOMOPH (L^3)

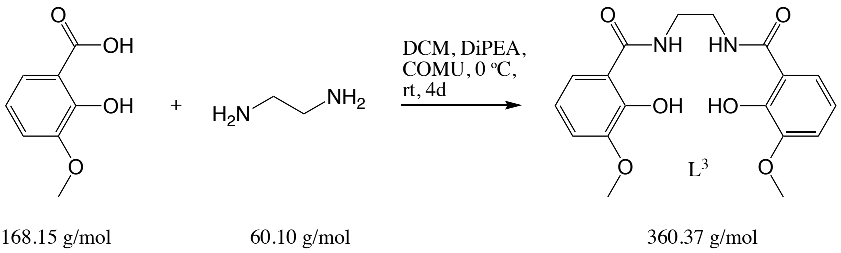

2-Hydroxy-3-methoxybenzoic acid (2.00 g, 11.9 mmol) was dissolved in DCM (150 mL), N,N-Diisopropylethylamine (3.07 g, 23.8 mmol, ρ 0.742 g cm^{-3}, 4.14 mL) was added and the pale yellow solution was cooled over ice. The peptide coupling reagent COMU ((1-cyano-2-ethoxy-2-oxoethylidenaminooxy)dimethylamino-morpholino-carbenium hexafluorophosphate) (5.09 g, 11.9 mmol) was added to the mixture, upon which a colour change from pale yellow to bright orange was observed. The mixture was left to stir for 30 min at 0 °C, and for a further 30 min at room temperature. Ethylenediamine (286 mg, 4.76 mmol, ρ 0.899 g cm^{-3}, 318 μL) was added to the solution and the reaction was allowed to stir over night. After 12h formation of the product could be identified by the presence of a white precipitate. The reaction was allowed to stir for a subsequent 3d. The ligand was collected on a fritted glass filter, washed with DCM (3 $\times$ 20 mL) and air dried. Yield 1.12 g (65 %).

^{1}H NMR (400 MHz, DMSO-d$_6$, 300 K): δ (ppm) = 12.76 (bs, 2H, OH), 8.96 (bs, 2H, NH), 7.38 (dd, 2H, J = 8.16 Hz, 1.34 Hz, 1.16 Hz, $\mathrm{H_{arom}}$), 7.09 (dd, 2H, J = 8.05 Hz, 1.24 Hz, 1.00 Hz, $\mathrm{H_{arom}}$), 6.81 (t, 2H, J = 8.06 Hz, $\mathrm{H_{arom}}$), 3.77 (s, 6H, CH$_3$), 3.48 (m, 4H, CH$_2$). **^{13}C NMR** (400 MHz, DMSO-d$_6$, 300 K): δ (ppm) = 169.90 (2C, C=O), 150.91 (2C, C_{arom}-OR), 148.46 (2C, C_{arom}-OH), 118.64 (2C, C_{arom}), 117.76 (2C, C_{arom}), 115.41 (2C, C_{arom}), 114.86 (2C, C_{arom}), 55.78 (2C, OCH_3), 38.54 (2C, CH_2). CHN found: C, 58.57; H, 5.72; N, 7.78; calculated: C, 58.53; H, 5.73; N, 7.58 for $C_{18}H_{21}N_2O_{6.5}$ ($L^3 \cdot 0.5H_2O$).

7.3 Synthesis of Complexes

7.3.1 Synthesis of $[(2LI\text{-}1,2\text{-}HOPO)_2Ln]^-$ (Ln^{III}-2LI) complexes

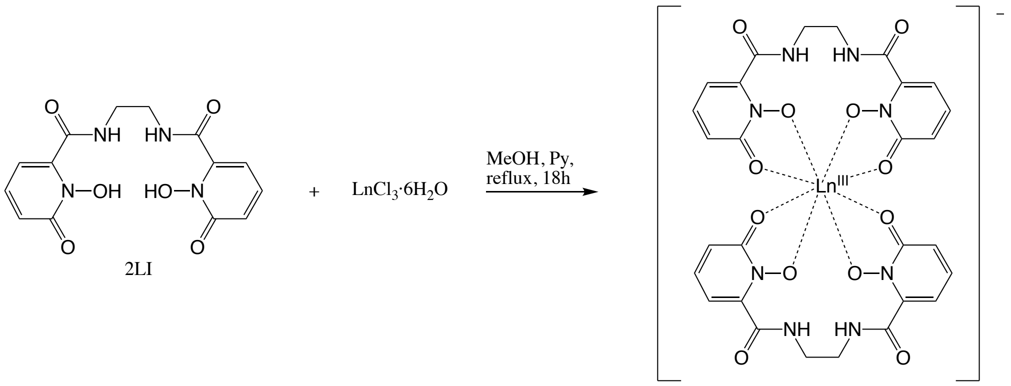

The ligand 2LI-1,2-HOPO (**2LI**) (0.90 mmol, 2.5 eq) was dissolved in methanol (10 mL), and a solution of the $Ln^{III}Cl_3 \cdot H_2O$ salt (0.36 mmol, 1 eq in 1 mL methanol) was added, followed by pyridine (300 μL). The mixture was heated and allowed to stir under reflux overnight. The resulting white precipitate was collected, dried, and redissolved in DMF for a vapour diffusion with diethyl ether to yield a colourless crystalline solid. Crystals suitable for X-ray crystallography were obtained either by diffusion of diethyl ether into a solution of DMF of the complex, or by recrystallisation from hot DMF.

$[Tb(2LI\text{-}1,2\text{-}HOPO)_2]PyH \cdot H_2O \cdot 2DMF \cdot 0.5MeOH$ (**Tb^{III}-2LI**). Yield 47 %. HR-ESI-MS (-) (MeOH): 823.07717 (calculated: 823.08 $[C_{28}H_{24}N_8O_{12}Tb]^-$). CHN found: C, 43.53; H, 4.55; N, 14.47; calculated: C, 43.77; H, 4.46; N, 14.22.

$[Dy(2LI\text{-}1,2\text{-}HOPO)_2]PyH \cdot 2.5DMF$ (**Dy^{III}-2LI**). Yield 42 %. HR-ESI-MS (-) (MeOH): 828.08174 (calculated: 828.08 $[C_{28}H_{24}DyN_8O_{12}]^-$). CHN found: C, 44.56; H, 4.66; N, 14.80; calculated: C, 44.63; H, 4.39; N, 14.78.

$[Er(2LI\text{-}1,2\text{-}HOPO)_2]PyH \cdot 2NH(CH_3)_2$ (**Er^{III}-2LI**). Yield 44 %. HR-ESI-MS (-) (MeOH):

830.08122 (calculated: 830.08 [$C_{28}H_{24}ErN_8O_{12}$]$^-$). CHN found: C, 44.64; H, 4.14; N, 15.34; calculated: C, 44.35; H, 4.43; N, 15.38.

7.3.2 Synthesis of mononuclear [Ln(5LIO-1,2-HOPO)$_2$]$^-$ complexes

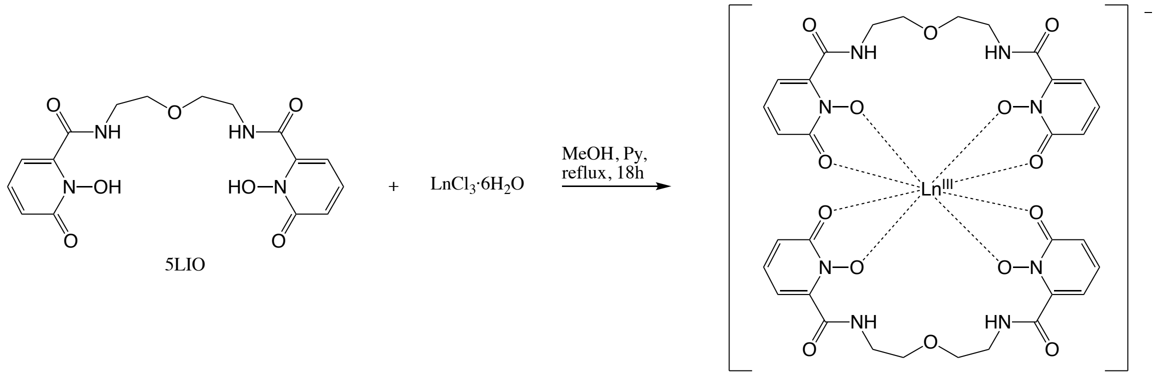

The ligand 5LIO-1,2-HOPO (**5LIO**) (0.90 mmol, 2.5 eq) was dissolved in methanol (10 mL), and a solution of the $Ln^{III}Cl_3{\cdot}H_2O$ salt (0.36 mmol, 1 eq in 1 mL methanol) was added, followed by pyridine (300 μL). The mixture was heated and allowed to stir under reflux overnight. The resulting white precipitate was collected and dried.

[Tb(5LIO-1,2-HOPO)$_2$]PyH (**Tb^{III}-5LIO**). Yield 60 %. HR-ESI-MS (-) (MeOH): 911.13015 (calculated: 911.13 [$C_{32}H_{32}N_8O_{14}Tb$]$^-$). CHN found: C, 44.60; H, 4.09; N, 12.83; calculated: C, 44.81; H, 3.86; N, 12.71.

[Dy(5LIO-1,2-HOPO)$_2$]PyH·H_2O·0.5DMF (**Dy^{III}-5LIO**). Yield 53 %. HR-ESI-MS (-) (MeOH): 916.13348 (calculated: 916.13 [$C_{32}H_{32}DyN_8O_{14}$]$^-$). CHN found: C, 44.05; H, 4.19; N, 12.82; calculated: C, 44.05; H, 4.18; N, 12.68.

7.3.3 *In situ* preparation of the [Ln(2LI-2,3-HOMOPH)$_2$]$^-$ complexes for MCD

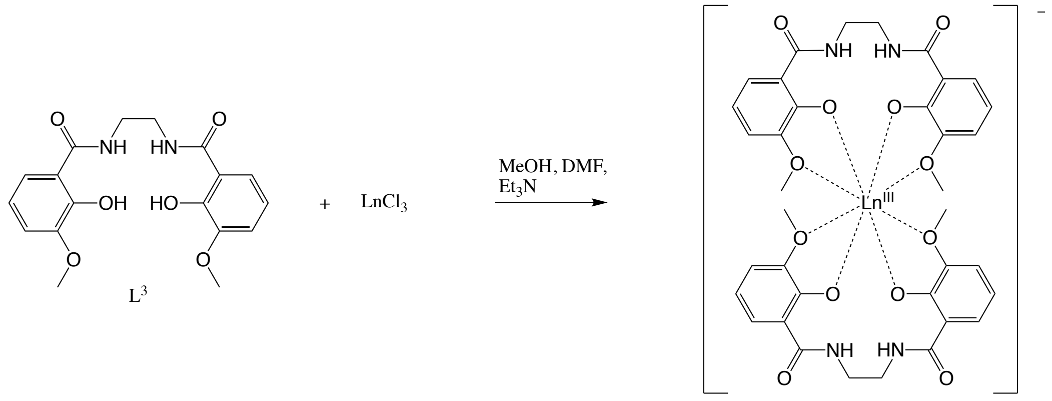

The anhydrous lanthanide salt (35 μmol, 1 equiv.) was dissolved in 1 mL of MeOH and added to a 5 mL volumetric flask containing a solution of L^3 (27.7 mg, 77 μmol, 2.2 equiv) in 2 mL of DMF. The mixture was heated, ethylenediamine was added as a base (107 μL, 10 equiv.) and the mixture was heated again. An additional 1.23 mL of DMF was added and MeOH was used to bring the volume of the solution up to the required 5 mL.

Dy^{III}-L^3. HR-ESI-MS (-) (MeOH/DMF): 880.1633 (calculated: 880.16 [$C_{36}H_{36}DyN_4O_{12}$]$^-$)
Er^{III}-L^3. HR-ESI-MS (-) (MeOH/DMF): 883.1662 (calculated: 882.16 100%, 883.16 68 % [$C_{36}H_{36}ErN_4O_{12}$]$^-$)

7.3.4 ^{1}H NMR titration of Lu^{III}-L^3

To ensure formation of a single complex in solution, an NMR titration was carried using the diamagnetic ion Lu^{III}. NMR tubes were prepared for a total volume of 0.52 mL containing 10 mg of **L^3**. A stock solution of **L^3** (2 mL, 87 mM, DMF-d$_7$) was prepared and distributed into four NMR tubes. Due to low solubility of anhydrous LuCl$_3$ a stock solution in MeOH-d$_4$ could not be prepared, therefore, the required amounts for each sample were weighed out individually. The ligand is expected to form a complex with a ligand/metal ratio of 2:1, therefore ratios of 1:0, 3:1, 2:1 and 1:1 were prepared. Each sample was prepared in the following way: 320 μL L^3 (1 equiv.) and 160 μL solutions of LuCl$_3$ were added to an NMR tube, the samples were heated, 40 μL (10 × ligand equiv.) of ethelynediamine were added and the samples were heated again.

L^3 in DMF-d_7 [μL]	$LuCl_3$ [mmol | mg]	MeOH-d_4 [μL]	Et_3N [μL]
320	9.3 | 2.6	160	40
320	13 | 3.9	160	40
320	28 | 7.8	160	40

L^3: **^{1}H NMR** (600 MHz, DMF-d_6, 300 K): δ (ppm) = 3.60 (s, 4H, CH_2), 3.79 (s, 3H, O-CH_3), 6.59 (m, 2H, H_{arom}), 6.95 (m, 2H, H_{arom}), 7.47 (dd, J = 8.13 Hz, 1.41 Hz, 2H, H_{arom})

Lu^{III}-L^3: **^{1}H NMR** (600 MHz, DMF-d_6, 300 K): δ (ppm) = 3.72 (s, 4H, CH_2), 3.75 (s, 6H, O-CH_3), 6.50 (m, 2H, H_{arom}), 6.79 (m, 2H, H_{arom}), 7.59 (dd, J = 8.07 Hz, 1.35 Hz, 2H, H_{arom}).

Appendix A

A.1 Appendices to Chapter 4

Table A.1: Details of the crystal structure determinations of the mononuclear Ln^{III}-2LI complexes

	Tb^{III}-2LI, (type A)	Tb^{III}-2LI, (type B)	Dy^{III}-2LI, (type A)	Dy^{III}-2LI, (type B)
formula	$C_{33.5}H_{32}N_9O_{12.5}Tb$	$C_{33}H_{42}N_9O_{14}Tb$	$C_{33.5}H_{32}DyN_9O_{12.5}$	$C_{42}H_{51}DyN_{12}O_{15}$
crystal system	monoclinic	orthorhombic	monoclinic	monoclinic
space group	P $2_1/c$	P *bca*	P $2_1/c$	P *c*
a /Å	37.6617(6)	8.26270(8)	37.5903(5)	13.7009(5)
b /Å	8.72704(13)	26.0470(2)	8.74742(9)	18.6217(6)
c /Å	23.2100(3)	34.4987(3)	23.1818(3)	9.5032(4)
β /°	107.2923(17)		107.4123(15)	108.574(4)
V /Å^3	7283.7(2)	7424.75(11)	7273.31(17)	2298.31(15)
Z	8	8	8	2
M_r	919.60	947.67	923.18	1126.44
F_{000}	3688	3840	3696	1146
d_c /Mg·m^{-3}	1.677	1.696	1.686	1.628
μ /mm^{-1}	10.224	1.987	11.669	1.709
max., min. transmission factors	0.4643, 0.4142[a]	1.000, 0.777[b]	0.641, 0.268[b]	0.84515, 0.84378[a]
X-radiation, λ /Å	Cu-Kα, 1.54184	Mo-Kα, 0.71073	Cu-Kα, 1.54184	Mo-Kα, 0.71073
data collect. temperat. /K	120(1)	120(1)	120(1)	120(1)
ϑ range /°	3.7 to 70.8	2.4 to 32.4	3.7 to 71.0	3.1 to 30.7
index ranges *h,k,l*	-46 ... 46, -10 ... 10, -28 ... 28	-12 ... 12, -37 ... 38, -51 ... 51	-45 ... 45, -10 ... 10, -28 ... 28	-19 ... 19, -26 ... 26, -13 ... 13
reflections measured	158141	161371	166094	89589
unique [R_{int}]	14021 [0.0739]	13029 [0.0516]	13978 [0.0557]	19565 [0.059]
observed [$I \geq 2\sigma(I)$]	12473	10825	13059	13827
data / restraints /parameters	14021 / 83 / 1031	13029 / 0 / 549	13978 / 1206 / 1085	19565 / 622 / 646
GooF on F^2	1.011	1.082	1.052	1.008
R indices [$F > 4\sigma(F)$] $R(F)$, $wR(F^2)$	0.0334, 0.0810	0.0349, 0.0743	0.0416, 0.0995	0.0426, 0.0923
R indices (all data) $R(F)$, $wR(F^2)$	0.0394, 0.0848	0.0466, 0.0784	0.0450, 0.1015	0.0733, 0.1010
absolute structure parameter	-	-	-	-0.010(5)
largest residual peaks /e.Å^{-3}	0.763, -0.991	1.337, -1.290	1.112, -1.351	1.336, -0.634
CCDC deposition number	1578942	1578943	1578944	1578945

[a] semiempirical absorption correction. [b] numerical absorption correction.

Table A.2: Example input for Gaussian optimisations of the 1,2-HOPO complexes

```
#p opt=tight ub3lyp/gen 5d pseudo=read int=ultrafinegrid scf=(maxcycle=500)

<Title card>

-1 1

<Geometry specification>

C N O H 0
6-31G(d,p)
****
Dy 0
MWB55
****

Dy 0
MWB55
```

Table A.3: Relative energies of the four different structures in kcal mol^{-1}.

	a-edge D_2	*a*-edge S_4	*g*-edge *cis*	*g*-edge *trans*
Dy^{III}-2LI	0.00	0.43	8.31	10.07
Dy^{III}-5LIO	4.26[a]	5.62	0.93	0.00

[a] One mode of –2.38 cm^{-1} was found for this structure.

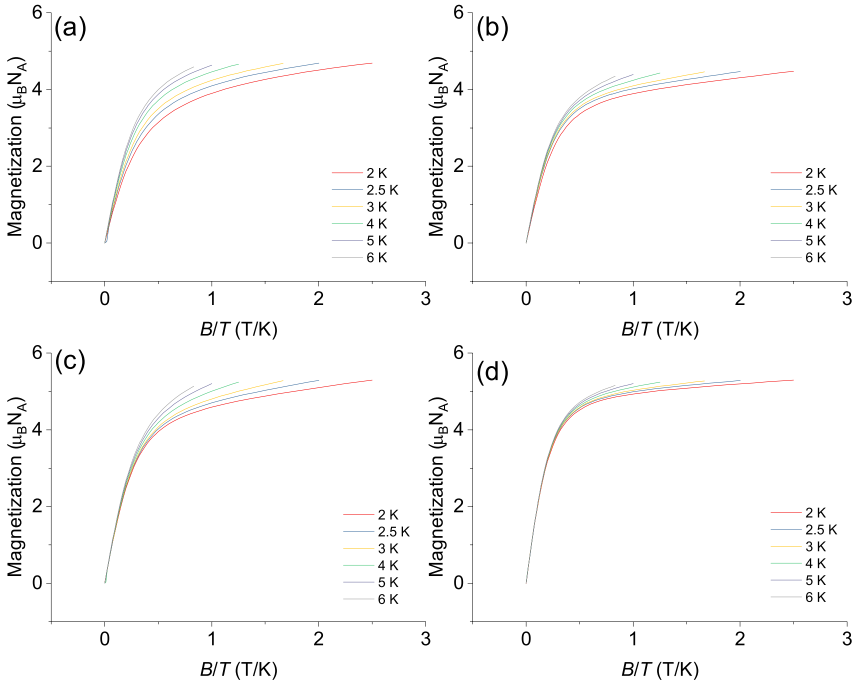

Figure A.1: *M vs. B*/T plots of (a) Tb^{III}-2LI and (b) Tb^{III}-5LIO and (c) Dy^{III}-2LI and (d) Dy^{III}-5LIO.

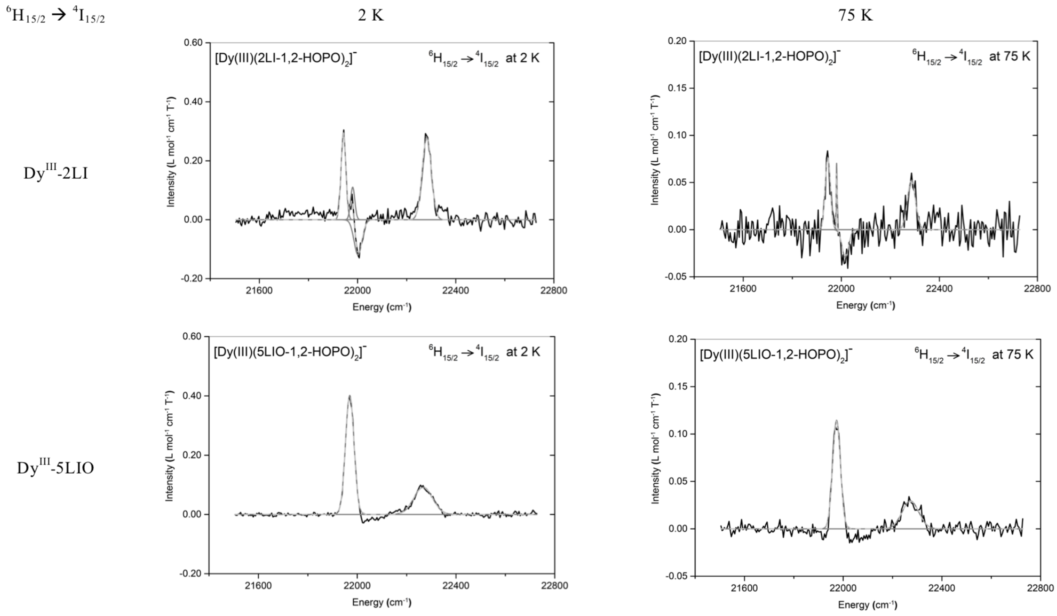

Figure A.2: Deconvoluted MCD spectra of the transition $^6H_{15/2} \rightarrow {}^4I_{15/2}$ for [Dy(2LI-1,2-HOPO)$_2$]$^-$ and [Dy(5LIO-1,2-HOPO)$_2$]$^-$ at 2 and 75 K. Solid black lines represent the measured data, solid dark grey lines the individual fitted Gaussians, and the dashed light grey lines the overall fit.

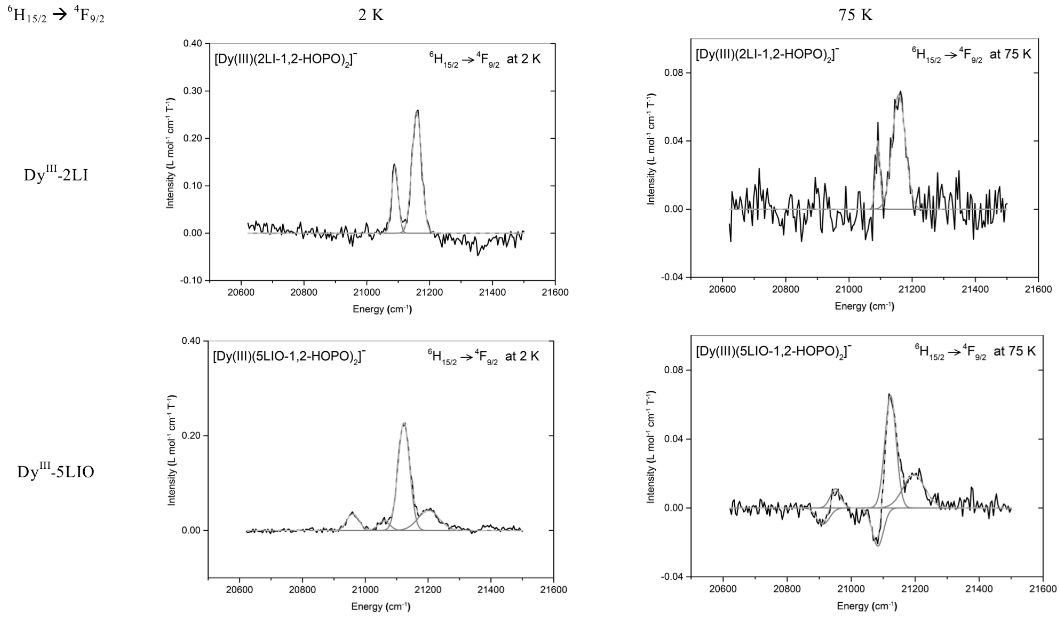

Figure A.3: Deconvoluted MCD spectra of the transition $^6H_{15/2} \rightarrow {}^4F_{9/2}$ for [Dy(2LI-1,2-HOPO)$_2$]$^-$ and [Dy(5LIO-1,2-HOPO)$_2$]$^-$ at 2 and 75 K. Solid black lines represent the measured data, solid dark grey lines the individual fitted Gaussians, and the dashed light grey lines the overall fit.

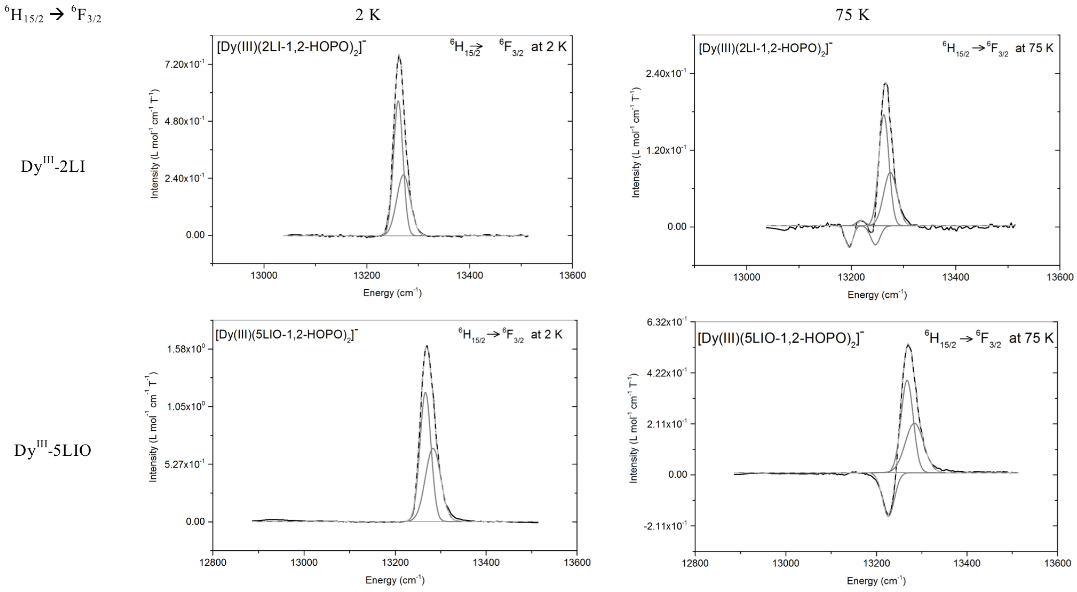

Figure A.4: Deconvoluted MCD spectra of the transition $^6H_{15/2} \rightarrow {}^6F_{3/2}$ for [Dy(2LI-1,2-HOPO)$_2$]$^-$ and [Dy(5LIO-1,2-HOPO)$_2$]$^-$ at 2 and 75 K. Solid black lines represent the measured data, solid dark grey lines the individual fitted Gaussians, and the dashed light grey lines the overall fit.

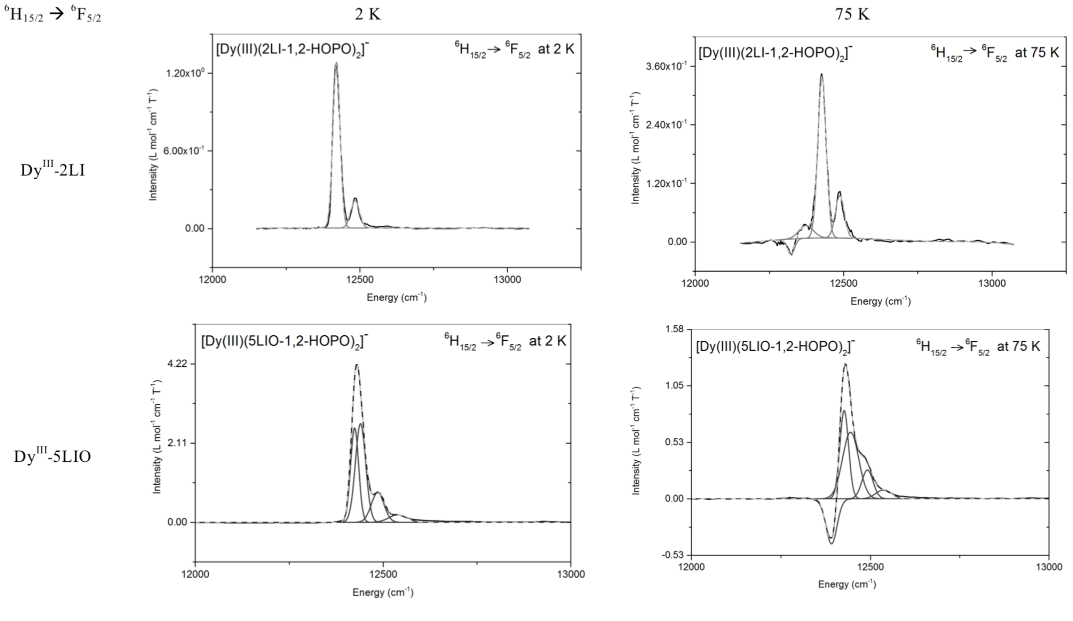

Figure A.5: Deconvoluted MCD spectra of the transition $^6H_{15/2} \rightarrow {}^6F_{5/2}$ for [Dy(2LI-1,2-HOPO)$_2$]$^-$ and [Dy(5LIO-1,2-HOPO)$_2$]$^-$ at 2 and 75 K. Solid black lines represent the measured data, solid dark grey lines the individual fitted Gaussians, and the dashed light grey lines the overall fit.

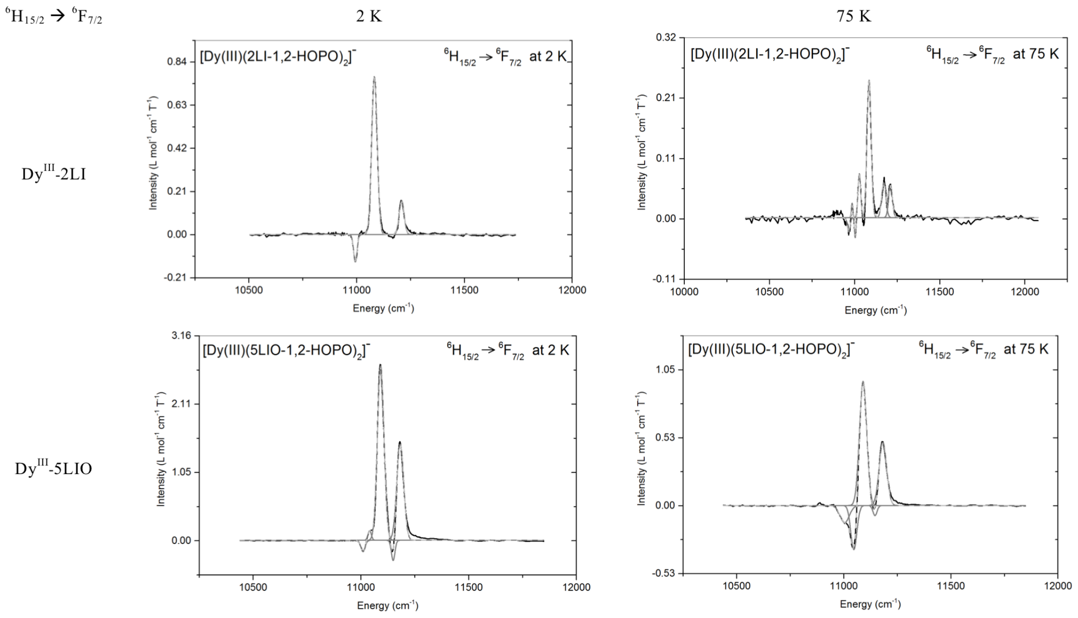

Figure A.6: Deconvoluted MCD spectra of the transition $^6H_{15/2} \rightarrow {}^6F_{7/2}$ for [Dy(2LI-1,2-HOPO)$_2$]$^-$ and [Dy(5LIO-1,2-HOPO)$_2$]$^-$ at 2 and 75 K. Solid black lines represent the measured data, solid dark grey lines the individual fitted Gaussians, and the dashed light grey lines the overall fit.

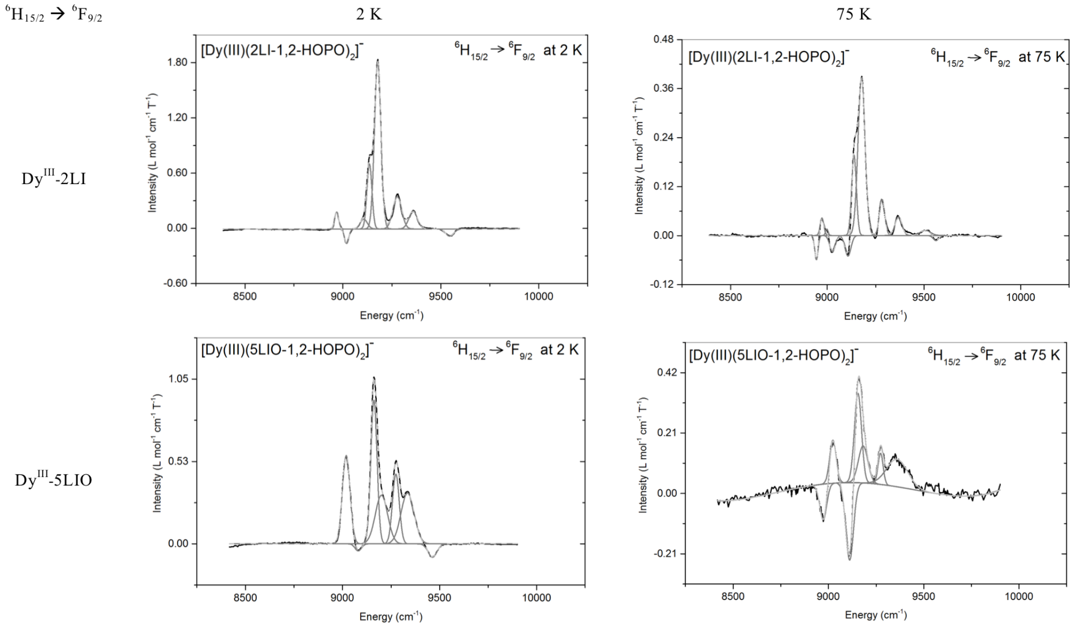

Figure A.7: Deconvoluted MCD spectra of the transition $^6H_{15/2} \rightarrow {}^6F_{9/2}$ + $^6H_{7/2}$ for [Dy(2LI-1,2-HOPO)$_2$]$^-$ and [Dy(5LIO-1,2-HOPO)$_2$]$^-$ at 2 and 75 K. Solid black lines represent the measured data, solid dark grey lines the individual fitted Gaussians, and the dashed light grey lines the overall fit.

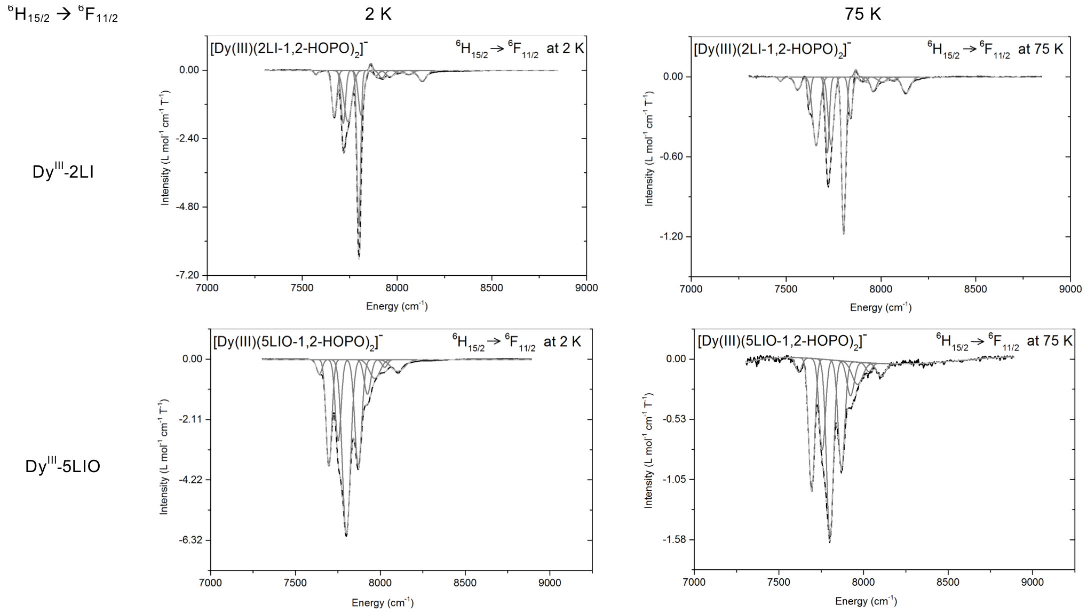

Figure A.8: Deconvoluted MCD spectra of the transition $^6H_{15/2} \rightarrow {}^6F_{11/2}$ + $^6H_{9/2}$for [Dy(2LI-1,2-HOPO)$_2$]$^-$ and [Dy(5LIO-1,2-HOPO)$_2$]$^-$ at 2 and 75 K. Solid black lines represent the measured data, solid dark grey lines the individual fitted Gaussians, and the dashed light grey lines the overall fit.

Table A.4: Experimental energies (cm^{-1}) and intensities (L mol^{-1} cm^{-2} T^{-1}) of the [Dy^{III}(2LI-1,2-HOPO)$_2$]$^-$ MCD spectra over the temperature range 2-75 K. The intensity of transition to $^6H_{5/2}$ was too weak and not determined.

			Energy					Intensity			
	Ref[118]	2 K	10 K	25 K	50 K	75 K	2 K	10 K	25 K	50 K	75 K
$^6H_{9/2}$ + $^6F_{11/2}$	7832	-	-	-	7472.3	7470.7	-	-	-	-0.4242	-0.8853
		7574.4	7572.6	7564.9	7561.0	7560.3	-3.846	-4.783	-5.074	-4.759	-3.970
		-	-	7624.3	7621.2	7621.1	-	-	-4.891	-5.975	-4.542
		7669.2	7668.8	7666.0	7661.4	7658.2	-51.94	-50.21	-40.61	-30.00	-23.68
		7716.4	7715.8	7716.6	7717.3	7717.0	-53.57	-42.06	-32.21	-22.99	-15.13
		7740.8	7739.8	7740.6	7740.0	7736.6	-95.75	-78.81	-51.93	-27.51	-19.14
		7798.4	7799.3	7801.8	7803.2	7803.7	-132.2	-109.5	-81.31	-47.65	-32.55
		7810.6	7814.4	7832.8	7838.4	7839.5	-57.32	-41.50	-16.15	-10.58	-8.294
		7863.0	7861.0	7862.4	7864.3	7867.3	4.796	3.032	2.255	1.518	1.154
		7888.4	7896.5	7896.5	7897.8	7895.5	-6.994	-5.795	-3.270	-1.273	-0.9072
		7920.2	7924.0	7921.8	7920.4	7919.4	-10.07	-5.493	-2.859	-1.459	-0.7609
		7963.2	7962.7	7962.2	7960.8	7960.8	-11.16	-9.417	-6.779	-4.814	-4.481
		8010.3	8008.5	8007.3	8004.9	8005.7	-3.615	-3.036	-2.059	-2.311	-2.172
		8061.7	8060.1	8059.7	8061.7	8060.7	-7.150	-5.566	-3.262	-2.207	-1.227
		8133.4	8132.8	8131.9	8132.7	8133.0	-21.04	-18.95	-13.76	-8.624	-6.819
$^6H_{7/2}$ + $^6F_{9/2}$	9196	-	8942.9	8943.2	8943.7	8944.1	-	-0.3631	-1.329	-1.489	-1.275
		8968.5	8969.1	8969.6	8970.7	8973.0	4.523	3.837	2.144	1.498	0.9960
		-	-	8993.7	8994.7	8998.3	-	-	0.3381	0.3142	0.1794
		9019.4	9020.3	9022.1	9023.9	9027.5	-4.300	-3.336	-2.252	-1.262	-1.449
		-	-	-	9083.7	-	-	-	-	0.0288	-
		9106.9	9108.7	9097.9	9108.8	9107.3	4.764	4.206	0.9692	-0.4602	-1.957
		9135.6	9134.9	9136.0	9137.6	9138.4	22.44	17.89	14.39	8.784	6.002
		9177.7	9177.0	9177.9	9177.5	9177.3	74.45	62.38	40.60	25.38	17.59
		9277.3	9277.3	9281.3	9282.9	9283.3	19.47	14.98	8.331	4.517	3.028
		9358.4	9358.5	9362.7	9366.4	9368.2	10.31	8.377	4.529	3.145	2.012
		-	-	9559.0	9498.7	9506.7	-	-	-	0.9850	0.8320
		9545.2	9549.0	-	9563.2	9561.8	-4.021	-2.886	-1.120	-0.6441	-0.4612
$^6F_{7/2}$	11131	10994	10995	10997	11000	11003	3.040	2.507	1.382	0.578	0.562
		-	-	11024	11026	11028	-	-	1.140	2.142	1.712
		11083	11083	11084	11085	11085	27.89	24.91	17.86	12.17	8.228
				11172	11171	11171	-	-	2.291	3.048	2.134
		11209	11209	11210	11211	11211	5.424	5.945	3.995	2.504	1.755
		-	-	-	12323	12322	-	-	-	-0.4255	-0.9496
$^6F_{5/2}$	12492	-	-	12368	12373	12373	-	-	0.4776	1.296	1.559
		12420	12421	12423	12425	12427	38.83	34.39	24.99	16.10	11.54
		12483	12484	12486	12487	12487	7.818	6.461	5.460	3.977	3.232
		-	-	13193	13194	13196	-	-	-0.1703	-0.4479	-0.6081
$^6F_{3/2}$	13278	-	-	13215	13212	13218	-	-	0.1591	0.1288	0.1756
		-	-	13239	13242	13246	-	-	-0.1714	-0.5469	-0.6666
		13261	13261	13261	13263	13262	13.00	11.44	7.765	5.185	4.220
		13271	13272	13275	13273	13275	8.484	7.534	5.314	3.769	2.669
		21090	21089	21092	21090	21091	3.654	3.146	2.071	0.7350	0.7446
$^4F_{9/2}$	21150	21159	21159	21160	21161	21158	9.787	8.985	5.664	3.153	3.498
		21942	21942	21943	21942	21945	7.172	6.209	3.813	3.360	2.024
$^4I_{15/2}$	22217	21980	21982	21980	21983	21981	2.365	2.030	0.9909	0.7310	0.3132
		22002	22004	22009	22013	22016	-4.834	-4.364	-3.612	-0.9562	-0.9988
		22282	22283	22284	22280	22286	12.92	9.492	5.755	3.854	2.154
		22282	22283	22284	22280	22286	12.92	9.492	5.755	3.854	2.154

Table A.5: Experimental energies (cm^{-1}) and intensities ($L\ mol^{-1}\ cm^{-2}\ T^{-1}$) of the $[Dy^{III}(5LIO\text{-}1,2\text{-}HOPO)_2]^-$ MCD spectra over the temperature range 2-75 K. The intensity of transition to $^6H_{5/2}$ was too weak and not determined.

		Energy					Intensity				
	Ref[118]	2 K	10 K	25 K	50 K	75 K	2 K	10 K	25 K	50 K	75 K
$^6H_{9/2}$ + $^6F_{11/2}$	7832	7640.7	7641.3	7626.8	7628.0	7616.5	-20.78	-17.79	-14.58	-6.801	-5.597
		7697.0	7697.2	7693.9	7693.7	7693.1	-156.9	-148.3	-107.9	-71.04	-51.74
		7751.3	7751.1	7755.0	7756.0	7755.8	-121.8	-99.65	-83.23	-56.44	-36.82
		7799.6	7800.0	7801.0	7801.7	7801.4	-363.2	-342.45	-211.2	-115.4	-78.57
		7869.9	7870.3	7869.3	7868.5	7869.5	-190.4	-159.4	-121.5	-66.13	-46.31
		7923.8	7921.0	7926.2	7923.6	7922.8	-58.72	-55.67	-33.64	-29.92	-15.87
		7967.0	7962.3	7977.2	7966.3	7963.7	-51.73	-48.46	-25.49	-16.34	-15.25
		8025.4	8023.2	8029.8	8018.6	8031.2	-11.52	-12.09	-8.554	-5.658	-3.545
		8102.6	8103.7	8108.0	8103.7	8103.2	-42.02	-36.60	-29.48	-20.57	-7.215
$^6H_{7/2}$ + $^6F_{9/2}$	9196	-	-	8972.2	8975.8	8972.6	-	-	-3.328	-3.993	-5.618
		9019.1	9020.8	9021.1	9022.8	9023.3	27.86	21.95	13.67	9.665	6.402
		9081.0	9082.0	9104.9	9108.1	9111.4	-1.859	-2.004	-6.64	-10.98	-13.75
		9161.8	9161.4	9160.4	9157.2	9154.7	36.68	35.82	28.21	16.03	14.56
		9200.5	9202.1	9200.8	9185.1	9181.9	24.78	21.98	13.89	9.922	8.020
		9274.7	9275.9	9276.0	9275.1	9273.5	19.52	19.44	13.59	6.533	3.621
		9334.7	9338.3	9343.9	9351.5	9360.5	27.46	25.10	12.48	8.960	13.25
		9463.2	9466.3	9467.9	9477.5	-	-4.797	-3.084	-2.666	-1.423	-
$^6F_{7/2}$	11131	11010	11006	11003	11005	11004	-3.779	-2.953	-4.354	-7.168	-7.124
		11041	11037	11053	11048	11045	2.990	2.468	-3.984	-9.535	-10.92
		11092	11091	11091	11091	11091	103.0	91.56	70.38	50.10	39.28
		11150	11149	11149	11148	11146	-5.881	-3.830	-1.917	-1.507	-1.525
		11182	11181	11182	11182	11182	53.86	52.21	38.47	25.92	19.83
		11227	11228	11227	11230	11226	9.991	7.659	5.814	4.305	2.912
$^6F_{5/2}$	12492	-	-	12389	12388	12388	-	-	-3.641	-10.22	-12.70
		12424	12424	12423	12424	12423	67.29	58.67	36.12	23.63	16.81
		12440	12437	12438	12439	12438	90.14	82.62	64.16	39.04	27.63
		12486	12483	12482	12482	12478	33.38	32.05	27.55	23.51	22.92
		12539	12540	12537	12541	12538	11.87	10.32	7.512	3.960	3.752
$^6F_{3/2}$	13278	-	-	13228	13228	13226	-	-	-2.078	-5.189	-5.956
		13267	13266	13267	13266	13268	35.61	31.78	25.88	16.71	12.80
		13283	13283	13285	13286	13284	28.18	25.22	16.86	12.62	10.30
$^4F_{9/2}$	21150	-	-	-	-	20912	-	-	-	-	-0.4746
		20960	20959	20961	20959	20951	1.694	1.782	1.193	0.7445	0.4496
		21059	21061	21057	21059	-	0.9125	1.105	0.4063	0.1352	-
		-	-	21080	21081	21083	-	-	-0.1876	-0.5265	-0.9792
		21123	21124	21124	21124	21123	10.54	10.05	6.645	4.372	2.877
		21201	21202	21198	21199	21196	3.565	3.270	2.975	1.757	1.655
$^4I_{15/2}$	22217	21970	21970	21971	21971	21973	17.18	16.39	11.38	7.153	4.493
		22267	22269	22267	22273	22272	8.696	7.895	7.064	3.338	2.491

Table A.6: Total coefficients of the M_J projections of the RASSI coupled wave function for the optimised Dy$^{\mathrm{III}}$ complexes.

Kramers Doublet	Energy (cm^{-1})	Dy$^{\mathrm{III}}$-2LI-*a*-D$_2$	Energy (cm^{-1})	Dy$^{\mathrm{III}}$-2LI-*a*-S$_4$
1	0	$0.75\vert\pm15/2>$; $0.18\vert\pm7/2>$	0	$0.77\vert\pm15/2>$; $0.19\vert\pm7/2>$
2	48.55	$0.26\vert\pm5/2>$; $0.22\vert\pm3/2>$; $0.14\vert\pm9/2>$; $0.13\vert\pm7/2>$; $0.11\vert\pm11/2>$; $0.10\vert\pm1/2>$	56.301	$0.52\vert\pm5/2>$; $0.29\vert\pm3/2>$; $0.10\vert\pm11/2>$
3	55.661	$0.26\vert\pm5/2>$; $0.24\vert\pm9/2>$; $0.14\vert\pm15/2>$; $0.11\vert\pm1/2>$	63.978	$0.44\vert\pm9/2>$; $0.22\vert\pm1/2>$; $0.20\vert\pm7/2>$; $0.15\vert\pm15/2>$
4	106.612	$0.45\vert\pm9/2>$; $0.44\vert\pm7/2>$	115.833	$0.49\vert\pm7/2>$; $0.43\vert\pm9/2>$
5	137.527	$0.41\vert\pm11/2>$; $0.17\vert\pm3/2>$; $0.15\vert\pm13/2>$; $0.15\vert\pm5/2>$	138.087	$0.53\vert\pm11/2>$; $0.17\vert\pm13/2>$; $0.17\vert\pm5/2>$; $0.13\vert\pm3/2>$
6	210.805	$0.48\vert\pm13/2>$; $0.28\vert\pm11/2>$; $0.14\vert\pm3/2>$	219.002	$0.61\vert\pm13/2>$; $0.21\vert\pm11/2>$; $0.11\vert\pm3/2>$
7	234.618	$0.29\vert\pm1/2>$; $0.22\vert\pm13/2>$; $0.14\vert\pm3/2>$; $0.12\vert\pm5/2>$	278.878	$0.46\vert\pm3/2>$; $0.24\vert\pm5/2>$; $0.17\vert\pm11/2>$; $0.13\vert\pm13/2>$
8	303.766	$0.48\vert\pm13/2>$; $0.28\vert\pm11/2>$; $0.14\vert\pm3/2>$	283.227	$0.76\vert\pm1/2>$; $0.12\vert\pm9/2>$; $0.12\vert\pm7/2>$

Table A.7: Total coefficients of the M_J projections of the RASSI coupled wave function for the optimised Dy$^{\mathrm{III}}$ complexes.

Kramers Doublet	Energy (cm^{-1})	Dy$^{\mathrm{III}}$-5LIO-*g-trans*	Energy (cm^{-1})	Dy$^{\mathrm{III}}$-5LIO-*g-cis*
1	0	$0.41\vert\pm9/2>$; $0.30\vert\pm13/2>$; $0.12\vert\pm15/2>$	0	$0.76\vert\pm15/2>$; $0.12\vert\pm11/2>$
2	10.543	$0.60\vert\pm11/2>$; $0.12\vert\pm9/2>$; $0.10\vert\pm7/2>$	12.433	$0.44\vert\pm1/2>$; $0.29\vert\pm3/2>$; $0.11\vert\pm5/2>$
3	84.507	$0.39\vert\pm7/2>$; $0.16\vert\pm13/2>$; $0.12\vert\pm15/2>$	75.157	$0.36\vert\pm13/2>$; $0.20\vert\pm9/2>$; $0.18\vert\pm3/2>$; $0.12\vert\pm7/2>$; $0.10\vert\pm5/2>$
4	122.35	$0.23\vert\pm7/2>$; $0.22\vert\pm13/2>$; $0.19\vert\pm9/2>$; $0.13\vert\pm5/2>$	97.865	$0.37\vert\pm13/2>$; $0.22\vert\pm5/2>$; $0.16\vert\pm7/2>$; $0.13\vert\pm11/2>$
5	153.229	$0.57\vert\pm5/2>$; $0.11\vert\pm7/2>$	137.131	$0.24\vert\pm9/2>$; $0.20\vert\pm11/2>$; $0.17\vert\pm7/2>$; $0.14\vert\pm5/2>$; $0.12\vert\pm1/2>$
6	202.406	$0.62\vert\pm3/2>$; $0.16\vert\pm1/2>$	195.805	$0.29\vert\pm1/2>$; $0.26\vert\pm3/2>$; $0.16\vert\pm9/2>$; $0.14\vert\pm7/2>$
7	247.007	$0.50\vert\pm1/2>$; $0.15\vert\pm15/2>$; $0.13\vert\pm3/2>$	226.982	$0.34\vert\pm5/2>$; $0.33\vert\pm7/2>$; $0.11\vert\pm11/2>$; $0.10\vert\pm3/2>$
8	292.705	$0.43\vert\pm15/2>$; $0.16\vert\pm13/2>$; $0.15\vert\pm11/2>$	291.217	$0.35\vert\pm11/2>$; $0.29\vert\pm9/2>$; $0.20\vert\pm13/2>$

Table A.8: Crystal field parameters to describe the J = 15/2 ground-state multiplet splitting of Dy$^{\text{III}}$. The parameters are calculated for the optimised structures by decoupling of the wave function in terms of Extended Stevens operators and are given in cm^{-1}. These parameters result in a recovery factor of the crystal field matrix of 97.05 %, 97.18 % 96.59 % and 96.25 %, respectively.

		Dy$^{\text{III}}$-2LI-*a*-D$_2$	Dy$^{\text{III}}$-2LI-*a*-S$_4$	Dy$^{\text{III}}$-5LIO-*g*-*trans*	Dy$^{\text{III}}$-5LIO-*g*-*cis*
k	q	B_k^q	B_k^q	B_k^q	B_k^q
2	-2	-0.00004	-0.00033	0.00321	-0.00077
2	-1	0.00018	-0.00029	-1.05442	-1.64086
2	0	-0.51880	-0.58877	-0.17129	-0.27034
2	1	0.00003	-0.00001	-0.00228	-0.00052
2	2	0.28870	0.00150	-1.12960	0.81781
4	-4	-0.00001	0.01130	-0.00004	0.00001
4	-3	0.00000	0.00005	0.04180	0.03811
4	-2	0.00000	0.00001	0.00008	0.00002
4	-1	0.00000	0.00001	-0.01976	-0.01327
4	0	-0.00098	-0.00092	0.00494	-0.00427
4	1	0.00000	0.00000	-0.00012	-0.00001
4	2	-0.00917	-0.00004	-0.01901	-0.02352
4	3	0.00001	-0.00003	0.00026	0.00004
4	4	0.04209	-0.04173	0.00558	-0.00710
6	-6	0.00000	0.00000	0.00000	0.00000
6	-5	0.00000	0.00000	-0.00081	0.00021
6	-4	0.00000	0.00008	0.00000	0.00000
6	-3	0.00000	0.00000	-0.00030	0.00012
6	-2	0.00000	0.00000	0.00000	0.00000
6	-1	0.00000	0.00000	-0.00013	0.00014
6	0	-0.00005	-0.00005	0.00000	0.00000
6	1	0.00000	0.00000	0.00000	0.00000
6	2	-0.00003	0.00000	-0.00013	-0.00015
6	3	0.00000	0.00000	0.00000	0.00000
6	4	0.00013	-0.00013	0.00005	0.00009
6	5	0.00000	0.00000	0.00000	0.00000
6	6	0.00014	0.00000	0.00023	-0.00031

Extended Stevens operators (ESO) of the ground multiplet are calculated by SINGLE_-ANISO within MOLCAS 8.0. The decoupling of the wave function is in terms of the ESO Crystal-Field Hamiltonian:

$$H_{CF} = \sum_{k-2,4,6} \sum_{q=-k,k} [B_k^q O_k^q] \tag{A.1}$$

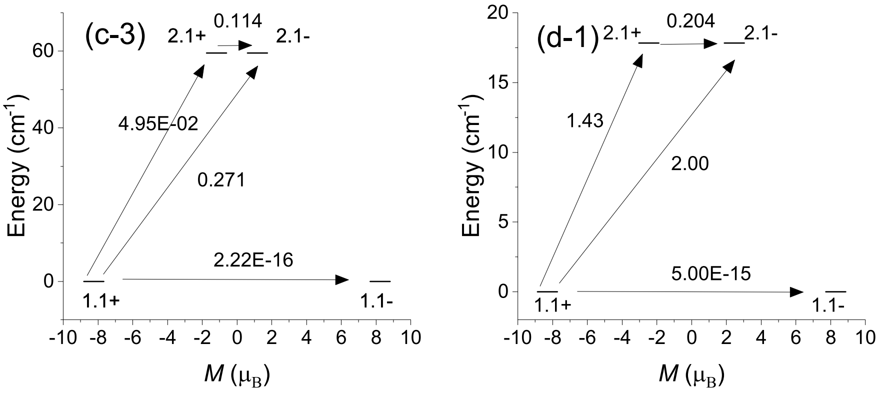

Figure A.9: *Ab initio* predicted relaxation pathways of the crystal structures of (c) Dy^{III}-2LI and (d) Dy^{III}-5LIO. The corresponding numbers at each arrow indicate the mean average matrix elements $[(|\mu_x|+|\mu_y|+|\mu_z|)/3]$ that connect the stationary points. A given relaxation pathway is expected to be relevant above a factor of around 10^{-1}-10^{-3}.

Table A.9: *Ab initio* predicted relaxation pathways of all calculated Dy^{III} complexes. Listed are the first excitation energies, absolute magnetic moments (stationary points) of the states and the mean average matrix elements $[(|\mu_x|+|\mu_y|+|\mu_z|)/3]$ that connect the stationary points. A given relaxation pathway is expected to be relevant above a factor of around 10^{-1}-10^{-3}.

	Dy^{III}-2LI			Dy^{III}-5LIO	
	(c-1)	(c-2)	(c-3)	(d-1)	(d-2)
EES1-EGS (cm^{-1})	80.54	82.96	59.54	17.82	36.55
|M| (1.1)	8.95	9.09	8.24	8.29	9.15
|M| (2.2)	3.43	5.73	1.18	2.45	3.59
1.1+ → 1.1− (QTM)	0.00	0.00	0.00	0.00	0.00
1.1+ → 2.1+ (thermal)	0.79	0.58	0.05	1.43	0.27
1.1+ → 2.1− (Orbach/Raman)	0.74	0.21	0.27	2.00	0.30
2.1+ → 2.1− (TA-QTM)	0.27	0.13	0.11	0.20	0.03

Table A.10: *Ab initio* calculated excitation energies, g-tensors, magnetic axis orientations, and total coefficients of the M_J projections of the RASSI coupled wave function of the doublets of the first two doublets of the remaining Tb^{III} crystal structures.

	Doublets	Energy [cm^{-1}]	g-tensors gx	gy	gz	∠D1-Dy-DX °	Total coefficients of the M_J projections of functionthe RASSI coupled wave
(a-1)	Tb^{III}-2LI (Type A)						
	1	0.000/ 8.133	0.000	0.000	14.6211	-	0.57|±6>; 0.21|±4>; 0.11|±2>/ 0.68|±6>; 0.16|±4>
	2	29.490/ 55.856	0.000	0.000	9.6272	22.3	0.37|±5>; 0.31|±3>; 0.20|±1>/ 0.65|±5>; 0.16|±2>; 0.11|±3>
(a-2)	Tb^{III}-2LI[a] (Type A)						
	1	0.000/ 2.898	0.000	0.000	15.9450	-	0.73|±6>; 0.19|±4>/ 0.79|±6>; 0.16|±4>
	2	44.175/ 61.818	0.000	0.000	11.0712	24.1	0.49|±5>; 0.28|±3>; 0.14|±1>/ 0.73|±5>; 0.18|±2>
(a-3)	Tb^{III}-2LI (Type B)						
	1	0.000/ 9.000	0.0000	0.0000	15.4563	-	0.65|±6>; 0.20|±4>/ 0.78|±6>; 0.17|±4>
	2	44.013	-	-	-	-	0.34|±3>; 0.29|±5>; 0.18|±1>; 0.16|0>
	3	79.029/ 94.452	0.0000	0.0000	6.8173	82.5	0.38|±5>; 0.36|±3>; 0.12|±1>/ 0.27|±1>; 0.25|±2>; 0.23|0>; 0.15|±6>
(b-1)	Tb^{III}-5LIO[b]						
	1	0.000/ 0.415	0.0000	0.0000	17.4955	-	0.94|±6>/ 0.94|±6>
	2	68.621/ 70.078	0.0000	0.0000	17.5321	89.3	0.61|±1>; 0.19|±3>/ 0.44|±2>; 0.35|0>; 0.10|±1>
(b-2)	Tb^{III}-5LIO[c]						
	1	0.000/ 0.344	0.0000	0.0000	17.8574	-	0.99|±6>/ 1.00|±6>
	2	57.496/ 57.558	0.000	0.0000	17.5679	84.7	0.78|±1>; 0.12|±3>/ 0.48|0>; 0.39|±2>

[a] Two independent complex molecules are present in the asymmetric unit of the type A crystal structures. In the CIF file the labels of this molecule appear with an "a" in the notation to distinguish it from the other molecule, *e.g.* O1' appears as O1a'. [b] Calculations were carried out using the coordinates from the previously published Eu^{III}-5LIO crystal structure.[71] [c] Calculations were carried out using the coordinates from the previously published Gd^{III}-5LIO crystal structure.[72]

Table A.11: *Ab initio* calculated excitation energies, g-tensors, magnetic axis orientations, and total coefficients of the M_J projections of the RASSI coupled wave function of the doublets of the first two doublets of the remaining Dy^{III} crystal structures.

	Doublets	Energy	g-tensors			∠D1-Dy-DX °	Total coefficients of the M_J projections of the RASSI coupled wave function
		[cm^{-1}]	gx	gy	gz		
(c-1)	Dy^{III}-2LI (Type A)						
	1	0.000	0.0494	0.9761	17.9039	-	0.80|±15/2>
	2	80.544	0.6432	3.6560	13.0830	58.3	0.25|±9/2>; 0.17|±7/2>; 0.13|±11/2>; 0.12|±5/2>; 0.11|±13/2>; 0.11|±1/2>
(c-2)	Dy^{III}-2LI[a] (Type A)						
	1	0.000	0.0311	0.6303	18.1827	-	0.80|±15/2>
	2	82.957	0.5768	1.0871	16.3512	45.5	0.24|±13/2>; 0.24|±9/2>; 0.20|±11/2>
(c-3)	Dy^{III}-2LI (Type B)						
	1	0.000	1.0006	1.6009	16.4739	-	0.74|±15/2>; 0.21|±7/2>
	2	59.543	11.0495	7.5633	2.3655	3.14	0.51|±5/2>; 0.29|±3/2>
(d-1)	Dy^{III}-5LIO[b]						
	1	0.000	0.7791	2.8529	16.5771	-	0.71|±15/2>
	2	17.822	0.9833	2.2310	15.6135	71.7	0.24|±1/2>; 0.21|±3/2>; 0.20|±5/2>; 0.13|±15/2>; 0.10|±7/2>
(d-2)	Dy^{III}-5LIO[c]						
	1	0.000	0.1101	0.4429	18.3100	-	0.81|±15/2>
	2	36.549	0.0663	0.6558	17.3249	65.5	0.21|±5/2>; 0.20|±3/2>; 0.19|±7/2>; 0.16|±1/2>

[a] Two independent complex molecules are present in the asymmetric unit of the type A crystal structures. In the CIF file the labels of this molecule appear with an "a" in the notation to distinguish it from the other molecule, *e.g.* O1' appears as O1a'. [b] Calculations were carried out using the coordinates from the previously published Eu^{III}-5LIO crystal structure in.[71] [c] Calculations were carried out using the coordinates from the previously published Gd^{III}-5LIO crystal structure.[72]

Table A.12: Energies of the $^7F_6$ multiplet splitting and total coefficients of the M_J projections of the RASSI coupled wave function using the different crystal structure coordinates of Tb^{III}-2LI.

WF	Energy (cm^{-1})	Tb^{III}-2LI (a-1)	Energy (cm^{-1})	Tb^{III}-2LI (a-2)	Energy (cm^{-1})	Tb^{III}-2LI (a-3)
1	0.000	0.57|±6>; 0.21|±4>; 0.11|±2>	0.000	0.73|±6>; 0.19|±4>	0.000	0.65|±6>; 0.20|±4>
2	8.133	0.68|±6>; 0.16|±4>	2.898	0.79|±6>; 0.16|±4>	9.000	0.78|±6>; 0.17|±4>
3	29.49	0.37|±5>; 0.31|±3>; 0.20|±1>	44.175	0.49|±5>; 0.28|±3>; 0.14|±1>	44.013	0.34|±3>; 0.29|±5>; 0.18|±1>; 0.16|0>
4	55.856	0.65|±5>; 0.16|±2>; 0.11|±3>	61.818	0.73|±5>; 0.18|±2>	79.029	0.38|±5>; 0.36|±3>; 0.12|±1>
5	81.555	0.36|±4>; 0.20|±6>; 0.12|±5>; 0.12|±3>; 0.12|±1>	91.369	0.46|±4>; 0.17|±6>; 0.10|±1>	94.452	0.27|±1>; 0.25|±2>; 0.23|0>; 0.15|±6>
6	101.082	0.27|±4>; 0.23|±3>; 0.18|0>; 0.13|±5>	116.464	0.28|±3>; 0.27|±5>; 0.17|±0>; 0.13|±2>	135.401	0.45|±2>; 0.15|±6>; 0.14|±4>; 0.12|0>; 0.10|±1>
7	111.295	0.30|±2>; 0.19|±1>; 0.17|±6>; 0.12|0>; 0.11|±5>; 0.11|±3>	124.625	0.49|±3>; 0.42|±2>	137.808	0.41|±1>; 0.31|±5>; 0.22|±2>
8	124.121	0.24|±4>; 0.23|±1>; 0.17|±6>; 0.13|±2>; 0.12|±3>; 0.10|0>	130.437	0.37|±1>; 0.31|±4>; 0.17|±6>	172.024	0.60|±1>; 0.18|±5>; 0.10|±4>
9	134.073	0.21|±5>; 0.21|±2>; 0.20|±3>; 0.18|±1>; 0.17|±4>	140.177	0.38|±4>; 0.23|±3>; 0.22|±2>	181.376	0.34|0>; 0.32|±2>; 0.12|±5>
10	276.421	0.32|±3>; 0.28|±2>; 0.20|±1>	284.141	0.79|±2>; 0.14|±0>	318.707	0.59|±3>; 0.27|±5>
11	284.835	0.38|±2>; 0.26|±1>; 0.18|±4>; 0.13|±5>	290.301	0.68|±1>; 0.25|±3>	322.25	0.55|±4>; 0.23|±2>
12	290.584	0.38|±3>; 0.33|0>; 0.13|±1>	312.577	0.47|±1>; 0.23|±3>; 0.10|±5>	337.909	0.51|±3>; 0.24|±5>; 0.11|±4>
13	299.15	0.37|±1>; 0.22|±4>; 0.17|±2>; 0.10|±5>; 0.10|0>	317.624	0.46|±0>; 0.25|±4>; 0.11|±3>	342.332	0.55|±4>; 0.26|±2>

Table A.13: Energies of the $^7\mathrm{F}_6$ multiplet splitting and total coefficients of the M_J projections of the RASSI coupled wave function using the different crystal structure coordinates of Tb$^{\mathrm{III}}$-5LIO.

WF	Energy (cm^{-1})	Tb$^{\mathrm{III}}$-5LIO (b-1)	Energy (cm^{-1})	Tb$^{\mathrm{III}}$-5LIO (b-2)
1	0.000	0.94|±6>	0.000	0.99|±6>
2	0.415	0.94|±6>	0.344	1.00|±6>
3	68.621	0.61|±1>; 0.19|±3>	57.496	0.78|±1>; 0.12|±3>
4	70.078	0.44|±2>; 0.35|±0>; 0.10|±1>	57.558	0.48|0>; 0.39|±2>
5	101.188	0.87|±5>; 0.11|±3>	167.282	0.43|±3>; 0.24|±1>; 0.16|±5>
6	102.695	0.78|±5>; 0.17|±3>	171.895	0.51|±2>; 0.20|±4>; 0.13|±5>; 0.11|±1>
7	180.781	0.76|±4>; 0.19|±2>	224.174	0.71|±5>; 0.20|±2>
8	190.671	0.70|±4>; 0.18|±2>	229.961	0.67|±5>; 0.10|±1>
9	218.690	0.70|±3>; 0.19|±1>	273.694	0.48|±4>; 0.25|±3>; 0.14|±5>
10	248.361	0.69|±2>; 0.19|±4>	313.639	0.42|±3>; 0.20|0>; 0.12|±5>; 0.12|±2>; 0.11|±4>
11	255.889	0.54|±3>; 0.31|±1>; 0.13|±5>	337.026	0.67|±4>; 0.20|±1>
12	346.577	0.70|±1>; 0.24|±3>	463.814	0.42|±3>; 0.37|±1>
13	350.151	0.43|±0>; 0.42|±2>; 0.14|±4>	465.133	0.41|±2>; 0.25|±4>; 0.17|0>; 0.13|±3>

Table A.14: Energies of the $^{6}H_{15/2}$ multiplet splitting and total coefficients of the M_J projections of the RASSI coupled wave function using the different crystal structure coordinates of Dy^{III}-2LI.

Kramers Doublet	Energy (cm^{-1})	Dy^{III}-2LI (c-1)	Energy (cm^{-1})	Dy^{III}-2LI (c-2)	Energy (cm^{-1})	Dy^{III}-2LI (c-3)
1	0.000	0.80|±15/2>	0	0.80|±15/2>	0.000	0.74|±15/2>; 0.21|±7/2>
2	80.544	0.25|±9/2>; 0.17|±7/2>; 0.13|±11/2>; 0.12|±5/2>; 0.11|±13/2>; 0.11|±1/2>	82.957	0.24|±13/2>; 0.24|±9/2>; 0.20|±11/2>	59.543	0.51|±5/2>; 0.29|±3/2>
3	90.053	0.26|±5/2>; 0.19|±3/2>; 0.13|±9/2>; 0.12|±7/2>; 0.11|±11/2>	104.413	0.24|±7/2>; 0.18|±5/2>; 0.16|±3/2>; 0.12|±1/2>; 0.11|±11/2>; 0.11|±9/2>	70.536	0.40|±9/2>; 0.20|±7/2>; 0.20|±1/2>
4	144.543	0.35|±7/2>; 0.22|±9/2>; 0.16|±5/2>; 0.14|±11/2>	151.807	0.25|±7/2>; 0.22|±5/2>; 0.16|±11/2>	130.669	0.45|±7/2>; 0.43|±9/2>
5	177.911	0.27|±13/2>; 0.21|±11/2>; 0.14|±9/2>; 0.14|±3/2>	182.437	0.27|±13/2>; 0.25|±9/2>; 0.16|±7/2>; 0.14|±3/2>; 0.10|±1/2>	158.912	0.50|±11/2>; 0.18|±5/2>; 0.15|±13/2>; 0.15|±3/2>
6	261.749	0.44|±13/2>; 0.19|±5/2>; 0.17|±11/2>	263.643	0.30|±13/2>; 0.24|±5/2>; 0.20|±11/2>	252.175	0.57|±13/2>; 0.21|±11/2>; 0.13|±3/2>
7	337.427	0.40|±3/2>; 0.22|±1/2>; 0.16|±5/2>; 0.11|±11/2>	350.523	0.51|±3/2>; 0.23|±5/2>; 0.14|±11/2>	308.340	0.34|±1/2>; 0.20|±3/2>; 0.12|±13/2>; 0.12|±5/2>; 0.10|±11/2>
8	359.448	0.45|±1/2>; 0.14|±9/2>; 0.11|±11/2>; 0.11|±7/2>; 0.11|±3/2>	364.699	0.55|±1/2>; 0.19|±9/2>; 0.15|±7/2>	332.016	0.38|±1/2>; 0.22|±3/2>; 0.12|±5/2>

Table A.15: Energies of the ^{6}H$_{15/2}$ multiplet splitting and total coefficients of the M_J projections of the RASSI coupled wave function using the different crystal structure coordinates of Dy^{III}-5LIO.

Kramers Doublet	Energy (cm^{-1})	Dy^{III}-5LIO (d-1)	Energy (cm^{-1})	Dy^{III}-5LIO (d-2)
1	0.000	0.71|±15/2>	0.000	0.81|±15/2>
2	17.822	0.24|±1/2>; 0.21|±3/2>; 0.20|±5/2>; 0.13|±15/2>; 0.10|±7/2>	36.549	0.21|±5/2>; 0.20|±3/2>; 0.19|±7/2>; 0.16|±1/2>
3	68.949	0.28|±9/2>; 0.19|±13/2>; 0.18|±11/2>; 0.13|±7/2>; 0.12|±5/2>	149.849	0.29|±13/2>; 0.24|±9/2>; 0.14|±11/2>; 0.10|±1/2>
4	96.470	0.23|±13/2>; 0.21|±7/2>; 0.16|±11/2>; 0.11|±3/2>; 0.11|±1/2>;	184.934	0.26|±11/2>; 0.23|±7/2>; 0.15|±13/2>; 0.14|±1/2>
5	157.950	0.22|±9/2>; 0.16|±7/2>; 0.15|±1/2>; 0.14|±13/2>; 0.12|±11/2>; 0.12|±5/2>	269.719	0.27|±9/2>; 0.15|±11/2>; 0.15|±5/2>; 0.13|±3/2>; 0.12|±7/2>
6	249.595	0.24|±5/2>; 0.22|±3/2>; 0.20|±7/2>; 0.11|±9/2>	365.456	0.22|±11/2>; 0.21|±13/2>; 0.19|±9/2>; 0.14|±7/2>; 0.14|±5/2>
7	300.626	0.34|±1/2>; 0.25|±3/2>; 0.16|±5/2>; 0.11|±9/2>	397.144	0.20|±7/2>; 0.17|±11/2>; 0.16|±5/2>; 0.13|±13/2>; 0.13|±9/2>; 0.12|±3/2>
8	335.324	0.33|±11/2>; 0.26|±13/2>; 0.16|±9/2>; 0.11|±7/2>	476.031	0.45|±1/2>; 0.32|±3/2>; 0.16|±5/2>

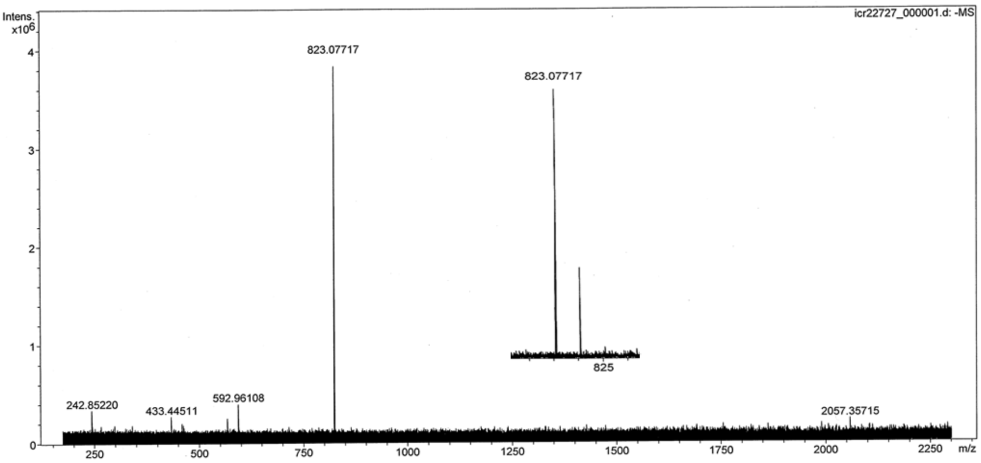

Figure A.10: Negative mass spectrum of Tb^{III}-2LI.

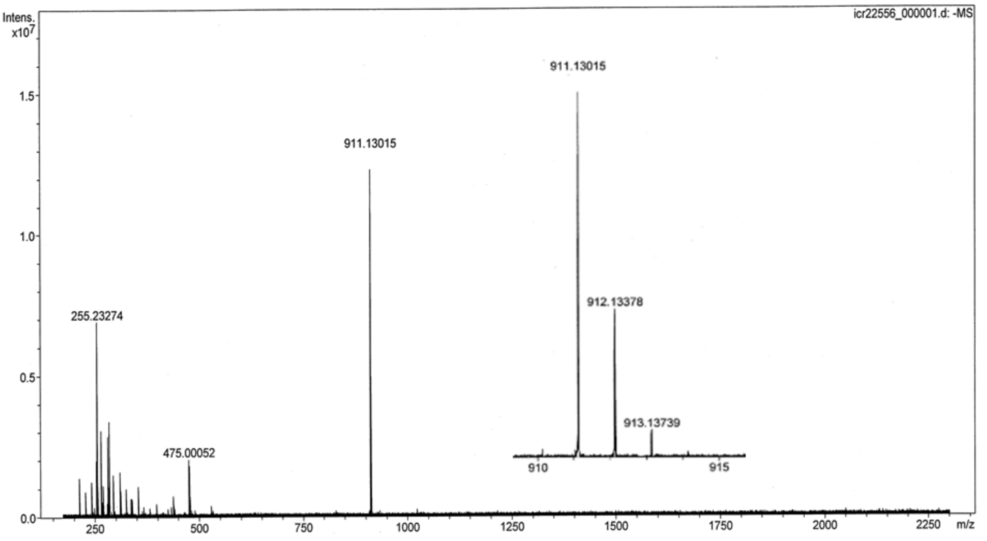

Figure A.11: Negative mass spectrum of Tb^{III}-5LIO.

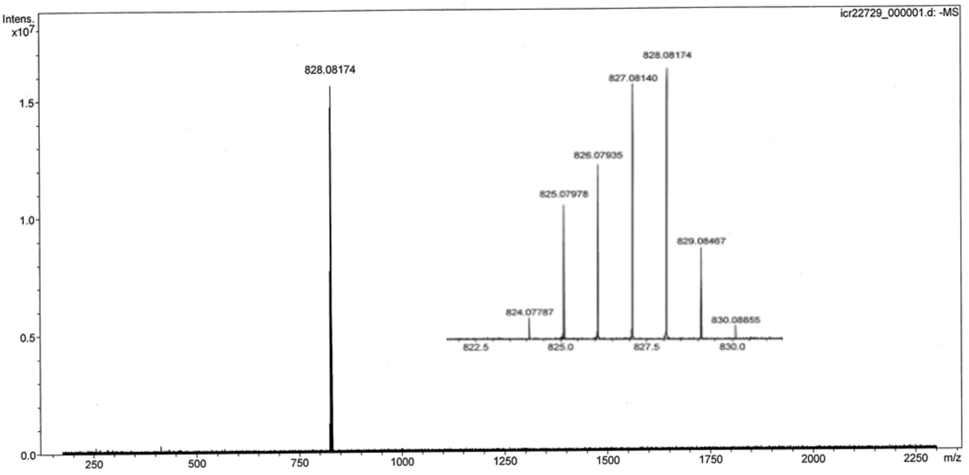

Figure A.12: Negative mass spectrum of Dy^{III}-2LI.

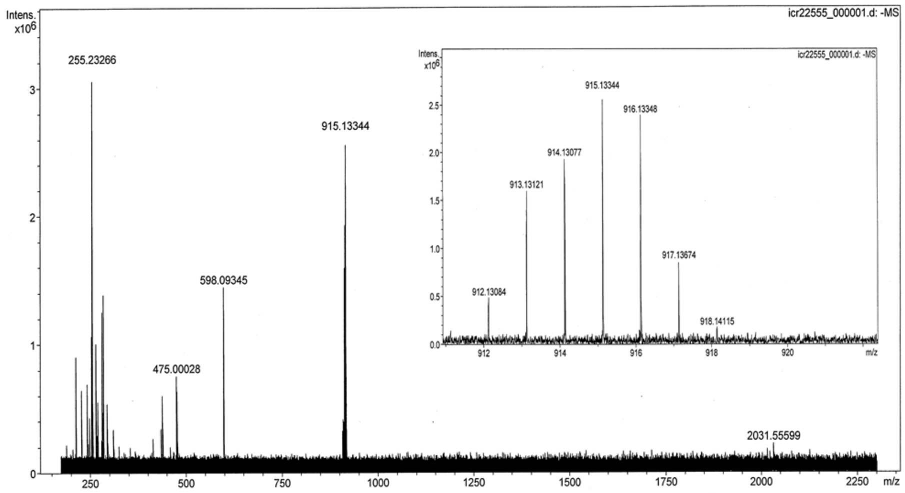

Figure A.13: Negative mass spectrum of Dy^{III}-5LIO.

A.2 Appendices to Chapter 5

Table A.16: Coordinates of the DFT optimised structures of Er$^{\mathrm{III}}$-2LI-*a*-D$_2$ and Er$^{\mathrm{III}}$-2LI-*a*-S$_4$.

Er$^{\mathrm{III}}$-2LI-*a*-D$_2$				Er$^{\mathrm{III}}$-2LI-*a*-S$_4$			
C	0.772	2.393	1.985	C	2.068	2.444	0.727
N	2.046	1.871	1.710	C	2.940	3.559	0.678
C	-3.088	-2.591	2.184	H	3.189	3.946	-0.302
C	-3.007	-3.753	2.942	C	3.439	4.119	1.845
H	-3.939	-4.193	3.269	H	4.103	4.975	1.791
C	-1.753	-4.309	3.243	C	3.092	3.587	3.098
H	-1.697	-5.215	3.838	H	3.456	3.996	4.030
C	-0.661	3.567	-2.859	C	2.245	2.489	3.176
H	0.313	3.981	-3.087	C	1.900	1.932	4.539
C	-1.837	4.155	-3.300	C	0.766	0.097	5.779
H	-1.797	5.060	-3.897	H	1.253	-0.883	5.862
C	-3.082	3.592	-2.975	H	1.072	0.711	6.631
H	-4.022	4.026	-3.285	C	-0.766	-0.097	5.779
C	3.157	3.608	2.888	H	-1.072	-0.711	6.631
H	4.094	4.048	3.199	H	-1.253	0.883	5.862
C	1.908	4.164	3.213	C	-1.900	-1.932	4.539
H	1.863	5.069	3.810	C	-2.245	-2.489	3.176
C	0.735	3.571	2.772	C	-3.092	-3.587	3.098
H	-0.241	3.979	3.000	H	-3.456	-3.996	4.030
C	3.196	-2.574	-2.271	C	-3.439	-4.119	1.845
C	3.121	-3.736	-3.029	H	-4.103	-4.975	1.791
H	4.055	-4.172	-3.356	C	-2.940	-3.559	0.678
C	1.870	-4.299	-3.330	H	-3.189	-3.946	-0.302
H	1.819	-5.206	-3.926	C	-2.068	-2.444	0.727
C	-0.588	-3.715	2.782	C	-2.444	2.068	-0.727
H	0.392	-4.123	2.991	C	-3.559	2.940	-0.678
C	0.702	-3.712	-2.869	H	-3.946	3.189	0.302
H	-0.276	-4.125	-3.079	C	-4.119	3.439	-1.845
C	-3.143	2.430	-2.215	H	-4.975	4.103	-1.791
C	3.223	2.447	2.128	C	-3.587	3.092	-3.098
N	2.024	-2.004	-1.833	H	-3.996	3.456	-4.030
C	0.747	-2.533	-2.084	C	-2.489	2.245	-3.176
N	-1.963	1.861	-1.797	C	-1.932	1.900	-4.539
N	-1.919	-2.015	1.746	C	-0.097	0.766	-5.779
C	-0.691	2.389	-2.073	H	-0.711	1.072	-6.631
C	-0.640	-2.537	1.997	H	0.883	1.253	-5.862
C	-4.454	-2.029	1.862	C	0.097	-0.766	-5.779
C	-4.499	1.861	-1.867	H	0.711	-1.072	-6.631
C	4.559	-2.005	-1.949	H	-0.883	-1.253	-5.862
C	4.583	1.885	1.780	C	1.932	-1.900	-4.539
H	3.680	0.281	0.950	C	2.489	-2.245	-3.176
H	3.663	-0.405	-1.104	C	3.587	-3.092	-3.098
O	5.588	-2.650	-2.290	H	3.996	-3.456	-4.030
O	5.615	2.535	2.103	C	4.119	-3.439	-1.845
O	-5.480	-2.680	2.203	H	4.975	-4.103	-1.791
O	-5.535	2.505	-2.190	C	3.559	-2.940	-0.678
H	-3.567	-0.424	1.017	H	3.946	-3.189	0.302
H	-3.588	0.262	-1.037	C	2.444	-2.068	-0.727
C	-5.712	-0.180	0.776	N	-1.218	-0.761	4.560
H	-5.793	0.803	1.258	H	-0.982	-0.378	3.636
H	-6.559	-0.795	1.092	N	1.218	0.761	4.560

C	5.807	-0.149	-0.863	H	0.982	0.378	3.636
H	5.883	0.834	-1.345	N	1.760	1.954	2.006
H	6.657	-0.760	-1.179	N	-1.760	-1.954	2.006
C	5.820	0.036	0.671	N	-0.761	1.218	-4.560
H	5.910	-0.947	1.151	H	-0.378	0.982	-3.636
H	6.673	0.651	0.971	N	0.761	-1.218	-4.560
C	-5.727	0.005	-0.757	H	0.378	-0.982	-3.636
H	-6.583	0.616	-1.058	N	-1.954	1.760	-2.006
H	-5.812	-0.978	-1.238	N	1.954	-1.760	-2.006
N	-4.514	0.667	-1.226	O	2.273	2.556	5.570
N	-4.487	-0.835	1.222	O	-2.273	-2.556	5.570
N	4.585	-0.810	-1.309	O	2.556	-2.273	-5.569
N	4.604	0.691	1.139	O	-2.556	2.273	-5.569
Er	0.047	-0.071	-0.044	Er	0.000	0.000	0.000
O	-1.943	0.706	-1.050	O	0.902	0.880	2.005
O	-1.919	-0.859	1.000	O	-0.902	-0.880	2.005
O	0.322	1.760	-1.584	O	1.526	1.840	-0.275
O	0.361	-1.901	1.491	O	-1.526	-1.840	-0.275
O	-0.238	1.758	1.497	O	1.840	-1.526	0.275
O	-0.257	-1.902	-1.578	O	-1.840	1.526	0.275
O	2.032	0.716	0.963	O	0.880	-0.902	-2.005
O	2.018	-0.848	-1.087	O	-0.880	0.902	-2.005

Table A.17: Coordinates of the DFT optimised structures of Dy^{III}-L^3-*a*-D_2 and Dy^{III}-L^3-*a*-S_4.

Dy^{III}-L^3-*a*-D_2				Dy^{III}-L^3-*a*-S_4			
C	-0.681	2.635	-2.164	C	0.695	2.883	-1.844
C	3.113	-2.548	-2.285	C	0.651	4.057	-2.580
C	3.069	-3.710	-3.082	H	-0.290	4.544	-2.809
H	4.018	-4.114	-3.418	C	1.865	4.614	-3.035
C	1.862	-4.314	-3.418	H	1.846	5.533	-3.612
H	1.849	-5.206	-4.036	C	3.074	3.989	-2.748
C	0.645	3.776	2.952	H	4.018	4.399	-3.088
H	-0.294	4.254	3.206	C	3.125	2.794	-2.003
C	1.862	4.313	3.418	C	4.470	2.180	-1.752
H	1.849	5.205	4.036	C	5.660	0.236	-0.732
C	3.070	3.710	3.082	H	5.738	-0.641	-1.392
H	4.018	4.114	3.418	H	6.525	0.878	-0.924
C	-3.070	3.710	-3.082	C	5.660	-0.240	0.731
H	-4.018	4.114	-3.418	H	6.524	-0.883	0.923
C	-1.862	4.314	-3.418	H	5.739	0.636	1.392
H	-1.849	5.205	-4.036	C	4.468	-2.184	1.752
C	-0.644	3.776	-2.952	C	3.123	-2.796	2.003
H	0.294	4.254	-3.206	C	3.071	-3.991	2.747
C	-3.113	-2.548	2.285	H	4.015	-4.402	3.088
C	-3.070	-3.710	3.082	C	1.862	-4.615	3.035
H	-4.018	-4.114	3.418	H	1.842	-5.534	3.612
C	-1.862	-4.314	3.418	C	0.649	-4.057	2.581
H	-1.849	-5.205	4.036	H	-0.293	-4.544	2.809
C	0.644	-3.776	-2.952	C	0.693	-2.884	1.844
H	-0.295	-4.254	-3.206	C	-0.693	1.845	2.884
C	-0.644	-3.776	2.952	C	-0.648	2.581	4.057
H	0.294	-4.254	3.206	H	0.293	2.809	4.544
C	3.113	2.548	2.285	C	-1.862	3.036	4.615
C	-3.113	2.548	-2.285	H	-1.842	3.613	5.534
C	-0.681	-2.635	2.164	C	-3.071	2.749	3.990
C	0.681	2.635	2.165	H	-4.015	3.090	4.401
C	0.681	-2.635	-2.164	C	-3.122	2.004	2.795
C	4.460	-1.979	-1.948	C	-4.468	1.754	2.183
C	4.460	1.979	1.948	C	-5.660	0.734	0.239
C	-4.460	-1.979	1.948	H	-6.524	0.927	0.881
C	-4.460	1.979	-1.948	H	-5.738	1.394	-0.638
H	-3.518	0.476	-0.965	C	-5.660	-0.729	-0.237
H	-3.518	-0.476	0.965	H	-6.525	-0.921	-0.880
O	-5.526	-2.531	2.340	H	-5.739	-1.389	0.639
O	-5.526	2.531	-2.340	C	-4.470	-1.750	-2.181
O	5.526	-2.531	-2.340	C	-3.125	-2.002	-2.794
O	5.526	2.531	2.340	C	-3.074	-2.746	-3.989
H	3.518	-0.476	-0.965	H	-4.018	-3.086	-4.400
H	3.518	0.476	0.965	C	-1.865	-3.034	-4.614
C	5.651	-0.135	-0.759	H	-1.846	-3.611	-5.533
H	5.734	0.825	-1.291	C	-0.652	-2.580	-4.057
H	6.511	-0.751	-1.036	H	0.289	-2.809	-4.544
C	-5.651	-0.135	0.759	C	-0.695	-1.844	-2.883
H	-5.734	0.825	1.290	N	4.461	-1.008	1.054
H	-6.511	-0.751	1.036	H	3.531	-0.676	0.777
C	-5.651	0.135	-0.759	N	4.461	1.004	-1.054

H	-5.734	-0.825	-1.290	H	3.532	0.674	-0.778
H	-6.511	0.751	-1.036	N	-4.460	1.056	1.007
C	5.651	0.135	0.759	H	-3.531	0.779	0.676
H	6.511	0.751	1.036	N	-4.462	-1.052	-1.005
H	5.734	-0.825	1.290	H	-3.532	-0.776	-0.674
N	4.449	0.841	1.189	O	5.532	2.719	-2.173
N	4.449	-0.841	-1.190	O	5.530	-2.723	2.172
N	-4.449	-0.841	1.189	O	-5.532	-2.170	-2.720
N	-4.449	0.841	-1.189	O	-5.530	2.175	2.722
Dy	0.000	0.000	0.000	Dy	0.000	0.000	0.000
O	1.815	0.879	1.067	O	1.836	1.091	-0.818
O	1.815	-0.879	-1.067	O	1.835	-1.092	0.818
O	-0.446	1.992	1.598	O	-0.429	2.205	-1.312
O	-0.446	-1.992	-1.598	O	-0.430	-2.204	1.312
O	0.446	1.992	-1.598	O	0.429	-1.312	-2.205
O	0.446	-1.992	1.598	O	0.430	1.312	2.205
O	-1.815	0.879	-1.067	O	-1.836	-0.817	-1.091
O	-1.815	-0.879	1.067	O	-1.835	0.819	1.092
C	-1.896	1.987	-1.826	C	1.751	-1.515	-2.791
C	1.896	1.987	1.826	H	2.003	-2.580	-2.789
C	1.896	-1.987	-1.826	H	1.772	-1.119	-3.811
C	-1.896	-1.987	1.826	H	2.432	-0.953	-2.158
C	-1.771	-2.544	-1.863	C	1.753	1.514	2.791
H	-1.825	-3.578	-1.508	H	2.006	2.578	2.789
H	-2.460	-1.919	-1.302	H	1.774	1.117	3.811
H	-1.990	-2.495	-2.934	H	2.434	0.952	2.158
C	-1.771	2.544	1.863	C	-1.751	2.792	-1.514
H	-1.825	3.578	1.508	H	-1.772	3.812	-1.118
H	-2.460	1.919	1.302	H	-2.003	2.790	-2.579
H	-1.990	2.495	2.934	H	-2.432	2.159	-0.952
C	1.771	-2.544	1.863	C	-1.753	-2.790	1.515
H	1.990	-2.495	2.934	H	-1.775	-3.810	1.118
H	1.825	-3.578	1.508	H	-2.005	-2.788	2.579
H	2.460	-1.919	1.302	H	-2.434	-2.157	0.953
C	1.771	2.544	-1.863	C	-1.912	-1.538	-2.225
H	1.990	2.495	-2.934	C	1.910	-2.227	1.539
H	1.825	3.578	-1.508	C	1.912	2.225	-1.539
H	2.460	1.919	-1.302	C	-1.910	1.540	2.226

Table A.18: Coordinates of the DFT optimised structures of Er^{III}-L^3-*a*-D_2 and Er^{III}-L^3-*a*-S_4.

Er^{III}-L^3-*a*-D_2				Er^{III}-L^3-*a*-S_4			
C	-0.652	2.626	-2.149	C	0.652	2.838	-1.864
C	3.085	-2.542	-2.280	C	0.592	4.030	-2.568
C	3.036	-3.706	-3.073	H	-0.357	4.484	-2.828
H	3.982	-4.114	-3.411	C	1.802	4.650	-2.945
C	1.826	-4.309	-3.402	H	1.772	5.585	-3.496
H	1.809	-5.203	-4.017	C	3.022	4.065	-2.619
C	0.611	3.769	2.932	H	3.962	4.520	-2.909
H	-0.330	4.247	3.180	C	3.088	2.854	-1.903
C	1.826	4.309	3.402	C	4.443	2.270	-1.629
H	1.809	5.203	4.017	C	5.649	0.282	-0.716
C	3.036	3.706	3.073	H	5.737	-0.550	-1.430
H	3.982	4.114	3.411	H	6.508	0.943	-0.863
C	-3.036	3.706	-3.073	C	5.649	-0.287	0.715
H	-3.982	4.114	-3.411	H	6.508	-0.948	0.861
C	-1.826	4.309	-3.402	H	5.738	0.546	1.429
H	-1.809	5.203	-4.017	C	4.441	-2.274	1.628
C	-0.611	3.769	-2.932	C	3.086	-2.856	1.903
H	0.330	4.247	-3.180	C	3.019	-4.068	2.619
C	-3.085	-2.542	2.280	H	3.959	-4.523	2.908
C	-3.036	-3.706	3.073	C	1.799	-4.651	2.945
H	-3.982	-4.114	3.411	H	1.768	-5.586	3.496
C	-1.826	-4.309	3.402	C	0.590	-4.030	2.568
H	-1.809	-5.203	4.017	H	-0.360	-4.483	2.829
C	0.611	-3.769	-2.932	C	0.650	-2.838	1.864
H	-0.330	-4.247	-3.180	C	-0.650	1.864	2.838
C	-0.611	-3.769	2.932	C	-0.589	2.569	4.030
H	0.330	-4.247	3.180	H	0.360	2.829	4.483
C	3.085	2.542	2.280	C	-1.799	2.946	4.651
C	-3.085	2.542	-2.280	H	-1.768	3.497	5.586
C	-0.652	-2.626	2.149	C	-3.019	2.621	4.067
C	0.652	2.626	2.149	H	-3.959	2.911	4.523
C	0.652	-2.626	-2.149	C	-3.086	1.905	2.855
C	4.433	-1.976	-1.947	C	-4.441	1.631	2.273
C	4.433	1.976	1.947	C	-5.649	0.718	0.285
C	-4.433	-1.976	1.947	H	-6.508	0.865	0.946
C	-4.433	1.976	-1.947	H	-5.737	1.432	-0.547
H	-3.496	0.469	-0.966	C	-5.649	-0.713	-0.284
H	-3.496	-0.469	0.966	H	-6.509	-0.859	-0.944
O	-5.497	-2.531	2.340	H	-5.738	-1.427	0.549
O	-5.497	2.531	-2.340	C	-4.443	-1.627	-2.271
O	5.497	-2.531	-2.340	C	-3.088	-1.902	-2.854
O	5.497	2.531	2.340	C	-3.022	-2.618	-4.066
H	3.496	-0.469	-0.966	H	-3.963	-2.907	-4.521
H	3.496	0.469	0.966	C	-1.802	-2.944	-4.650
C	5.629	-0.133	-0.759	H	-1.772	-3.495	-5.585
H	5.714	0.826	-1.289	C	-0.593	-2.568	-4.030
H	6.488	-0.752	-1.037	H	0.357	-2.829	-4.483
C	-5.629	-0.133	0.759	C	-0.652	-1.863	-2.838
H	-5.714	0.826	1.289	N	4.444	-1.061	0.995
H	-6.488	-0.752	1.037	H	3.516	-0.684	0.781

C	-5.629	0.133	-0.759	N	4.445	1.057	-0.996
H	-5.714	-0.826	-1.289	H	3.516	0.681	-0.782
H	-6.488	0.752	-1.037	N	-4.444	0.998	1.060
C	5.629	0.133	0.759	H	-3.515	0.783	0.683
H	6.488	0.752	1.037	N	-4.445	-0.994	-1.058
H	5.714	-0.826	1.289	H	-3.516	-0.780	-0.682
N	4.425	0.836	1.190	O	5.502	2.860	-1.983
N	4.425	-0.836	-1.190	O	5.500	-2.864	1.983
N	-4.425	-0.836	1.190	O	-5.502	-1.981	-2.861
N	-4.425	0.836	-1.190	O	-5.500	1.985	2.863
Er	0.000	0.000	0.000	Er	0.000	0.000	0.000
O	1.791	0.866	1.065	O	1.817	1.086	-0.800
O	1.791	-0.866	-1.065	O	1.816	-1.087	0.800
O	-0.469	1.979	1.577	O	-0.462	2.083	-1.422
O	-0.469	-1.979	-1.577	O	-0.464	-2.083	1.422
O	0.469	1.979	-1.577	O	0.462	-1.422	-2.083
O	0.469	-1.979	1.577	O	0.464	1.422	2.083
O	-1.791	0.866	-1.065	O	-1.817	-0.799	-1.086
O	-1.791	-0.866	1.065	O	-1.816	0.801	1.087
C	-1.869	1.978	-1.819	C	1.801	-1.789	-2.535
C	1.869	1.978	1.819	H	1.876	-2.876	-2.631
C	1.869	-1.978	-1.819	H	2.021	-1.304	-3.492
C	-1.869	-1.978	1.819	H	2.472	-1.428	-1.761
C	-1.797	-2.527	-1.837	C	1.803	1.787	2.535
H	-1.853	-3.560	-1.482	H	1.879	2.875	2.631
H	-2.481	-1.899	-1.273	H	2.023	1.303	3.492
H	-2.019	-2.476	-2.907	H	2.474	1.427	1.761
C	-1.796	2.527	1.837	C	-1.801	2.536	-1.787
H	-1.853	3.561	1.482	H	-2.021	3.493	-1.303
H	-2.481	1.899	1.273	H	-1.877	2.632	-2.875
H	-2.019	2.476	2.907	H	-2.473	1.762	-1.427
C	1.797	-2.527	1.837	C	-1.803	-2.534	1.788
H	2.019	-2.476	2.907	H	-2.023	-3.491	1.304
H	1.853	-3.560	1.482	H	-1.879	-2.630	2.876
H	2.481	-1.899	1.273	H	-2.474	-1.760	1.428
C	1.797	2.527	-1.837	C	-1.880	-1.503	-2.231
H	2.019	2.476	-2.907	C	1.879	-2.232	1.504
H	1.853	3.560	-1.482	C	1.880	2.231	-1.504
H	2.481	1.899	-1.273	C	-1.878	1.505	2.232

Table A.19: Coordinates of the DFT optimised structures of $\mathrm{Dy^{III}}$-$\mathrm{L^4}$ and $\mathrm{Er^{III}}$-$\mathrm{L^4}$.

$\mathrm{Dy^{III}}$-$\mathrm{L^4}$				$\mathrm{Er^{III}}$-$\mathrm{L^4}$			
C	0.796	2.409	1.956	C	-0.776	-2.411	1.925
C	0.672	3.747	2.359	C	-0.645	-3.750	2.318
H	-0.322	4.131	2.560	H	0.351	-4.133	2.511
C	1.799	4.580	2.413	C	-1.769	-4.587	2.373
H	1.682	5.621	2.701	H	-1.649	-5.629	2.654
C	3.050	4.105	2.032	C	-3.024	-4.114	2.002
H	3.905	4.766	1.963	H	-3.878	-4.777	1.934
C	4.552	2.407	1.070	C	-4.536	-2.413	1.057
C	4.552	-2.407	-1.070	C	-4.536	2.413	-1.057
C	3.050	-4.105	-2.032	C	-3.024	4.114	-2.002
H	3.905	-4.766	-1.963	H	-3.878	4.777	-1.934
C	1.799	-4.580	-2.413	C	-1.769	4.587	-2.373
H	1.682	-5.620	-2.701	H	-1.648	5.629	-2.654
C	0.672	-3.747	-2.359	C	-0.645	3.750	-2.318
H	-0.322	-4.131	-2.560	H	0.352	4.133	-2.511
C	0.796	-2.409	-1.956	C	-0.776	2.411	-1.925
C	-0.796	-2.409	1.956	C	0.776	2.411	1.925
C	-0.672	-3.747	2.359	C	0.645	3.751	2.318
H	0.322	-4.131	2.560	H	-0.352	4.133	2.511
C	-1.799	-4.580	2.413	C	1.769	4.587	2.373
H	-1.682	-5.621	2.701	H	1.648	5.629	2.654
C	-3.050	-4.105	2.032	C	3.024	4.114	2.002
H	-3.905	-4.766	1.963	H	3.878	4.777	1.934
C	-4.552	-2.407	1.070	C	4.536	2.413	1.057
C	-4.552	2.407	-1.070	C	4.536	-2.413	-1.057
C	-3.050	4.105	-2.032	C	3.024	-4.114	-2.002
H	-3.905	4.766	-1.963	H	3.878	-4.777	-1.934
C	-1.799	4.580	-2.413	C	1.769	-4.587	-2.373
H	-1.682	5.621	-2.701	H	1.649	-5.629	-2.654
C	-0.672	3.747	-2.359	C	0.645	-3.751	-2.318
H	0.322	4.131	-2.560	H	-0.351	-4.133	-2.511
C	-0.796	2.409	-1.956	C	0.776	-2.411	-1.925
N	4.991	-1.085	-1.039	N	-4.975	1.091	-1.032
H	4.691	-0.445	-1.761	H	-4.670	0.452	-1.754
N	4.991	1.085	1.039	N	-4.975	-1.091	1.032
H	4.691	0.445	1.761	H	-4.670	-0.452	1.754
N	-4.991	-1.085	1.039	N	4.975	1.091	1.032
H	-4.691	-0.445	1.761	H	4.670	0.452	1.754
N	-4.991	1.085	-1.039	N	4.975	-1.091	-1.032
H	-4.691	0.445	-1.761	H	4.670	-0.452	-1.754
O	5.255	3.290	0.515	O	-5.242	-3.295	0.503
O	5.255	-3.290	-0.515	O	-5.242	3.295	-0.504
O	-5.255	3.290	-0.515	O	5.242	-3.295	-0.503
O	-5.255	-3.290	0.515	O	5.242	3.295	0.504
Dy	0.000	0.000	0.000	Er	0.000	0.000	0.000
C	-2.110	-1.888	1.724	C	2.093	1.893	1.702
C	-2.110	1.888	-1.724	C	2.093	-1.893	-1.702
C	2.110	1.888	1.724	C	-2.093	-1.893	1.702
C	2.110	-1.888	-1.724	C	-2.093	1.893	-1.702
C	6.170	-0.728	-0.243	C	-6.154	0.729	-0.240
C	6.170	0.728	0.243	C	-6.154	-0.729	0.239
C	-6.170	-0.728	0.243	C	6.154	0.729	0.240
C	-6.170	0.728	-0.243	C	6.154	-0.729	-0.239

C	3.229	2.747	1.677	C	-3.209	-2.754	1.655
C	3.229	-2.747	-1.677	C	-3.209	2.754	-1.656
C	-3.229	-2.747	1.677	C	3.209	2.754	1.656
C	-3.229	2.747	-1.677	C	3.209	-2.754	-1.655
H	-6.198	1.432	0.594	H	6.184	-1.429	0.602
H	-7.101	0.894	-0.807	H	7.085	-0.898	-0.804
H	-7.101	-0.894	0.807	H	7.085	0.898	0.804
H	-6.198	-1.432	-0.594	H	6.184	1.429	-0.601
H	6.198	1.432	-0.594	H	-6.184	-1.429	-0.602
H	7.101	0.894	0.807	H	-7.085	-0.898	0.804
H	6.198	-1.432	0.594	H	-6.184	1.429	0.601
H	7.101	-0.894	-0.807	H	-7.085	0.898	-0.804
O	-0.259	-1.597	-1.711	O	0.273	1.591	-1.680
O	0.259	1.597	-1.711	O	-0.273	-1.591	-1.680
O	-0.259	1.597	1.711	O	0.273	-1.591	1.680
O	0.259	-1.597	1.711	O	-0.273	1.591	1.680
N	2.116	0.493	1.418	N	-2.100	-0.497	1.403
H	1.658	-0.125	2.097	H	-1.643	0.120	2.083
N	2.116	-0.493	-1.418	N	-2.100	0.497	-1.403
H	1.658	0.125	-2.097	H	-1.643	-0.120	-2.083
N	-2.116	0.493	-1.418	N	2.100	-0.497	-1.403
H	-1.658	-0.125	-2.097	H	1.643	0.120	-2.083
N	-2.116	-0.493	1.418	N	2.100	0.497	1.403
H	-1.658	0.125	2.097	H	1.643	-0.120	2.083
H	2.973	0.109	1.049	H	-2.957	-0.112	1.036
H	2.973	-0.109	-1.049	H	-2.957	0.112	-1.036
H	-2.973	-0.109	1.049	H	2.957	0.112	1.036
H	-2.973	0.109	-1.049	H	2.957	-0.112	-1.036

Table A.20: Crystal field parameters to describe the J = 15/2 ground-state multiplet splitting of Dy$^{\mathrm{III}}$ optimised structures. The parameters are calculated for the optimised structures by decoupling of the wave function in terms of Extended Stevens operators and are given in cm^{-1}. These parameters result in a recovery factor of the crystal field matrix of 97.05 %, 97.18 %, 98.51%, 98.56% and 97.73 %, respectively.

		Dy$^{\mathrm{III}}$-2LI-a-D$_2$	Dy$^{\mathrm{III}}$-2LI-a-S$_4$	Dy$^{\mathrm{III}}$-L^3-a-D$_2$	Dy$^{\mathrm{III}}$-L^3-a-S$_4$	Dy$^{\mathrm{III}}$-L^4
k	q	B_k^q	B_k^q	B_k^q	B_k^q	B_k^q
2	-2	-0.00004	-0.00033	-0.00046	0.00355	-0.00015
2	-1	0.00018	-0.00029	0.00048	-0.00003	-0.01428
2	0	-0.51880	-0.58877	-3.86548	-4.04727	-3.75472
2	1	0.00003	-0.00001	0.00062	0.00469	-0.00061
2	2	0.28870	0.00150	0.40986	0.01516	4.13212
4	-4	-0.00001	0.01130	-0.00002	-0.02172	0.00001
4	-3	0.00000	0.00005	0.00001	-0.00001	0.00017
4	-2	0.00000	0.00001	0.00000	-0.00002	0.00000
4	-1	0.00000	0.00001	-0.00001	0.00002	0.00025
4	0	-0.00098	-0.00092	0.00408	0.00412	0.00670
4	1	0.00000	0.00000	-0.00001	-0.00009	0.00000
4	2	-0.00917	-0.00004	0.00903	0.00024	0.03263
4	3	0.00001	-0.00003	0.00000	0.00011	0.00002
4	4	0.04209	-0.04173	0.02597	0.01596	-0.02748
6	-6	0.00000	0.00000	0.00000	0.00000	0.00000
6	-5	0.00000	0.00000	0.00000	0.00000	0.00001
6	-4	0.00000	0.00008	0.00000	0.00005	0.00000
6	-3	0.00000	0.00000	0.00000	0.00000	0.00000
6	-2	0.00000	0.00000	0.00000	0.00000	0.00000
6	-1	0.00000	0.00000	0.00000	0.00000	0.00000
6	0	-0.00005	-0.00005	-0.00004	-0.00004	0.00001
6	1	0.00000	0.00000	0.00000	0.00000	0.00000
6	2	-0.00003	0.00000	0.00004	0.00000	-0.00034
6	3	0.00000	0.00000	0.00000	0.00000	0.00000
6	4	0.00013	-0.00013	-0.00014	-0.00013	0.00054
6	5	0.00000	0.00000	0.00000	0.00000	0.00000
6	6	0.00014	0.00000	-0.00010	0.00000	-0.00002

Table A.21: Crystal field parameters to describe the J = 15/2 ground-state multiplet splitting of Er$^{\text{III}}$ optimised structures. The parameters are calculated for the optimised structures by decoupling of the wave function in terms of Extended Stevens operators and are given in cm^{-1}. These parameters result in a recovery factor of the crystal field matrix of 99.38 %, 99.31 %, 99.67 %, 99.49 % and 99.04 %, respectively.

		Er$^{\text{III}}$-2LI-a-D$_2$	Er$^{\text{III}}$-2LI-a-S$_4$	Er$^{\text{III}}$-L^3-a-D$_2$	Er$^{\text{III}}$-L^3-a-S$_4$	Er$^{\text{III}}$-L^4
k	q	B_q^k	B_q^k	B_q^k	B_q^k	B_q^k
2	-2	-0.00308	0.00103	-0.00621	-0.00627	-0.00333
2	-1	-0.00146	-0.00008	0.00214	-0.02855	0.00036
2	0	0.12613	0.10874	-0.95260	1.76371	-1.66942
2	1	0.00243	-0.00087	-0.00139	-0.02658	-0.00023
2	2	-0.31044	0.00087	-2.42830	-0.00498	-1.45355
4	-4	-0.00002	-0.02289	-0.00010	-0.01752	-0.00025
4	-3	-0.00032	-0.00008	0.00000	-0.00011	0.00000
4	-2	0.00006	0.00001	0.00001	0.00006	-0.00003
4	-1	-0.00002	0.00000	0.00001	0.00019	0.00000
4	0	-0.00247	0.00070	-0.00248	-0.00288	0.00362
4	1	0.00003	-0.00002	0.00002	0.00018	0.00001
4	2	0.02005	0.00001	0.00475	0.00004	-0.01042
4	3	-0.00003	-0.00012	-0.00005	-0.00028	0.00001
4	4	-0.00726	-0.02024	-0.02047	-0.00757	-0.04195
6	-6	0.00000	0.00000	0.00000	0.00000	0.00000
6	-5	-0.00002	0.00000	0.00000	0.00001	0.00000
6	-4	0.00000	0.00017	0.00000	-0.00018	0.00000
6	-3	-0.00001	0.00000	0.00000	0.00000	0.00000
6	-2	0.00000	0.00000	0.00000	0.00000	0.00000
6	-1	0.00000	0.00000	0.00000	0.00001	0.00000
6	0	0.00000	-0.00010	0.00003	-0.00006	-0.00009
6	1	0.00000	0.00000	0.00000	0.00001	0.00000
6	2	0.00046	0.00000	0.00034	0.00000	-0.00043
6	3	0.00000	0.00000	0.00000	0.00000	0.00000
6	4	0.00052	0.00026	0.00003	-0.00005	0.00056
6	5	0.00000	0.00000	0.00000	0.00000	0.00000
6	6	0.00054	0.00000	0.00041	0.00000	0.00018

Table A.22: Fitted (exp) and ligand field theory calculated (calc) energies (cm^{-1}) for Er^{III}-2LI, Er^{III}-L^3 and Dy^{III}-L^3.

	Er^{III}-2LI	Er^{III}-2LI-a-S_4	Er^{III}-L^3	Er^{III}-L^3-a-S_4		Dy^{III}-L^3	Dy^{III}-L^3-a-S_4
	(exp)	(calc)	(exp)	(calc)		(exp)	(calc)
4I(11/2)	10295.92759	10195.372	10223.65516	10140.729	6F(11/2)	7796.42885	7777.583
	10303.53869	10195.372	10251.88953	10140.729		7874.14776	7835.304
	10329.15245	10213.262	10270.71598	10151.802		7933.37033	7923.678
	10363.35966	10213.262	10305.8144	10151.802		8049.109	7937.556
	10384.30535	10244.401	10336.62888	10187.226		8240.24555	7983.728
	10406.96849	10244.401	10365.15049	10187.226			8038.464
		10257.005		10238.802			8062.108
		10257.005		10238.802			8092.664
		10258.841		10313.319			8124.285
		10258.841		10313.319			8133.275
		10271.516		10333.159			8242.549
		10271.516		10333.159			
	12371.62433	12448.918	12451.83548	12512.138	6F(9/2)	8991.82275	9168.32
4I(9/2)	12569.25187	12448.918	12485.6377	12512.138		9077.8151	9279.203
	12725.85315	12567.551	12533.34446	12529.354		9121.59821	9294.269
	12743.71468	12567.551	12555.84141	12529.354		9217.00011	9312.36
	12770.79701	12580.476	12585.28556	12544.172		9303.52794	9401.167
		12580.476		12544.172		9398.63086	9416.204
		12666.814		12613.451		9452.46851	9416.704
		12666.814		12613.451		9542.51651	9558.948
		12712.136		12690.218			9566.503
		12712.136		12690.218			
	15326.61802	15638.526	15179.30912	15483.88	6H(5/2)		10250.052
4F(9/2)	15373.03992	15638.526	15285.1809	15483.88			10528.496
	15404.10686	15681.233	15311.44292	15614.186			10701.735
	15457.59877	15681.233	15340.5416	15614.186			
	15498.7146	15686.262	15398.84378	15718.982	6F(7/2)	11086.10996	11238.385
			15448.70748	15718.982		11127.60559	11249.87
		15686.262		15770.574		11175.47994	11290.993
		15722.624		15770.574		11243.91521	11306.624
		15722.624		15783.383			
		15743.701		15783.383	6F(5/2)	12474.43541	12655.006
		15743.701	18380.78912	18769.522		12543.37786	12659.125
4S(3/2)	18471.32083	18857.912	18451.74561	18769.522		12600.41798	12695.581
	18510.68928	18857.912	18494.71601	18934.67			
		18877.243	18533.53506	18934.67	6F(3/2)	13323.80148	13462.162
		18877.243				13371.90152	13466.468
	19155.41602	19332.27	19109.16909	19320.336			
2H(11/2)	19230.48664	19332.27	19142.60847	19320.336			
	19313.14353	19354.1	19190.54365	19352.82			
	19384.25823	19354.1	19238.86569	19352.82			
		19362.137	19276.56281	19370.39			
		19362.137	19315.99117	19370.39			
		19395.726		19385.935			
		19395.726		19385.935			
		19397.879		19400.803			
		19397.879		19400.803			
		19437.425		19405.776			
		19437.425		19405.776			
	20559.05849	21024.58	20458.6024	20856.155			
	20614.00575	21024.58	20532.49984	20856.155			
4F(7/2)	20683.60503	21041.572	20587.18844	21017.526			
	20721.70895	21041.572	20685.11421	21017.526			
		21097.146		21095.651			
		21097.146		21095.651			
		21109.103		21200.932			
		21109.103		21200.932			

4F(5/2)	22303.01428	22651.107	22182.26119	22580.973
+	22636.61792	22651.107	22228.08127	22580.973
4F(3/2)		22670.555	22507.22905	22597.87
		22670.555	22534.78102	22597.87
		22676.524	22630.78934	22687.232
		22676.524	22656.91699	22687.232
		23055.852		22987.373
		23055.852		22987.373
		23063.093		23150.438
		23063.093		23150.438
2H(9/2)	24619.79855	24700.462	24448.10638	24700.71
	24668.07422	24700.462	24570.08478	24700.71
	24810.03651	24793.958	24705.39256	24767.238
	24853.45812	24793.958		24767.238
		24809.188		24805.698
		24809.188		24805.698
		24880.434		24833.978
		24880.434		24833.978
		24920.32		24888.633
		24920.32		24888.633
4G(11/2)	26358.07322	26884.661	26287.90203	26913.707
	26438.89481	26884.661	26317.87416	26913.707
	26504.16001	26901.379	26364.59546	26921.154
	26546.69509	26901.379	26393.30169	26921.154
	26575.92392	26932.717	26416.75862	26948.846
	26639.35129	26932.717	26462.80196	26948.846
		26984.585	26489.25375	26957.54
		26984.585	26511.32209	26957.54
		27017.145	26534.07683	27001.232
		27017.145	26560.50136	27001.232
		27060.528	26590.21371	27004.425
		27060.528		27004.425

Table A.23: Energies of the ^{6}H$_{15/2}$ multiplet splitting and total coefficients of the M_J projections of the RASSI coupled wave function of the optimised Dy$^{\text{III}}$ complexes of L^3 and L^4.

KD	E [cm^{-1}]	Dy$^{\text{III}}$-L^3-a-D$_2$	E [cm^{-1}]	Dy$^{\text{III}}$-L^3-a-S$_4$	E [cm^{-1}]	Dy$^{\text{III}}$-L^4
1	0.00	$0.98\vert\pm15/2>$	0.00	$1.00\vert\pm15/2>$	0.00	$0.78\vert\pm13/2>$; $0.22\vert\pm9/2>$
2	159.79	$0.96\vert\pm13/2>$	175.67	$1.00\vert\pm13/2>$	33.20	$0.51\vert\pm15/2>$; $0.43\vert\pm11/2>$
3	238.00	$0.96\vert\pm11/2>$	248.79	$1.00\vert\pm11/2>$	94.94	$0.45\vert\pm15/2>$; $0.32\vert\pm11/2>$; $0.21\vert\pm7/2>$
4	311.57	$0.94\vert\pm9/2>$	320.67	$0.99\vert\pm9/2>$	232.80	$0.44\vert\pm9/2>$; $0.31\vert\pm5/2>$; $0.16\vert\pm13/2>$
5	402.18	$0.93\vert\pm7/2>$	419.94	$0.97\vert\pm7/2>$	417.16	$0.35\vert\pm7/2>$; $0.26\vert\pm3/2>$; $0.16\vert\pm11/2>$; $0.11\vert\pm9/2>$
6	501.55	$0.79\vert\pm5/2>$; $0.18\vert\pm3/2>$	522.63	$0.82\vert\pm5/2>$; $0.17\vert\pm3/2>$	594.32	$0.38\vert\pm5/2>$; $0.24\vert\pm7/2>$; $0.17\vert\pm9/2>$; $0.12\vert\pm3/2>$
7	671.74	$0.81\vert\pm3/2>$; $0.18\vert\pm5/2>$	699.45	$0.82\vert\pm3/2>$; $0.18\vert\pm5/2>$	686.83	$0.76\vert\pm1/2>$; $0.20\vert\pm3/2>$
8	717.93	$0.96\vert\pm1/2>$	750.03	$0.96\vert\pm1/2>$	776.54	$0.37\vert\pm3/2>$; $0.29\vert\pm5/2>$; $0.14\vert\pm7/2>$; $0.14\vert\pm1/2>$

Table A.24: Energies of the $^4I_{15/2}$ multiplet splitting and total coefficients of the M_J projections of the RASSI coupled wave function of the optimised Er^{III} complexes of 2LI.

KD	E [cm^{-1}]	Er^{III}-2LI-*a*-D$_2$	E [cm^{-1}]	Er^{III}-2LI-*a*-S$_4$
1	0.00	0.43|±15/2>; 0.26|±11/2>; 0.12|±7/2>; 0.11|±5/2>	0.00	0.83|±7/2>
2	38.64	0.33|±5/2>; 0.17|±13/2>; 0.16|±3/2>; 0.15|±15/2>	34.15	0.74|±5/2>; 0.26|±3/2>
3	62.23	0.33|±3/2>; 0.20|±9/2>; 0.17|±7/2>; 0.10|±1/2>	60.36	0.92|±9/2>
4	95.34	0.47|±1/2>; 0.24|±3/2>	96.59	0.91|±15/2>
5	196.04	0.30|±7/2>; 0.26|±1/2>; 0.21|±9/2>	203.92	0.94|±11/2>
6	242.83	0.60|±13/2>; 0.32|±9/2>	247.77	0.70|±3/2>; 0.23|±5/2>
7	292.81	0.28|±15/2>; 0.26|±11/2>; 0.20|±7/2>; 0.17|±5/2>	293.01	0.90|±1/2>
8	319.61	0.31|±11/2>; 0.20|±3/2>; 0.16|±5/2>; 0.10|±9/2>	326.06	0.98|±13/2>

Table A.25: Energies of the $^4I_{15/2}$ multiplet splitting and total coefficients of the M_J projections of the RASSI coupled wave function of the optimised Er^{III} complexes of ligands L^3 and L^4.

KD	E [cm^{-1}]	Er^{III}-L^3-*a*-D$_2$	E [cm^{-1}]	Er^{III}-L^3-*a*-S$_4$	E [cm^{-1}]	Er^{III}-L^4
1	0.00	0.62|±15/2>; 0.21|±11/2>	0.00	0.74|±5/2>; 0.24|±3/2>	0.00	0.74|±15/2>; 0.19|±11/2>
2	33.87	0.41|±1/2>; 0.25|±5/2>; 0.16|±3/2>; 0.10|±9/2>	12.21	0.71|±7/2>; 0.25|±1/2>	122.10	0.75|±9/2>; 0.12|±13/2>
3	43.10	0.73|±13/2>	40.79	0.73|±3/2>; 0.24|±5/2>	151.19	0.56|±7/2>; 0.14|±5/2>; 0.10|±3/2>; 0.10|±1/2>
4	67.41	0.22|±15/2>; 0.21|±13/2>; 0.19|±7/2>; 0.12|±11/2>; 0.12|±3/2>	59.47	0.54|±1/2>; 0.26|±7/2>; 0.19|±9/2>	188.82	0.45|±5/2>; 0.22|±7/2>; 0.15|±3/2>; 0.14|±9/2>
5	147.84	0.44|±11/2>; 0.24|±9/2>; 0.11|±3/2>	132.20	0.79|±9/2>; 0.20|±1/2>	293.51	0.72|±11/2>; 0.23|±15/2>
6	230.54	0.32|±3/2>; 0.32|±1/2>; 0.22|±5/2>; 0.11|±7/2>	224.14	0.97|±15/2>	317.59	0.83|±13/2>
7	272.04	0.33|±9/2>; 0.25|±7/2>; 0.19|±11/2>; 0.15|±1/2>	267.37	0.97|±11/2>	509.59	0.48|±3/2>; 0.34|±5/2>; 0.13|±1/2>
8	368.07	0.31|±5/2>; 0.30|±7/2>; 0.16|±9/2>; 0.16|±3/2>	375.34	0.99|±13/2>	585.16	0.72|±1/2>; 0.20|±3/2>

Bibliography

[1] Sessoli, R.; Gatteschi, D.; Caneschi, A.; Novak, M. A. Magnetic bistability in a metal-ion cluster. *Nature* **1993**, *365*, 141–143.

[2] Sessoli, R.; Tsai, H. L.; Schake, A. R.; Wang, S.; Vincent, J. B.; Folting, K.; Gatteschi, D.; Christou, G.; Hendrickson, D. N. High-spin molecules: [Mn12O12(O2CR)16(H2O)4]. *J. Am. Chem. Soc.* **1993**, *115*, 1804–1816.

[3] Christou, G.; Gatteschi, D.; Hendrickson, D. N.; Sessoli, R. Single-molecule magnets. *Mrs Bulletin* **2000**, *25*, 66–71.

[4] Schake, A. R.; Tsai, H.-L.; Webb, R. J.; Folting, K.; Christou, G.; Hendrickson, D. N. High-Spin Molecules: Iron(III) Incorporation into [Mn12O12(O2CMe)16(H2O)4] To Yield [Mn8Fe4O12(O2CMe)16(H2O)4] and Its Influence on the S = 10 Ground State of the Former. *Inorg. Chem.* **1994**, *33*, 6020–6028.

[5] Long, J.; Guari, Y.; Ferreira, R. A. S.; Carlos, L. D.; Larionova, J. Recent advances in luminescent lanthanide based Single-Molecule Magnets. *Coord. Chem. Rev.* **2018**, *363*, 57–70.

[6] Krivorotov, I. N.; Emley, N. C.; Garcia, A. G.; Sankey, J. C.; Kiselev, S. I.; Ralph, D. C.; Buhrman, R. A. Temperature dependence of spin-transfer-induced switching of nanomagnets. *Phys. Rev. Lett.* **2004**, *93*, 1677–1686.

[7] Jacobs, I. S.; Bean, C. P.; Rado, G. T.; Suhl, H. Magnetism, vol. 3. *Academic, New York* **1963**, 271–348.

[8] Feltham, H. L.; Brooker, S. Review of purely 4f and mixed-metal nd-4f single-molecule magnets containing only one lanthanide ion. *Coord. Chem. Rev.* **2014**, *276*, 1–33.

[9] Ako, A. M.; Hewitt, I. J.; Mereacre, V.; Clérac, R.; Wernsdorfer, W.; Anson, C. E.; Powell, A. K. A Ferromagnetically Coupled Mn19 Aggregate with a RecordS=83/2 Ground Spin State. *Angew. Chem.* **2006**, *118*, 5048–5051.

[10] Neese, F.; Pantazis, D. A. What is not required to make a single molecule magnet. *Faraday Discuss.* **2011**, *148*, 229–238.

[11] Guo, F. S.; Day, B. M.; Chen, Y. C.; Tong, M. L.; Mansikkamäki, A.; Layfield, R. A. A Dysprosium Metallocene Single-Molecule Magnet Functioning at the Axial Limit. *Angew. Chem. Int. Ed.* **2017**, *56*, 11445–11449.

[12] Abragam, A.; Bleaney, B. *Electron Paramagnetic Resonance of Transition Ions | A. Abragam and B. Bleaney | 9780199651528 | Oxford University Press Canada*; Oxford University Press: Oxford, UK, 1970.

[13] Rinehart, J. D.; Long, J. R. Exploiting single-ion anisotropy in the design of f-element single-molecule magnets. *Chem. Sci.* **2011**, *2*, 2078.

[14] Ishikawa, N.; Sugita, M.; Ishikawa, T.; Koshihara, S. Y.; Kaizu, Y. Lanthanide double-decker complexes functioning as magnets at the single-molecular level. *J. Am. Chem. Soc.* **2003**, *125*, 8694–8695.

[15] Gómez-Coca, S.; Aravena, D.; Morales, R.; Ruiz, E. Large magnetic anisotropy in mononuclear metal complexes. *Coord. Chem. Rev.* **2015**, *289-290*, 379–392.

[16] Ding, Y. S.; Chilton, N. F.; Winpenny, R. E.; Zheng, Y. Z. On Approaching the Limit of Molecular Magnetic Anisotropy: A Near-Perfect Pentagonal Bipyramidal Dysprosium(III) Single-Molecule Magnet. *Angew. Chem. Int. Ed.* **2016**, *55*, 16071–16074.

[17] Ishikawa, N.; Sugita, M.; Tanaka, N.; Ishikawa, T.; Koshihara, S. Y.; Kaizu, Y. Upward temperature shift of the intrinsic phase lag of the magnetization of bis(phthalocyaninato)terbium by ligand oxidation creating an S = 1/2 spin. *Inorg. Chem.* **2004**, *43*, 5498–5500.

[18] Benelli, C.; Gatteschi, D. Magnetism of lanthanides in molecular materials with transition-metal ions and organic radicals. *Chem. Rev.* **2002**, *102*, 2369–2387.

[19] Upadhyay, A.; Singh, S. K.; Das, C.; Mondol, R.; Langley, S. K.; Murray, K. S.; Rajaraman, G.; Shanmugam, M. Enhancing the effective energy barrier of a Dy(III) SMM using a bridged diamagnetic Zn(II) ion. *Chem. Commun.* **2014**, *50*, 8838–8841.

[20] Sun, W.-B.; Yan, P.-F.; Jiang, S.-D.; Wang, B.-W.; Zhang, Y.-Q.; Li, H.-F.; Chen, P.; Wang, Z.-M.; Gao, S. High symmetry or low symmetry, that is the question: high performance Dy(III) single-ion magnets by electrostatic potential design. *Chem. Sci.* **2016**, *7*, 684–691.

[21] Ida, Y.; Ghosh, S.; Ghosh, A.; Nojiri, H.; Ishida, T. Strong Ferromagnetic Exchange Interactions in Hinge-like Dy(O2Cu)2 Complexes Involving Double Oxygen Bridges. *Inorg. Chem.* **2015**, *54*, 9543–9555.

[22] Mori, F.; Nyui, T.; Ishida, T.; Nogami, T.; Choi, K.-Y.; Nojiri, H. Oximate-Bridged Trinuclear Dy-Cu-Dy Complex Behaving as a Single-Molecule Magnet and Its Mechanistic Investigation. *J. Am. Chem. Soc.* **2006**, *128*, 1440–1441.

[23] Raptopoulou, C. P.; Sanakis, Y.; Psycharis, V.; Pissas, M. Zig-zag [MnIII4] clusters from polydentate Schiff base ligands. *Polyhedron* **2013**, *64*, 181–188.

[24] Bender, M.; Comba, P.; Demeshko, S.; Großhauser, M.; Müller, D.; Wadepohl, H. Theoretically Predicted and Experimentally Observed Relaxation Pathways of two Heterodinuclear 3d-4f Complexes. *Z. Anorg. Allg. Chem.* **2015**, *641*, 2291–2299.

[25] Malmqvist, P. Å.; Roos, B. O.; Schimmelpfennig, B. The restricted active space (RAS) state interaction approach with spin-orbit coupling. *Chem. Phys. Lett.* **2002**, *357*, 230–240.

[26] Rudowicz, C. Transformation relations for the conventional Okq and normalised O'kq Stevens operator equivalents with k= 1 to 6 and -k=< q=< k. *Journal of Physics C: Solid State Physics* **1985**, *18*, 1415.

[27] Ungur, L.; den Heuvel, W.; Chibotaru, L. F. Ab initio investigation of the non-collinear magnetic structure and the lowest magnetic excitations in dysprosium triangles. *New J. Chem.* **2009**, *33*, 1224–1230.

[28] Lines, M. E. Orbital angular momentum in the theory of paramagnetic clusters. *J. Chem. Phys.* **1971**, *55*, 2977–2984.

[29] Palii, A. V.; Tsukerblat, B. S.; Coronado, E.; Clemente-Juan, J. M.; Borrás-Almenar, J. J. Orbitally dependent magnetic coupling between cobalt (II) ions: The problem of the magnetic anisotropy. *J. Chem. Phys.* **2003**, *118*, 5566–5581.

[30] Gingsberg, A. P. Magnetic exchange in transition metal complexes vi: Aspects of exchange coupling in magnetic cluster complexes. *Inorg. Chim. Acta Rev.* **1971**, *5*, 45–68.

[31] Lines, M. E. Magnetic Properties of Co Cl 2 and Ni Cl 2. *Phys. Rev.* **1963**, *131*, 546.

[32] van Leusen, J.; Speldrich, M.; Schilder, H.; Kögerler, P. Comprehensive insight into molecular magnetism via CONDON: Full vs. effective models. *Coord. Chem. Rev.* **2015**, *289-290*, 137–148.

[33] Hiller, M.; Krieg, S.; Ishikawa, N.; Enders, M. Ligand-Field Energy Splitting in Lanthanide-Based Single-Molecule Magnets by NMR Spectroscopy. *Inorg. Chem.* **2017**, *56*, 15285–15294.

[34] Comba, P.; Enders, M.; Grosshauser, M.; Hiller, M.; Müller, D.; Wadepohl, H. Solution and solid state structures and magnetism of a series of linear trinuclear compounds with a hexacoordinate LnIII and two terminal NiII centers. *Dalton Trans.* **2016**, *46*, 138–149.

[35] Marx, R.; Moro, F.; Dörfel, M.; Ungur, L.; Waters, M.; Jiang, S.-D.; Orlita, M.; Taylor, J.; Frey, W.; Chibotaru, L. F.; Others, Spectroscopic determination of crystal field splittings in lanthanide double deckers. *Chemical Science* **2014**, *5*, 3287–3293.

[36] Pedersen, K. S.; Ungur, L.; Sigrist, M.; Sundt, A.; Schau-Magnussen, M.; Vieru, V.; Mutka, H.; Rols, S.; Weihe, H.; Waldmann, O.; Others, Modifying the properties of 4f single-ion magnets by peripheral ligand functionalisation. *Chem. Sci.* **2014**, *5*, 1650–1660.

[37] Comba, P.; Enders, M.; Grosshauser, M.; Hiller, M.; Klingeler, R.; Meyer, F.; Müller, D.; Powell, A. K.; Wadepohl, H. Magnetic anisotropy in linear trinuclear transition metal – lanthanide complexes. *Inorg. Chem., in preparation*

[38] Comba, P.; Großhauser, M.; Klingeler, R.; Koo, C.; Lan, Y.; Müller, D.; Park, J.; Powell, A.; Riley, M. J.; Wadepohl, H. Magnetic Interactions in a Series of Homodinuclear Lanthanide Complexes. *Inorg. Chem.* **2015**, *54*, 11247–11258.

[39] Abragam, A.; Pryce, M.-H. L. Theory of the nuclear hyperfine structure of paramagnetic resonance spectra in crystals. *Proc. R. Soc. Lond. A* **1951**, *205*, 135–153.

[40] Heß, B. A.; Marian, C. M.; Wahlgren, U.; Gropen, O. A mean-field spin-orbit method applicable to correlated wavefunctions. *Chem. Phys. Lett.* **1996**, *251*, 365–371.

[41] Schimmelpfennig, B.; Maron, L.; Wahlgren, U.; Teichteil, C.; Fagerli, H.; Gropen, O. On the combination of ECP-based CI calculations with all-electron spin-orbit mean-field integrals. *Chem. Phys. Lett.* **1998**, *286*, 267–271.

[42] Barra, A.-L.; Caneschi, A.; Cornia, A.; Gatteschi, D.; Gorini, L.; Heiniger, L.-P.; Sessoli, R.; Sorace, L. The origin of transverse anisotropy in axially symmetric single molecule magnets. *J. Am. Chem. Soc.* **2007**, *129*, 10754–10762.

[43] Görller-Walrand, C.; Fluyt, L. *Handbook on the Physics and Chemistry of Rare Earths*; Elsevier B.V., 2010; Vol. 40; Chapter 244.

[44] Görller-Walrand, C.; Binnemans, K. In *Handbook on the Physics and Chemistry of Rare Earths*; Gschneidner, K. A. J., Erying, L., Eds.; Elsevier Science B.V., 1996; Vol. 23; Chapter 155, pp 121–283.

[45] Stevens, K. W. H. Matrix elements and operator equivalents connected with the magnetic properties of rare earth ions. *Proc. Phys. Soc., London* **1952**, *65A*, 209–215.

[46] Elliott, R. J.; Stevens, K. W. H. The theory of the magnetic properties of rare earth salts: cerium ethyl sulfate. *Proc. R. Soc. London, Ser. A: Mathematical, Physical and Engineering Sciences* **1952**, *215*, 437–453.

[47] Elliott, R. J.; Stevens, K. W. H. The magnetic properties of certain rare earth ethyl sulfates. *Proc. R. Soc. London, Ser. A: Mathematical, Physical and Engineering Sciences* **1953**, *219*, 387–404.

[48] Elliott, R. J.; Stevens, K. W. H. The theory of magnetic-resonance experiments on salts of the rare earths. *Proc. R. Soc. London, Ser. A: Mathematical, Physical and Engineering Sciences* **1953**, *218*, 553–566.

[49] Wybourne, B. G. *Spectroscopic Properties of Rare Earths*; John Wiley & Sons, Inc.: New York, 1965.

[50] Newman, D. J. Theory of lanthanide crystal fields. *Adv. Phys.* **1971**, *20*, 197–256.

[51] Dieke, G. H. Spectra and energy levels of rare earth ions in crystals. **1968**,

[52] Ofelt, G. S. Structure of the f6 configuration with application to rare earth ions. *J. Chem. Phys.* **1963**, *38*, 2171–2180.

[53] Judd, B. R. Optical absorption intensities of rare earth ions. *Phys. Rev.* **1962**, *127*, 750–761.

[54] Sorace, L.; Gatteschi, D. In *Lanthanides and Actinides in Molecular Magnetism*; Layfield, R. A., Murugesu, M., Eds.; Wiley-VCH Verlag GmbH & Co. KGaA, 2015; pp 1–25.

[55] Baldov\'\i, J. J.; Borrás-Almenar, J. J.; Clemente-Juan, J. M.; Coronado, E.; Gaita-Ariño, A. Modeling the properties of lanthanoid single-ion magnets using an effective point-charge approach. *Dalton Trans.* **2012**, *41*, 13705–13710.

[56] Jø rgensen, C. K.; Pappalardo, R.; Schmidtke, H.-H. Do the "Ligand Field'" Parameters in Lanthanides Represent Weak Covalent Bonding? *J. Chem. Phys.* **1963**, *39*, 1422–1430.

[57] Urland, W. On the ligand-field potential for f electrons in the angular overlap model. *Chem. Phys.* **1976**, *14*, 393–401.

[58] Flanagan, B. M.; Bernhardt, P. V.; Krausz, E. R.; Lüthi, S. R.; Riley, M. J. A ligand-field analysis of the trensal (h3trensal = 2,2',2"-tris(salicylideneimino)triethylamine) ligand. An application of the angular overlap model to lanthanides. *Inorg. Chem.* **2002**, *41*, 5024–5033.

[59] Hartree, D. R. The wave mechanics of an atom with a non-coulomb central field. Part II. Some results and discussion. Mathematical Proceedings of the Cambridge Philosophical Society. 1928; pp 111–132.

[60] Reiher, M. Relativistic Douglas–Kroll–Hess theory. *Wiley Interdisciplinary Reviews: Computational Molecular Science* **2012**, *2*, 139–149.

[61] Douglas, M.; Kroll, N. M. Quantum electrodynamical corrections to the fine structure of helium. *Annals of Physics* **1974**, *82*, 89–155.

[62] Hess, B. A. Relativistic electronic-structure calculations employing a two-component no-pair formalism with external-field projection operators. *Phys. Rev. A* **1986**, *33*, 3742.

[63] Veryazov, V.; Widmark, P.-O.; Serrano-Andrés, L.; Lindh, R.; Roos, B. O. 2MOLCAS as a development platform for quantum chemistry software. *International journal of quantum chemistry* **2004**, *100*, 626–635.

[64] Karlström, G.; Lindh, R.; Malmqvist, P.-Å.; Roos, B. O.; Ryde, U.; Veryazov, V.; Widmark, P.-O.; Cossi, M.; Schimmelpfennig, B.; Neogrady, P.; Others, MOLCAS: a program package for computational chemistry. *Comput. Mater. Sci.* **2003**, *28*, 222–239.

[65] Aquilante, F.; De, V. L.; Ferre, N.; Ghigo, G.; Malmqvist, P.-A.; Neogrady, P.; Pedersen, T. B.; Pitonak, M.; Reiher, M.; Roos, B. O.; Serrano-Andres, L.; Urban, M.; Veryazov, V.; Lindh, R. MOLCAS 7: the next generation. *J. Comput. Chem.* **2010**, *31*, 224–247.

[66] Chibotaru, L. F.; Ungur, L. Ab initio calculation of anisotropic magnetic properties of complexes. I. Unique definition of pseudospin Hamiltonians and their derivation. *J. Chem. Phys.* **2012**, *137*, 64112.

[67] Chibotaru, L. F. Ab initio methodology for pseudospin Hamiltonians of anisotropic magnetic complexes. *Adv. Chem. Phys.* **2013**, *153*, 397–519.

[68] Daumann, L. J.; Tatum, D. S.; Andolina, C. M.; Pacold, J. I.; Dáléo, A.; Law, G. L.; Xu, J.; Raymond, K. N. Effects of Ligand Geometry on the Photophysical Properties of Photoluminescent Eu(III) and Sm(III) 1-Hydroxypyridin-2-one Complexes in Aqueous Solution. *Inorg. Chem.* **2016**, *55*, 114–124.

[69] Daumann, L. J.; Tatum, D. S.; Snyder, B. E.; Ni, C.; Law, G. L.; Solomon, E. I.; Raymond, K. N. New insights into structure and luminescence of EuIII and SmIII complexes of the 3,4,3-LI(1,2-HOPO) ligand. *J. Am. Chem. Soc.* **2015**, *137*, 2816–2819.

[70] Jamieson, E. R.; Eppley, H. J.; Geselbracht, M. J.; Johnson, A. R.; Reisner, B. A.; Smith, S. R.; Stewart, J. L.; Watson, L. A.; Williams, B. S. Inorganic chemistry and IONiC: An online community bringing cutting-edge research into the classroom. *Inorg. Chem.* **2011**, *50*, 5849–5854.

[71] Moore, E. G.; Xu, J.; Jocher, C. J.; Werner, E. J.; Raymond, K. N.; Iii, E. " Cymothoe sangaris ": An Extremely Stable and Highly Luminescent 1 , 2-Hydroxypyridinonate Chelate of Eu (III) " Cymothoe sangaris ": An Extremely Stable and Highly Luminescent. *J. Am. Chem. Soc.* **2006**, *64*, 1–3.

[72] Moore, E. G.; Xu, J.; Jocher, C. J.; Castro-Rodriguez, I.; Raymond, K. N. Highly luminescent lanthanide complexes of 1-hydroxy-2-pyridinones. *Inorg. Chem.* **2008**, *47*, 3105–3118.

[73] Llunell, M.; Casanova, D.; Cirera, J.; Alemany, P.; Alvarez, S. Shape (2.1). 2013.

[74] Pinsky, M.; Avnir, D. Continuous Symmetry Measures. 5. The Classical Polyhedra. *Inorg. Chem.* **1998**, *37*, 5575–5582.

[75] Cirera, J.; Ruiz, E.; Alvarez, S. Shape and spin state in four-coordinate transition-metal complexes: The case of the d6 configuration. *Chem. Eur. J.* **2006**, *12*, 3162–3167.

[76] Casanova, D.; Cirera, J.; Llunell, M.; Alemany, P.; Avnir, D.; Alvarez, S. Minimal Distortion Pathways in Polyhedral Rearrangements. *J. Am. Chem. Soc.* **2004**, *126*, 1755–1763.

[77] Casanova, D.; Llunell, M.; Alemany, P.; Alvarez, S. The rich stereochemistry of eight-vertex polyhedra: A continuous shape measures study. *Chem. Eur. J.* **2005**, *11*, 1479–1494.

[78] Hendrickx, M. F. A.; Mironov, V. S.; Chibotaru, L. F.; Ceulemans, A. An Ab initio study of the ligand field and charge-transfer transitions of Cr(Cn)63- and Mo(CN)63-. *J. Am. Chem. Soc.* **2003**, *125*, 3694–3695.

[79] Dolg, M.; Stoll, H.; Preuss, H. A combination of quasirelativistic pseudopotential and ligand field calculations for lanthanoid compounds. *Theor. Chim. Acta* **1993**, *85*, 441–450.

[80] Dolg, M.; Stoll, H.; Savin, A.; Preuss, H. Energy-adjusted pseudopotentials for the rare earth elements. *Theor. Chim. Acta* **1989**, *75*, 173–194.

[81] Jiang, Z.-X.; Liu, J.-L.; Chen, Y.-C.; Liu, J.; Jia, J.-H.; Tong, M.-L. Lanthanoid single-ion magnets with the LnN <sub>10</sub> coordination geometry. *Chem. Commun.* **2016**, *52*, 6261–6264.

[82] Liu, J.; Chen, Y. C.; Liu, J. L.; Vieru, V.; Ungur, L.; Jia, J. H.; Chibotaru, L. F.; Lan, Y.; Wernsdorfer, W.; Gao, S.; Chen, X. M.; Tong, M. L. A Stable Pentagonal Bipyramidal Dy(III) Single-Ion Magnet with a Record Magnetization Reversal Barrier over 1000 K. *J. Am. Chem. Soc.* **2016**, *138*, 5441–5450.

[83] Zhang, P.; Zhang, L.; Wang, C.; Xue, S.; Lin, S. Y.; Tang, J. Equatorially coordinated lanthanide single ion magnets. *J. Am. Chem. Soc.* **2014**, *136*, 4484–4487.

[84] Oyarzabal, I.; Ruiz, J.; Seco, J. M.; Evangelisti, M.; Camón, A.; Ruiz, E.; Aravena, D.; Colacio, E. Rational electrostatic design of easy-axis magnetic anisotropy in a ZnII-DyIII-ZnIIsingle-molecule magnet with a high energy barrier. *Chem. Eur. J.* **2014**, *20*, 14262–14269.

[85] Gavrikov, A. V.; Efimov, N. N.; Dobrokhotova, Z. V.; Ilyukhin, A. B.; Vasilyev, P. N.; Novotortsev, V. M. Novel mononuclear Ln complexes with pyrazine-2-carboxylate and acetylacetonate co-ligands: remarkable single molecule magnet behavior of a Yb derivative. *Dalton Trans.* **2017**, *46*, 11806–11816.

[86] Biswas, S.; Bejoymohandas, K. S.; Das, S.; Kalita, P.; Reddy, M. L.; Oyarzabal, I.; Colacio, E.; Chandrasekhar, V. Mononuclear Lanthanide Complexes: Energy-Barrier Enhancement by Ligand Substitution in Field-Induced DyIIISIMs. *Inorg. Chem.* **2017**, *56*, 7985–7997.

[87] Ma, P.; Hu, F.; Wan, R.; Huo, Y.; Zhang, D.; Niu, J.; Wang, J. Magnetic double-tartaric bridging mono-lanthanide substituted phosphotungstates with photochromic and switchable luminescence properties. *J. Mater. Chem. C* **2016**, *4*, 5424–5433.

[88] Sun, W.-B.; Han, B.-L.; Lin, P.-H.; Li, H.-F.; Chen, P.; Tian, Y.-M.; Murugesu, M.; Yan, P.-F. Series of dinuclear and tetranuclear lanthanide clusters encapsulated by salen-type and β-diketionate ligands: single-molecule magnet and fluorescence properties. *Dalton Trans.* **2013**, *42*, 13397.

[89] Ge, J. Y.; Cui, L.; Li, J.; Yu, F.; Song, Y.; Zhang, Y. Q.; Zuo, J. L.; Kurmoo, M. Modulating Single-Molecule Magnetic Behavior of a Dinuclear Erbium(III) Complex by Solvent Exchange. *Inorg. Chem.* **2017**, *56*, 336–343.

[90] Xue, S.; Zhao, L.; Guo, Y.-N.; Deng, R.; Guo, Y.; Tang, J. A series of tetranuclear lanthanide complexes comprising two edge-sharing triangular units with field-induced slow magnetic relaxation for Dy4 species. *Dalton Trans.* **2011**, *40*, 8347.

[91] Yao, B.; Gu, B.; Su, M.; Li, G.; Ma, Y.; Li, L.; Wang, Q.; Cheng, P.; Zhang, X. Single-molecule magnet behavior in a mononuclear dysprosium(III) complex with 1-methylimidazole. *RSC Advances* **2017**, *7*, 2766–2772.

[92] Görller-Walrand, C.; Binnemans, K. In *Handbook on the Physics and Chemistry of Rare Earths*; Gschneidner, K. A. J., Erying, L., Eds.; 1998; Vol. 25; Chapter 167, pp 101–264.

[93] Origin (OriginLab, Northampton, MA).

[94] Schäffer, C. E. A perturbation representation of weak covalent bonding. *Struct. Bond.* **1968**, *5*, 68–95.

[95] Rana, R.; Shertzer, J.; Kaseta, F.; Garvey, R.; Rana, D.; Feng, S. Optical spectra and energy level analysis of Dy(III): LaCl3. *J. Chem. Phys.* **1988**, *88*, 2242–2248.

[96] Ryabov, I. D. On the operator equivalents and the crystal-field and spin Hamiltonian parameters. *Appl. Magn. Reson.* **2009**, *35*, 481–494.

[97] Roos, B. O.; Taylor, P. R.; Siegbahn, E. M. A complete active space SCF method (CASSCF) using a density matrix formulated super-?CI approach. *Chem. Phys.* **1980**, *48*, 157–173.

[98] Ungur, L.; Van den Heuvel, W.; Chibotaru, L. F. Ab initio investigation of the non-collinear magnetic structure and the lowest magnetic excitations in dysprosium triangles. *New J. Chem.* **2009**, *33*, 1224.

[99] Shannon, R. D. Revised Effective Ionic Radii and Systematic Studies of Interatomie Distances in Halides and Chaleogenides. *Acta Cryst.* **1976**, *A32,*, 751–767.

[100] Comba, P.; Daumann, L. J.; Klingeler, R.; Koo, C.; Riley, M. J.; Roberts, A. E.; Wadepohl, H.; Werner, J. Correlation of Structural and Magnetic Properties in a Set of Mononuclear Lanthanide Complexes. *Chem. Eur. J.* **2018**, *24*, 5319–5330.

[101] Leuenberger, M. N.; Loss, D. Spin tunneling and phonon-assisted relaxation in-acetate. *Phys. Rev. B: Condens. Matter* **2000**, *61*, 1286–1302.

[102] Frisch, M. J. et al. Gaussian 09. 2009.

[103] Ellens, A.; Andres, H.; Meijerink, A.; Blasse, G. Spectral-line-broadening study of the trivalent lanthanide-ion series.I. Line broadening as a probe of the electron-phonon coupling strength. *Phys. Rev. B: Condens. Matter* **1997**, *55*, 173–179.

[104] Ellens, A.; Andres, H.; ter Heerdt, M.; Wegh, R.; Meijerink, A.; Blasse, G. Spectral-line-broadening study of the trivalent lanthanide-ion series.II. The variation of the electron-phonon coupling strength through the series. *Phys. Rev. B: Condens. Matter* **1997**, *55*, 180–186.

[105] Kiel, A. Temperature-dependent linewidth of excited states in crystals. I. Line broadening due to adiabatic variation of the local fields. *Phys. Rev.* **1962**, *126*, 1292–1297.

[106] Jørgensen, C. K.; Judd, B. R. Hypersensitive pseudoquadrupole transitions in lanthanides. *Mol. Phys.* **1964**, *8*, 281–290.

[107] Gruen, D. M.; Dekock, C. W.; McBeth, R. L. Electronic Spectra of Lanthanide Compounds in the Vapor Phase. *Adv. Chem.* **1967**, *71*, 102–121.

[108] Gruen, D. M. Absorption Spectra of Gaseous NdBr3 and NdI3. *J. Chem. Phys.* **1966**, *45*, 455.

[109] Peacock, R. D. The intensities of lanthanide f-f transitions. *Rare Earths* **1975**, *22*, 83–122.

[110] Choppin, G. R.; Fellows, R. L. Hypersensitivity in complexes of Nd(III) and Ho(III) with monobasic ligands. *J. Coord. Chem.* **1974**, *3*, 209–215.

[111] Fellows, R. L.; Choppin, G. R. Hypersensitivity in complexes of neodymium(III) and holmium(III) with dibasic and polybasic ligands. *J. Coord. Chem.* **1974**, *4*, 79–85.

[112] Henrie, D. E.; Fellows, R. L.; Choppin, G. R. Hypersensitivity in the electronic transitions of lanthanide and actinide complexes. *Coord. Chem. Rev.* **1976**, *18*, 199–224.

[113] Sommerer, S. O. Absorption Spectra of Lanthanide Complexes in Solution. *Appl. Spectrosc. Rev.* **1991**, *26*, 151–202.

[114] Misra, S. N.; John, K. Difference and Comparative Absorption Spectra and Ligand Mediated Pseudohypersensitivity for 4f-4f Transitions of Pr(III) and Nd(III). *Appl. Spectrosc. Rev.* **1993**, *28*, 285–325.

[115] Katzin, L. I. Absorption and circular dichroic spectral studies of europium(III) complexes with sugar acids and amino acids, with remarks on "hypersensitivity". *Inorg. Chem.* **1969**, *8*, 1649–1654.

[116] Rechkemmer, Y.; Fischer, J. E.; Marx, R.; Doerfel, M.; Neugebauer, P.; Horvath, S.; Gysler, M.; Brock-Nannestad, T.; Frey, W.; Reid, M. F.; van Slageren, J. Comprehensive Spectroscopic Determination of the Crystal Field Splitting in an Erbium Single-Ion Magnet. *J. Am. Chem. Soc.* **2015**, *137*, 13114–13120.

[117] Goff, G. S.; Cisneros, M. R.; Kluk, C.; Williamson, K.; Scott, B.; Reilly, S.; Runde, W. Synthesis and structural characterization of molecular Dy(III) and Er(III) tetra-carbonates. *Inorg. Chem.* **2010**, *49*, 6558–6564.

[118] Fry, J. L.; Caspers, H. H.; Rast, H. E.; Miller, S. A. Optical Absorption and Fluorescence Spectra of Dy(III) in LaF3. *J. Chem. Phys.* **1968**, *2342*, 2342–2348.

Acknowledgements

First and foremost, I would like to thank my supervisor, Prof. Dr. Peter Comba for his guidance and continuous support. Not only did he provide mentoring scientifically but also more broadly (including on the ski slopes). I greatly appreciate the opportunity to come and study here in Heidelberg, for the chance to expand my chemistry knowledge into the more theoretical side, and for the challenge of doing both experimental and computational work.

I would also like to thank my co-supervisor, Prof. Dr. Rüdiger Klingeler, for his helpful feedback and input on my progress.

Dr. Bodo Martin, thank you for all your help, input, mentoring and extensive knowledge in theoretical chemistry. Thanks also for racing down slopes with me and correcting my english every now and then.

I am the grateful recipient of a scholarship and must acknowledge the Heidelberg Graduate School of Mathematical and Computational Methods for the Sciences (HGS MathComp), founded by DFG grant GSC 220 in the German Universities Excellence Initiative.

Computational work was partly carried out on the computers of the Interdisciplinary Center for Science Computing (IWR) and the cluster JUSTUS of the Baden-Würtemberg HPC (bwHPC). Acknowledgement must also go to the support by the state of Baden-Würtemberg through bwHPC and the German Research Foundation (DFG) through the grant number INST 40/467-1 FUGG.

Thanks to Prof. Dr. Mark Riley for his work on the ligand field theory calculations. Thanks Mark also for allowing me to gain experience in the MCD lab, for all your help and expertise and for dragging me out of the lab on a Sunday night to have dinner with your family.

To Herr Dr. Dennis Müller for a comprehensive introduction into SMMs and all things MOLCAS. Thanks also for proof reading my abstract and answering my questions even long after graduating.

Thank you to Dr. Changhyun Koo for always having time to answer my silly questions.

Prof. Dr. Lena Daumann, thank you for your enthusiasm and encouragement, for helping me in the early stages of my project and for being a great friend.

Prof. Dr. Rajaraman Gopalan, thank you for a great conference/workshop in India on SMMs and the opportunity to interact with others in the field. Also, for your input at conferences and, more recently, for answering last minute questions.

To the members of AK Comba/Linti, past and present, thanks for all the cake. Bianca Pokrandt und Maik Jakob für die liebe Unterstützung. Als ich erst angekommen bin bis jetzt, wart ihr immer offen und freundlich, und ihr habt mir riesig geholfen hier wohl zu fühlen. Katharina Bleher, Miriam Starke and Steffen Ott for sessions in the gainz room. Thomas Josephy, for his collaboration in the lab. To everyone for being generally lovely as well as for all the BBQs, coffee breaks, interesting conversations and ice-cream: Saskia Krieg, Patrick Cieslik, Pardeep Kumar, Dieter Faltermeier, Daniela Guzmán Angel, Marko Hermsen, Dr. Marion Kerscher, Dr. Velmurugan Gunasekaran, Prof. Dr. Ashutosh Gupta, Michael Gast, Philipp Siebenbürger and Philipp Butzug, as well as Dr. Michael Grosshauser, Dr. Katharina Rück, Dr. Annika Eisenschmidt, Dr. Johannes Straub, Dr. Nina Butzug, Dr. Tulika Gupta, Tanju Eligüzel, Christina Schneider.

Marlies von Schönebeck-Schilli and Karin Stelzer for keeping us all in check, for making administration bearable, and for being so friendly.

Thank you also to my Forschis: Ben Thomitzni, Thines Kanagasundaram, Christoph Brunken and Ezgi Ojala. Thank you all for your hard work, cooperation and perseverance.

My dear friends, Victoria Ponce, Diego Costa and Fereydoon Taheri, thanks for all the arguments I was able to witness and enjoy. But truly, thank you for your friendships. And to the rest of the Friday crew - Michael Gabel, Priyata Kalra, Julia Jäger,

Lutz Büch, Mangayarkarasi Rajakrishnan and Priscilla Costa - thanks for all the parties, sleep overs, water balloon fights, outings and forgotten evenings.

Dr. Simone Bosch for supporting me in every way possible, especially in getting settled in to life in Heidelberg. You really have helped me in so many ways. From paying for my coffees to translating my abstract. Thank you also to the entire Bosch family for being so welcoming on so many occasions. Danke schön!

Thank you to the Emig family as well, for a very special first Christmas here in Germany.

To the many people I have shared a flat with, cheers for all the chats, chips and chocolates. Cheers to Linda, Natalie, Patrick, Matthias, Jana, Volker, Franzi and Katrin. Thanks especially to Leonie Weber, Hülya Erbil and William Strigel - for being generally awesome.

A big thanks also to the Awesome Potatoes for making Wednesday evenings something to look forward to.

To Emil, Deni, Safak, and Ecem for the wonderful friendships, and Emil for helping me cycle my furniture across town.

To my window buddies back in Australia: Myles Atkinson, Jessica Bilyj and Dr. Tim Zerk, it was a pleasure to banter with you once again. Cheers also to Blake Connolly for his general knowledge about computers and helping me pimp my laptop. To Dr. Tri Le for not throwing me into the recycling bin.

Emeritus Prof. Lawrence Gahan for the cross-continental swivel chair. Thank you for your continual support and mentoring. For your encouragement and also for knocking sense into me every now and then. Oh yeah, and for proof reading my thesis, mustn't forget to mention that.

Thank you to all my wonderful friends in Australia for providing support from afar. Thank you especially to Amy, Tegen, Bethan and Rohin for random messages, visits, and everything else. You guys are the best.

To my FameLab champion, Dr. Veli Vural Uslu. You have unfortunately had to deal with the worst sides of me the past few weeks. Thank you for all the breakfasts, ice-cream, coffee, tea, walks, drives, movies, chats and everything else that you do to keep me sane. I don't know how I would have survived this time without you.

Finally to my family, who I have very unkindly abandoned for the past three years, thank you for your ongoing support in this crazy endeavour of mine. To Kamala, Michael, Jimmy and Gordy, to Arun and Nat, and to my dear parents, you are amazing.

Eidesstattliche Versicherung gemäß § 8 der Promotionsordnung der Naturwissenschaftlich-Mathematischen Gesamtfakultät der Universität Heidelberg

1. Bei der eingereichten Dissertation zu dem Thema

Experimental and computational investigations into the ligand field effects
on the anisotropy of mononuclear 4f complexes

handelt es sich um meine eigenständig erbrachte Leistung.

2. Ich habe nur die angegebenen Quellen und Hilfsmittel benutzt und mich keiner unzulässigen Hilfe Dritter bedient. Insbesondere habe ich wörtlich oder sinngemäß aus anderen Werken übernommene Inhalte als solche kenntlich gemacht.

3. Die Arbeit oder Teile davon habe ich wie folgt/bislang nicht1) an einer Hochschule des In- oder Auslands als Bestandteil einer Prüfungs- oder Qualifikationsleistung vorgelegt.

Titel der Arbeit:

Hochschule und Jahr:

Art der Prüfungs- oder Qualifikationsleistung:

4. Die Richtigkeit der vorstehenden Erklärungen bestätige ich.

5. Die Bedeutung der eidesstattlichen Versicherung und die strafrechtlichen Folgen einer unrichtigen oder unvollständigen eidesstattlichen Versicherung sind mir bekannt.

Ich versichere an Eides statt, dass ich nach bestem Wissen die reine Wahrheit erklärt und nichts verschwiegen habe.

Heidelberg 05.06.2018
Ort und Datum

Unterschrift

---

1) Nicht Zutreffendes streichen. Bei Bejahung sind anzugeben: der Titel der andernorts vorgelegten Arbeit, die Hochschule, das Jahr der Vorlage und die Art der Prüfungs- oder Qualifikationsleistung.

12/2012